

NASA Contractor Report 174917

Confined Turbulent Swirling Recirculating Flow Predictions

M.T. Abujelala and D.G. Lilley

*Oklahoma State University
Stillwater, Oklahoma*

May 1985

Prepared for
Lewis Research Center
Under Grant NAG 3-74



National Aeronautics and
Space Administration

TABLE OF CONTENTS

Chapter	Page
I. INTRODUCTION	1
1.1 Turbulent Swirling Flow and Its Observed Physical Features	1
1.2 Practical Need and Method of Investigation of Swirling Flows	3
1.3 The Present Study Objectives	4
1.4 Outline of the Thesis	6
II. PREVIOUS STUDIES IN TURBULENT SWIRLING FLOW	8
2.1 Introduction	8
2.2 Numerical Analysis of Swirling Flows	8
2.2.1 Numerical Techniques	8
2.2.2 Accuracy of the Predictions	9
2.3 Experimental Investigation of Swirling Flows . .	12
2.3.1 Measurement Techniques	12
2.3.2 Experimental Study Findings	12
2.4 Summary of the Chapter	14
III. THE STARPIC COMPUTER CODE	15
3.1 Introduction	15
3.2 Flow Equations and Grid System	16
3.3 Computational Techniques	17
3.4 Boundary Conditions	19
3.5 Code Deck Descriptions	21
3.6 Closure	22
IV. TURBULENCE MODELING OF TURBULENT FLOWS	23
4.1 Introduction	23
4.2 Turbulent Flow Structure	24
4.3 Turbulence Modeling Approach	25
4.4 A Brief Review of Turbulence Models	28
4.4.1 Prandtl Mixing Length Model	28
4.4.2 Energy Model (Prandtl's 1945 Model) . . .	29
4.4.3 Two-Equation Models of Turbulence	30
4.4.4 Stress-Equation Models	31
4.4.5 Algebraic Stress Models	33
4.5 Summary	33

Chapter	Page
V. THE k - ϵ TURBULENCE MODEL AND RECENT EXTENSIONS	35
5.1 The k - ϵ Turbulence Model	35
5.2 The k - ϵ Empirical Constants	36
5.3 Shortcomings of the k - ϵ Model	37
5.4 Previous Proposed Extensions	39
5.5 Closure	42
VI. TURBULENCE PARAMETERS DEDUCTION FROM SWIRLING CONFINED FLOW MEASUREMENTS	43
6.1 Introduction	43
6.2 Analytic Inverse Methods	44
6.3 Findings and Discussion	44
6.3.1 Assumptions and Parameters Normalizations	45
6.3.2 Effects of Swirl on Turbulence Parameters	46
6.3.3 Effects of Strong Contraction Nozzle on Turbulence Parameters	48
6.4 Closure	49
VII. EXTENSION OF THE k - ϵ TO CONFINED SWIRLING RECIRCULATING FLOWS	50
7.1 Introduction	50
7.2 Previously Proposed Extension and Its Invalidity	51
7.3 Parameter Optimization from Time-Mean Data	52
7.4 C_μ Formulation From Detailed Turbulence Data	54
7.5 Predictive Capability of C_μ Formulation vs. Optimized Parameters	55
7.6 Validity of Standard k - ϵ Model and C_μ Formulation	56
7.6.1 Time-Mean Axial and Swirl Velocities	56
7.6.2 Zero Velocity Envelope and Time-Mean Centerline Velocity	57
7.6.3 Turbulence Parameters	57
7.6.4 Summary	58
7.7 Validation of the Proposed C_μ Formulation for Nonswirling and Pipe Flow Applications	58
7.8 Closure	59
VIII. GENERAL PREDICTIONS FOR CONFINED TURBULENT SWIRLING FLOW	60
8.1 Scope and Method of Approach	60
8.2 Effects of Convergence Criterion and Inlet Boundaries on the Prediction Accuracy	61

Chapter	Page
8.2.1 Effect of Refinement of Convergence Criterion	62
8.2.2 Effect of Inlet Boundary Specifications	63
8.2.2.1 Effect of Inlet Kinetic Energy Profiles	63
8.2.2.2 Effect of Inlet Velocity Profiles	64
8.3 General Predictions for Flowfield with $D/d = 2$	69
8.3.1 Effects of Swirl Strength	70
8.3.2 Effects of Downstream Contraction Nozzle	71
8.4 General Predictions for Flowfield with $D/d = 1.5$	73
8.4.1 Effects of Swirl Strength	73
8.4.2 Effects of Downstream Contraction Nozzle	73
8.5 General Predictions for Flowfield with $D/d = 1$	74
8.5.1 Effects of Swirl Strength	74
8.5.2 Effects of Downstream Contraction Nozzle	75
8.6 General Predictions with Standard $k-\epsilon$ Model	75
8.7 Summary and Discussion	76
8.7.1 Effects of Expansion Ratio and Swirl Strength	76
8.7.2 Superiority of the C_μ Formulation Model	77
8.8 Closure	78
IX. CONCLUSIONS AND RECOMMENDATIONS	79
9.1 Conclusions	79
9.2 Recommendations	80
REFERENCES	81
APPENDIX A - TABLES	91
APPENDIX B - FIGURES	147

NOMENCLATURE

A	- Combustion chamber cross-sectional area
a	- Downstream nozzle area
C_1, C_2, C_μ	- k- ϵ model constants
D	- Combustion chamber diameter
d	- Inlet nozzle diameter
k	- Kinetic energy of turbulence
L	- Contraction nozzle downstream distance
ℓ	- Length scale
R	- Inlet nozzle radius = d/2
s	- Swirl number
$v=u, v, w$	- time-mean velocity (in x-, r-, θ directions)
x, r, θ	- Axial, radial azimuthal cylindrical polar coordinates
X	- Downstream distance from domain inlet
ϵ	- Turbulence energy dissipation rate
ϕ	- Swirl vane angle with respect to facility axis (except in Chapter III)
μ	- Turbulent viscosity
ρ	- Time-mean density
Ψ	- Stream function
ω	- Vorticity
γ	- Kinematic viscosity

Subscripts

n	- Relating to Swirler hub
m	- Station maximum value
o	- Value at inlet to flowfield
x	- Relating to axial direction
θ	- Relating to swirl direction

Superscripts

$()_t$	- Time-mean average
$()'$	- Fluctuating quantity

CHAPTER I

INTRODUCTION

1.1 Turbulent Swirling Flow and Its Observed Physical Features

Turbulent swirling flows are of considerable practical importance. In heat generators, the designers of combustion chambers and industrial furnaces generate swirl to assist in the stabilization of the flame and to promote rapid mixing. In heat transfer devices, the swirling flow is utilized to increase the rate of heat transfer. And in nature, swirl creates a drag force by causing trailing vortices which occur when the separated flow over the aircraft wings rolls up into vortex cores at the wing tips. The swirl can be imparted to the flow by different means. The physical geometry and aerodynamic purpose are the main factors which lead to the method of imposing swirl on flowfields, adjustable vane swirlers, rotating the inner or the outer cylinders of annular flows, tangential inlet jets, and other techniques. The degree of swirl usually is characterized by the swirl number S , which is a nondimensional number representing axial flux of swirl momentum divided by axial flux of axial momentum times equivalent nozzle radius. It is described at length in References 1 through 3 and in Section 8.2.2.2 of Chapter 8.

Swirling flows have been classified by King et al. (4) according to the wall boundary conditions as follows:

1. Unconfined swirling flows where the wall effects are negligible.

2. Confined swirling flows in short, large-diameter chambers where side wall effects strongly interact with the swirl to produce significant secondary flows.

3. Confined swirling flows in tubes where circumferential wall effects interact strongly with the swirl flow.

The time-mean and the turbulence characteristics of swirling flow are generally affected by the wall boundary. A swirling flow in a stationary duct or annulus possesses the characteristics of a vortex motion with axial motion along the duct or annulus. The swirl motion decays, and the flow characteristics approach those of a pure axial flow. The axial and swirling velocities of swirling flow in an annulus with the inner cylinder rotated, develop with distance along the annulus and become fully developed at certain lengths (5).

Vortex breakdown has been observed in the swirling flows through nozzles and diffusers, and in combustion chambers. The occurrence and place of vortex breakdown depend on a balance between the magnitude of the swirl, the external pressure gradient, and the degree of divergence of the flow. The greater the adverse pressure gradient, or the degree of divergence, the lesser is the swirl that is needed for the vortex core to breakdown, and the higher the swirl, the more the breakdown moves up into position from downstream (6). A vortex core forms after the occurrence of the vortex breakdown phenomena and establishment of a reverse flow zone. It processes about the axis of the flow on the boundary between the zero velocity and the zero streamline. A variety of forms of vortex breakdown and their characteristics has been recently

identified by Leibovich (7). Most recently, a book edited by Swift et al. (8) has brought together recent developments in studies of vortex flows.

Experimental and numerical studies (2, 9-11) show that swirl has effects on turbulent flows; jet growth, entrainment, and decay; and flame size, shape, stability, and combustion intensity are affected by the degree of swirl imparted to the flow. It is found that the swirling jets spread more quickly and the mean velocity decays more rapidly than in a nonswirling jet. In duct flows, at high swirl strength, back flow can occur in the central region of the flow. The central back flow plays an important role in flame stabilization by providing a hot flow of recirculated combustion products and a reduced velocity region where flame speed and flow velocity can be matched.

1.2 Practical Need and Method of Investigation of Swirling Flows

Because of the inherent importance of swirling flows in many engineering applications, their investigation has been the subject of continued interest of many fluid mechanic researchers. The field of turbomachinery is among the various implementations of the swirling flow. The increased interest in high performance of this equipment produced the need to minimize the losses through the engine components. Chief among these components are the combustors. Combustor losses are mainly attributed to pressure drop, incomplete combustion and flame stabilization problems. The most fruitful avenue of approach to eliminate these losses is through understanding the phenomena which generate them. This can be accomplished through accurate knowledge of the characteristics of the combustor design parameters.

The understanding of the detailed nature of the behavior of the swirling flows can be aided not only by experiments, but also by their predictions. Early attempts to predict swirling flows with simple boundary and geometric conditions, and with constant fluid properties followed the integral approach, that is, velocity profiles were assumed for the flow and the integral equations of motion were solved (12, 13). Recently, a more general prediction method has been used. This solves the motion governing differential equations rather than the integral equations via mathematical models incorporating numerical finite difference computer codes. Improvement and use of these techniques will significantly increase understanding and reduce the time and cost of development.

The present study forms a theoretical part of a project on the investigation of flowfields found in typical combustor geometries. The partial differential equations of conservation of mass, momentum (in x , r , and θ directions), turbulence kinetic energy and its dissipation are solved using an advanced version (14), called STARPIC, of the Imperial College TEACH-T computer program (15). This code solves the corresponding finite difference equations of the motion governing equations using a semi-implicit line-by-line method for values at points of a variable size rectangular grid, with variable under-relaxation. The turbulence characteristics are described by a modified version of the k - ϵ turbulence model. This code will be described in more detail in Chapter 3.

1.3 The Present Study Objectives

The present study is directed towards an understanding of the aerodynamics of the flow occurring in an isothermal can-type combustor

flowfield. To attain this goal of more accurate prediction of the characteristics of the flowfield under consideration, the following objectives are considered.

1. Evaluating the sensitivity of the predicted results to different inlet boundary condition types.
2. Investigate the effects of the degree of contraction of the flow at the exit of the domain.
3. Develop an advanced version of the $k-\epsilon$ turbulence model to more accurately predict confined turbulent swirling recirculating flows.
4. Perform experimental tests as needed to verify the precision of the theoretical developments.

The first of these is intended to demonstrate the need to use realistic inlet boundary conditions in order to predict more correctly the subsequent flowfield. The second objective increases the range of application of the code by the inclusion of downstream contraction nozzle effects. The development of a suitable advanced turbulence model from detailed turbulence measurements is the subject of objective 3. The resulting powerful model is to be expected to simulate the flowfield more realistically, and predictions are made to demonstrate this.

From an economical point of view, it is necessary to use computational fluid dynamics procedures rather than experimental approaches for a better definition and understanding of the flowfields in the combustor. However, the most viable approach would be for a parallel, interactive, theoretical and experimental program to be used. Thus, the last objective of this study is to perform experimental tests as needed to verify the precision of the theoretical developments.

1.4 Outline of the Thesis

The first chapter of this nine-chapter thesis is the introduction. Turbulent swirling flows and their observed physical features are briefly described. This chapter highlights some of the practical needs and methods of investigation of the swirling flows. Finally, the objectives of the present study was stated and justified.

Chapter II presents the method of investigation of swirling flows. Both numerical and experimental studies of other workers are explored. The experimental study findings and the accuracy of the predictions of those workers are discussed.

The flow governing equations, the grid system and the computational techniques employed in computer code (STARPIC) of the present study are presented in Chapter III. The boundary conditions imposed and the code deck are also discussed in this chapter.

Chapter IV provides a brief description of the structure of turbulent flows and the mathematical models which are expected to represent the flow behavior. This chapter is concerned with the survey of the contributions of many workers to the understanding of the characteristics of turbulent flows, and with the turbulent flow structure and its modeling approaches. Various turbulence models are discussed: Prandtl mixing length, energy, one- and two-equation models, algebraic and Reynold stress closures. Among the two-equation models, is the $k-\epsilon$ turbulence model. This model is the subject of the following chapter.

The structure of the $k-\epsilon$ turbulence model and method of evaluating its constants are reported in Chapter V. This chapter exhibits the previously proposed extensions of the $k-\epsilon$ model and the limitation of each extension. Chapter V provides the background for the extension of

the $k-\epsilon$ model to applications in turbulent confined swirling flows, as shown in Chapter VII.

Chapter VI, on the other hand, analyzes recent turbulence measurements, provided by another worker, to investigate the flow boundary and swirl strength effects on the characteristics of the turbulence parameters. Also this chapter provides useful information that helps in extending the $k-\epsilon$ model to the cited flow type.

A validation study of the previously proposed extension of the $k-\epsilon$ turbulence model to swirling flow applications is conducted in Chapter VII. As a consequence of this validation, two extensions to this model are proposed: the first is accomplished by optimizing the model constants according to the available data; the second provides an empirical formulation for the $k-\epsilon$ model constant C_μ . The predictive capability of both extensions are tested by comparing the results with measurements obtained by other workers using a 5-hole pitot probe and a hot wire anemometer.

Finally, Chapters VIII and IX are the closing chapters of this effort. The former presents general predictions; the effects of imposed boundaries and swirling flow strength on the flowfield characteristics are all investigated at length. The boundary types include the inlet flow profile specifications, and the expansion and the contraction ratios at the inlet and at the exit of the flow domain, respectively. The latter, Chapter IX, summarizes the main conclusions of the present study.

There are also two appendices which provide the tables and figures which are presented in this study.

CHAPTER II

PREVIOUS STUDIES IN TURBULENT SWIRLING FLOW

2.1 Introduction

Numerous theoretical and experimental swirl flow combustion studies currently exist. The former have been obtained through the use of mathematical modeling of the combustor flow domain; usually finite difference techniques are employed in such modeling processes. Several text books (16, 17, 18), recent papers (11, 20-22) and more recently an international conference (19) exemplify studies and give soluable insight into our understanding of the swirl phenomenon. On the other hand, the latter have been conducted using different measurement techniques. Chief among these techniques are pitot probes, hot-wires and laser anemometers.

2.2 Numerical Analysis of Swirling Flows

2.2.1 Numerical Techniques

The flow of an incompressible viscous fluid in two space dimensions is most often treated by the stream function-vorticity ψ - ω formulation. However, the grid nonuniformities and high swirl produce problems in this technique (22). Also, the use of the stream function and vorticity as the dependent variables causes complications and difficulties in implementing the boundary conditions for closed systems. The advantage

of the stream function-vorticity technique in reducing the number of partial differential equations may be outweighed by the above difficulties.

To overcome the problems mentioned above in using ψ - ω formulation, more recent emphasis is being placed on direct solution for primitive variables p , u , v , and w instead of ψ - ω . This is based on the numerical solution of a finite difference representation of the Navier Stokes equations in primitive variable form.

Examples of the previous studies which have employed the aforementioned techniques are summarized and displayed in Table I. The essential differences between the various computer codes which were employed in these studies, are the method of deriving the finite difference equation for the set of governing equations, which were selected to simulate the physical process, and the location of variables in the grid system.

2.2.2 Accuracy of the Predictions

The capability of current computational fluid dynamic codes has been evaluated by many workers. Most recently, Sturgess (40) evaluated the physical modeling embodied in such codes. Such evaluation was achieved by a detailed comparison against related experimental data. It has been demonstrated that qualitatively correct predictions have been obtained for a variety of complex flows. Absolute accuracy has not yet been demonstrated. The discrepancy may be attributed to the physical model and numerical methods employed. Following are samples of the recent validation work found in the literature.

Hendricks and Brighton (41) investigated mixing of a turbulent jet with a coaxial slower-moving secondary stream in a constant diameter tube. The analysis involved a numerical solution of the governing flow equations which were simplified by the Prandtl boundary layer assumptions. The effective viscosity was calculated from a modified version of the two-equation turbulence model. They found that the predicted centerline velocity lags the experimental data by about one pipe radius while the maximum pressure point is arrived at about three radii too soon. However, the value of the predicted maximum wall pressure is in excellent agreement with the data. Also, it was found that the predictions of swirling flow were more accurate than of nonswirling ones. Generally, good agreement between the calculated results and the corresponding experimental data was obtained.

Predictions of isothermal and reacting flows in two dimensional combustor geometries were reported by Jones and McGuirk (42). Turbulent transport was approximated via a variable density form of the $k-\epsilon$ turbulence model. Their predictions for a two dimensional gaseous-fueled combustor indicated that the physical models used were capable of calculating the flow pattern and heat release fairly well.

An evaluation of currently available turbulence and combustion models as applied in gas turbine-like flows was performed by Syed and Sturgess (43). They used the $k-\epsilon$ model and the eddy breakup model in their predictions. They found that the turbulence model predicted mean flow quantities to an accuracy of about 85 percent in regions of parabolic flow and qualitatively well-predicted in elliptic flow regions. The size and strength of the recirculation zone were underpredicted by about 20 percent.

Morse (44) conducted theoretical and experimental work in order to evaluate the performance of turbulence models as applied to turbulent swirling flow. Performances of mean flow closures (Reynolds stresses components are assumed to be locally determined) and Reynolds stresses closure (Reynolds stresses are obtained from transport equations) were discussed in detail. He reported that the difference between the rate of spread of a round jet and a plane jet issuing into stagnant surroundings cannot be predicted using mean flow closures. In addition, these models fail to reflect the experimentally observed increase in spreading rate with swirl number. Also, he concluded that the Reynolds stresses model failed to bring good agreement for corresponding plane and axisymmetric shear flows.

A numerical simulation of the isothermal flow in a diffusion-flame research combustor was carried out by Sturgess and Syed (45). An axisymmetric finite difference solution of the time-averaged, steady-state, elliptic form of the Reynolds equations was used with closure provided by a two-equation turbulence model. This simulation gave acceptable agreement with experimental data in many respects, except the prediction of the recovery rate of a central near-wake region. The authors provided detailed explanation of the source of the discrepancy.

Generally, the findings of these studies show that turbulence modeling and numerical errors are not great enough to allow false conclusions to be drawn about the main physical characteristics of the flow. Also, it should be mentioned here that turbulent swirling flows are complex, and the level of accuracy and reliability of the predicted results strongly depend on the complexity of the flow.

2.3 Experimental Investigation of Swirling Flows

2.3.1 Measurement Techniques

Experimental observations of swirling flows have been made for a number of years. Their preliminary approach was by means of a pitot-static probe which consists of an open-ended tube placed to face the direction of the flow, together with another open-ended piece of tube placed at right angles to the direction of flow. Later, more elaborate equipment was used to measure the magnitude and direction of fluid velocity. This instrument is the 5-hole pitot probe. As more detailed flow characteristics were needed, the hot-wire anemometer was used. Very recently, Perry (46) described this tool in detail, in terms of a variety of constructions of hot wire applications and theories. Finally, the advent of a laser doppler velocimeter (LDV) has had a significant impact on data acquisition in complex flow under the combustion environment. Table II displays a collection of the previous studies which employed the aforementioned measurement techniques.

2.3.2 Experimental Study Findings

The relevance of the swirling flows to the aircraft industry has encouraged many researchers to study its characteristics. Mostly, the findings of these studies have been used for the evaluation of the capability of current computational fluid dynamics codes for use as a design and analysis tool in gas turbine combustor development. The following selected studies are provided to exemplify such investigations.

Murakami et al. (47) performed an experimental investigation of swirling flows in cylindrical ducts. Two different types of swirl flows, namely a forced and a free vortex type, were introduced in the test section. The former was introduced by an axial flow type impeller located in the swirl chamber, and the latter was developed by a radial guide vane swirler. It was found that the cited swirling flow shows three kinds of flow patterns in its course of decay: forced-free vortex type, transitional type, and forced vortex type. Also, it was found that the swirl strength decreases exponentially along the pipe axis and its decrement varies with the change of the flow pattern.

Swirling flows in stationary channels were investigated by Sukhovich (34). A stream of air was supplied to the working zone by a nozzle of area 0.7 times the channel area. The secondary, swirling flow was imparted to the flow through an annular gap, formed by the outer surface of the nozzle and the inner surface of the working tube. His analysis of the experimental data showed that the axial and tangential stresses are anisotropic and the turbulent viscosities depend on the swirl strength and coordinants. Also, he found that at high gradient of annular velocity and Richardson number, the turbulent viscosity for the tangential component of momentum is lower than the corresponding one for axial component of momentum.

Measurements in a model combustor composed of two confined coaxial swirling jets under noncombustion conditions were reported by Vu and Gauldin (38). Swirl for the inner jet was generated by a small axial flow swirl generator with fixed vanes, and that for the outer jet was imposed on the flow by adjustable vanes. Detailed time-mean and fluctuating flow measurements were obtained for coswirl and counterswirl

conditions with a directional pitot probe and hot-wire anemometer. It was noticed that the outer swirl has a strong effect on the formation of a recirculation zone and on mixing characteristics in the inner jet shear layer. Also, they found that high levels of turbulent fluctuations and large dissipation rates characterize the central flow region for both coswirl and counterswirl conditions, while the outer flow regions exhibit relatively low turbulence levels.

Confined turbulent swirling flow data obtained from a single hot-wire using the six-orientation techniques was reported by Jackson and Lilley (10). Swirl was imparted to the incoming flow by means of a variable angle flat vane swirler (3). The effects of swirl strength and degree of contraction of the flow at the exit of the flow domain were carefully examined. The effect of swirl on the time mean velocity field was found to shorten the corner recirculation zone length and to generate the existence of a central recirculation zone, which is followed by a processing vortex core region. The central recirculation zone was reduced and the turbulence levels and shear stresses were found to increase by introducing a nozzle of area reduction ratio of 4 located 2 chamber diameters downstream of the flowfield.

2.4 Summary of the Chapter

The material which is presented in this chapter exhibits the most relevant work to the subject of confined turbulent swirling flows. It provides valuable insight into the directions to be taken in the investigation of such flows, and affords an up-to-date data base to help in validating and improving of the physical models and numerical techniques.

CHAPTER III

THE STARPIC COMPUTER CODE

3.1 Introduction

In recent years, there has been considerable progress in the combustor flowfield predictions using finite-difference numerical procedures. Several fluid flow computational techniques have been employed to improve the flowfield simulation and turbulence modeling. These techniques included method of approach, grid system, numerical stability and many others.

The computer program STARPIC (acronym for Swirling Turbulent Axisymmetric Recirculating flow in Practical Isothermal Combustor geometries) is among the previous codes which are displayed in Table I. Most recently, the code has been expanded to include reacting flows (29, 48). The isothermal version of this code has been selected to be employed in the theoretical aspects of the present investigations. This selection was made because STARPIC is the best code yet available for predicting isothermal flowfields in axisymmetric combustor geometries. This code is an advanced version of the TEACH computer code (15). A complete description of the finally developed computer program, with a full explanation of the equations, source terms, revised cell volumes for axial and radial velocities, constants occurring and techniques for handling turbulent swirling flow near curved boundaries, is available (14). Therefore, it will be described only briefly in the following

sections, so that it will be available whenever is needed to refer to it.

3.2 Flow Equations and Grid System

The geometry under consideration and the corresponding experimental and solution domains are shown in Figures 1 and 2, respectively. It can be easily foreseen that recirculation zones will exist within the solution domain and as a consequence, the governing equations are elliptic. The set of axisymmetric governing equations may be compactly represented in the following appropriate form:

$$\frac{\partial}{\partial X} (\rho u \phi - \Gamma_{\phi} \frac{\partial \phi}{\partial X}) + \frac{\partial}{\partial r} [\rho v \phi - \Gamma_{\phi} \frac{\partial \phi}{\partial r}] = S_{\phi}^{\phi}$$

where ϕ is any of the flow variables (u, v, \dots etc). Γ_{ϕ} is the corresponding effective exchange coefficient and S_{ϕ}^{ϕ} is a source term. This equation may formally be integrated, over a typical cell, to yield:

$$\int_W^E [\rho u \phi - \Gamma_{\phi} \frac{\partial \phi}{\partial X}] dA + \int_S^N [\rho v \phi - \Gamma_{\phi} \frac{\partial \phi}{\partial r}] dA = \rho \int V S_{\phi}^{\phi} dV$$

where N, S, E, W and P refer to north, south, east, and west of the cell and the reference location in the cell, and A and V are the area of the cell boundary and the cell volume, respectively. If the variables are assumed to be linear inside the cell, the above equation can be rewritten as:

$$[\rho u \phi - \Gamma_{\phi} \frac{\partial \phi}{\partial X}]_E A_E - [\rho u \phi - \Gamma_{\phi} \frac{\partial \phi}{\partial X}]_W A_W + [\rho v \phi - \Gamma_{\phi} \frac{\partial \phi}{\partial r}]_N A_N - [\rho v \phi - \Gamma_{\phi} \frac{\partial \phi}{\partial r}]_S A_S = [S_P^{\phi} \phi_P + S_U^{\phi}] \times V$$

where Γ_{ϕ} , S_P^{ϕ} , and S_U^{ϕ} are tabulated for each ϕ in Table III. The left-hand side of this equation represents the total transport across the

cell boundaries by convection and diffusion. This resultant difference equation has the following form (49):

$$(A_p - S_p) \phi_p = \sum_n A_n \phi_n + S_u$$

where: \sum_n denotes summation over neighboring nodes of a typical grid node P; A_n are influence coefficients; and $A_p = \sum_n A_n$. The pressure is obtained by combining the continuity and momentum equations in the manner explained by Caretto et al. (50).

The flow domain is overlaid with a grid whose nodes are formed by the intersections of arbitrarily spaced coordinate lines. as shown in Figure 3. The u and v velocities, shown as arrows in the diagram, are located mid-way between the grid intersections. All other variables are located at the grid nodes. This staggered-grid system was originated by Harlow and Welch (51) and was earlier adopted by Patankar and Spalding (52) and many others. This grid arrangement has two special merits: first it places u and v velocities between the pressure that drives them, and it is easy to calculate the pressure gradients that effect them; and second, these velocities are directly available for the calculations of the convective fluxes across the boundaries of the control volumes surrounding the grid nodes (20). It should be noted that the axial velocity reference location is (I,J) even though it actually represents the velocity positioned at (I-1/2,J)

3.3 Computational Techniques

Solution of the system of finite difference transport equations with appropriate boundary conditions is achieved by means of an iteration procedure. Firstly an initial or intermediate value of the

pressure field is used to solve for an intermediate velocity field. Then, continuity is enforced, by solving the equations for pressure change and thereby determining the required adjustments to the pressures. Corrections to the pressure and velocity field are applied and the equations for the remaining variables are then solved in turn. The iteration is terminated when the correct solution satisfies the difference equations within a certain percentage of a global measure, such as the total mean flow rate or inlet momentum, depending on the variable in question (0.9 percent or less has been adopted for this study).

The value of ϕ at each grid node is related to its neighbors via

$$\phi_P = A_N^\phi \phi_N + A_S \phi_S + [A_E^\phi \phi_E + A_W^\phi \phi_W + S^\phi]$$

where N, S, E, and W are neighboring locations of P, the A's are coefficients combining the convection and diffusion effects of the flow and S^ϕ incorporates any existing source terms, which are calculated from the geometry, properties and dependent variables of the previous iterations. Convective and diffusive fluxes are determined from a hybrid difference scheme. Thus diffusion is neglected when the flow is highly convective and "upward difference" formulas are employed to express the differentials. On the other hand, when the diffusion is comparable with convection, the former is taken into account by employing a central difference numerical scheme. With the aid of a tri-diagonal algorithms and with the assumption that the quantity in brackets is known, all ϕ_P 's may be calculated along any grid line. In this manner, one can traverse along all the lines in a vertical direction sequentially from left to right of the integration domain.

In order to avoid numerical instabilities, under-relaxation has been employed, that is

$$\phi = f\phi_j + (1-f)\phi_{j-1}$$

where f is the under-relaxation factor $0 < f < 1$ and f equals 1 when applied to the pressure field, ϕ is the resultant value obtained from the present iteration cycle ϕ_j and the previous iteration cycle values ϕ_{j-1} . The optimum value of this factor depends on the geometry and the boundary conditions under consideration.

3.4 Boundary Conditions

At the inlet plane, all variables are given definite fixed values. The axial and radial velocity profiles can be flat or an experimental distribution. The swirl velocity profile can be assumed to be that of solid body rotation or any specific distribution. The swirl number and the velocity profile types are the important features of the inlet velocity profiles. The value of k is assumed to be:

$$k_i = 0.03 \times (u_i^2 + v_i^2 + w_i^2)$$

where i is the grid location across the inlet, while ϵ is calculated from:

$$\mu_t = C_\mu P k^2 / \epsilon$$

After μ_t is estimated by mixing length theory as shown below:

$$\mu_{t_i} = k_i^{3/2} / (0.005R)$$

where R is the combustion chamber radius.

Near the wall boundaries, tangential velocities are connected with their zero wall values by way of the tangential shear stress wall functions, and the normal velocities are given zero normal gradients. The ϵ values are fixed using the length scale near the wall and the current value of k . The k and pressure are given zero normal gradients everywhere except at the inlet.

At the center line, the axial velocity and energy dissipation rate gradients, and the radial velocity are set equal to zero, while the swirl velocity is assumed to be that of the solid body rotation. The axial velocities at the outlet are deduced from their upstream values by adding a fixed amount which ensures overall mass conservation. The radial velocities are assumed to be zero while the other variables are assigned zero gradients.

Since the flowfield boundaries are positioned midway between grid points, they coincide with normal velocities. This simplifies the insertion of specific boundary conditions by controlling the value of the coupling coefficients and the false source term. This will be clear if the difference equation is rewritten as:

$$\sum_n a_n (\phi_p - \phi_n) = S_p \phi_p + S_u$$

$$n = N, S, E, \text{ and } W$$

which implies that if any link, say a_s is broken and S_p is set equal to zero, then S_u represents the resulting flux of the neighbors. On the other hand, if the right hand side of the above equation is set equal to zero on the given boundary by using a false source term, then ϕ_p equals the specified boundary value.

3.5 Code Deck Descriptions

STARPIC has thirteen routines in addition to the main code. A detailed description of these routines is available (14). Here a brief summary of the main features of each code are given.

The main routine specifies the grid size and coordinates in addition to the values of the field parameters at the inlet plane. The present study added a section which automatically generates a stepped grid for simulation of the exit nozzle. Once the grid size and coordinates and the domain boundaries are specified, subroutine INIT is called to set values of numerous geometric quantities concerned with the grid structure, and to initialize most variables to zero or other reference values. Also, the main code controls the flow to the other routines for each iteration as shown in Figure 4. After convergence is obtained, the final results are printed out and/or stored on magnetic tapes or disks.

Subroutines CALCU, CALCV, CALCP, CALCW, CALCTE and CALCED are called in sequence for each iteration to update the axial and radial velocity fields, pressure, swirl velocity, kinetic energy and energy dissipation fields, respectively. Each of these routines calls PROMOD to modify the finite difference equation coefficients or other variables near walls or other boundaries where particular conditions apply. Once the call returns from PROMOD, routine LISOLV is called to update a particular variable over the entire flowfield by applying a TDMA technique to all the lines in the r-direction sequentially from left to right of the integration domain. Finally, fluid properties are updated by calling PROP, and the totals of the absolute residuals are calculated. This cycle is repeated until convergence is achieved.

3.6 Closure

This chapter has presented the numerical techniques and solution procedure incorporated in the STARPIC computer program by which the governing difference equations of the flowfield are solved. The techniques employed are general and flexible and may be applied to calculate various flow situations governed by different boundary conditions. Prediction of a turbulent recirculating swirling flow using this code will be accomplished in Chapter VIII of this study.

CHAPTER IV

TURBULENCE MODELING OF TURBULENT FLOWS

4.1 Introduction

Most flows occurring in nature and in engineering applications are turbulent. Among those which an engineer commonly considers are: those which are unconfined by walls, such as the smoke plume from an industrial stack; flows near one wall, such as that in the vicinity of a turbine blade and an aircraft wings; and those which are confined duct flows. Those flows are characterized by high levels of fluctuating vorticity.

There are many books which approach turbulence in descriptive and experimental ways. Among the older texts is Townsend's book (53), which analyzes a wealth of experimental information with deep physical insight. Tenneks and Lumley (54) described a wide variety of fluid phenomena and the basic tools of turbulence theories, while Launder and Spalding (55) have provided in their book the main concepts of turbulence modeling and have shown what progress had been made and what problems remained. Finally, Wolfgang, and Bradshaw et al. (56, 57) provided two recent books which present a lecture series on prediction methods and turbulence modeling of turbulent flows.

At the same time, many papers have given a considerable contribution to turbulent flow understanding. Launder and Spalding (58) reviewed the problem of making numerical predictions of turbulent flow.

A turbulence model that permits predictions of both near wall and free shear flow was developed and evaluated by experimental data, while Saffman (59) eliminated some uncertainty regarding boundary conditions imposed at or near a solid boundary from turbulence model equations. Launder et al. (60) gave particular attention to the approximation of the pressure-strain correlations, and presented numerical solutions of the model equations for a selection of strained homogeneous flow and for two-dimensional inhomogeneous shear flows. Finally, a phenomenological theory of turbulence was given by Golowin (61). For further reading see, for example, References (62) through (70).

4.2 Turbulent Flow Structure

Turbulent flow of an incompressible fluid may be considered as a super position of eddies of different scales. The motion of large eddies which obtain energy from the mean flow is unstable and results in smaller eddies which in turn feed even smaller ones. In other words, the energy cascades from eddies of low frequency to those of high frequency. This process continues until the kinetic energy of turbulence dissipates (viscous dissipation). If there is no continuous external source of energy, the turbulence will decay. However, the interaction between the turbulent stresses and the velocity gradient in the mean flow prevents the turbulence from decaying by supplying the energy through the frequency spectrum. This process is termed 'production' and the ratio of the production of energy to its viscous dissipation is a measure of the state of equilibrium of the flow.

The eddy size at a given location in the flowfield is determined mainly by the flow domain and the flow local viscosity. For

sufficiently large Reynolds numbers, the small scale turbulence fluctuations are expected to be statistically isotropic (the statistical properties of the turbulence have no preference for direction) and to exhibit a universal scale similarity in their spectral behavior. However, in the near wall region where the local Reynolds number decreases, the fine scale turbulence is no longer isotropic, regardless of how large the global Reynolds number becomes (71). The flow is not turbulent but viscous within the smallest eddies, and molecular effects are dominant (44). The gradient of the small scale eddies plays a dominant role in problems of heat and mass transfer by turbulence (72).

4.3 Turbulence Modeling Approach

From the discussion of the previous section, it can be concluded that the turbulent flow consists of large scale phenomena and small scale ones, and the characteristics of these scales are different. Therefore, it is very difficult to simulate them by the same approach. Large eddy simulation methods have been found useful in the study of large scale phenomena (73-76), and the small scale ones have been investigated by means of turbulent closure models (55, 77, 78). The former is a method midway between exact simulation and time-averaged modeled computation, which computes the large eddies explicitly and models only the small ones. Detailed descriptions of this method is beyond the scope of this study. The latter approach will be presented briefly in the next paragraphs.

The most widely used turbulence closure models today are the eddy viscosity models and the Reynolds stress model. The first approach is

based on the eddy viscosity concept, which relates the Reynold stresses to the mean velocity gradient via:

$$\overline{-\rho u_i u_j} = \mu_t \left(\frac{\partial u_i}{\partial x_j} + \frac{\partial u_j}{\partial x_i} \right) - \frac{2}{3} \rho k \delta_{ij} \quad (4.1)$$

where δ_{ij} is the kronecker delta, k is the kinetic energy of turbulence (defined as $1/2 \overline{u_i u_i}$) and μ_t is turbulent viscosity.

The forms of this equation appropriate to an axisymmetric flow are

$$\begin{aligned} \overline{-\rho u^2} &= 2 \mu_{xx} \frac{\partial u}{\partial x} - \frac{2}{3} \rho k \\ \overline{-\rho v^2} &= 2 \mu_{rr} \frac{\partial v}{\partial r} - \frac{2}{3} \rho k \\ \overline{-\rho w^2} &= 2 \mu_{\theta\theta} \frac{v}{r} - \frac{2}{3} \rho k \\ \overline{-\rho u v} &= \mu_{rx} \left(\frac{\partial u}{\partial r} + \frac{\partial v}{\partial x} \right) \\ \overline{-\rho u w} &= \mu_{x\theta} \frac{\partial w}{\partial x} \\ \overline{-\rho v w} &= \mu_{r\theta} r \frac{\partial}{\partial r} \left(\frac{w}{r} \right) \end{aligned} \quad (4.2)$$

From inspection of these equations, it is evident that for fully developed flow (v and $\frac{\partial u}{\partial x} = 0$) the normal stress components are equal, but in reality, the anisotropy is most pronounced. However, this defect is not too serious because the normal stress term is generally of minor importance in the Navier-Stokes equations for simple flows (e.g. thin shear layer flow). Also, the eddy viscosity concept breaks down in flow regions where the shear stresses and velocity gradient have opposite signs. Once again, this defect has little influence on the overall

predictions because regions with negative eddy viscosity (mathematically) are in most cases small (71). Another observation is that zero velocity gradient provides zero shear stress, however, in flows where the asymmetry is pronounced, the positions of zero shear stresses and zero velocity gradient do not coincide (79). Generally, there is a limit to the applicability of models of this type, but the seriousness of their inherent defects will vary from one flow case to another.

In the second approach (Reynolds stress model), individual turbulent stresses are represented by partial differential equations which may be derived from the Navier-Stokes equations. It should be noted that these equations contain correlations of one degree higher order correlations (e.g. $\overline{u_i u_j}$ contains $\overline{u_i u_j u_k}$) and other unknown functions of the velocity and pressure correlations as described in the next section. In order that these equations may be solved, all such correlations have to be modeled in terms of variables which are known or determinant, and the accuracy of the turbulence model is strongly related to this modeling process. Thus a model of this type requires a large number of equations to be solved, which makes the model costly and difficult to use.

Generally, the following steps are taken for the construction of a turbulence model (80):

1. A set of properties that is sufficient to characterize the turbulent motion is chosen.
2. A set of algebraic or differential equations which govern the distribution of these properties throughout the flowfield is derived.

3. Constants or functions which are used to model some of the parameters are deduced from experimental data or from more fundamental theories.

The universality of a turbulence model is controlled by the number of constants that need to be adjusted and by the number of differential equations that need to be solved. The greater the number of differential equations and the lesser the number of constants that the model employs, the greater is the universality of the model. However, this increases the complexity of the computational problem and complicates the procedures of optimizing the set of constants. Complete universality will never be achieved (80).

4.4 A Brief Review of Turbulence Models

A number of turbulence models have been proposed over the past few years. These models consists of either zero, one or multi-equations which when solved with the time-mean flow equations allow calculation of the turbulence properties and simulate the behavior of real fluids. Generally, most of the suggested models concentrate on the approximation of the Reynolds stress tensor which appears in the time-averaged Navier-Stokes equations. A brief description of selected zero, one, two and multi-equation turbulence models is presented in the following subsections.

4.4.1 Prandtl Mixing Length Model

Flows in a turbulent boundary layer are usually analyzed in terms of the Prandtl hypothesis, which relates the eddy viscosity directly to the local velocity gradient via:

$$\nu_t = \ell^2 \left(\frac{\partial u_i}{\partial x_j} \frac{\partial u_j}{\partial x_i} \right)^{1/2}$$

The axisymmetric form of this equation may be written as:

$$\begin{aligned} \nu_t = \ell_m^2 [& 2 \left(\frac{\partial u}{\partial x} \right)^2 + 2 \left(\frac{\partial v}{\partial r} \right)^2 + 2 \left(\frac{v}{r} \right)^2 + \left(\frac{\partial u}{\partial r} + \frac{\partial v}{\partial x} \right)^2 \\ & + \left\{ r \frac{\partial}{\partial r} \left(\frac{w}{r} \right) \right\}^2 + \left(\frac{\partial w}{\partial x} \right)^2]^{1/2} \end{aligned} \quad (4.3)$$

where ℓ_m is the mixing length which has to be prescribed empirically.

The mixing length is usually expressed as a fraction of the width of the shear layer or mixing layer, and then generally assumed constant across the layer in regions remote from walls. The major shortcoming of this model is that it makes no allowance for diffusion and convective transport of turbulent viscosity.

4.4.2 Energy Model [Prandtl's 1945 Model]

In order to eliminate the aforementioned shortcoming of the mixing length hypothesis, the eddy viscosity is expressed in terms of the length scale and the kinetic energy of turbulence k via:

$$\mu_t = C_\mu \rho k^{1/2} \ell \quad (4.4)$$

where C_μ is an empirical constant and ℓ is a length scale of turbulence which is proportional to the size of the energy-containing eddies.

Again, the length scale is a function of the flow geometry. The kinetic energy of turbulence is determined from the solution of a differential equation which expresses its transport. This model, with C_μ as a fixed empirical constant, is applicable only to flows or flow regions where

the local Reynolds number is sufficiently high (78). Hence, References (82-84) proposed low Reynolds number versions of the model by adding an exact viscous diffusion term to the k-equation and by replacing some of the model constants with functions of the turbulent Reynolds number. However, these new modifications have failed to predict strongly accelerating boundary layers. Generally, this model works well only in relative simple flows.

4.4.3 Two-Equation Models of Turbulence

These models employ the same formula for turbulent viscosity which was described in the previous model. However, in these models both the turbulence kinetic energy and the length scale are determined by solving their transport equations. Since the k field may be obtained from the solution of the k-equation, any combination of $Z = k^m \epsilon^n$ is possible to provide a mixing length field without solution of its transport equation. Different combinations of m and n values give different models; examples of this:

$n = -2$ and $m = 1$ gives $k-\omega$ model

$n = -1$ and $m = 3/2$ gives $k-\epsilon$ model

The latter gives the most widely adapted variable which is the dissipation rate $\epsilon (= k^{3/2}/\ell)$. Both the dependence of the k-equation on ϵ and the relative simplicity of deriving the ϵ -equation have provided this parameter many advantages over the other combinations of n and m .

Launder and Spalding (55) described the various two-equation models at length in terms of their derivations, applications and limitations. The

k-ε model is the subject of the next chapter, however, discussion of the other two-equation turbulence models is beyond the scope of this study.

4.4.4 Stress-Equation Models

The models discussed so far lack the ability to account for the transport of the individual stresses. This is because they assume that the local state of turbulence can be characterized by one velocity scale $\sqrt{\overline{u_i^2}}$ and that the individual stresses can be related to this scale.

In order to account properly for the transport of the individual stresses, models were developed which employ transport equations for $\overline{u_i u_j}$. These models are often called second-order-closure schemes.

The Reynolds stress transport equations for a fluid of uniform density ρ and with diminished buoyance effects may be expressed in this form:

$$\begin{aligned} u_k \frac{\partial}{\partial x_k} \overline{u_i u_j} = & - \left[\frac{\partial}{\partial x_k} \overline{u_k u_i u_j} + \frac{1}{\rho} \left(\overline{\frac{\partial u_j}{\partial x_i} P} + \overline{\frac{\partial u_i}{\partial x_j} P} \right) \right] \\ & - \left[\overline{u_i u_k} \frac{\partial u_j}{\partial x_k} + \overline{u_i u_k} \frac{\partial u_i}{\partial x_k} \right] + \frac{p}{\rho} \left(\frac{\partial u_i}{\partial x_j} + \frac{\partial u_j}{\partial x_i} \right) \\ & - 2 \nu \frac{\partial}{\partial x_k} \overline{\frac{\partial u_i}{\partial x_k} \frac{\partial u_j}{\partial x_k}} \end{aligned} \quad (4.5)$$

or in words:

$$\begin{aligned} \text{Convection transport} = & -[\text{diffusion transport}] \\ & - [\text{stress production}] + [\text{pressure strain}] \\ & - \text{viscous dissipation} \end{aligned}$$

Summation over the three equations for the normal stresses $\overline{u_i^2}$ provides the equation for the turbulent kinetic energy k . The right hand side of Equation (4.5) contains a number of correlations of turbulent

quantities. These correlations must be prescribed before the above equation is employed in a model of turbulence motion. Usually, the diffusion, pressure-strain and dissipation terms are approximated by models relating them to the Reynolds stresses, the mean velocity field and the length scale. Below are some approximation techniques which have been accepted by many workers for the turbulence quantities:

1. For isotropic flow, the dissipation term can be approximated by $2/3 \epsilon \delta_{ij}$ where δ_{ij} is as described in Equation (4.1) and ϵ is the turbulence dissipation.

2. The divergence of the fluctuating velocity transport equations derives the Poisson's equation for pressure, which can be used to eliminate the pressure-strain term (for example in Reference 60).

3. References (60), (79) and (85) suggested different models for the diffusion term.

Further details on the precise forms of the above turbulence quantities modeling is available in Reference (86).

Taking into consideration the above approximations, a variety of models have been proposed (60, 87-89). A relatively simple model which was proposed by Launder and his co-workers (60, 89) is displayed here with the same previous assumptions.

$$u_k \frac{\partial \overline{u_i u_j}}{\partial x_k} = C_S \frac{\partial}{\partial x_k} \left(\frac{k}{\epsilon} \overline{u_m u_k} \frac{\partial \overline{u_i u_j}}{\partial x_m} \right) - \overline{u_i u_k} \frac{\partial u_j}{\partial x_k} - \overline{u_j u_k} \frac{\partial u_i}{\partial x_k}$$

convective transport = diffusive transport - stress production

$$- C_1 \frac{\epsilon}{k} (\overline{u_i u_j} - \frac{2}{3} \delta_{ij} k) - C_2 (P_{ij} - \frac{2}{3} \delta_{ij} P) - \frac{2}{3} \epsilon \delta_{ij} \quad (4.6)$$

pressure strain viscous dissipation

where C_S , C_1 and C_2 are constants that need to be prescribed. P_{ij} is the stress production of component $\overline{u_i u_j}$ defined in Equation (4.5) and P is the stress production of the kinetic energy as defined in the transport equation of k . As mentioned in the previous section, these models consist of a large number of differential equations whose solution is costly. Hence the use of such models is limited.

4.4.5 Algebraic Stress Models

An algebraic stress model is a simplified version of the Reynolds stress model. It has been derived by simplifying the differential transport equations such that they reduce to algebraic expressions which are easy to solve, but still retain most of their basic features. The differential equations are converted into algebraic expressions by eliminating the gradients of the dependent variables which appear in the transport equations. The resulting general equation which corresponds to Equation (4.5) is:

$$\overline{u_i u_j} = \frac{k}{P + \epsilon(C_1 - 1)} \left[\frac{2}{3} \delta_{ij} \{C_2 P + \epsilon(C_1 - 1)\} + P_{ij} (1 - C_2) \right] \quad (4.7)$$

where P and P_{ij} are as defined in Equation (4.6). The background to two equations is described at length elsewhere (86, 90). Application of a variety of these models has been reported in References (78), (91), and (92).

4.5 Summary

The present chapter provides a brief description of the structure of turbulent flows and the mathematical models which are expected to

represent the flow behavior. The first three sections consist of a survey of the contributions of many workers to the understanding of the characteristics of the turbulent flows, and with the turbulent flow structure and its modeling approaches. Various turbulence models are discussed in the fourth section. The Prandtl mixing length model was presented to demonstrate the non-equation models, and the energy model represents the one-equation models. The $k-\epsilon$ turbulence model is among the two-equation models which are recommended for many flows. As the flow becomes more complex, a higher order model is required, thus the Reynolds stresses model and algebraic stress model were presented.

CHAPTER V

THE k-ε TURBULENCE MODEL AND RECENT EXTENSIONS

5.1 The k-ε Turbulence Model

The k-ε model has been used by many workers (2, 43, 55, 93-95) to provide realistic predictions of the velocity fields and the turbulence parameters. This model involves two transport equations for turbulence characteristics. One of these equations governs the distribution throughout the field of the turbulence energy k, which measures the local kinetic energy of the fluctuating motion; the other governs the turbulence energy dissipation rate ε. The k equation can be obtained from the exact transport equation of the Reynolds stresses $\overline{u_i u_j}$ by summation over the three equations for the normal stresses. The resulting equations for the axisymmetric cylindrical flows are as shown below:

$$\begin{aligned} \rho u \frac{\partial k}{\partial x} + \rho v \frac{\partial k}{\partial r} &= \frac{1}{r} \frac{\partial}{\partial r} \left[r \frac{\mu_e}{\sigma_k} \frac{\partial k}{\partial r} \right] + \frac{\partial}{\partial x} \left[\frac{\mu_e}{\sigma_k} \frac{\partial k}{\partial x} \right] + G - \rho \epsilon \\ &\quad (5.1) \\ \rho u \frac{\partial \epsilon}{\partial x} + \rho v \frac{\partial \epsilon}{\partial r} &= \frac{1}{r} \frac{\partial}{\partial r} \left[r \frac{\mu_e}{\sigma_\epsilon} \frac{\partial \epsilon}{\partial r} \right] + \frac{\partial}{\partial x} \left[\frac{\mu_e}{\sigma_\epsilon} \frac{\partial \epsilon}{\partial x} \right] + C_1 G \epsilon / k \\ &\quad - C_2 \rho \epsilon^2 / k \end{aligned}$$

The values usually adapted for the empirical constants C_1 , C_2 , σ_k and σ_ϵ are those quoted in Reference 55; they are listed in Table IV. The generation term is:

$$G = \mu_e \left[2 \left\{ \left(\frac{\partial u}{\partial x} \right)^2 + \left(\frac{\partial v}{\partial r} \right)^2 + \left(\frac{v}{r} \right)^2 \right\} + \left(\frac{\partial u}{\partial r} + \frac{\partial v}{\partial x} \right)^2 + \left\{ r \frac{\partial}{\partial r} \left(\frac{w}{r} \right) \right\}^2 + \left(\frac{\partial w}{\partial x} \right)^2 \right]$$

where μ_e is the sum of turbulent and laminar viscosities. Knowledge of k and ϵ allows the length scale λ and turbulent viscosity μ_t to be determined from which the turbulent shear stresses can be evaluated via:

$$\mu_t = C_\mu \rho k^2 / \epsilon \quad (5.2)$$

and Equation 4.2.

To account for the wall effect in the near-wall regions, equations are introduced to link velocities, k and ϵ on the wall to those in the near-wall region. These equations, called "wall functions", are introduced and used in finite difference calculations at near-wall points. They occur in the momentum equations and k -generation terms, and their implementation is discussed elsewhere (55) together with appropriate near-wall ϵ specification. The main assumptions considered in these formulations are:

1. Convection and diffusion of turbulence kinetic energy are nearly negligible.
2. Eddy viscosity is isotropic.
3. The sublayer extends up to a value of wall function parameter y^+ equal to 11.63.
4. The length scale is proportional to the normal distance from the wall.

5.2 The k - ϵ Empirical Constants

References (79) and (96) discussed in some detail the basis for choosing the k - ϵ constants. Therefore, it may suffice to mention here that C_μ is fixed by the requirement that in a constant stress layer

production and dissipation of ϵ are balanced [$\tau_w/(\rho k) = C_\mu^{1/2}$], C_2 is determined by reference to the decay of grid turbulence, and C_1 is chosen so that the von Karman constant equals 0.42. The 'Schmidt' numbers σ_k and σ_ϵ are fixed by computer optimization in Reference (97). The main assumptions considered in determining the k- ϵ constants are: the flow is not far from equilibrium so that the convection and diffusion are small compared to production and dissipation terms; and the turbulent Reynolds number is high. These assumptions have led to the nonuniversality of the model constants; even in certain fairly simple flows, some constants require different values. Usually, the extension of the model applicability is achieved by algebraic formulation of C_2 and C_μ to account for a specified flow case. These formulations will be discussed later.

5.3 Shortcomings of the k- ϵ Model

The width of applicability of this model was tested earlier by Reference (59), who considered nine substantially different kinds of turbulent flow. The model demonstrated the capability of prediction of both near-wall and free shear flow phenomena without adjustments to constants or functions. However, in some flow cases this model has some shortcomings, a brief summary of which is provided below.

Habib and Whitelaw (35) found that the velocity minimum and maximum on the centerline for confined swirling flows with coaxial jets are not correctly predicted. However, the measured values of the two components of the rms value of the velocity fluctuation and the kinetic energy are in excellent agreement with the predicted values. This led to their support of Gibson (91) that the assumption of a constant value of C_μ is

inappropriate in curved flows and they remark, that empirical adjustments to constants may produce better results.

Syed and Sturgess (98) predicted the rms value of axial velocity fluctuation, turbulence parameters, velocity profiles and turbulence shear stresses for coaxial jets in confined sudden expansion flows. A maximum error of about 27 percent was obtained in the rms values. The maximum discrepancy in the predicted velocity profiles was found at the centerline. The maximum level of turbulent shear stress was predicted as occurring at a lesser radius than was measured. This led to the conclusion that the dissipation rate is not represented correctly and/or the convection of shear stress is not negligible and its value is not based mainly on the local properties.

Measured and predicted streamline contours, velocity and turbulence intensity profiles for isothermal flow in axisymmetric models of combustor geometries were compared by Whitelaw and Green (99). It was seen that the turbulence modeling errors are prevalent in regions of recirculation, flow development, and in the near-wall region.

The finding of Sturgess and Syed (45) for isothermal flow in widely spaced coaxial jet, diffusion-flame combustors was that the transport of turbulent stress is involved in producing the local centerline axial velocity peak. This peak cannot be predicted by the eddy-viscosity model because the turbulence characteristics are derived from the velocity profiles and eddy viscosity. Such models are incapable of calculating the correct flow characteristics in regions of negligible velocity gradient, particularly if transport of turbulent shear stress of a sign opposite to that appropriate for the local velocity gradient

is significant. Therefore, Reference (45) recommended to take into account the transport of turbulent shear stress.

5.4 Previous Proposed Extensions

The above mentioned problems have commanded considerable attention from many investigators. Most of the investigators have agreed that some of the model shortcomings can be eliminated by algebraic formulation of C_2 and C_μ . Usually, these corrections are expected either to account for low Reynolds number or streamline curvature effects, or both.

Early, Jones and Launder (97) added a new term,

$$-2 \mu \left(\frac{\partial k}{\partial y} \right)^{1/2}$$

to the k-equation to represent the energy dissipation rate at the wall.

Also, another term,

$$2 \mu \mu_t \left(\frac{\partial^2 u}{\partial y^2} \right)$$

was added to the ϵ -equation in order for the peak level of the turbulent kinetic energy to agree with experimental data. Both C_2 and C_μ were modeled to account for low Reynolds number effect via:

$$\begin{aligned} C_\mu &= 0.09 \exp [-2.5/(1 + R_t/50)] \\ C_2 &= 2.0 [1.0 - 0.3 \exp (-R_t^2)] \end{aligned} \tag{5.3}$$

where $R_t = \rho k^2/(\epsilon \mu)$.

This model was tested by Jones and Launder (100) as applied to isothermal low Reynolds number pipe flow, and wall boundary layer with

streamwise pressure gradient and wall injection. The model predictions were not completely in accord with the experimental data.

Launder et al. (101) incorporated the streamline curvature effects on the turbulence structure in the $k-\epsilon$ model. The direct effect of curvature in the model is limited to a single empirical coefficient whose magnitude is directly proportional to a Richardson number based on a time scale of the energy-containing eddies. For boundary layer flow types, the proposed C_2 formulation is:

$$C_2 = C_2' (1 - 0.2 R_i) \quad (5.4)$$

where C_2' is the C_2 value before the correction, and the Richardson number is defined as:

$$R_i = \frac{k^2}{\epsilon} \frac{w}{r^2} \frac{\partial}{\partial r} (rw) \quad (5.5)$$

where w is the swirl velocity. The model was applied to a variety of boundary layer flows developing over curved and spinning surfaces; satisfactory agreement with experiments was obtained. On the other hand, Reference (102) solved Reynolds equations using the $k-\epsilon$ model in the separated flow region, and both the $k-\epsilon$ model and the $k-\epsilon-\overline{u'v'}$ models in the region downstream of the separation. He showed that in the redevelopment region the three-equation turbulence model does not offer worthwhile advantages over the two-equation $k-\epsilon$ model.

Ljuboza and Rodi (103) replaced the empirical constant C_μ by a function which was derived by reducing a model from the Reynolds stress transport equations to algebraic expression by introducing simplifying assumptions about the convection and diffusion terms. Good results were

obtained when this model was applied to a wall jet in stagnant surroundings, or in a moving stream.

Hanjalic and Launder (104) introduced into the ϵ -equation a term proportional to

$$k \frac{\partial \bar{u}_i}{\partial x_j} \frac{\partial \bar{u}_j}{\partial x_m} \epsilon_{ijk} \epsilon_{lmk}$$

where ϵ_{ijk} stands for the third-order alternating tensor. For thin shear flows this term reduced to $k (\frac{\partial \bar{u}}{\partial y})^2$. This correction is expected to promote a higher rate of dissipation for irrotational strains as opposed to for rotational strains. Indeed, they found that this minor modification brought substantial improvement to the prediction of boundary layers in an adverse pressure gradient.

The streamline curvature correction proposed by Reference (77) was derived from the Reynolds-stress equations, as described by Reference (91). Also, they adapted a modification which accounts for the preferential influence of normal stresses and the dissipation of turbulent energy; this modification was originally proposed by Reference (105) for strong accelerated flows. This correction has led to greatly improved agreement with experimental data when applied to the recirculating flow in an annulus, and a plane twin-parallel jet in still air.

Karasu (5) used the turbulent viscosity μ_e , which is calculated from the k - ϵ model, in the solution of the axial and radial moments of swirling pipe flow. The tangential eddy viscosity $\mu_{r\phi}$ was employed in the solution of the tangential momentum; the expression used is given by

$$\mu_{r\theta} = \rho \kappa^2 r^2 \left| r \frac{\partial}{\partial r} \frac{w}{r} \right| + \mu \quad (5.6)$$

where κ is a constant considered to be 0.042 and μ is the laminar viscosity. His prediction for pipe swirling flow that exhibits combined vortex were generally comparable with the experimental data. However, the prediction of the axial velocity at the initial location of pipe flow that exhibits solid body rotation was poorly compared with the measurements.

Finally, good agreement with experimental data was obtained (106) when a modified k - ϵ model was applied to fully developed pipe flow. The modified version can be used without introducing the empirical wall function formulas.

5.5 Closure

A brief description of shortcomings and recommended corrections to the standard two-equation k - ϵ turbulence model suggested by previous investigators are presented. It has been found that the model predictive capability can be increased by a simple empirical modification of the model governing equations and this modification works only well for the flow under consideration. Thus the universality of the model has never been obtained.

CHAPTER VI

TURBULENCE PARAMETERS DEDUCTION FROM SWIRLING CONFINED FLOW MEASUREMENTS

6.1 Introduction

Specification of the turbulent stresses is required in order to solve the Reynolds equations for time-mean velocities. This is usually obtained via the turbulent viscosity μ_t . Chapter V exhibits some simple models for the specification of μ_t , especially in boundary layer flows, however, these models are not useful for recirculating flows. Currently, two-equation models are popular in these circumstances. The present work emphasizes the k - ϵ version of the two-equation models in the context of swirling recirculating flows. As mentioned earlier, this model solves differential equations for the turbulence energy, k , and the turbulence dissipation, ϵ . From these the turbulent viscosity can be specified.

From the above introduction, it is foreseen that the precision of the predictions strongly depends on the accuracy of the turbulent viscosity values. The evaluation of a turbulence model and hence the μ_t values can be performed through the use of analytical inverse methods which are described in the next section.

6.2 Analytic Inverse Methods

Evaluation of the accuracy of a turbulence model may be obtained by comparing the calculated time-mean values and turbulence parameters with experimental data. Alternatively, Equation (4.2) may be used to make deductions directly from experimental data. Velocity gradients are calculated from experimental time-mean velocities using a suitable finite difference technique. Once the velocity gradients are obtained the turbulent viscosity components can be calculated via Equation (4.2). Implementing the Prandtl mixing length model, the mixing length ℓ_m can be deduced from Equation (4.3) where Equation (4.2) provides the value of μ_{rx} . The other length scale calculation follows from replacing μ_t by μ_{rx} in Equation (4.4) and setting C_μ to its conventional value of 0.09. Resulting length scale values are presented in Section 6.3.

In using Equations (4.2) and (4.3), lack of detailed axial time-mean velocity gradients has led to these terms being dropped. In non-swirling and moderately swirling flows, they are usually small, except near recirculation zones. At high swirl, the central recirculation zone develops and this simplification cannot faithfully be invoked (107). However, it will be only in quite small regions of the flow that errors of any significant magnitude might occur.

6.3 Findings and Discussion

The present chapter was initiated to analyze the fluctuating and time-mean turbulence data presented in Reference (10). The data are for nonswirling and swirling flows in an axisymmetric test section with expansion ratio $D/d = 2$, which may be equipped with a contraction nozzle of area ratio 4 located at $L/D = 2$. The swirl is imparted to the flow

by means of an adjustable-angle vane swirler (3). The Boussinesq's eddy viscosity was used, as explained in the previous section, to calculate turbulent viscosity component from each measured Reynolds stress and its corresponding time-mean velocity gradient term. Also, from this mean component of turbulent viscosity the length scale of energy containing eddies was obtained using the measured kinetic energy of turbulence with the parameter C_μ given its standard value.

6.3.1 Assumptions and Parameters Normalizations

Based on the available data, curves are usually fitted to the spatial distribution of measured time-mean values before further analytical manipulation. However, in case of complex flows, it is very difficult, or it may be impossible, to find a general correlation of the data along the flowfield. Therefore, the data were hand smoothed and then the values are read in from the corrected curves. The data considered were for swirl vane angles of 0, 45 and 70 degrees. The radial velocity gradients were determined analytically from the corrected data. The axial velocity gradients were ignored because their values were unavailable and are expected to be considerably less than the radial gradient values in most flow situations studied here.

The turbulent viscosity was normalized with respect to the swirler inlet uniform axial velocity u_0 (deduced independently from a measurement upstream of the swirler), fluid density and combustor diameter. The turbulence kinetic energy was normalized with respect to u_0^2 . The length scale and mixing length were nondimensionalized with respect to the combustor diameter. The normalized values of the viscosity in the r - x plane μ_{rx} , the length scale and the kinetic energy are displayed in

Tables V through X. Also, the other viscosity components are tabulated as a fraction of μ_{rx} values ($\sigma_{ij} = \mu_{rx}/\mu_{ij}$) and displayed among these tables. The tabulated μ_{rx} and length scale were computer plotted and are shown in Figures 5 through 10.

6.3.2 Effects of Swirl on Turbulence Parameters

The swirl vane angles ϕ considered in this study are 0 (swirler removed), 45, and 70 degrees. Part (a) of Figures 5 through 7 displays the nondimensionalized turbulent viscosity μ_{rx} and part (b) shows the normalized length scale λ as defined in Equation (4.4) for $\phi = 0, 45,$ and 70 degrees, respectively. Also, the corresponding values of these parameters are displayed in parts (a) and (b) of Tables V through X, respectively. It should be noted that the allowed maximum range of the values plotted in Figures 5 through 7 was 2, and the data beyond this range was assigned the range maximum values. The actual values of the affected points can be found in Tables V through VII. Parts (c) through (f) of these tables exhibit the other turbulence parameters such as turbulence energy k and other turbulent viscosity components.

The μ_{rx} profiles shown in part (a) of Figures 5 through 7 reveal that the μ_{rx} values marginally increase as the swirl strength increases from zero to a moderate value and sharply increase beyond this range. Comparison of these figures with the mean velocity plots presented in Reference (10) indicates that the peak of μ_{rx} may or may not coincide with the peak of the velocity gradients. Inspection of part (b) of Figures 5 through 7 shows that the normalized length scale profiles are almost similar to the corresponding μ_{rx} profiles for each swirl case and therefore, the swirl dependency of length scale is revealed. Parts (a)

and (b) of Tables V through VII tabulated the plotted values of the normalized turbulence viscosity and the length scale, respectively.

Part (c) of Tables V through VII displays the mixing length values obtained from Equation (4.3), with the axial velocity gradients ignored, using the curve fitted data of Reference (10). Comparison between these tables reveals that the mixing length values are slightly higher for swirl vane angle ϕ for 45 degrees than for $\phi = 0$ or 70 degrees. However, the presented values for $\phi = 0$ degrees are smaller than the corresponding ones for 70 degrees. It is expected that these findings are due to the effect of swirling motion of the flow on the eddy size distribution.

Part (d) of Tables V through VII contrasts the kinetic energy of turbulence distributions as the swirl strength increases. The tables show that results for moderate swirl are slightly higher than the corresponding ones for nonswirling flow. The most dramatic effect of swirl is seen at high swirl values. The turbulence energy maximum values occur in regions of recirculation and regions of high stress.

The degree of nonisotropy has increased in magnitude, consistent with the increase in swirl strength throughout the entire flowfield, as can be seen from part (e) of Tables V through VII. Also, it can be noticed that the turbulent viscosity in the rx-plane may be higher or lower than its corresponding value in the other planes depending on the location of the point in the flowfield.

Generally, the effect of increase of swirl strength is the considerable increase in all the turbulence parameters considered--that is, increase in rx-viscosity, kinetic energy of turbulence, length scales, and degrees of nonisotropy. The peak location of these parameters

depends on the parameter under consideration. Overall, the swirl produces a large-scale effect on the turbulence parameters and, therefore, its effects should be considered in the turbulence modeling.

6.3.3 Effects of Strong Contraction Nozzle on Turbulence Parameters

Comparison of results of the previous sub-section with the corresponding ones of Abujelala et al. (108) shows that the general results which were obtained from the corrected curves are similar to those obtained directly from the scattered data. Therefore, a decision was made to employ the measured values in the calculations involved in this sub-section. The normalized turbulent viscosity in the rx-plane and the length scale for swirl vane angles of 0, 45 and 70 degrees, and with a strong contraction nozzle of area ratio 4 located at $L/D = 2$ are presented in parts (a) and (b) of Figures 8 through 10, respectively. The nozzle diameter is half the combustor diameter. Some of the plotted points were assigned the maximum values allowed if the normalized values were larger than 2. Actual values are included in the corresponding tables. The effect of the contraction nozzle on turbulence parameters was tabulated and is presented in Tables VIII through X. The construction of these tables is similar to Tables V through VII.

Comparison between Figures 8 through 10 and Figures 5 through 7 reveals that the nozzle tends to increase the μ_{rx} and ℓ values in the shear layers and to decrease them elsewhere. It is suggested that this is because of the high velocity gradients which are generated by accelerating the flow near the centerline. The similarity between the profiles shown in parts (a) and (b) of Figures 8 through 10 was unaffected

by the presence of the nozzle. The data of these figures were obtained from parts (a) and (b) of Tables VIII through X.

Parts (c) through (g) of Tables VIII through X show that the contraction nozzle generally changes the turbulence characteristics. This effect increases as the swirl strength increases. Parts (c) and (d) of these tables reveal that the nozzle tends to increase the mixing length and the kinetic energy in the region of recirculation, and to reduce their values near the wall. This is because the presence of a contraction nozzle accelerates the flow near the centerline and decelerates it close to the wall. Parts (e), (f) and (g) of Tables VIII through X show a high degree of nonisotropy due to the presence of the nozzle. This is expected because of the streamline curvature effects which increase as the contraction increases. Summarizing, the presence of a strong contraction nozzle change the turbulence characteristics dramatically, and its presence should be taken into consideration in turbulence modeling.

6.4 Closure

The data of confined swirling flow obtained from a hot-wire using the six-orientation technique were numerically analyzed. The effects of swirl strength and a strong contraction nozzle on the turbulence parameters were evaluated. It was found that with the swirl strength and the contraction have strong effects on the turbulence parameters. Generally, the most dramatic effect of the increase of swirl is the considerable increase in all the parameters considered. The presence of a strong contraction nozzle tends to increase the parameter values in regions of acceleration where large radial velocity gradients occur and to reduce them in the deceleration region near the outer boundary.

CHAPTER VII

EXTENSION OF THE k - ϵ TO CONFINED SWIRLING RECIRCULATING FLOWS

7.1 Introduction

Turbulent swirling recirculating flows are used in many practical situations. They provide the fundamentals of physical processes occurring in aircraft combustors and in industrial furnaces. These types of flow are characterized by strong streamline curvature, complex eddy structures and high turbulence intensities. The practical need for computation of this category of flows has encouraged many workers to attempt to develop turbulence models that can provide accurate information about such flows. However, most of these attempts have provided models that are only applicable for a certain flow, and these models must be modified to accommodate flows of greater complexity.

The different models may conventionally be distinguished by the number of turbulence properties which appear as dependent variables of the differential equations, as described in Chapter IV. The most widely used model is the k - ϵ turbulence model which was briefly described in Chapter V. This model showed shortcomings as applied to turbulent recirculating confined swirling flow (2): it provides inaccurate predictions for the size and strength of the recirculation zones. It is expected that the turbulence model over-predicts the dissipation of the kinetic energy of the flow, therefore, the centrifugal forces produce a

shorter central recirculation core than the measurements show. Hence, in order to extend the $k-\epsilon$ model to confined swirling flows, some corrections concerning the ϵ -equation have to be made. The general approach, as shown in Chapter V, is to consider the streamline curvature effects through the modeling of the constant C_2 . This follows in the next section.

7.2 Previously Proposed Extension and Its Invalidity

Reynolds (109) defined the Richardson number for swirling flows as:

$$R_i = \frac{2 \frac{w}{r} \frac{\partial}{\partial r} (r w)}{\left(\frac{\partial u}{\partial r}\right)^2 + \left[r \frac{\partial}{\partial r} \left(\frac{w}{r}\right)\right]^2} \quad (7.1)$$

An extensive preliminary study was conducted to evaluate this equation and Equation (5.5) as applied to turbulent swirling recirculating flows. The distribution of predicted C_2 and mean velocity values using the two expressions for the Richardson number along with Equation (5.4) were compared and the results show that Equation (7.1) provides better predictions than Equation (5.5). Therefore Equation (7.1) along with Equation (5.4) was selected for the evaluation of the inclusion of the streamline curvature effects through modeling C_2 .

Equation (5.4) with the Richardson number as defined by Equation (7.1) was added to the ϵ -equation of the $k-\epsilon$, and the flowfield for swirl vane angles of 45 and 70 degrees was predicted using STARPIC computer code which is described in Chapter IV. The value of C_2 was not allowed to be less than 0.1 and not greater than 2.4, with C_μ and the other model constants assigned the conventional values. The distribution of C_2 values over the flowfield is displayed in Tables XI and

XII. Table XI displays a moderate swirl strength flowfield ($\phi = 45$ degrees), and Table XII exhibits the flowfield for a stronger swirl strength ($\phi = 70$ degrees); the C_2 values not included in the above mentioned range have been replaced by a (-) sign. The corresponding velocity profiles for $\phi = 45$ and 70 degrees are displayed in Figures 11 and 12, respectively. Inspection of the predicted data associated with these figures reveals that the corrected ϵ -equation under-predicted the dissipation of the flow energy. The dominant centrifugal forces drive the flow off the centerline. Similar results were obtained for the $\phi = 70$ degrees.

7.3 Parameter Optimization From Time-Mean Data

It is clear from the previous section that the variation of the C_2 parameter given in Equation (5.4) does not enhance the predictions of turbulent swirling recirculating flows, and it was decided to optimize the k - ϵ model constants for the flow under consideration. It was mentioned in Section 5.2 that only σ_k and σ_ϵ were fixed by computer optimization. However, because of lack of the necessary experimental data, C_μ and C_2 were also optimized in this study. The constant σ_k was dropped from the optimization because of the feeling that the k -equation produces sufficient accuracy in determining the k -values. An effective optimization code is the Hill Algorithm. Kuester (110) described this method at length, in terms of its mathematical formulation and practical applications. It need be described only briefly here. Therefore, it is described only briefly in this section.

The optimization procedure is based on the direct search method proposed by References (111) and (112). This method has proven

effective in solving some problems where the variables are constrained. The procedure requires a starting point that satisfies the constraints and does not lie in the boundary zones. The effect of a small stepping in the first variable on the objective function is evaluated. If an improvement in the objective function were obtained without violating the boundary zones or constraints, the step size is reduced, and the direction of movement is reversed. The next variable is in turn stepped by a small distance parallel to the axis. The same acceleration or deceleration and reversal procedure is followed for all variables in consecutive repetitive sequences until the convergence criteria is satisfied.

The parameters C_μ , C_2 , and σ_ϵ were optimized by minimizing the maximum absolute discrepancy between predicted axial and swirl velocity and the corresponding experimental values. These experimental values were obtained using a five-hole pitot probe (9). The optimum constants were obtained by an iterative computer procedure; the velocity fields, after the iteration limit was exceeded, were compared with the experiments. Because of the rather large computing time that would have been required if the iteration was continued until the convergence criterion was fully achieved, only 80 iterations were performed during each optimization cycle, with current flowfield values taken as initial values for the next optimization cycle in each case. The k - ϵ constants optimum values obtained after 20 optimization cycles were found to be only marginally dependent on swirl strength. The values obtained for this wide range of swirl strengths ($\phi = 45$ to 70 degrees) are displayed in Table XIII. It should be noted that these values are not as good as the Table IV values in the prediction of nonswirling flows.

7.4 C_μ Formulation From Detailed Turbulence Data

The analysis of the detailed turbulence measurement of (10) presented in Chapter VI are being employed here to provide the background for producing an empirical formulation for the k - ϵ C_μ parameter. Inspection of the normalized rx-viscosity μ_{rx} and length scale ℓ , shown in Figures 5 through 10 of that chapter reveals a strong similarity between the radial profiles. That is

$$\mu_t / (\rho u_o D)$$

is almost proportional to ℓ/D . Since

$$\mu_t = C_\mu \rho k^{1/2} \ell$$

or equivalently

$$\mu_t / (\rho u_o D) = (C_\mu k^{1/2} / u_o) (\ell/D)$$

it follows that

$$C_\mu k^{1/2} / u_o$$

is approximately constant throughout the flowfield. That is:

$$C_\mu = A u_o / k^{1/2} \quad (7.2)$$

where A is a constant independent of spatial position in the flow.

Using an optimization procedure similar to that described in Section 7.3, optimal values of A , C_2 and σ_ϵ have been deduced for the present situation: It was found that

$$\begin{aligned}
A &= 0.0083 \\
C_2 &= 1.804 \\
\sigma_\epsilon &= 1.455
\end{aligned}
\tag{7.3}$$

The flowfields for inlet swirl vane angles of $\phi = 45$ and 70 degrees have been predicted using the C_μ variation as given by Equation (7.2), with the optimized values of Equation (7.3) used in this and other equations occurring in the simulation. Parts (a) and (b) of Table XIV exhibit the values of predicted k and C_μ obtained in this manner for corresponding inlet swirl are angles of $\phi = 45$ and 70 degrees, respectively. Values vary throughout the flow domain. The predictions using the aforementioned C_μ variation are validated in the following sections.

7.5 Predictive Capability of C_μ Formulation vs. Optimized Parameters

The time-mean flowfields corresponding to the swirl vane angle $\phi = 45$ and 70 degrees, which were obtained by two different approaches, are compared in this section. Parts (a) of Tables XV and XVI display the predicted flowfield using the C_μ formulation for $\phi = 45$ and 70 degrees, while parts (b) of these tables exhibit the predicted flowfield using the optimum k - ϵ model constants for the same above swirl strengths.

Generally, the comparison between Tables XV and XVI reveals that both methods provide very close predictions. However, the predicted centerline velocity values of parts (a) of these tables reduced considerably as compared with the parts (b) values, and became close to the experimental values as will be seen in the next section. Thus the

C_μ formulation predictions are superior over the ones of the optimum values in the region of recirculation.

7.6 Validity of Standard $k-\epsilon$ Model and C_μ Formulation

7.6.1 Time-Mean Axial and Swirl Velocities

The predicted velocity profiles for swirl vane angles of 45 and 70 degrees using the C_μ formulation of Equation (7.2) are compared with the five-hole probe (9) and hot-wire (10) measured data, as can be seen in Figures 13 and 14, respectively. Inspection of these figures reveals that very good agreement between the predicted results and the experimental data has been achieved. Note that the measured inlet profiles are plotted at the $x/D = 0$ location; in fact these are actually the values measured immediately downstream of the swirler, at the location $x/D = -0.11$. It is convenient to retain these values on the profile plots in the prediction study, although clearly results at the $x/D = 0$ location are then not only directly comparable with the inlet station data of References (9 and 10), which are taken precisely at $x/D = 0$. These comments apply also to other plots given in the thesis. The discrepancies in the centerline velocity values at the peak of the central recirculation core are expected due to the assumption of axisymmetry at that location.

Figures 15 and 16 exhibit predictions similar to Figures 13 and 14, except the standard $k-\epsilon$ model was used in these predictions. Inspection of these figures reveals that inaccurate predictions for the size and strength of the recirculation zone were obtained by using the standard $k-\epsilon$ model. The inaccuracy of the standard model can be easily seen by comparing the measurements of Yoon and Lilley (9), and Jackson and

Lilley (19) for swirl vane angles of 45 and 70 degrees as shown in Figures 13 and 14 against the corresponding predicted velocity profiles displayed in Figures 15 and 16, respectively. However, as mentioned in the previous paragraph, the predicted results using the C_μ formulation has shown very good agreement with experimental data. Thus it is clear that the C_μ formulation has provided superior results over the standard $k-\epsilon$ model.

7.6.2 Zero Velocity Envelope and Time-Mean Centerline Velocity

Figures 17 and 18 show a comparison of the predicted central recirculation zone boundary using the standard $k-\epsilon$ model and its modified version (variable C_μ) with corresponding data (9, 10) for swirl vane angles of 45 and 70 degrees. The predicted central recirculation zone envelope using C_μ variation is in very good agreement with the data, with a small discrepancy near the peak of the recirculation zone core. However, using the standard model produces a less realistic shorter central recirculation zone.

Predicted centerline velocity longitudinal variation using the aforementioned methods as compared with the measurements of References (9) and (10) is shown in Figures 19 and 20 for the same previous swirl strengths. Notice that the negative values are slightly over-predicted in absolute magnitude--a trend which was also found by others (35, 98) as reported in Chapter V.

7.6.3 Turbulence Parameters

The predicted kinetic energy, k and its dissipation rate, ϵ using the standard and the modified version of the $k-\epsilon$ model are compared with

the corresponding hot-wire data for swirl vane angles 45 and 70 degrees as shown in Figures 21 and 22, respectively. Both versions of the $k-\epsilon$ model have provided qualitatively good predictions. The modified model shows closer predicted values of k and ϵ to the experimental data (especially within the recirculation zone and far downstream of the inlet domain, respectively) than the standard model.

7.6.4 Summary

In summary, the C_μ variation has provided better predictions of the time-mean and the turbulence parameters than the standard model. Also, the size of the recirculation zone, especially for swirling flow and the centerline velocity are quantitatively very well predicted by using the proposed C_μ formulation as described in Section 7.4 of this chapter.

7.7 Validation of the Proposed C_μ Formulation for Nonswirling and Pipe Flow Applications

It was mentioned earlier, Section 7.4, that the C_μ formula was obtained via a simple optimization procedure. The optimum values were obtained by minimizing the difference between the predicted and measured axial and swirl velocity values for the flowfield of swirl vane angle = 45 degrees. The validity of the proposed formulation as applied to a higher swirl strength flow field (70 degrees) has been shown in the previous section. Two more test cases are being conducted in this section to show the generality of this model. A nonswirling flow through a circular duct with expansion ratio $d/D = 2$ and a swirling flowfield with $d/D = 1$ (pipe flow) are considered for this test.

Figures 23 through 25 give the comparison between the predicted time-mean velocity fields and the corresponding measurements. Predicted

axial velocity profiles for nonswirling flow are compared with the experimental data of Yoon and Lilley (9), as seen in Figure 23. Figures 24 and 25 exhibit the comparison between the predicted axial and swirl velocity profiles and the measurements of Jackson and Lilley (10) for swirl vane angles 45 and 70 degree fields, respectively. An examination of these figures reveals that the predictions are in very good accord with experimental data, particularly when the experimental scatter is borne in mind. This finding along with the previous section conclusion lead to the generality of the proposed C_μ formula for applications to a circular duct flow with and without abrupt expansion.

7.8 Closure

An evaluation of the standard $k-\epsilon$ model and its previously-available extensions as applied to turbulent recirculating confined swirling flow has been presented. Neither the standard model nor its extensions show effective capability for predicting turbulent recirculating swirling flows. Recent experimental data on swirling confined flows, obtained with a five-hole pitot probe and a six-orientation hot-wire probe, are used to obtain optimum values of the turbulence parameters C_1 , C_2 and σ_ϵ , and a special C_μ formulation for swirling flows, respectively. General predictions of moderately and strongly swirling flows with these techniques are more accurate than the predictions with the standard or previous simple extensions of the $k-\epsilon$ turbulence model. The predicted centerline velocity using the C_μ formulation has been found superior to the corresponding velocity given by the optimum values. The application of the C_μ formula to nonswirling flow and pipe flow has shown the generality of this model.

CHAPTER VIII

GENERAL PREDICTIONS FOR CONFINED TURBULENT SWIRLING FLOW

8.1 Scope and Method of Approach

This chapter first discusses predictions which deal with the flow through the inlet swirler with vane angles set to $\phi = 45$ and 70 degrees. Various types of inlet profiles assumptions are considered and the similarity and differences in the ensuing flowfield predictions are noted. Predictions are then exhibited for a range of swirl strengths correspond to $\phi = 0, 45$ and 70 degrees using measured inlet axial, radial and swirl velocity profiles in each case. Downstream nozzle contraction ratio and inlet domain expansion ratio effects are investigated. The ensuing flowfields are characterized via velocity profiles and streamline patterns, and illustrate the large scale effects of inlet swirl, expansion ratio and outlet nozzle on flowfields.

The prediction procedure starts with the solution of partial differential equations of conservation of mass, momentum in $x, r,$ and θ directions, turbulent kinetic energy and its dissipation rate, which govern two-dimensional axisymmetric steady flow via the STARPIC computer program. the solution techniques which have been implemented in this computer program are described at length in Chapter IV. All the results to be given in Sections 2 through 6 of the present chapter are obtained via the C_μ formulation model as described in the previous chapter, see

Section 7.4. Similar predictions using the standard k- ϵ model are presented for flowfields with $D/d = 2, 1.5$ and 1 . The former was obtained earlier (2) and shows the same general trends for the effects of swirl and downstream contraction nozzle on the flowfield, it is not shown here. The predictions of the other two flowfields are discussed in Section 8.6. This chapter emphasizes the more advantageous C_μ formulation model, which gives a more accurate simulation of the flowfield.

The code is operated in the manner described in Chapter IV, with the desired parameters being computed to convergence with a 23×21 nonuniform grid covering a flow domain of length 4 times the combustor chamber diameter for sequential swirl vane angles of $0, 45$, and 70 degrees.

The open ended flowfield with expansion ratios of 1.5 and 1 are covered by 23×15 and 23×9 nonuniform grid systems, respectively. It should be noted that the refinement of the grid was necessary only for highly and moderately expanding flow. The downstream contraction nozzle was simulated by the way of a staircase approach that represents a 45 degree slope; it is accommodated at $L/D = 2$ by way of two steps, six cells each, in the radial direction. Even this relatively coarse subdivision enables useful predictions to be obtained.

8.2 Effects of Convergence Criterion and Inlet Boundaries on the Prediction Accuracy

The nature of the confined swirling flows produce the need for an iterative procedure for the solution of the flow governing differential equations, thus the accuracy of the final results depends on the convergence criterion considered. It is obvious that the smaller its value

the more accurate predictions are obtained. Also, the accuracy of the prediction of the cited flow depends on the boundary conditions applied around the flow domain. Therefore, it is important to define adequately the boundary conditions, especially at the inlet to the flow domain. The effects of inlet turbulence energy (and hence the effect of dissipation rate), inlet velocity profiles and degree of convergence are evaluated in this study.

8.2.1 Effect of Refinement of Convergence Criterion

In order to find the most economical convergence criterion that provides acceptably accurate predictions, a study was conducted to evaluate its effect on the predicted values. Two convergence criterion were selected: in the former, all the normalized residual source sums for each variable were required to be less than 0.009; and in the latter were required to be less than 0.004. Results of the evaluation are displayed in Table XV, XVI, and XVIII.

Parts (a) and (b) of Table XVII display the residual source sums for a moderate convergence criterion and a more stringent one, respectively. The flowfield axial and swirl velocity distributions, after achieving the displayed values, are exhibited in part (a) of Tables XV, XVI, and XVIII. The former shows the flowfield predictions using part (a) of Table XVII while the latter was obtained from part (b) of the same table. Inspection of these tables reveals that the corresponding predicted values of the two tables are very close. The average deviations observed in the axial velocity field values for swirl vane angles 45 and 70 degrees are approximately 1.0 percent and 1.5 percent, respectively. These values sharply reduce as the location moves far

from the centerline of the flowfield. The maximum deviation was noticed to be about 3 percent in the centerline velocity values which are located very far downstream of the inlet domain. The tangential velocity values show a maximum deviation of less than 1 percent over the entire flowfield.

Examination of the data presented in Tables XV (described in Section 7.5) and XVII has led to the conclusion that the predicted values using part (b) of Table XVII values show no preference over the correspondings which were obtained from part (a) of Table XVII. However, the former prediction method requires a computer time more than 1.5 times that of the latter one. Therefore, to reduce the expense of the computer time, the convergence criterion = 0.009 was selected for all further predictions.

8.2.2 Effect of Inlet Boundary Specifications

8.2.2.1 Effect of Inlet Kinetic Energy Profiles. To investigate the effect of the inlet kinetic energy k profiles on the predicted values, three types of specification of k were considered:

1. Inlet k is assumed to be a constant obtained from the average inlet axial velocity:

$$k = 0.03 u_{v,0}^2 \quad (8.1)$$

2. Inlet k is allowed to vary with radius and is a function of local inlet time-mean axial velocity at each radial location

$$k = 0.03 u_o^2 \quad (8.2)$$

3. Inlet k is allowed to vary with radius and is a function of local inlet total time-mean velocity at each radial location

$$k = 0.03 (u_0^2 + v_0^2 + w_0^2) \quad (8.3)$$

The factor 0.03 in these equations is the recommended constant given an inlet relative turbulence intensity of 0.245. Predictions using these three inlet k assumptions with realistic inlet velocity values (measured u , v , and w velocities are given in part (a) of Tables VX and XVI, and in Tables XIX and XX. Parts (a) and (b) of Tables XIX and XX display the predicted axial and swirl velocities for swirl vane angles 45 and 70 degrees, respectively. These tables illustrate that there is little change in velocity predictions with changes in the inlet k specification. The third expression for the inlet k looks like the most realistic one, therefore, it has been chosen for all further predictions.

8.2.2.2 Effect of Inlet Velocity Profiles. Numerical predictions of confined turbulent swirling flows are presented using various inlet velocity starting conditions for the case of swirl vane angles equal to 45 and 70 degrees. In all cases considered, the inlet kinetic energy of turbulence k is specified as in the third case of the previous subsection, that is the total local time-mean velocity magnitude has been used in specifying k at any radial position across the inlet domain. The inlet dissipation rate is specified as in a generally accepted way (14, 58). The validity of the flowfield predictions resulting from the choice of inlet profiles is assessed by comparing the predicted velocity profiles with corresponding experimental velocity profiles (10, 37).

Four possible specifications of the inlet velocities are considered:

Case 1. Flat inlet axial and swirl velocities with radial velocity zero are assumed. that is, both u and w are constant valued:

$$u_0 = \text{constant}$$

$$w_0 = u_0 \tan \phi$$

where ϕ is the swirl vane angle.

Case 2. As Case 1, except that the inlet swirl velocity profile is assumed to be that of solid body rotation:

$$u_0 = \text{constant}$$

$$w_0 = w_{m,0} \cdot r/R$$

where $w_{m,0}$ is the maximum orifice values of w which occurs at the outer edge $r = R$ of the inlet. The value of $w_{m,0}$ is so chosen as to maintain the swirl number S' the same as Case 1 for similarity purposes is now described. Defining

$$S = \frac{G_\theta}{G_x d/2} \quad (8.4)$$

where

$$G_\theta = \int_0^\infty (\rho u w + \overline{\rho u' w'}) r^2 dr \quad (8.5)$$

is the axial flux of swirl momentum, including the x - θ direction turbulent shear stress term

$$G_x = \int_0^\infty (\overline{\rho u^2} + (p - p_\infty)) r dr \quad (8.6)$$

is the axial flow of axial momentum including the x direction turbulent normal stress term and a pressure term.

One useful deduction is possible when solid body rotation plug flow is assumed at the nozzle. That is, axial velocity u is a constant flow profile and swirl velocity w increases from 0 (at $r = 0$) to $w_{m,0}$ (at $r = d/2$), the outer wall of the nozzle. Then local static pressure p and local swirl velocity w are related via

$$p - p_{\infty} = -\frac{1}{2} \rho (w^2 - w_{m0}^2)$$

where

p_{∞} = static absolute pressure at $r = d/2$ at the inlet station, $x/D = 0$.

If the pressure contribution to G_x is retained in the form of a $w^2/2$ term, but the turbulent stress terms are omitted, the analysis leads immediately to

$$G_{\theta} = \frac{\pi}{2} \rho u_0 w_{m0} (d/2)^3$$

$$G_x = \frac{\pi}{2} \rho u_0^2 (d/2)^2 (1 - (G/2)^2)$$

where $G = w_{m0}/u_0$ represents the ratio of maximum velocities measured at the exit plane. Thus the swirl strength can be inferred from

$$S = \frac{G/2}{1 - (G/2)^2} \quad (8.7)$$

if pressure is included in the G_x definition, and

$$S' = G/2 \quad (8.8)$$

if pressure is omitted in G_x . Both S and S' are called swirl numbers, but a given velocity distribution gives different S and S' values. The theoretical S vs. G seems to be valid only for low swirl strengths with $S < 0.2$, see Refs. 1 and 113. For higher degrees of swirl, however, the

axial velocity distributions deviates from plug flow considerably - the major portion of the flow leaves the orifice near the outer edge (1, 3, 11, 113, and 114). Then measured S values (including pressure contribution) are higher (114) than measured G values would suggest via Eq. (8.7). In many practical experiments, S' values are calculated and quoted based on experimental swirler exit velocity profiles only, with the pressure contribution omitted, see for example, Ref. 115. Pressure variations still exist, although quoted S' values do not make use of these values. Under these circumstances, for a vane swirler with swirl vane angle ϕ , it can be shown (116) approximately that

$$S' = \frac{2}{3} \left[\frac{1 - (d_h/d)^3}{1 - (d_h/d)^2} \right] \tan \phi \quad (8.9)$$

with plug flow solid body rotation exit velocity profiles. Table XXI reveals how ϕ , S' and G are related under such conditions for the swirl vane angles of special interest.

In this study, the swirl velocity is deduced in the manner $[\phi \sim S' \sim G]$, with appropriate radial gradients being automatically set up in the computer program. Notice that a gross error would be made if Eq. (8.7) were to be used to set up the inlet velocities $[\phi \sim S \sim G]$, since Eq. (8.9) is valid for S' values, not S values. In fact, corresponding G values would be much lower than those of Table I, with G asymptotically approaching 2 and ϕ and S tend to 90 degrees and ∞ , respectively.

Case 3. Measured inlet axial and swirl velocities are used (28) with radial velocity assumed to be zero.

Case 4. Measured inlet axial, radial and swirl velocity values are used, taking data from recent hot wire data in close vicinity of the swirler exit.

Consider first the flowfield resulting when the inlet swirl vane angle is 45 degrees. Figures 26a through 29a show predicted velocity profiles at various downstream axial stations, obtained when the inlet velocity profiles are specified by Cases 1 through 4 respectively. Inspection of these figures is quite revealing and may be assessed in the light of pitot probe and hot wire experimental data (9, 10).

Cases 1 and 2 for swirl vane angle $\phi = 45$ degrees covered in Figures 26a and 27a give central recirculation zones terminating at about $X/D = 2.0$, with the first case having a wider and slightly longer zone. The central recirculation zones extend beyond 2.5 chamber diameters downstream of the inlet domain for the Cases 3 and 4, for the same swirl strength as can be seen in Figures 28a and 29a. Case 3 shows a thicker boundary layer at the wall than case 4. Initial spreading rates vary considerably: only in Cases 3 and 4 does the central recirculation zone begin immediately on entry to the larger chamber, with Case 4 spreading most rapidly in the initial region. Cases 1 and 2 do not possess enough centrifugal effect because of their unrealistic inlet swirl velocity profiles. Also, Cases 1 through 3 do not have a radial component of velocity to encourage inlet radial spreading of the streamlines. These inlet flow ideas may be confirmed by observing the size of the corner recirculation zone. Cases 2 and 4 exhibit shorter corner zones, with only Case 4 also possessing the correct central activity near the inlet -- rapid spreading with a central recirculation flow beginning immediately. Comparison of the predictions with the

experimental data (9, 10) as shown in Figure 13 clearly indicates that the inlet conditions of Case 4 are superior in allowing realistic flow-field predictions.

Figures 26b through 29b correspond to Figures 26a through 29a but with the swirl vane angle increased to 70 degrees. Now the strong centrifugal forces present in the incoming flow play their part. Initial spreading rates are very high with no corner recirculation zones in all cases, except that of Case 3 seen in Figure 28b. All central recirculation zones begin immediately at the inlet and are much wider and longer than those with $\phi = 45$ degrees. Cases 1 and 2 predicted the centerline velocity more closely to the experimental data than Cases 3 and 4. However, the swirl velocity profiles are better predicted in Cases 3 and 4 than the other cases.

A general deduction may be made from Figures 26 through 29 when compared with the experimental data (9, 10). Results demonstrate that the type of inlet velocity profiles shows a clearer effect on the predictions of the 45 degree swirl vane angle flowfield than the corresponding one of 70 degrees. Also, it shows that realistic predictions are forthcoming only from the inclusion of the most accurate axial, radial and swirl velocity profiles as inlet conditions. Similar conclusions were reported by Abujelala and Lilley (2) using the STARPIC computer program along with the standard $k-\epsilon$ turbulence model.

8.3 General Predictions for Flowfield with $D/d = 2$

The effects of swirl strength and downstream contraction nozzle are discussed in this section. In discussing the effects of swirl strength, the velocity field predictions for swirl vane angles of 0, 45, and 70

degrees, using measured swirler exit u , v and w velocity profiles in each case, are considered. Two ratios are employed in the investigation of the influence of downstream contraction nozzle. As mentioned earlier, the predictions are obtained via the STARPIC computer code along with the modified k - ϵ model; the model parameter C_μ formulation is described in Section 7.4.

8.3.1 Effects of Swirl Strength

The effects of swirl strength on the flow pattern are firstly investigated via a flow visualization technique, which uses neutrally-buoyant helium-filled soap bubbles, as shown in Figure 30. This figure shows the swirl effects qualitatively. To obtain quantitative values, predictions were made for different swirl strengths. The velocity field predictions for swirl vane angles 0, 45, and 70 degrees are displayed in Figure 23 and parts (a) and (b) of Figure 29, respectively. The corresponding three-dimensional representations are given in Figure 31. Here the ordinate of normalized axial velocity is shown impressively as a function of normalized flowfield position. The flow is from right to left, with the sizes and shapes of corner and central recirculation zones being clearly evident, along with the axial and swirl velocity magnitudes.

The predicted effects of swirl shown in Figures 23 and 29 confirm in general the well-known ideas about swirl effects on axisymmetric turbulent confined jet flows (115). Under nonswirling conditions a large corner recirculation zone exists which extends approximately to $x/D = 2.3$ for the expansion geometry $D/d = 2$ and to $x/D = 1.25$ for $D/d = 1.43$, see Refs. (93) and (117). Both these results are consistent

with an attachment point about 8 step heights downstream of the expansion plane, as found by other researchers (9, 20, 26). The centerline axial velocity changes gradually from its inlet value as downstream development occurs. However, as the degree of inlet swirl is increased to 45 degrees, axial velocity profiles change dramatically. Near the inlet a central toroidal recirculation zone appears and the corner recirculation zone shortens considerably. Under strong swirl condition of equal to 70 degrees, a much wider central recirculation region is established. It promotes a very large forward velocity near the confining walls rather than a corner recirculation region.

Generally, the following results can be drawn from Figures 23 and 29:

1. The higher the swirl strength, the higher the centrifugal force, hence the larger the central recirculation zone core diameter;
2. The stronger the swirl strength, the longer the central zone extends downstream;
3. The corner recirculation zone size reduces sharply as swirl strength increases.

8.3.2 Effects of Downstream Contraction Nozzle

This section discusses the prediction of the flowfields with a downstream contraction nozzle located at $L/D = 1$ and 2 for nonswirling, moderate and strong swirl strengths, which correspond to swirl vane angles $\phi = 0, 45$, and 70 degrees, respectively. Two nozzles of area ratio 2 (weak) and 4 (strong) are being used. The weaker one has its upstream face contoured in a quarter circle; the stronger one has its upstream face in a 45 degree slope. These are typical of exit nozzle

for ramjet and gas turbine combustors, respectively, and shown schematically in Figure 2.

The nozzle area ratio and location effects on the predicted flowfield, using the STARPIC computer code with the standard $k-\epsilon$ model, were discussed at length by Abujelala and Lilley (2). They reported that the weak nozzle produces minor effects on the predicted flowfield, especially at low swirl strengths and at high L/D value. The finding can be seen in Figure 30, which displays the flowfield photographically. Therefore, only the strong nozzle effects are explored numerically in the present study, with the nozzle located at axial stations $L/D = 1$ and 2 downstream of the domain inlet.

Under nonswirling conditions, the blockage effects are minimal at either nozzle location -- the central forward flow is accelerated and the large corner recirculation remains. Under intermediate and strong swirl conditions, however, the effects of the 4 to 1 area reduction are dramatic at either nozzle location. The corner recirculation zone is encouraged to occur. This is expected due to the grid size near the nozzle wall; the nozzle should accelerate the flow. The central recirculation zone is removed, particularly for the moderate swirl strength, and a small annular recirculation zone is formed for the strong swirl strength flowfield, as also found experimentally (9, 10), and numerically (48). These effects are seen in parts (a) through (c) of Figures 32 (with $L/D = 1$) and 33 (with $L/D = 2$) for swirl vane angles $\phi = 0, 45$, and 70 degrees, respectively. These figures show axial and swirl velocity profiles and may be compared with the earlier Figures 23 and 29 which were for the open-ended flowfield. The strong contractions also result in very large swirl velocity magnitudes and gradients in

central core regions, which prevail throughout the flow domain for both moderate and strong swirl strengths.

Generally, the predicted nozzle effects on the flowfield characteristics are in good agreement with the experimental data (9, 10), except the values just upstream of the nozzle obstacle; the predictions show a small corner recirculation zone. However, the experimental data display an accelerated flow near the wall. It is expected that better predictions will be obtained if the grid size is further refined, especially near the nozzle location.

8.4 General Predictions for Flowfield with $D/d = 1.5$

8.4.1 Effects of Swirl Strength

The time-mean axial and swirl velocity profiles were predicted for nonswirling, moderate and strong swirl flows which correspond to swirl vane angles of 0, 45 and 70 degrees, respectively, as shown in parts (a), (b) and (c) of Figure 34. Inspection of this figure reveals that the size of the corner recirculation zone reduces and the central recirculation zone builds up as swirl strength increases. These observations are in accord with the results in Section 8.3.1. The predicted axial and swirl velocity values are higher than the corresponding ones for the flowfield with $D/d = 2$ as a result of the flow area reduction.

8.4.2 Effects of Downstream Contraction Nozzle

In these particular predictions, a contraction nozzle of area ratio 4 is located only at $L/D = 2$ downstream of the inlet domain, since inspection of Figures 32 and 33 shows that the nozzle produces

comparable effects at either one or two diameters downstream of the inlet. The predicted axial and swirl velocity profiles for swirl vane angles of 0, 45 and 70 degrees are displayed in parts (a), (b) and (c) of Figure 35, respectively.

Comparison of the predicted velocity profiles displayed in Figure 33 and the corresponding ones of Figure 35 reveals that the presence of the nozzle produces effects similar to those reported in Section 8.3.1. However, the absolute velocity magnitudes are higher. The small central recirculation zone which appears in Figure 33c is not seen in part (c) of Figure 35, for the case of $\phi = 70$ degrees.

8.5 General Predictions for Flowfield with $D/d = 1$

8.5.1 Effects of Swirl Strength

The previous sections describe a flowfield with an abrupt expansion. That flowfield has been found to be characterized by a complex flow with recirculation zones. This section discusses a flowfield that is found in a circular cross-sectioned duct flow without inlet expansion. The predicted results are computer plotted and displayed in Figure 36. Three swirl strengths vary from zero to strong swirl as described in Section 8.3.1 are shown in parts (a), (b) and (c) of this figure. Figure 36 shows no corner recirculation zone for nonswirling and moderately swirling flows. However, the strongly swirling flow ($\phi = 70$) shows a very small central recirculation zone close to the domain inlet. This is expected due to the balance between the kinetic energy of the flow and the centrifugal force at low and moderate swirl strengths. The aforementioned observations, extracted from Figure 36,

are in accord with expectations. Vortex breakdown may occur only in high swirling flows (6).

8.5.2 Effects of Downstream Contraction Nozzle

The predictions presented in this section are similar to the ones of Section 8.3.1 and 8.4.1, except that there is no flow expansion in the present case, and more uniform flow approaches the nozzle. The predicted profiles for time-mean axial and swirl velocity for swirl vane angles of 0, 45 and 70 degrees are displayed in Figure 37. Inspection of this figure reveals that the general effects of the presence of the nozzle are again expected. The flow accelerates as the nozzle is approached. The central recirculation zone disappears, even at the highest swirl strength considered.

8.6 General Predictions with Standard k- ϵ Model

Previous predictions shown so far have been obtained with the C_μ formulation model and general flow trends exhibited. How do these predictions compare with standard k- ϵ model predictions? It is interesting to see and compare the possibilities. Indeed, for the $D/d = 2$ case, predictions were given in Ref. (2) for the open-ended flow and the flow with a strong nozzle at $L/D = 2$. These may be compared with Figures 29 and 33, respectively, of the present study. Corresponding results for $D/d = 1.5$ are given in Figures 38 and 39, and these may be compared with Figures 34 and 35. similar results for $D/d = 1$ are given in Figures 40 and 41 and these may be compared with Figures 36 and 37.

8.7 Summary and Discussion

8.7.1 Effects of Expansion Ratio and Swirl Strength

Sections 8.3.1 and 8.6 have shown that the expansion ratio can considerably affect the aerodynamics, flame shape, heat transfer and stability limits, especially at high expansion ratio and high swirl strength. However, a few studies of the effect of levels of expansion upon confined swirling and nonswirling jets have been found in the literature. The reattachment point (the point at which the dividing streamline strikes to the wall) has been found of particular interest in studying the effects of expansion on nonswirling flow, and thus expansion effects on the axial extent of the flow separation regions (118-121).

In this study three expansion ratios are considered: 2, 1.5, and 1. Computer plots of predicted streamline patterns using the C_μ formulation model for each expansion ratio for 0, 45 and 70 degrees of swirl respectively, are displayed in Figures 42 through 44. Part (a) of these figures represent flowfield patterns for nonswirling flow, and parts (b) and (c) show the streamline plot for $\phi = 45$ and 70 degrees, respectively.

Comparison between part (a) of Figure 42 through Figure 44 reveals that the length of the corner recirculation zone (CRZ) increases almost linearly with expansion ratio. These figures show that the CRZ extends to about 3, 2 and 0 times the combustion chamber diameter for $D/d = 2$, 1.5 and 1, respectively. These results are in accord with the finding of Beck and Roschke (118), who reported that the reattachment length should increase linearly with both Reynolds number and the dimensionless

geometric ratio of step height and inlet nozzle diameter. In addition, the maximum reattachment length and the Reynolds number at which this occurs, depends on the type of inlet velocity profiles and on the flow geometry (119).

Parts (b) and (c) of Figures 42 through 44 show effects of the expansion ratio and swirl strengths on the width and length of the central recirculation zone. It is clear from inspection of these figures that the expansion ratio alters the streamline patterns of the flowfield. In the case of 45 degrees swirl, it seems that as the expansion ratio decreases, the beginning of the central recirculation zone moves further downstream of the inlet to the flow domain; as the expansion ratio approaches one, no recirculation zone occurs in the flow domain. However, the effects of reducing the expansion ratio on a $\phi = 70$ degree flowfield are seen to be that the central recirculation zone sharply reduces in size, becoming very small as the expansion ratio reduces to the nonexpanded case.

8.7.2 Superiority of the C_μ Formulation Model

Comparison of general time-mean velocity experimental data of Refs. (9, 10, 122), obtained using a five-hole pitot probe and hot-wire, indicate that the predictions using the proposed C_μ formulation are superior to these using the standard $k-\epsilon$ model. This is especially true regarding the central recirculation core diameter and length, and magnitudes of axial and swirl velocities. Figures 13, 14, 23 through 25, 45 and 46, give predictions with the C_μ formulation model and compare them with experimental data. The agreement is generally very good and better than would be seen were the standard $k-\epsilon$ predictions used instead.

8.8 Closure

A numerical prediction using the $k-\epsilon$ turbulence model, with C_μ formulation obtained from recent experimental data, and different inlet flow boundary condition assumptions has been applied to a confined swirling flow. Inlet flow boundary conditions have been demonstrated to be extremely important in simulating a flowfield via numerical calculations. Predictions with either flat inlet profiles, solid body rotation or zero radial velocity are inappropriate.

Predictions are given for a full range of swirl strengths using measured inlet axial, and swirl velocity profiles. The predicted velocity profiles illustrate the large-scale effects of inlet swirl on flowfields. Predictions are included for the effects of the presence of a strong downstream contraction nozzle and the expansion ratio on the flowfield. It appears that a strong nozzle has pronounced effects on swirl flow cases, with discouragement of central recirculation zones, and forward flow in highly swirled vortex core regions further downstream. The expansion ratio value has large-scale effects on the size and location of the recirculation zones.

CHAPTER IX

CONCLUSIONS AND RECOMMENDATIONS

9.1 Conclusions

Upon the completion of this numerical study for the two-dimensional axisymmetric confined turbulent swirling flow, the following conclusions were reached:

1. Inlet flow boundary conditions have been demonstrated to be extremely important in simulating a flowfield via numerical calculations. Prediction with either flat inlet profiles, solid body rotation or zero radial velocity are inappropriate.
2. The presence of a downstream contraction nozzle has shown considerable effects on the flowfield characteristics. It appears that a weak nozzle has only a minor effect on the flow. In the swirl flow cases, a weak nozzle leads to the discouragement of central recirculation zones with stronger vortex cores downstream possessing negative axial velocities. A stronger nozzle has more pronounced effects on swirl flow cases, and forward flow in highly swirled vortex core regions further downstream.
3. The degree of swirl strength and the expansion ratio have strong effects on the characteristics of confined turbulent swirling flow. In a nonswirling flow, a large corner recirculation zone exists in the flowfield with an expansion ratio greater than 1. However, as the degree of inlet swirl increases, the size of the zone decreases and

a central recirculation zone appears near the inlet. Generally, the size of the central zone increases with swirl strength and expansion ratio.

4. Neither the standard $k-\epsilon$ model nor its previous extensions show effective capability of predicting confined turbulent swirling flows. However, either deduced optimum values of three parameters in the model or the empirical C_μ formulation obtained via careful analysis of the available turbulence data can provide more acceptable accuracy in the prediction of these swirling flows.

9.2 Recommendations

Turbulence modeling has taken the attention of many investigators over the years. The complexity of the subject has limited the use of proposed models to the flow cases that they were derived for. The range of the applicability of these models can be extended through simple modifications to their parameters. This study exemplifies the extension of the $k-\epsilon$ model to confined turbulent swirling flows.

In derivation of the proposed C_μ formulation, the time-mean velocity axial gradients were ignored because of lack of detailed data. As mentioned in Chapter VI, this assumption may lead to false conclusions in regions of high recirculation. Therefore, it is advised to evaluate the effects of inclusion of the velocity axial gradients on the proposed model assumptions. Also, this evaluation can be obtained through a careful measurement of the length scale. Finally, near wall turbulence data are needed to examine the model performance close to the wall.

REFERENCES

1. Beer, J. M. and Chigier, N. A., Combustion Aerodynamics, Wiley, New York, 1972.
2. Abujelala, M. T., and Lilley, D. G., "Confined Swirling Flow Predictions," Paper AIAA 83-0310, Reno, Nevada, January 10-13, 1983.
3. Sander, G. F., and Lilley, D. G., "The Performance of an Annular Vane Swirler," Paper AIAA 83-1326, Seattle, Washington, June 27-29, 1983.
4. King, M. K., Rothfus, R. R., and Kermode, R. I., "Static Pressure and Velocity Profiles in Swirling Incompressible Tube Flow," AICHE Journal, Vol. 15, No. 6, 1969, pp. 837-842.
5. Karasu, Tahir, "Numerical Prediction of Incompressible Turbulent Swirling Flows in Circular-Sectioned Ducts and Annuli," Ph.D. Thesis, Imperial College of Science and Technology, London, June 1980.
6. Hall, M. G., "Vortex Breakdown," Annual Review of Fluid Mechanics, Vol. 4, 1972, pp. 195-218.
7. Leibovich, S., "The Structure of Vortex Breakdown," Annual Review of Fluid Mechanics, Vol. 10, 1978, pp. 221-246.
8. Swift, W. L., Barna, P. S., and Dalton, C., Vortex Flows, ASME, New York, 1980.
9. Yoon, H. K., and Lilley, D. G., "Five-Hole Pitot Probe Time-Mean Velocity Measurements in Confined Swirling Flows," Paper AIAA 83-0315, Reno, Nevada, January 10-13, 1983.
10. Jackson, T. W., and Lilley, D. G., "Single-Wire Flow Turbulence Measurements," Paper AIAA 83-1202, Seattle, Washington, June 27-29, 1983.
11. Lilley, D. G., "Swirl Flows in Combustion: A Review," AIAA Journal, Vol. 15, No. 8, 1977, pp. 1063-1078.
12. Dorfman, L. A., Hydrodynamic Resistance and Heat Loss of Rotating Solids, Oliver and Boyd, London, 1963.
13. Kreith, F., Advanced Heat Transfer, Vol. 5, 1968, pp. 129-251.

14. Lilley, D. G., and Rhode, D. L., STARPIC: A Computer Code for Swirling Turbulent Axisymmetric Recirculating Flows in Practical Isothermal Combustor Geometries, NASA CR-3442, 1982.
15. Gosman, A. D., and Pun, W. M., Calculation of Recirculating Flows, Rept. No. HTS/74/12, Dept. of Mech. Engrg., Imperial College, London, England, 1974.
16. Roache, P. J., Computational Fluid Dynamics, Albuquerque, Hermosa, 1972.
17. Chow, C. Y., An Introduction to Computational Fluid Mechanics, John Wiley, New York, 1979.
18. Patankar, S. V., Numerical Heat Transfer and Fluid Flow, Hemisphere-McGraw Hill, New York, 1980.
19. Taylor, C., and Schrefler, B. A., "Numerical Methods in Laminar and Turbulent Flow," Proceedings of the Second International Conference, Venice, Italy, 1981.
20. Lilley, D. G., "Primitive Pressure - Velocity Code for the Combustion of Strongly Swirling Flows," AIAA Journal, Vol. 14, No. 6, 1976, pp. 749-756.
21. McDonald, H., "Combustion Modeling in Two and Three Dimensions: Some Numerical Considerations," Prog. in Energy and Combustion Science, Vol. 5, 1979, pp. 97-122.
22. Lilley, D. G., "Prospects for Computer Modeling in Ramjet Combustors," Paper AIAA 80-1189, Hartford, Connecticut, June 30 - July 2, 1980.
23. Kubo, I., and Gouldin, F. C., "Numerical Calculations of Turbulent Swirling Flow," J. of Fluids Engineering, September 1975, pp. 310-315.
24. Gosman, A. D., Lockwood, F. C., and Loughhead, J. N., "Prediction of Recirculating, Swirling, Turbulent Flow in Rotating Disc Systems," Journal of Mech. Engrg. Science, Vol. 18, No. 3, 1976, pp. 142-148.
25. Mongia, H. C., and Smith, K. P., "An Empirical/Analytical Design Methodology for Gas Turbine Combustors," Paper AIAA 78-998, Las Vegas, Nevada, July 25-27, 1978.
26. Novick, A. S., Miles, G. A., and Lilley, D. G., "Numerical Simulation of Combustion Flowfields," Journal of Energy, Vol. 3, No. 2, 1979, pp. 95-105.

27. Serag-Eldin, M. A., and Spalding, D. B., "Computations of Three Dimensional Gas Turbine Combustion Chamber Flows," Transactions of the ASME, Journal of Engineering for Power, Vol. 101, July 1979, pp. 326-336.
28. Rhode, D. L., "Prediction and Measurements of Isothermal Flowfields in Axisymmetric Combustor Geometries," Ph.D. Thesis, School of Mech. and Aero. Engrg., Oklahoma State University, Stillwater, Oklahoma, December 1981.
29. Samples, J. W., "Prediction of Axisymmetric Chemically Reacting Combustor Flowfields," Ph.D. Thesis, School of Mech. and Aero. Engrg., Oklahoma State University, Stillwater, Oklahoma, May 1983.
30. Hiatt, G. F., and Powell, G. E., "Three-Dimensional Probe for Investigation of Flow Patterns," The Engineering, January 1962, pp. 165-170.
31. Mathur, M. L., and MacCallum, N. R. L., "Swirling Airjets Issuing from Vane Swirler: Enclosed Jets," Journal of the Inst. of Fuel, Vol. 40, June 1967, pp. 238-245.
32. Weske, D. R., and Sturov, G. YE., "Experimental Study of Turbulent Swirled Flows in a Cylindrical Tube," Fluid Mechanics - Soviet Research, Vol. 3, No. 1, 1974.
33. Owen, F. K., "Laser Velocimeter Measurements of a Confined Turbulent Diffusion Flame Burner," Paper AIAA 76-33, Washington, D.C., January 26-28, 1976.
34. Sukhovich, YE. P., "Experimental Investigation of Local Properties of Swirled Turbulent Flow in Cylindrical Channels," Fluid Mechanics - Soviet Research, Vol. 7, No. 3, 1978.
35. Habib, M. A., and Whitelaw, J. H., "Velocity Characteristics of Confined Coaxial Jets With and Without Swirl," Transaction of the ASME, Journal of Fluids Engrg., Vol. 102, 1980, pp. 47-53.
36. Johnson, B. V., and Bennett, J. C., Velocity and Concentration Characteristics and Their Cross Correlations for Coaxial Jets in a Confined Sudden Expansion, United Technologies Research Center, UTRC81-16, 1981.
37. Yoon, H. K., "Five-Hole Pitot Probe Time-Mean Velocity Measurements in Confined Swirling Flows," M.S. Thesis, School of Mech. and Aero. Engrg., Oklahoma State University, Stillwater, Oklahoma, June 1982.
38. Vu, B. T., and Gouldin, F. C., "Flow Measurements in a Model Swirl Combustor," AIAA Journal, Vol. 20, May 1982.

39. Janjua, S. I., McLaughlin, D. K., Jackson, T. W., and Lilley, D. G., "Turbulence Measurements in a Confined Jet Using a Six-Orientation Hot-Wire Probe Technique," Paper AIAA 82-1262, Cleveland, Ohio, June 21-23, 1982.
40. Sturgess, G. J., Aerothermal Modeling: Phase I, NASA CR-168202, 1983.
41. Hendricks, C. J., and Brighton, J. A., "The Prediction of Swirl and Inlet Turbulence Kinetic Energy Effects on Confined Jet Mixing," Transaction of the ASME, Journal of Fluids Engineering, 1975, pp. 51-59.
42. Jones, W. P., and McGuirk, J. J., Mathematical Modeling of Gas-Turbine Combustion Chamber, AGARD-CP-275, 1979.
43. Syed, S. A., and Sturgess, G. J., Validation Studies of Turbulence and Combustion Models for Aircraft Gas Turbine Combustors, HTD, Vol. 13, 1980, pp. 71-89.
44. Morse, A., "Axisymmetric Turbulent Shear Flows With and Without Swirl," Ph.D. Thesis, University of London, London, England, 1980.
45. Sturgess, G. J., and Syed, S. A., "Widely-Spaced Co-Axial Jet Diffusion-Flame Combustion: Isothermal Flow Calculations Using the Two-Equation Turbulence Model," Paper AIAA 82-0113, Orlando, Florida, January 11-14, 1982.
46. Perry, A. E., Hot-Wire Anemometry, Clarendon Press, Oxford, England, 1982.
47. Murakami, M., Kito, O., Katayama, Y., and Iida, Y., "An Experimental Study of Swirling Flow in Pipes," Bulletin of the JSME, Vol. 19, No. 128, 1976, pp. 118-126.
48. Harch, W. H., Numerical Modeling of Ramjet Combustors, AFWAL-TK-82-2113, 1983.
49. Gosman, A. D., Khalil, E. E., and Whitelaw, J. H., The Calculation of Two-Dimensional Turbulent Recirculating Flows, Turbulent Shear Flows I, Ed. Durst, Springer Verlag, 1979, pp. 237-255.
50. Coretto, L. S., Gosman, A. D., Patankar, S. V., and Spalding, D. B., "Two Calculation Procedures for Steady Three-Dimensional Flows with Recirculation," Proceedings of the Third International Conference on Numerical Method in Fluid Dynamics, Berlin, Heidelberg, New York, Springer, 1972.
51. Harlow, F. H., and Welch, J. E., "Numerical Calculation of Time Dependent Viscous Incompressible Flow of Fluid with Free Surface," Phys. Fluids, 1965, Vol. 8, pp. 2182-2189.

52. Patankar, S. V., and Spalding, D. B., "A Calculation Procedure for Heat, Mass and Momentum Transfer in Three Dimensional Parabolic Flows," Int. J. Heat Mass Transfer, Vol. 15, 1972, pp. 1787-1805.
53. Townsend, A. A., The Structure of Turbulent Shear Flow, Cambridge University Press, 1956.
54. Tennekes, H., and Lumley, J. L., A First Course in Turbulence, Prentice-Hall International, 1972.
55. Launder, B. E., and Spalding, D. B., Lecture in Mathematical Models of Turbulence, Dept. of Mech. Eng., Imperial College of Science, Academic Press, 1972.
56. Wolfgang, R., Prediction Methods for Turbulent Flows, Von Karman Institute for Fluid Dynamics, 1980.
57. Bradshaw, P., Cebeci, T., and Whitelaw, J., Engineering Calculation Methods for Turbulent Flows, Academic Press, London, England, 1981.
58. Launder, B. E., and Spalding, D. B., "The Numerical Computation of Turbulent Flows," Computer Method in Applied Mechanics and Engineering, Vol. 3, 1974, pp. 269-284.
59. Saffman, P. G., and Wilcox, D. C., "Turbulence-Model Predictions for Turbulent Boundary Layers," AIAA Journal, Vol. 12, No. 4, pp. 541-546.
60. Launder, B. E., Reece, G. J., and Rodi, W., "Progress in the Development of a Reynolds-Stress Turbulence Closure," J. Fluid Mech., Vol. 68, No. 3, 1975, pp. 537-566.
61. Golvin, A. M., "A Phenomenological Theory of Turbulence," Fluid Mechanics, Soviet Research, Vol. 7, No. 3, 1978, pp. 161, 167.
62. Leslie, D. C., Developments in The Theory of Turbulence, Clarendon Press, Oxford, England, 1973.
63. Marthy, S. N. B., Project Squid on Turbulence in Internal Flows, Hemisphere, Washington, 1976.
64. Bradshaw, P., Topics in Applied Physics: Turbulence, Vol. 12, Springer Verlag Berlin Heidelberg, 1976.
65. Schumann, U., "Realizable of Reynolds Stress Turbulence Models," The Physics of Fluids, Vol. 20, No. 5, 1977, pp. 721-725.
66. Kennedy, L. A., "Turbulent Combustion," AIAA Progress in Astronautics and Aeronautics, Vol. 58, 1977.
67. Weber, H. E., Turbulent Boundary Layers, ASME, New York, 1979.

68. Bradbury, L. J. S., Durst, F., Launder, B. E., Schmidt, F. W., and Whitelaw, J. H., Turbulent Shear Flows: 2, Springer-Verlag Berlin Heidelberg, 1980.
69. Libby, P. A., and Williams, F. A., Topics in Applied Physics: Turbulent Reacting Flows, Vol. 44, Springer-Verlag Berlin Heidelberg, 1980.
70. Rodi, W., Turbulent Buoyant Jets and Plumes, Pergamon Press, New York, 1982.
71. Schumann, U., Grotzbach, G., and Keister, L., "Direct Numerical Simulation of Turbulence," A Lecture in Reference 57.
72. Moffat, H. R., "Some Developments in Theory of Turbulence," Journal of Fluid Mechanics, Vol. 106, 1981, pp. 27-47.
73. Kim, H. J., and Moin, P., Large Eddy Simulation of Turbulent Channel Flow...ILLIAC IV Calculation, AGARD, No. 271, 1979.
74. McMillan, D. J., and Ferzigen, J. H., "Direct Testing of Subgrid-Scale Models," AIAA Journal, Vol. 17, 1979, pp. 1340-1345.
75. Moin, P., and Kim, J., Numerical Investigation of Turbulent Channel Flow, NASA TM 81309, 1981.
76. Yoshizawa, A., "A Statistically-Derived Subgrid Model for the Large-Eddy Simulation of Turbulence," Phys. Fluids, Vol. 25, 1982, pp. 1532-1537.
77. Leschziner, M. A., and Rodi, W., "Calculation of Annular and Twin Parallel Jets Using Various Descretization Schemes and Turbulence-Model Variations," Transactions of the ASME, Vol. 103, 1981, pp. 254-360.
78. Rodi, W., "Examples of Turbulence Models for Incompressible Flows," AIAA Journal, Vol. 20, No. 7, 1982, pp. 872-879.
79. Hanjalic, K., and Launder, B. E., "A Reynolds Stress Model of Turbulence and Its Application to Thin Shear Flows," J. Fluid Mech., Vol. 52, 1972, pp. 609-638.
80. Ng, K. H., and Spalding, D. B., "Turbulence Model for Boundary Layers Near Walls," The Physics of Fluids, Vol. 15, 1972, pp. 20-30.
81. Lilley, D. G., Numerical Solution of Turbulent Swirling Flows, Computational Methods and Problems in Aeronautical Fluid Dynamics, (B. L. Hewitt, et al., eds.), Academic Press, London, 1976, pp. 492-525.
82. Hassid, S., and Poreh, M., "A Turbulent Energy Model for Flows with Drag Reduction," ASME Paper 75-FE-H, 1975.

83. Norris, L. H., and Reynolds, W. C., Turbulent Channel Flow with a Moving Wavy Boundary, Dept. of Mechanical Engineering, Stanford University, Stanford, California, Rept. FM-10, 1975.
84. Reynolds, W. C., "Computation of Turbulent Flows," Annual Review of Fluid Mechanics, Vol. 8, 1976, pp. 269-289.
85. Daly, B. J., and Harlow, F. H., "Transport Equations of Turbulence," Phys. Fluids, Vol. 13, 1970, p. 2634.
86. Rodi, W., "Turbulence Modeling for Environmental Problems," A Lecture in Ref. 57.
87. Lumley, J. L., and Khajeh-Nouri, B., "Computation of Turbulent Transport," Advances in Geophysics, Vol. A18, 1974, pp. 169-192.
88. Lewellen, W. S., Teske, M., and Donaldson, C. du P., "Variable Density Flows Computed by a Second-Order Closure Description of Turbulence," AIAA Journal, Vol. 14, 1976, pp. 382-397.
89. Gibson, M. M., and Launder, B. E., "Ground Effects on Pressure Fluctuations in the Atmospheric Boundary Layer," Journal of Fluid Mechanics, Vol. 86, 1978, pp. 491-511.
90. Koosinlin, M. L., and Lockwood, F. C., "The Prediction of Axisymmetric Turbulent Boundary Layers," AIAA Journal, Vol. 12, No. 4, 1974, pp. 547-554.
91. Gibson, M. M., "An Algebraic Stress and Heat-Flux Model for Turbulent Shear Flow with Streamline Curvature," Int. J. Heat Mass Transfer, Vol. 21, 1978, pp. 1609-1617.
92. Sinder, M. M., and Harsha, P. T., Assessment of Turbulence Models for Scramjet Flowfields, NASA CR 3643, 1982.
93. Moon, L. E., and Rudinger, G., "Velocity Distribution in the Abruptly Expanding Circular Duct," ASME J. of Fluids Engineering, Vol. 99, 1977, pp. 226-230.
94. Ideriah, F. J. R., "Numerical Procedure for Calculation Partly Elliptic Flows," J. Mech. Engineering Sci., Vol. 21, 1979, pp. 372-380.
95. Green, A., and Whitelaw, J. H., "Measurements and Calculations of the Isothermal Flow in Axisymmetric Models of Combustor Geometries," J. Mech. Engineering, Sci., Vol. 22, 1980, pp. 119-124.
96. Abujelala, M. T., and Lilley, D. G., "Limitations and Empirical Extensions of the $k-\epsilon$ Model as Applied to Turbulent Confined Swirling Flows," Paper AIAA 84-04111, Reno, Nevada, January 9-12, 1984.

97. Jones, W. P., and Launder, B. E., "The Prediction of Laminarization with a Two-Equation Model of Turbulence," Int. J. Heat Mass Transfer, Vol. 15, 1972, pp. 301-314.
98. Syed, S. A., and Sturgess, G. J., "Velocity and Concentration Characteristics and Their Gross Correlations for Coaxial Jets in Confined Sudden Expansion. Part II: Predictions," Proceedings, ASME Symposium on Fluid Mechanics of Combustion Stress, Boulder, Colorado, June 22-23, 1981, pp. 145-160.
99. Whitelaw, H. J., and Green, A., "Measurements and Calculations of the Isothermal Flow in Axisymmetric Models of Combustor Geometries," J. Mech. Engineering Science, Vol. 22, 1980, pp. 117-124.
100. Jones, W. P., and Launder, B. E., "The Calculation of Low Reynolds Number Phenomena with a Two-Equation Model of Turbulence," Int. Journal of Heat and Mass Transfer, Vol. 16, 1973, pp. 1119-1129.
101. Launder, B. E., Priddin, C. H., and Sharma, B. I., "The Calculation of Turbulent Boundary Layers on Spining and Curved Surface," Transactions of the ASME, J. of Fluids Engineering, Vol. 99, March 1977, pp. 231-238.
102. Durst, F., and Rostogi, A. R., Theoretical and Experimental Investigations of Turbulent Flows with Separation, Turbulent Shear Flows (Durst, F., Launder, B. E., Schmidt, F. W., and Whitelaw, J. H., eds.), Springer-Verlag, Berlin Heidelberg, Germany, Vol. 1, 1973, pp. 205-219.
103. Ljuboja, M., and Rodi, W., "Calculation of Turbulent Wall Jets with an Algebraic Reynolds Stress Model," Transactions of the ASME, J. of Fluids Engineering, Vol. 102, September 1980, pp. 351-356.
104. Hanjalic, K., and Launder, B. E., "Sensitizing the Dissipation Equation to Irrotational Strains," Transactions of the ASME, J. of Fluids Engineering, Vol. 102, March 1980, pp. 34-40.
105. Hanjalic, K., and Launder, B. E., Preferential Spectral Transport by Irrotational Straining, Turbulent Boundary Layers, edited by Weber, H. E., ASME, New York, 1979, pp. 101-109.
106. Lam, C. K. G., and Bremhost, K., "A Modified Form of the $k-\epsilon$ Model for Predicting Wall Turbulence," Transactions of the ASME, J. of Fluids Engineering, Vol. 103, September 1981, pp. 456-460.
107. Lilley, D. G., "Analytical Inverse of the Turbulent Swirl Flow Boundary Layer Equations," Paper AIAA-75-856, Hartford, Conn., June 16-18, 1975.

108. Abujelala, M. T., Jackson, T. W., and Lilley, D. G., "Turbulence Parameter Variation in Confined Swirling Flows," Studies in Progress, Oklahoma State University, Stillwater, Okla., 1984.
109. Reynolds, W. C. So, Turbulence Velocity Scales for Swirling Flows, Turbulence in Internal Flows (Murthy, S.N. B., ed.) Hemisphere Corp., Washington, 1976, pp. 347-369.
110. Kuester, J. L., and Mize, J. H., Optimization Techniques with FORTRAN, McGraw-Hill Book Company, New York, 1973.
111. Rosenbrock, H. H., "An Automatic Method for Finding the Greatest or Least Value of a Function," Computer Journal, Vol. 3, 1960, pp. 175-184.
112. Rosenbrock, H. H., and Storcy, C., Computational Technique for Chemical Engineers, Pergamon Press, New York, 1960.
113. Chigier, N. A., and Beer, J. M., "Velocity and Static Pressure Distributions in Swirling Air Jets Issuing from Annular and Divergent Nozzles," J. of Basic Engng., December 1964, pp. 788-798.
114. Chigier, N. A., and Chervinsky, A., "Experimental Investigation of Swirling Vortex Motion in Jets," ASME Journal of Applied Mechanics, Vol. 89, June 1967, pp. 443-451.
115. Kerr, N. M., and Fraser, D., "Swirl, Part I: Effect on Axisymmetrical Turbulent Jets," J. Inst. Fuel, Vol. 38, December 1965, pp. 519-526.
116. Gupta, A. K., Lilley, D. G., and Syred, N., Swirl Flows, Abacus Press, Tunbridge Wells, England, 1983 (in press).
117. Chaturvedi, M. C., "Flow Characteristics of Axisymmetric Expansions," Proc. Journal Hydraulics Division, ASCE, Vol. 89, No. HYE, 1963, pp. 61-92.
118. Buck, L. H., and Koschke, E. J., "Shear-Layer Flow Regions and Wave Instabilities and Reattachment of an Abrupt Circular Channel Expansion," Transaction of the ASME Journal of Applied Mechanics, September 1972, pp. 677-681.
119. Roschke, E. J., and Buck, L. H., "The Influence of Upstream Conditions on Flow Reattachment Lengths Downstream of an Abrupt Circular Channel Expansion," J. Biomechanics, Vol. 9, 1976, pp. 481, 483.
120. Nozaki, T., and Hatta, K., "Reattachment Flow Issuing from a Finite Width Nozzle," Bulletin of the JSME, Vol. 25, No. 200, 1982, pp. 196-203.

121. Yang, B. T., and Yu, M. H., "The Flowfield in a Suddenly Enlarged Combustion Chamber," AIAA Journal, Vol. 21, January 1983, pp. 92-97.
122. Scharrer, G. L., Studies in Progress, Oklahoma State University, Stillwater, Okla., 1984.

APPENDIX A

TABLES

TABLE I

PREVIOUS NUMERICAL STUDIES OF SWIRLING FLOW

Ref/Year	Flow Type	Method of Prediction	Main Parameters Discussed
23/1975	Axisymmetric incompressible turbulent swirling flow.	2-D ψ, ω k, ϵ	Flame circulation, effect of inner and outer swirl, axial velocity ratio and Reynolds number on recirculation zone.
24/1976	Recirculating swirling turbulent flow in rotating disc systems.	2-D ψ, ω k, ϵ	Disc torque and stream function, tangential velocity contours and turbulence parameters.
22/1976	Inert and reacting recirculating flow with strong swirl in an axisymmetric combustor.	2-D p, u, v k, ϵ	Effect of swirl number and vane angles on flowfield.
25/1978	Advanced combustion systems of reverse flow annular configuration.	3-D p, u, v $\omega, k-\epsilon$	Prediction of stream flame, velocity, fuel air ratio and temperature profiles.
26/1979	Axisymmetric prechamber dump combustor	2-D p, u, v $k-\epsilon$	Expansion ratio, swirler dimension and double concentric reverse swirler
27/1979	Three-dimensional, swirling recirculating turbulent flow inside can combustors.	3-D, p, u, v $k-\epsilon$ and λ_m	Velocity, temperature and Nusselt number distributions.
28/1981	Turbulent swirling flow in axisymmetric combustor geometries.	2-D p, u, v $k-\epsilon$	Recirculation zones characteristics and velocity profiles.
29/1983	Axisymmetric turbulent reacting and nonreacting swirling flows.	2-D ρ, u, v $k-\epsilon$, Two-step global reaction	Velocity and temperature profiles, and carbon monoxide and nitrogen oxide distributions.

TABLE II

PREVIOUS EXPERIMENTAL STUDIES OF SWIRLING FLOW

Ref/Year	Flow Type	Method of Measurement	Main Parameters Evaluated
30/1962	Reacting and nonreacting flow in an aircraft and an industrial type combustor.	Water cooled three-dimensional pitot probe	Mean velocity profiles, recirculating boundaries and turbulence contours.
31/1967	Free and enclosed swirling jets from vane swirlers.	Pitot probe	Swirler efficiency, velocity profiles and recirculation zone size.
32/1974	Turbulent swirled flow in a cylindrical tube.	Hot-wire anemometer and pressure probe	Effect of swirl intensity on velocity profiles and on distribution of the eddy stress tensors.
33/1976	Initial mixing region of confined turbulent diffusion flame burner.	Laser velocimeter	Axial and tangential mean velocity profiles, rms and probability density distribution of velocity fluctuations.
34/1978	Swirled turbulent flow in cylindrical channels.	Pressure probes	Stresses tensors and turbulent viscosities and effect of centrifugal forces on the momentum transport in the flow.
35/1980	Confined coaxial jets with and without swirl.	Pressure probes, hot-wire and laser dopplers anemometer	Influence of confinement and swirl on the flow and mean velocity measurements.
36/1981	Coaxial jets discharging into a large axisymmetric duct.	Laser doppler velocimeter	Mean and fluctuating velocity and concentration distributions.

TABLE II (Continued)

37/1982	Confined swirling recirculating flow in axisymmetric combustor geometrics.	5-Hole pitot probe	Effects of swirl strength and end boundary on the main velocity profiles.
38/1982	Coaxial jet mixing in a pipe under coswirl and counterswirl conditions.	Pitot probe and hot-wire anemometer.	Mean velocity profiles and recirculation zone.
39/1982	Confined jet with and without swirl.	Six-orientation hot-wire	Mean and fluctuating velocity profiles.

TABLE III
THE FORM OF THE COMPONENTS OF
THE LINEARIZED SOURCE

ϕ	Γ_ϕ	$S_\phi^\dagger/\text{Vol.}$	$S_u^\dagger/\text{Vol.}$
1	0	0	0
u	μ	0	$S^u - \frac{\partial p}{\partial x}$
v	μ	$-2 \frac{\mu}{r^2}$	$S^v + \frac{\rho w^2}{r} - \frac{\partial p}{\partial r}$
w	μ	0	$-\frac{\rho vw}{r} - \frac{w}{r^2} \frac{\partial}{\partial r} (r\mu)$
k	μ/σ_k	$-C_\mu C_D \rho^2 k/\mu$	G
ϵ	μ/σ_ϵ	$-C_2 \rho \epsilon/k$	$C_1 C_\mu G \rho k/\mu$

In this table certain quantities are defined as follows:

$$S^u = \frac{\partial}{\partial x} \left(\mu \frac{\partial u}{\partial x} \right) + \frac{1}{r} \frac{\partial}{\partial r} \left(r\mu \frac{\partial v}{\partial x} \right)$$

$$S^v = \frac{\partial}{\partial x} \left(\mu \frac{\partial u}{\partial r} \right) + \frac{1}{r} \frac{\partial}{\partial r} \left(r\mu \frac{\partial v}{\partial r} \right)$$

$$G = \mu \left[2 \left\{ \left(\frac{\partial u}{\partial x} \right)^2 + \left(\frac{\partial v}{\partial r} \right)^2 + \left(\frac{v}{r} \right)^2 \right\} + \left(\frac{\partial u}{\partial r} + \frac{\partial v}{\partial x} \right)^2 \right. \\ \left. + \left\{ r \frac{\partial}{\partial r} \left(\frac{w}{r} \right) \right\}^2 + \left(\frac{\partial w}{\partial x} \right)^2 \right]$$

where $\mu = \mu_{\text{eff}}$ and Vol. stands for the cell control volume.

TABLE IV
THE k - ϵ EMPIRICAL CONSTANTS

C_μ	C_1	C_2	σ_k	σ_ϵ
0.09	1.44	1.92	1.00	1.30

TABLE V
TURBULENCE PARAMETERS FOR SWIRL VANE ANGLE $\phi = 0$ DEGREES

R/D	X/D				
	0.0	0.5	1.0	1.5	2.0
0.425	0.058	0.104	0.208	0.470	0.038
0.400	0.104	0.234	0.153	0.853	0.108
0.375	0.083	0.417	0.079	0.102	0.512
0.350	0.273	0.209	0.061	0.075	0.492
0.325	0.720	0.048	0.075	0.105	0.423
0.300	0.189	0.039	0.132	0.173	0.455
0.275	0.306	0.069	0.190	0.329	0.456
0.250	0.021	0.086	0.143	0.279	0.743
0.225	0.003	0.026	0.112	0.287	0.576
0.200	0.063	0.023	0.112	0.273	0.688
0.175	0.008	0.129	0.077	0.183	1.500
0.150	0.025	0.450	0.066	0.159	1.199
0.125	0.017	0.500	0.121	0.115	1.275
0.100	0.025	0.087	2.900	0.120	0.833
0.075	0.017	0.038	0.400	0.156	1.906
0.050	0.025	0.029	0.550	0.203	2.134
0.025	0.005	0.050	0.082	0.326	1.528
0.000	0.003	0.125	0.048	0.323	7.725

(a) $\mu_{rx}/(\rho u_0 D) \times 100$

TABLE V (Continued)

R/D	X/D				
	0.0	0.5	1.0	1.5	2.0
0.425	0.202	0.366	0.277	0.471	0.043
0.400	0.309	0.582	0.170	0.884	0.107
0.375	0.193	0.655	0.084	0.107	0.446
0.350	0.619	0.329	0.060	0.076	0.391
0.325	1.393	0.059	0.059	0.107	0.310
0.300	0.372	0.039	0.095	0.170	0.310
0.275	0.610	0.177	0.126	0.294	0.295
0.250	0.039	0.071	0.093	0.239	0.455
0.225	0.014	0.023	0.077	0.249	0.339
0.200	0.347	0.047	0.084	0.241	0.391
0.175	0.046	0.261	0.075	0.164	0.828
0.150	0.139	1.118	0.115	0.137	0.644
0.125	0.107	1.242	0.246	0.093	0.668
0.100	0.160	0.281	7.205	0.092	0.427
0.075	0.107	0.123	0.994	0.113	0.964
0.050	0.160	0.092	1.933	0.135	1.060
0.025	0.039	0.143	0.289	0.194	0.752
0.000	0.022	0.347	0.169	0.161	3.771

(b) ϵ/D

TABLE V (Continued)

R/D	x/D					
	0.0	0.5	1.0	1.5	2.0	2.5
0.425	0.044	0.047	0.093	0.108	0.011	0.013
0.400	0.074	0.086	0.045	0.169	0.023	0.023
0.375	0.045	0.132	0.018	0.018	0.088	0.033
0.350	0.079	0.056	0.011	0.011	0.077	0.049
0.325	0.424	0.011	0.011	0.015	0.058	0.082
0.300	0.116	0.007	0.017	0.021	0.059	0.063
0.275	0.130	0.009	0.023	0.031	0.056	0.056
0.250	0.003	0.011	0.017	0.030	0.084	0.050
0.225	0.001	0.006	0.014	0.035	0.062	0.059
0.200	0.056	0.008	0.016	0.035	0.071	0.071
0.175	0.026	0.044	0.016	0.025	0.146	0.053
0.150	0.079	0.179	0.022	0.024	0.111	0.061
0.125	0.053	0.224	0.048	0.023	0.112	0.126
0.100	0.079	0.074	1.204	0.028	0.070	0.148
0.075	0.053	0.034	0.200	0.039	0.152	0.119
0.050	0.079	0.026	0.303	0.052	0.161	0.109
0.025	0.016	0.050	0.049	0.081	0.110	0.122
0.000	0.009	0.125	0.030	0.079	0.525	0.180

(c) λ_m/D

TABLE V (Continued)

R/D	X/D				
	0.0	0.5	1.0	1.5	2.0
0.425	0.001	0.001	0.007	0.012	0.010
0.400	0.001	0.002	0.010	0.012	0.012
0.375	0.002	0.005	0.011	0.011	0.016
0.350	0.002	0.005	0.013	0.012	0.019
0.325	0.003	0.008	0.020	0.012	0.023
0.300	0.003	0.012	0.024	0.013	0.027
0.275	0.003	0.002	0.028	0.015	0.030
0.250	0.004	0.018	0.029	0.017	0.033
0.225	0.000	0.016	0.026	0.016	0.036
0.200	0.000	0.003	0.022	0.016	0.034
0.175	0.000	0.003	0.013	0.015	0.038
0.150	0.000	0.002	0.004	0.017	0.041
0.125	0.000	0.002	0.003	0.019	0.043
0.100	0.000	0.001	0.002	0.021	0.045
0.075	0.000	0.001	0.002	0.023	0.047
0.050	0.000	0.001	0.001	0.028	0.048
0.025	0.000	0.002	0.001	0.035	0.050
0.000	0.000	0.002	0.001	0.050	0.051
					0.052
					0.008
					0.011
					0.015
					0.017
					0.020
					0.023
					0.026
					0.030
					0.032
					0.034
					0.036
					0.038
					0.041
					0.043
					0.045
					0.047
					0.048
					0.050
					0.051
					0.044
					0.046

(d) k/u_0^2

TABLE VI

$$(a) \quad \mu_{RX}/(\rho \, u_0 \, D) \times 100$$

TABLE VI (Continued)

R/D	X/D				
	0.0	0.5	1.0	1.5	2.0
0.425	0.000	0.066	0.158	0.734	0.707
0.400	0.493	0.087	0.159	1.006	0.815
0.375	1.233	0.213	0.170	0.875	1.287
0.350	0.641	0.034	0.176	0.510	0.581
0.325	0.374	0.077	0.163	0.599	1.299
0.300	0.124	0.134	0.187	1.193	0.996
0.275	0.127	0.060	0.272	0.761	10.492
0.250	0.012	0.138	0.220	0.566	0.994
0.225	0.016	0.283	0.196	0.808	2.050
0.200	0.104	0.291	0.785	0.694	2.081
0.175	0.059	0.391	0.408	0.853	1.333
0.150	0.044	0.838	0.377	0.028	0.244
0.125	0.039	2.262	0.439	0.348	0.144
0.100	0.028	1.360	0.675	0.014	0.071
0.075	0.035	1.917	0.992	0.271	0.070
0.050	0.100	1.762	1.713	0.311	0.144
0.025	0.440	9.835	0.041	0.573	0.213
0.000	0.528	0.863	0.032	0.858	0.392

(b) α/D

TABLE VI (Continued)

R/D	x/D				
	0.0	0.5	1.0	1.5	2.0
0.425	0.000	0.036	0.028	0.121	0.093
0.400	0.076	0.044	0.029	0.121	0.108
0.375	0.122	0.035	0.030	0.110	0.160
0.350	0.092	0.007	0.032	0.076	0.084
0.325	0.057	0.016	0.031	0.090	0.139
0.300	0.024	0.029	0.034	0.181	0.152
0.275	0.019	0.013	0.050	0.104	0.632
0.250	0.002	0.028	0.040	0.088	0.190
0.225	0.003	0.055	0.047	0.122	0.349
0.200	0.015	0.057	0.087	0.106	0.242
0.175	0.009	0.072	0.087	0.110	0.142
0.150	0.007	0.117	0.071	0.004	0.037
0.125	0.008	0.186	0.079	0.050	0.020
0.100	0.007	0.144	0.081	0.003	0.011
0.075	0.008	0.117	0.077	0.038	0.013
0.050	0.021	0.099	0.107	0.042	0.024
0.025	0.067	0.333	0.019	0.062	0.041
0.000	0.069	0.142	0.018	0.084	0.107

(c) λ_m/D

TABLE VI (Continued)

R/D	X/D					
	0.0	0.5	1.0	1.5	2.0	2.5
0.425	0.013	0.079	0.030	0.014	0.006	0.007
0.400	0.012	0.085	0.028	0.014	0.006	0.005
0.375	0.011	0.092	0.026	0.013	0.005	0.004
0.350	0.010	0.089	0.024	0.013	0.006	0.004
0.325	0.010	0.064	0.022	0.012	0.006	0.005
0.300	0.011	0.050	0.020	0.012	0.007	0.005
0.275	0.012	0.041	0.019	0.013	0.007	0.005
0.250	0.014	0.031	0.018	0.013	0.008	0.005
0.225	0.017	0.025	0.017	0.014	0.009	0.006
0.200	0.024	0.022	0.017	0.014	0.011	0.007
0.175	0.040	0.018	0.016	0.013	0.010	0.006
0.150	0.044	0.017	0.016	0.013	0.009	0.006
0.125	0.040	0.016	0.016	0.014	0.008	0.007
0.100	0.032	0.017	0.015	0.014	0.009	0.008
0.075	0.022	0.017	0.015	0.014	0.011	0.011
0.050	0.013	0.017	0.016	0.013	0.012	0.012
0.025	0.009	0.018	0.017	0.013	0.013	0.015
0.000	0.008	0.018	0.017	0.012	0.016	0.019

(d) k/u_0^2

TABLE VI (Continued)

R/D	x/D					(e) $\sigma_{r\theta}$
	0.0	0.5	1.0	1.5	2.0	2.5
0.425	0.000	0.030	0.136	0.324	0.890	2.200
0.400	2.995	0.060	0.313	4.385	2.153	6.375
0.375	7.548	0.320	0.565	4.123	3.410	28.751
0.350	3.297	0.118	0.518	2.223	2.663	28.107
0.325	2.197	0.257	0.402	1.849	7.101	9.485
0.300	0.586	0.008	0.688	4.849	5.338	4.929
0.275	1.035	0.242	1.256	4.839	52.241	3.823
0.250	0.198	0.958	0.186	3.217	4.876	2.813
0.225	0.222	1.816	0.816	4.747	8.848	2.149
0.200	0.470	1.801	7.912	3.663	8.525	1.796
0.175	0.318	1.668	2.470	3.860	4.476	1.830
0.150	0.646	2.504	1.739	0.108	0.992	1.555
0.125	0.682	5.430	2.207	1.348	0.831	1.258
0.100	0.230	4.371	2.994	0.057	0.499	1.060
0.075	0.011	1.286	2.199	0.888	0.526	0.797
0.050	0.301	2.734	7.039	1.808	1.476	0.974
0.025	5.716	8.989	0.367	7.376	6.400	3.018
0.000	0.000	0.000	0.000	0.000	0.000	0.000

TABLE VII
TURBULENCE PARAMETERS FOR SWIRL VANE ANGLE $\phi = 70$ DEGREES

R/D	x/D					
	0.0	0.5	1.0	1.5	2.0	2.5
0.425	1.563	0.625	2.500	3.773	5.250	0.919
0.400	1.154	0.693	3.041	1.092	6.667	0.829
0.375	0.762	0.860	2.391	0.455	0.425	0.625
0.350	0.602	0.400	2.951	0.208	0.248	0.374
0.325	0.795	0.338	2.161	0.063	0.334	0.312
0.300	5.000	0.355	1.589	0.069	0.571	0.822
0.275	0.088	0.735	1.071	0.159	0.607	1.406
0.250	0.115	1.250	0.463	0.267	0.675	0.188
0.225	4.568	2.981	0.346	0.279	0.456	0.256
0.200	0.062	1.765	0.260	0.298	0.271	0.337
0.175	0.055	1.417	0.261	0.210	0.283	0.286
0.150	0.094	9.125	0.356	0.139	0.426	0.421
0.125	0.336	0.795	0.609	0.127	0.633	0.494
0.100	0.583	0.404	1.243	0.417	0.677	0.461
0.075	0.234	0.446	43.751	16.950	1.067	0.859
0.050	0.187	0.694	1.875	3.214	12.500	1.550
0.025	0.148	1.667	1.058	1.765	1.953	1.089
0.000	0.100	4.812	0.966	0.852	0.962	0.833

(a) $\mu_{rx}/(\rho u_0 D) \times 100$

TABLE VII (Continued)

R/D	X/D				
	0.0	0.5	1.0	1.5	2.0
0.425	0.579	0.202	1.242	3.827	5.325
0.400	0.440	0.229	1.542	1.108	7.063
0.375	0.303	0.304	1.253	0.482	0.414
0.350	0.248	0.162	1.610	0.211	0.202
0.325	0.334	0.146	1.193	0.063	0.269
0.300	2.130	0.157	0.864	0.064	0.460
0.275	0.035	0.365	0.561	0.135	0.503
0.250	0.024	0.624	0.240	0.224	0.575
0.225	0.936	1.528	0.182	0.249	0.400
0.200	0.012	0.824	0.140	0.282	0.242
0.175	0.013	0.746	0.145	0.198	0.257
0.150	0.038	4.834	0.206	0.120	0.363
0.125	0.147	0.426	0.362	0.100	0.340
0.100	0.299	0.218	0.744	0.302	0.464
0.075	0.130	0.245	25.984	0.434	0.278
0.050	0.111	0.391	1.083	11.357	0.616
0.025	0.090	0.976	0.599	1.966	6.547
0.000	0.054	2.966	0.537	0.980	0.980
				0.413	0.440

(b) λ/D

TABLE VII (Continued)

R/D	x/D				
	0.0	0.5	1.0	1.5	2.0
0.425	0.085	0.025	0.141	0.208	0.236
0.400	0.056	0.029	0.148	0.081	0.204
0.375	0.040	0.037	0.115	0.052	0.050
0.350	0.038	0.028	0.115	0.036	0.031
0.325	0.044	0.026	0.109	0.018	0.035
0.300	0.112	0.029	0.099	0.017	0.051
0.275	0.005	0.053	0.073	0.027	0.050
0.250	0.005	0.083	0.043	0.033	0.055
0.225	0.137	0.161	0.036	0.032	0.044
0.200	0.004	0.210	0.028	0.037	0.028
0.175	0.004	0.100	0.025	0.025	0.027
0.150	0.007	0.183	0.028	0.019	0.032
0.125	0.022	0.043	0.037	0.016	0.036
0.100	0.033	0.027	0.051	0.028	0.035
0.075	0.026	0.026	0.247	0.179	0.041
0.050	0.025	0.031	0.052	0.072	0.130
0.025	0.021	0.051	0.047	0.052	0.058
0.000	0.018	0.090	0.045	0.039	0.050

(c) ϵ_m/D

TABLE VII (Continued)

R/D	x/D					
	0.0	0.5	1.0	1.5	2.0	2.5
0.425	0.090	0.118	0.050	0.012	0.012	0.029
0.400	0.085	0.113	0.048	0.012	0.011	0.025
0.375	0.078	0.099	0.045	0.011	0.013	0.025
0.350	0.073	0.075	0.041	0.012	0.019	0.028
0.325	0.070	0.066	0.041	0.012	0.019	0.032
0.300	0.068	0.063	0.042	0.014	0.019	0.032
0.275	0.077	0.050	0.045	0.017	0.018	0.028
0.250	0.286	0.049	0.046	0.017	0.017	0.023
0.225	0.294	0.047	0.045	0.016	0.016	0.017
0.200	0.335	0.045	0.043	0.014	0.016	0.016
0.175	0.218	0.045	0.040	0.014	0.015	0.016
0.150	0.075	0.044	0.037	0.016	0.017	0.020
0.125	0.064	0.043	0.035	0.020	0.023	0.026
0.100	0.047	0.043	0.034	0.023	0.030	0.034
0.075	0.040	0.041	0.035	0.027	0.037	0.045
0.050	0.035	0.039	0.037	0.033	0.045	0.055
0.025	0.033	0.036	0.038	0.040	0.049	0.066
0.000	0.042	0.032	0.040	0.052	0.059	0.075

(d) k/u_0^2

TABLE VII (Continued)

R/D	X/D					
	0.0	0.5	1.0	1.5	2.0	2.5
0.425	0.396	0.590	2.040	5.704	11.168	0.527
0.400	4.287	0.577	8.425	4.562	40.801	3.895
0.375	3.760	1.028	8.114	1.813	2.258	1.857
0.350	3.032	0.774	13.381	0.813	1.266	0.893
0.325	3.897	0.799	9.910	0.282	1.827	0.900
0.300	20.393	1.009	6.958	0.370	2.929	3.032
0.275	0.227	2.671	4.684	1.011	3.331	5.702
0.250	0.154	4.875	1.558	1.915	4.499	0.947
0.225	3.141	12.169	1.096	2.518	3.917	1.356
0.200	0.036	7.168	0.858	2.446	2.547	1.782
0.175	0.180	4.877	0.791	1.196	2.118	1.594
0.150	0.226	26.829	0.831	0.638	2.332	1.772
0.125	0.324	1.806	1.652	0.428	1.791	1.402
0.100	0.682	0.779	4.333	1.135	1.614	0.550
0.075	0.756	0.946	95.480	62.387	1.714	0.830
0.050	1.660	2.045	5.751	15.665	13.690	1.599
0.025	1.342	17.261	10.372	16.961	9.376	2.635
0.000	0.000	0.000	0.000	0.000	0.000	0.000

(e) $\sigma_{r\theta}$

TABLE VIII
TURBULENCE PARAMETERS FOR SWIRL VANE ANGLE $\phi = 0$ DEGREES
WITH STRONG CONTRACTION NOZZLE AT $L/D = 2$

R/D	x/D					
	0.0	0.5	1.0	1.5	2.0	
0.400	9.999	0.120	0.069	0.106	0.080	
0.375	0.032	0.237	0.038	0.004	0.180	
0.350	3.056	3.081	0.033	0.111	0.412	
0.325	9.999	0.039	0.112	0.195	0.154	
0.300	0.041	0.019	0.159	0.234	0.204	
0.275	0.000	0.036	0.168	0.243	0.231	
0.250	0.001	0.065	0.202	0.172	0.253	
0.225	0.000	0.048	0.098	0.186	0.200	
0.200	0.015	0.035	0.105	0.154	0.336	
0.175	0.009	0.043	0.027	0.185	0.386	
0.150	0.028	0.032	0.062	0.142	0.264	
0.125	0.018	0.043	0.045	0.543	0.297	
0.100	0.010	12.483	0.110	0.123	0.275	
0.075	0.005	0.012	2.273	0.213	0.275	
0.050	0.004	0.080	8.330	0.214	0.586	
0.025	0.002	0.036	0.061	0.928	0.547	
0.000	0.002	0.005	0.025	0.521	0.335	

(a) $\mu_{rx}/(\rho u_0 D) \times 100$

TABLE VIII (Continued)

R/D	x/d				
	0.0	0.5	1.0	1.5	2.0
0.400	9.999	0.260	0.080	0.109	0.081
0.375	0.115	0.531	0.038	0.003	0.158
0.350	10.734	5.501	0.031	0.097	0.323
0.325	9.999	0.053	0.091	0.161	0.123
0.300	0.134	0.021	0.127	0.170	0.152
0.275	0.000	0.032	0.110	0.163	0.160
0.250	0.005	0.050	0.133	0.103	0.154
0.225	0.002	0.042	0.074	0.111	0.123
0.200	0.074	0.052	0.081	0.094	0.223
0.175	0.069	0.132	0.035	0.117	0.223
0.150	0.151	0.124	0.111	0.114	0.192
0.125	0.095	0.233	0.109	0.573	0.209
0.100	0.062	84.529	0.303	0.068	0.221
0.075	0.043	0.093	7.499	0.296	0.237
0.050	0.024	0.465	29.021	0.325	0.584
0.025	0.014	0.294	0.216	1.780	0.592
0.000	0.019	0.035	0.089	1.071	0.403

(b) x/d

TABLE VIII (Continued)

R/D	x/D —					(c) ϵ_m/D
	0.0	0.5	1.0	1.5	2.0	
0.400	9.999	0.045	0.020	0.023	0.024	0.024
0.375	0.038	0.070	0.009	0.005	0.034	0.034
0.350	0.315	0.191	0.008	0.020	0.040	0.040
0.325	9.999	0.008	0.019	0.030	0.023	0.023
0.300	0.048	0.005	0.021	0.027	0.029	0.029
0.275	0.000	0.007	0.021	0.026	0.030	0.030
0.250	0.001	0.008	0.021	0.020	0.027	0.027
0.225	0.000	0.008	0.014	0.019	0.023	0.023
0.200	0.014	0.009	0.016	0.018	0.034	0.034
0.175	0.008	0.014	0.009	0.022	0.031	0.031
0.150	0.014	0.012	0.013	0.021	0.026	0.026
0.125	0.011	0.014	0.013	0.044	0.030	0.030
0.100	0.007	0.199	0.020	0.021	0.027	0.027
0.075	0.005	0.005	0.080	0.024	0.026	0.026
0.050	0.004	0.013	0.125	0.021	0.029	0.029
0.025	0.002	0.005	0.008	0.027	0.020	0.020
0.000	0.003	0.006	0.022	0.062	0.052	0.052

TABLE VIII (Continued)

R/D	x/D				
	0.0	0.5	1.0	1.5	2.0
0.400	9.999	0.003	0.009	0.012	0.012
0.375	0.001	0.002	0.013	0.018	0.016
0.350	0.001	0.004	0.014	0.016	0.020
0.325	9.999	0.007	0.019	0.018	0.019
0.300	0.001	0.010	0.019	0.023	0.022
0.275	0.001	0.016	0.029	0.027	0.026
0.250	0.001	0.021	0.029	0.034	0.033
0.225	0.000	0.016	0.022	0.035	0.033
0.200	0.000	0.005	0.021	0.033	0.028
0.175	0.000	0.001	0.007	0.031	0.037
0.150	0.000	0.001	0.004	0.019	0.023
0.125	0.000	0.000	0.002	0.011	0.025
0.100	0.000	0.000	0.002	0.041	0.019
0.075	0.000	0.000	0.001	0.006	0.017
0.050	0.000	0.000	0.001	0.005	0.012
0.025	0.000	0.000	0.001	0.003	0.011
0.000	0.000	0.000	0.001	0.003	0.009

(d) k/u_0^2

TABLE VIII (Continued)

R/D	x/D				
	0.0	0.5	1.0	1.5	2.0
0.400	9.999	2.131	0.247	0.629	0.016
0.375	0.125	0.215	0.126	0.008	0.331
0.350	46.231	48.069	0.000	0.037	2.426
0.325	9.999	0.053	0.433	0.001	0.082
0.300	0.394	0.117	3.815	0.159	0.032
0.275	0.000	0.081	0.065	0.217	0.022
0.250	0.016	0.105	0.273	0.071	0.084
0.225	0.005	0.018	0.048	0.100	0.040
0.200	0.256	0.026	0.094	0.011	0.017
0.175	0.157	0.049	0.185	0.076	0.001
0.150	0.152	0.283	0.329	0.006	0.373
0.125	0.260	3.254	0.479	0.000	0.251
0.100	0.290	330.426	0.583	0.004	0.120
0.075	0.105	0.068	21.971	0.110	0.119
0.050	1.240	3.058	69.654	0.375	2.087
0.025	0.080	4.901	1.136	5.176	1.582
0.000	0.000	0.000	0.000	0.000	0.000

(e) $\sigma_{r\theta}$

TABLE VIII (Continued)

R/D	x/D					(f) σ_{rr}
	0.0	0.5	1.0	1.5	2.0	
0.400	9.999	0.543	0.512	0.300	0.141	0.141
0.375	0.255	1.283	0.206	0.005	0.141	0.141
0.350	46.462	16.068	0.016	0.098	1.022	1.022
0.325	9.999	0.818	0.108	0.127	0.527	0.527
0.300	0.062	0.343	0.264	0.523	0.282	0.282
0.275	0.000	0.191	0.198	0.144	0.101	0.101
0.250	0.273	0.233	0.303	0.069	0.006	0.006
0.225	0.080	0.012	0.157	0.292	0.165	0.165
0.200	0.107	0.052	0.156	0.041	0.344	0.344
0.175	12.424	0.940	0.057	0.362	0.918	0.918
0.150	1.624	12.445	1.131	0.100	0.332	0.332
0.125	1.069	3.695	2.483	0.329	0.635	0.635
0.100	1.438	1291.282	2.068	0.043	0.080	0.080
0.075	1.463	2.265	15.651	26.269	0.336	0.336
0.050	0.338	1.703	14.748	5.251	2.142	2.142
0.025	0.147	4.711	2.003	37.779	1.263	1.263
0.000	10.252	6.411	1.578	6.645	0.988	0.988

TABLE VIII (Continued)

R/D	X/D				
	0.0	0.5	1.0	1.5	2.0
0.400	9.999	0.975	0.576	3.249	0.224
0.375	0.213	2.839	0.111	0.023	0.631
0.350	21.580	41.433	0.108	0.640	0.805
0.325	9.999	1.945	0.217	3.039	5.688
0.300	0.142	0.260	0.551	0.925	1.759
0.275	0.000	0.289	0.555	0.978	1.788
0.250	0.009	0.432	0.899	0.475	2.002
0.225	0.026	0.435	0.839	0.482	0.606
0.200	0.593	0.936	0.446	0.753	1.095
0.175	1.902	5.073	23.214	0.623	1.229
0.150	1.365	3.269	4.808	1.142	2.510
0.125	1.265	11.678	2.929	6.612	1.487
0.100	1.647	10852.516	9.157	0.196	3.843
0.075	2.896	17.053	390.155	6.592	4.299
0.050	0.992	39.315	2208.476	9.236	221.103
0.025	1.004	155.020	33.729	226.107	249.102
0.000	0.000	0.000	0.000	0.000	0.000

(g) $\sigma_{\theta\theta}$

TABLE IX
TURBULENCE PARAMETERS FOR SWIRL VANE ANGLE $\phi = 45$ DEGREES
WITH STRONG CONTRACTION NOZZLE AT $L/D = 2$

R/D	x/D				
	0.0	0.5	1.0	1.5	2.0
0.425	9.999	0.297	9.999	9.999	9.999
0.400	0.229	0.421	0.814	0.224	0.272
0.375	0.375	0.330	0.605	0.282	0.112
0.350	0.410	0.208	0.434	0.555	0.065
0.325	0.000	0.096	0.689	0.340	0.046
0.300	0.156	0.352	1.043	0.316	0.091
0.275	0.016	0.493	1.064	0.287	0.048
0.250	0.069	0.605	1.709	0.431	0.077
0.225	0.146	4.568	7.686	0.304	0.096
0.200	0.190	0.730	1.539	0.616	0.103
0.175	0.058	1.287	0.792	0.338	0.125
0.150	0.052	0.319	0.527	0.344	0.094
0.125	0.000	0.541	0.347	0.188	0.137
0.100	0.561	0.060	0.244	0.167	0.083
0.075	9.999	0.132	0.270	0.206	0.121
0.050	1.063	0.191	0.386	0.364	0.218
0.025	2.064	0.530	0.305	2.822	2.267
0.000	1.208	0.629	2.654	1.298	1.190

(a) $\mu_{rx}/(\rho u_0 D) \times 100$

TABLE IX (Continued)

R/D	x/D				
	0.0	0.5	1.0	1.5	2.0
0.425		0.111	0.499	0.245	0.406
0.400	0.147	0.158	0.372	0.307	0.169
0.375	0.240	0.128	0.276	0.595	0.096
0.350	0.273	0.083	0.453	0.343	0.066
0.325	0.000	0.046	0.684	0.300	0.122
0.300	0.103	0.187	0.701	0.293	0.059
0.275	0.010	0.275	1.138	0.420	0.097
0.250	0.023	0.354	5.024	0.280	0.113
0.225	0.081	2.751	0.934	0.529	0.128
0.200	0.125	0.427	0.452	0.290	0.131
0.175	0.021	0.720	0.279	0.238	0.092
0.150	0.028	0.167	0.177	0.126	0.118
0.125	0.000	0.271	0.106	0.099	0.069
0.100	0.368	0.028	0.105	0.114	0.079
0.075		0.058	0.136	0.156	0.104
0.050	0.553	0.084	0.101	1.099	0.768
0.025	0.998	0.230	0.900	0.522	0.400
0.000	0.573	0.252			

(b) α/D

TABLE IX (Continued)

R/D	x/D				
	0.0	0.5	1.0	1.5	2.0
0.425		0.021		0.046	0.040
0.400		0.028	0.055	0.048	0.023
0.375	0.026	0.023	0.052	0.043	0.016
0.350	0.037	0.016	0.043	0.023	0.013
0.325	0.041	0.012	0.059	0.018	0.009
0.300	0.000	0.014	0.069	0.035	0.006
0.275	0.010	0.018	0.074	0.032	0.016
0.250	0.002	0.047	0.085	0.040	0.016
0.225	0.005	0.047	0.154	0.032	0.016
0.200	0.012	0.135	0.070	0.041	0.016
0.175	0.015	0.043	0.042	0.028	0.013
0.150	0.004	0.057	0.028	0.026	0.013
0.125	0.000	0.028	0.021	0.016	0.010
0.100	0.039	0.031	0.015	0.014	0.011
0.075		0.008	0.013	0.012	0.011
0.050	0.038	0.011	0.013	0.013	0.028
0.025	0.042	0.015	0.009	0.029	0.022
0.000	0.070	0.030	0.097	0.038	

(c) λ_m/D

TABLE IX (Continued)

R/D	x/D				
	0.0	0.5	1.0	1.5	2.0
0.425		0.088			0.006
0.400		0.087	0.033	0.010	0.005
0.375	0.030	0.082	0.033	0.010	0.006
0.350	0.030	0.077	0.030	0.011	0.006
0.325	0.028	0.053	0.029	0.012	0.007
0.300	0.028	0.044	0.029	0.014	0.008
0.275	0.032	0.040	0.028	0.012	0.008
0.250	0.105	0.036	0.028	0.013	0.009
0.225	0.040	0.034	0.029	0.015	0.008
0.200	0.028	0.036	0.033	0.017	0.011
0.175	0.097	0.039	0.038	0.017	0.013
0.150	0.044	0.045	0.044	0.026	0.017
0.125	0.025	0.049	0.047	0.028	0.018
0.100	0.029	0.057	0.065	0.035	0.030
0.075		0.064	0.082	0.040	0.054
0.050	0.046	0.064	0.100	0.067	0.108
0.025	0.053	0.066	0.113	0.081	0.108
0.000	0.055	0.077	0.107	0.076	0.109

(d) k/u_0^2

TABLE IX (Continued)

R/D	x/D					(e) $\sigma_{r\theta}$
	0.0	0.5	1.0	1.5	2.0	
0.425		0.613			1.419	
0.400	0.397	0.249	0.052	0.961	2.145	
0.375	1.322	0.066	2.017	1.536	1.199	
0.350	1.638	0.525	1.184	5.052	1.376	
0.325	0.000	0.400	1.937	3.695	2.546	
0.300	0.412	0.929	5.672	3.866	1.177	
0.275	0.165	1.112	5.840	3.735	2.268	
0.250	0.612	1.796	8.877	6.015	3.612	
0.225	2.227	14.873	50.120	5.041	3.702	
0.200	0.768	3.287	10.551	8.585	4.206	
0.175	0.570	7.811	5.295	6.749	2.533	
0.150	0.611	2.050	3.645	13.067	4.141	
0.125	0.000	2.708	2.296	2.909	1.462	
0.100	1.444	0.195	1.755	1.842	2.196	
0.075		0.296	0.735	0.838	2.071	
0.050	4.498	0.407	0.106	0.386	4.600	
0.025	22.104	0.465	0.151	1.478	0.000	
0.000	0.000	0.000	0.000	0.000	0.000	

TABLE IX (Continued)

R/D	x/D				
	0.0	0.5	1.0	1.5	2.0
0.425		0.290			2.198
0.400	0.442	0.003	7.433	0.203	0.807
0.375	2.385	0.030	1.810	0.639	0.396
0.350	10.666	0.002	4.992	65.494	0.234
0.325	0.000	0.269	0.238	21.297	
0.300	8.384	6.732	1.483	1.896	3.701
0.275	0.409	10.650	21.094	8.758	1.705
0.250	0.000	0.694	13.052	4.078	0.286
0.225	2.495	13.620	16.730	3.365	0.510
0.200	1.370	5.823	2.970	10.108	2.276
0.175	0.121	0.990	7.713	4.520	0.550
0.150	0.377	0.445	5.200	2.711	1.000
0.125	0.000	3.255	4.778	2.321	6.085
0.100	0.425	0.847	1.387	1.398	2.805
0.075		0.739	1.011	1.657	0.157
0.050	0.288	0.184	1.257	0.267	0.227
0.025	0.425	0.111	0.007	1.451	6.592
0.000	1.385	1.315	3.397	3.976	8.215

(f) σ_{rr}

TABLE IX (Continued)

R/D	x/D					2.0
	0.0	0.5	1.0	1.5		
0.425		1.056		3.878	2.075	
0.400	0.970	0.625	4.142	7.901	1.278	
0.375	1.791	0.533	2.832		0.603	
0.350	1.566	0.282	2.311	13.709	0.530	
0.325	0.000	0.172	4.848	74.522	0.835	
0.300	0.284	0.578	9.715	6.648	0.334	
0.275	0.016	0.859	4.935	5.205	0.334	
0.250	0.332	1.464	6.270	4.447	1.260	
0.225	3.400	15.801	24.725	3.786	1.618	
0.200	2.162	3.147	4.314	9.056	2.980	
0.175	0.686	4.692	2.746	4.605	7.144	
0.150	1.176	1.166	1.884	3.293	10.575	
0.125	0.000	2.897	2.180	128.524	7.718	
0.100	3.321	0.576	10.285	6.433	4.422	
0.075		2.186	4.726	14.118	2.865	
0.050	7.802	6.509	10.535	6.212	23.943	
0.025	13.732	170.080	26.051	925.650	1034.512	
0.000	0.000	0.000	0.000	0.000	0.000	
				(g) $\sigma_{\theta\theta}$		

TABLE X
TURBULENCE PARAMETERS FOR SWIRL VANE ANGLE $\phi = 70$ DEGREES
WITH STRONG CONTRACTION NOZZLE AT $L/D = 2$

R/D	x/D				
	0.0	0.5	1.0	1.5	2.0
0.425	0.560	0.492			2.027
0.400	5.533	0.183	0.128	0.053	1.417
0.375		0.380	0.444	0.147	0.768
0.350		0.199	15.901	0.188	0.130
0.325	1.878	0.947	0.995	0.134	0.914
0.300	0.150	0.163	0.426	0.632	0.177
0.275	0.030	2.039		0.130	0.333
0.250	0.160	0.080	10.206	0.609	0.174
0.225	1.516	0.157	29.387	0.219	0.626
0.200	0.153	1.557	0.046	0.130	6.971
0.175	0.179	0.414	0.120	0.243	3.196
0.150	0.022	0.265	0.102	0.524	3.727
0.125	0.265	0.034	0.173	0.727	20.399
0.100	0.636	0.089	0.683	6.190	17.081
0.075	0.473	0.509	11.625	1.600	0.666
0.050	0.321	3.683	8.936	1.779	1.239
0.025	0.389	5.461	6.023	0.930	
0.000	0.306	1.124	0.656	0.204	8.834

(a) $\mu_{rx}/(\rho u_0 D) \times 100$

TABLE X (Continued)

R/D	x/D				
	0.0	0.5	1.0	1.5	2.0
0.425	0.320	0.191			2.295
0.400	3.191	0.076	0.084	0.062	1.520
0.375		0.179	0.290	0.158	0.940
0.350		0.092	10.681	0.225	0.163
0.325	1.042	0.499	0.694	0.179	0.864
0.300	0.076	0.199	0.320	0.762	0.174
0.275	0.016	1.184		0.176	0.260
0.250	0.033	0.105	7.698	0.575	0.148
0.225	0.387	0.186	23.045	0.244	0.394
0.200	0.041	0.811	0.036	0.128	3.734
0.175	0.042	0.223	0.101	0.209	1.332
0.150	0.006	0.139	0.083	0.370	1.560
0.125	0.087	0.016	0.132	0.440	7.082
0.100	0.223	0.040	0.397	2.835	4.752
0.075	0.164	0.193	5.138	0.707	0.173
0.050	0.108	1.263	3.758	0.704	0.313
0.025	0.110	2.032	2.438	0.305	
0.000	0.071	0.426	0.264	0.057	1.684

(b) λ/D

TABLE X (Continued)

R/D	x/D					(c) λ_m/D
	0.0	0.5	1.0	1.5	2.0	
0.425	0.038	0.029			0.076	
0.400	0.117	0.019	0.024	0.004	0.027	
0.375		0.030	0.043	0.009	0.019	
0.350		0.022	0.257	0.021	0.016	
0.325	0.064	0.028	0.055	0.018	0.039	
0.300	0.007	0.008	0.032	0.035	0.018	
0.275	0.003	0.045		0.015	0.021	
0.250	0.006	0.008	0.137	0.030	0.017	
0.225	0.051	0.009	0.195	0.022	0.038	
0.200	0.007	0.026	0.010	0.016	0.125	
0.175	0.007	0.022	0.016	0.018	0.076	
0.150	0.003	0.019	0.012	0.030	0.072	
0.125	0.018	0.007	0.017	0.031	0.148	
0.100	0.028	0.010	0.024	0.065	0.099	
0.075	0.019	0.018	0.082	0.029	0.017	
0.050	0.012	0.042	0.065	0.029	0.024	
0.025	0.010	0.041	0.049	0.016		
0.000	0.012	0.025	0.019	0.012	0.105	

TABLE X (Continued)

R/D	x/D				
	0.0	0.5	1.0	1.5	2.0
0.425	0.038	0.082	0.029	0.009	0.010
0.400	0.037	0.071	0.029	0.011	0.011
0.375		0.055	0.027	0.009	0.008
0.350		0.057	0.027	0.007	0.014
0.325	0.040	0.044	0.025	0.008	0.013
0.300	0.047	0.008	0.022	0.007	0.020
0.275	0.044	0.037		0.007	0.017
0.250	0.297	0.007	0.022	0.014	0.031
0.225	0.190	0.009	0.020	0.010	0.043
0.200	0.176	0.046	0.020	0.013	0.071
0.175	0.221	0.043	0.017	0.017	0.071
0.150	0.187	0.045	0.019	0.025	0.102
0.125	0.114	0.054	0.021	0.034	0.160
0.100	0.101	0.060	0.037	0.059	0.184
0.075	0.103	0.086	0.063	0.063	0.193
0.050	0.108	0.105	0.070	0.079	
0.025	0.153	0.089	0.075	0.114	
0.000	0.230	0.086	0.076	0.157	0.340

(d) k/u_0^2

TABLE X (Continued)

R/D	x/D					
	0.0	0.5	1.0	1.5	2.0	
0.425	0.136	0.640			5.416	
0.400	36.696	0.578	0.173	0.032	35.588	
0.375		0.899	2.221	3.843	23.618	
0.350		0.600	89.058	1.782	5.635	
0.325	14.824	6.956	7.446	5.300	22.153	
0.300	1.159	3.203	5.184	13.683	5.863	
0.275	0.198	13.998		6.725	6.568	
0.250	0.629	3.869	245.115	23.098	3.924	
0.225	2.683	19.628	951.871	7.210	6.639	
0.200	0.228	49.839	0.968	3.192	57.832	
0.175	0.070	8.606	2.837	8.631	21.741	
0.150	0.033	4.295	4.013	9.512	20.289	
0.125	1.008	2.725	4.183	8.784	71.770	
0.100	3.907	0.798	6.883	16.116	5.235	
0.075	2.765	2.194	28.953	2.076	0.586	
0.050	2.481	10.205	17.453	5.924	2.039	
0.025	2.820	8.428	27.849	5.731		
0.000	0.000	0.000	0.000	0.000	0.000	

(e) $\sigma_{r\theta}$

TABLE X (Continued)

R/D	x/D				
	0.0	0.5	1.0	1.5	2.0
0.425	42.416	0.694			6.696
0.400	91.941	1.196	0.220	15.423	75.774
0.375		0.625	0.997	7.014	63.812
0.350		4.807	8.274	5.004	0.382
0.325	5.731	6.051	3.599	1.188	3.224
0.300	11.656	79.079	3.874	195.674	0.693
0.275	1.136	84.563		0.776	1.540
0.250	0.269	6.322	84.366	7.242	0.142
0.225	6.951	9.838	432.724	3.598	0.117
0.200	0.298	28.636	0.409	3.662	12.604
0.175	0.205	15.538	11.176	1.655	7.030
0.150	0.049	1.211	2.167	0.103	70.592
0.125	0.277	0.151	0.453	0.907	8.095
0.100	0.901	0.402	14.382	19.289	89.048
0.075	1.769	7.306	50.703	1.091	0.501
0.050	18.649	6.986	0.510	45.417	0.796
0.025	0.923	6.118	1.193	2.087	
0.000	0.423	3.038	0.881	0.122	4.590

(f) σ_{rr}

TABLE X (Continued)

R/D	x/D				
	0.0	0.5	1.0	1.5	2.0
0.425	0.819	1.919	15.466	2.047	92.350
0.400	10.394	0.351	8.069	1.273	10.536
0.375		0.466		41.959	14.077
0.350		0.367	859.259		0.000
0.325	6.700	1.660	10.551	1.202	7.380
0.300	0.425	1.001	1.781	9.983	1.760
0.275	0.054	6.330		0.665	2.157
0.250	0.258	0.541	115.123	29.299	2.819
0.225	3.645	2.691	185.508	2.848	4.070
0.200	0.298	10.604	0.528	5.951	274.483
0.175	0.277	2.774	1.380	32.209	1358.189
0.150	0.032	0.904	0.993	15.943	45.693
0.125	0.731	1.158	7.557	56.893	341.527
0.100	2.280	0.463	5.343	34.743	58.459
0.075	4.478	2.389	38.858	13.416	1.956
0.050	4.739	15.336	62.748	42.136	8.220
0.025	3.801	108.669	95.133	27.708	
0.000	0.000	0.000	0.000	0.000	0.000

(g) $\sigma_{\theta\theta}$

TABLE XI

DISTRIBUTION OF C_2 VALUES OVER THE FLOWFIELD OF $\phi = 45$ DEGREES
USING EQS. (5.4) AND (7.1)

$r/D \backslash x/D$	0.03	0.33	0.53	1.08	1.93	2.50
0.495	1.60	1.91	1.91	1.91	1.91	1.90
0.448	1.92	1.82	1.71	1.78	1.89	1.63
0.406	1.92	1.56	1.56	1.92	1.85	1.38
0.365	1.96	1.56	1.81	1.88	1.72	1.34
0.328	1.99	1.84	1.95	1.78	1.56	1.10
0.275	1.87	1.91	1.83	1.59	1.54	1.51
0.243	1.80	1.68	1.39	1.07	0.98	0.86
0.175	1.81	0.10	0.51	1.16	1.19	1.25
0.085	1.62	1.07	1.11	1.24	1.28	1.35
0.013	1.69	1.86	1.86	1.86	1.86	1.87

TABLE XII

DISTRIBUTION OF C_2 VALUES OVER THE FLOWFIELD OF $\phi = 70$ DEGREES
USING EQS. (5.4) AND (7.1)

$\begin{matrix} x/D \\ r/D \end{matrix}$	0.03	0.33	0.53	1.08	1.93	2.50
0.495	1.84	1.91	1.91	1.91	1.90	1.90
0.448	1.90	1.88	1.88	1.86	1.74	1.44
0.406	1.91	1.90	1.89	1.78	1.58	1.08
0.365	1.90	1.88	1.86	1.68	1.48	1.19
0.328	1.94	1.57	1.59	1.31	1.01	0.74
0.275	1.89	1.33	1.44	1.46	1.45	1.54
0.243	1.49	0.34	0.30	0.57	0.72	0.94
0.175	1.81	0.83	0.88	1.16	1.26	1.29
0.085	--	--	--	0.29	0.15	--
0.013	1.87	1.88	1.87	1.87	1.87	1.88

TABLE XIII

THE k - ϵ OPTIMUM CONSTANTS FOR SWIRLING FLOWS

C_μ	C_1	C_2	σ_k	σ_ϵ
0.125	1.44	1.5942	1.0	1.1949

TABLE XIV

PREDICTED NORMALIZED k and C_μ VALUES USING EQ. (7.2)

R/D	x/D					
	0.0	0.5	1.0	1.5	2.0	2.5
0.495	0.000	0.001	0.001	0.001	0.001	0.001
0.447	0.000	0.010	0.006	0.009	0.013	0.014
0.406	0.000	0.010	0.010	0.016	0.021	0.020
0.365	0.000	0.012	0.020	0.026	0.028	0.025
0.327	0.000	0.022	0.031	0.035	0.034	0.029
0.275	0.000	0.035	0.042	0.043	0.040	0.032
0.243	0.246	0.034	0.045	0.045	0.041	0.033
0.175	0.061	0.031	0.044	0.044	0.040	0.032
0.085	0.003	0.029	0.038	0.038	0.035	0.029
0.012	0.000	0.029	0.035	0.036	0.033	0.027
			k/u ₀ ²			

R/D	x/D					
	0.0	0.5	1.0	1.5	2.0	2.5
0.495	0.000	0.230	0.284	0.278	0.239	0.223
0.447	0.000	0.084	0.112	0.090	0.072	0.070
0.406	0.000	0.083	0.083	0.066	0.058	0.059
0.365	0.000	0.077	0.059	0.052	0.050	0.053
0.327	0.000	0.057	0.047	0.045	0.045	0.049
0.275	0.000	0.044	0.041	0.040	0.042	0.046
0.243	0.017	0.045	0.039	0.039	0.041	0.046
0.175	0.034	0.047	0.040	0.040	0.042	0.046
0.085	0.155	0.049	0.043	0.043	0.044	0.049
0.012	0.389	0.049	0.044	0.044	0.046	0.050
			C _μ			

(a) $\phi = 45$ deg.

R/D	x/D						k/u ₀ ²
	0.0	0.5	1.0	1.5	2.0	2.5	
0.495	0.000	0.004	0.003	0.004	0.004	0.005	0.005
0.447	0.000	0.026	0.024	0.034	0.039	0.035	0.035
0.406	0.000	0.031	0.045	0.054	0.055	0.046	0.046
0.365	0.000	0.047	0.068	0.072	0.069	0.056	0.056
0.327	0.000	0.068	0.083	0.085	0.078	0.062	0.062
0.275	0.000	0.081	0.095	0.094	0.085	0.068	0.068
0.243	0.632	0.081	0.096	0.096	0.086	0.069	0.069
0.175	0.031	0.078	0.091	0.091	0.082	0.066	0.066
0.085	0.012	0.071	0.079	0.078	0.071	0.058	0.058
0.012	0.002	0.069	0.075	0.073	0.066	0.055	0.055

R/D	X/D						C _μ
	0.0	0.5	1.0	1.5	2.0	2.5	
0.495	0.000	0.125	0.148	0.139	0.126	0.124	0.124
0.447	0.000	0.052	0.054	0.045	0.042	0.045	0.045
0.406	0.000	0.048	0.039	0.036	0.036	0.039	0.039
0.365	0.000	0.038	0.032	0.031	0.032	0.035	0.035
0.327	0.000	0.032	0.029	0.029	0.030	0.033	0.033
0.275	0.000	0.029	0.027	0.027	0.029	0.032	0.032
0.243	0.010	0.029	0.027	0.027	0.028	0.032	0.032
0.175	0.047	0.030	0.028	0.028	0.029	0.032	0.032
0.085	0.076	0.031	0.030	0.030	0.031	0.035	0.035
0.012	0.183	0.032	0.030	0.031	0.032	0.035	0.035

(b) $\phi = 70^\circ$.

TABLE XV
PREDICTED AXIAL AND SWIRL VELOCITIES FOR SWIRL VANE ANGLE
 $\phi = 45$ DEGREES

R/D	x/D						u/u ₀
	0.0	0.5	1.0	1.5	2.0	2.5	
0.495	0.000	0.598	0.448	0.383	0.351	0.327	
0.447	0.000	0.618	0.486	0.412	0.371	0.341	
0.406	0.000	0.560	0.449	0.388	0.355	0.326	
0.365	0.000	0.416	0.363	0.339	0.319	0.298	
0.327	0.000	0.199	0.263	0.276	0.271	0.261	
0.275	0.000	-0.067	0.117	0.167	0.186	0.196	
0.243	1.881	-0.168	0.025	0.094	0.128	0.152	
0.175	0.924	-0.276	-0.150	-0.055	0.008	0.062	
0.085	0.135	-0.335	-0.303	-0.198	-0.111	-0.028	
0.012	0.069	-0.347	-0.346	-0.242	-0.148	-0.057	

u/u_0

R/D	X/D					
	0.0	0.5	1.0	1.5	2.0	2.5
0.495	0.000	0.519	0.513	0.528	0.584	0.649
0.447	0.000	0.543	0.565	0.594	0.638	0.682
0.406	0.000	0.553	0.594	0.628	0.655	0.675
0.365	0.000	0.578	0.647	0.668	0.670	0.661
0.327	0.000	0.645	0.704	0.699	0.674	0.641
0.275	0.000	0.763	0.749	0.706	0.653	0.593
0.243	1.866	0.778	0.738	0.682	0.619	0.551
0.175	0.811	0.635	0.615	0.564	0.501	0.433
0.085	0.191	0.316	0.326	0.301	0.266	0.226
0.012	0.073	0.047	0.049	0.045	0.040	0.034

w/u_0

(a) Using Eq. (7.2)

TABLE VX (Continued)

R/D	x/D						u/u ₀
	0.0	0.5	1.0	1.5	2.0	2.5	
0.495	0.000	0.609	0.444	0.366	0.363	0.344	
0.447	0.000	0.634	0.522	0.451	0.396	0.360	
0.406	0.000	0.569	0.479	0.410	0.371	0.341	
0.365	0.000	0.421	0.366	0.343	0.324	0.305	
0.327	0.000	0.169	0.244	0.270	0.268	0.263	
0.275	0.000	-0.082	0.096	0.153	0.175	0.190	
0.243	1.881	-0.172	0.004	0.077	0.113	0.140	
0.175	0.924	-0.281	-0.178	-0.083	-0.018	0.035	
0.085	0.135	-0.347	-0.344	-0.249	-0.160	-0.081	
0.012	0.069	-0.361	-0.395	-0.306	-0.210	-0.122	

 u/u_0

R/D	X/D						w/u ₀
	0.0	0.5	1.0	1.5	2.0	2.5	
0.495	0.000	0.511	0.472	0.453	0.524	0.613	
0.447	0.000	0.544	0.554	0.576	0.624	0.667	
0.406	0.000	0.553	0.582	0.638	0.664	0.673	
0.365	0.000	0.572	0.657	0.694	0.687	0.667	
0.327	0.000	0.653	0.731	0.726	0.691	0.649	
0.275	0.000	0.771	0.776	0.725	0.664	0.602	
0.243	1.866	0.785	0.757	0.695	0.627	0.559	
0.175	0.811	0.631	0.620	0.569	0.506	0.439	
0.085	0.191	0.305	0.325	0.305	0.270	0.230	
0.012	0.073	0.045	0.049	0.046	0.041	0.035	

 w/u_0

(b) Using Table XIII

TABLE XVI
PREDICTED AXIAL AND SWIRL VELOCITIES FOR SWIRL VANE ANGLE
 $\phi = 70$ DEGREES

R/D	x/D				
	0.0	0.5	1.0	1.5	2.0
0.495	0.000	0.833	0.605	0.463	0.398
0.447	0.000	0.741	0.581	0.468	0.413
0.406	0.000	0.549	0.465	0.413	0.378
0.365	0.000	0.297	0.323	0.330	0.316
0.327	0.000	0.076	0.190	0.236	0.242
0.275	0.000	-0.149	0.004	0.084	0.117
0.243	2.963	-0.261	-0.108	-0.015	0.034
0.175	0.403	-0.432	-0.315	-0.206	-0.133
0.085	0.375	-0.555	-0.495	-0.385	-0.293
0.012	-0.074	-0.585	-0.548	-0.439	-0.342
			u/u_0		
					0.370
					0.379
					0.346
					0.293
					0.231
					0.129
					0.062
					-0.072
					-0.200
					-0.240

R/D	x/D				
	0.0	0.5	1.0	1.5	2.0
0.495	0.000	0.791	0.780	0.826	0.916
0.447	0.000	0.854	0.907	0.960	1.021
0.406	0.000	0.889	0.979	1.017	1.042
0.365	0.000	0.987	1.058	1.061	1.045
0.327	0.000	1.104	1.105	1.075	1.026
0.275	0.000	1.150	1.092	1.033	0.957
0.243	3.011	1.099	1.035	0.971	0.890
0.175	0.850	0.860	0.820	0.766	0.694
0.085	0.408	0.431	0.422	0.396	0.357
0.012	0.186	0.064	0.063	0.059	0.054
			w/u_0		
					0.990
					1.067
					1.049
					1.013
					0.964
					0.868
					0.794
					0.606
					0.308
					0.046

(a) Using Eq. (7.2)

TABLE XVI (Continued)

R/D	x/D						u/u ₀
	0.0	0.5	1.0	1.5	2.0	2.5	
0.495	0.000	0.816	0.570	0.433	0.384	0.368	
0.447	0.000	0.712	0.538	0.440	0.397	0.374	
0.406	0.000	0.523	0.442	0.396	0.364	0.338	
0.365	0.000	0.293	0.324	0.325	0.308	0.286	
0.327	0.000	0.098	0.210	0.242	0.240	0.226	
0.275	0.000	-0.117	0.038	0.102	0.124	0.129	
0.243	2.963	-0.230	-0.071	0.010	0.047	0.066	
0.175	0.403	-0.413	-0.281	-0.174	-0.108	-0.058	
0.085	0.375	-0.552	-0.471	-0.349	-0.257	-0.177	
0.012	-0.074	-0.589	-0.528	-0.402	-0.303	-0.214	

u/u₀

R/D	x/d						w/u ₀
	0.0	0.5	1.0	1.5	2.0	2.5	
0.495	0.000	0.809	0.823	0.883	0.963	1.014	
0.447	0.000	0.871	0.942	0.997	1.052	1.083	
0.406	0.000	0.911	1.002	1.035	1.055	1.053	
0.365	0.000	0.996	1.061	1.060	1.040	1.005	
0.327	0.000	1.088	1.092	1.059	1.009	0.948	
0.275	0.000	1.136	1.069	1.006	0.929	0.845	
0.243	3.011	1.094	1.013	0.943	0.859	0.768	
0.175	0.850	0.867	0.806	0.743	0.666	0.582	
0.085	0.408	0.439	0.418	0.385	0.342	0.294	
0.012	0.186	0.065	0.063	0.058	0.051	0.044	

w/u₀

(b) Using Table XIII

TABLE XVII
NORMALIZED RESIDUAL SOURCE SUMS

ϕ°	UMON	VMON	WMON	MASS
45	0.0090	0.0039	0.0086	0.0068
70	0.0075	0.0028	0.0087	0.0027

(a) Moderate Convergence Criteria

ϕ°	UMON	VMON	WMON	MASS
45	0.0040	0.0016	0.0035	0.0034
70	0.0034	0.0010	0.0040	0.0006

(b) Fine Convergence Criteria

PREDICTED AXIAL AND SWIRL VELOCITIES USING FINE CONVERGENCE CRITERIA

R/D	x/D					w/u ₀
	0.0	0.5	1.0	1.5	2.0	
0.495	0.000	0.522	0.515	0.530	0.584	0.649
0.447	0.000	0.545	0.567	0.596	0.639	0.683
0.406	0.000	0.554	0.596	0.629	0.656	0.675
0.365	0.000	0.579	0.648	0.669	0.670	0.662
0.327	0.000	0.646	0.704	0.699	0.675	0.642
0.275	0.000	0.762	0.749	0.707	0.654	0.596
0.243	1.866	0.777	0.738	0.683	0.621	0.554
0.175	0.811	0.635	0.615	0.565	0.503	0.436
0.085	0.191	0.317	0.326	0.302	0.267	0.227
0.012	0.073	0.047	0.049	0.046	0.040	0.034

(a) $\phi = 45^\circ$.

TABLE XVIII (Continued)

R/D	x/D						u/u ₀
	0.0	0.5	1.0	1.5	2.0	2.5	
0.495	0.000	0.825	0.610	0.462	0.398	0.381	
0.447	0.000	0.727	0.575	0.454	0.405	0.387	
0.406	0.000	0.527	0.438	0.396	0.367	0.346	
0.365	0.000	0.274	0.306	0.317	0.306	0.287	
0.327	0.000	0.096	0.187	0.232	0.236	0.224	
0.275	0.000	-0.105	0.018	0.096	0.121	0.124	
0.243	2.963	-0.221	-0.087	0.006	0.045	0.059	
0.175	0.403	-0.423	-0.295	-0.179	-0.113	-0.072	
0.085	0.375	-0.588	-0.504	-0.374	-0.281	-0.207	
0.012	-0.074	-0.634	-0.574	-0.441	-0.339	-0.253	

R/D	x/D					
	0.0	0.5	1.0	1.5	2.0	2.5
0.495	0.000	0.786	0.746	0.853	0.963	1.002
0.447	0.000	0.857	0.944	1.003	1.063	1.093
0.406	0.000	0.899	1.031	1.055	1.071	1.069
0.365	0.000	1.040	1.092	1.080	1.056	1.020
0.327	0.000	1.142	1.112	1.072	1.020	0.960
0.275	0.000	1.158	1.073	1.011	0.933	0.851
0.243	3.011	1.100	1.012	0.944	0.859	0.771
0.175	0.850	0.866	0.805	0.743	0.664	0.582
0.085	0.408	0.440	0.420	0.387	0.342	0.294
0.012	0.186	0.066	0.063	0.058	0.051	0.044
			w/u ₀			
			(b) $\phi = 70$ deg.			

TABLE XIX
PREDICTED AXIAL AND SWIRL VELOCITIES USING EQ. (8.1)

R/D	x/D					
	0.0	0.5	1.0	1.5	2.0	2.5
0.495	0.000	0.590	0.439	0.375	0.342	0.319
0.447	0.000	0.606	0.468	0.397	0.360	0.333
0.406	0.000	0.548	0.430	0.376	0.345	0.320
0.365	0.000	0.407	0.354	0.331	0.312	0.294
0.327	0.000	0.207	0.266	0.275	0.269	0.260
0.275	0.000	-0.046	0.132	0.174	0.190	0.199
0.243	1.881	-0.151	0.045	0.106	0.136	0.158
0.175	0.924	-0.270	-0.129	-0.035	0.025	0.074
0.085	0.135	-0.339	-0.288	-0.174	-0.087	-0.009
0.012	0.069	-0.355	-0.334	-0.217	-0.122	-0.036
			u/u ₀			

R/D	x/D					
	0.0	0.5	1.0	1.5	2.0	2.5
0.495	0.000	0.526	0.526	0.551	0.606	0.663
0.447	0.000	0.547	0.576	0.609	0.652	0.692
0.406	0.000	0.557	0.606	0.636	0.661	0.679
0.365	0.000	0.585	0.652	0.668	0.669	0.661
0.327	0.000	0.645	0.700	0.692	0.668	0.638
0.275	0.000	0.753	0.736	0.693	0.643	0.589
0.243	1.866	0.774	0.724	0.669	0.609	0.546
0.175	0.811	0.646	0.609	0.554	0.492	0.427
0.085	0.191	0.326	0.326	0.298	0.261	0.222
0.012	0.073	0.048	0.049	0.045	0.039	0.033
			w/u ₀			

(a) $\phi = 45$ deg.

TABLE XIX (Continued)

R/D	X/D				
	0.0	0.5	1.0	1.5	2.0
0.495	0.000	0.838	0.608	0.467	0.402
0.447	0.000	0.742	0.583	0.470	0.416
0.406	0.000	0.548	0.465	0.414	0.379
0.365	0.000	0.295	0.323	0.330	0.317
0.327	0.000	0.075	0.190	0.235	0.241
0.275	0.000	-0.150	0.004	0.082	0.114
0.243	2.963	-0.261	-0.110	-0.016	0.030
0.175	0.403	-0.432	-0.318	-0.210	-0.137
0.085	0.375	-0.557	-0.499	-0.389	-0.295
0.012	-0.074	-0.588	-0.552	-0.443	-0.344
			u/u_0		
					0.377
					0.385
					0.349
					0.294
					0.230
					0.125
					0.056
					-0.078
					-0.206
					-0.246

R/D	X/D				
	0.0	0.5	1.0	1.5	2.0
0.495	0.000	0.798	0.785	0.830	0.919
0.447	0.000	0.857	0.911	0.864	1.024
0.406	0.000	0.890	0.982	1.020	1.044
0.365	0.000	0.989	1.060	1.063	1.045
0.327	0.000	1.104	1.106	1.075	1.024
0.275	0.000	1.148	1.090	1.030	0.960
0.243	3.011	1.096	1.032	0.967	0.862
0.175	0.850	0.856	0.816	0.762	0.687
0.085	0.408	0.429	0.420	0.393	0.353
0.012	0.186	0.064	0.063	0.059	0.053
			w/u_0		
					0.993
					1.068
					1.049
					1.011
					0.960
					0.862
					0.787
					0.598
					0.303
					0.045

(b) $\phi = 70$ deg.

TABLE XX
PREDICTED AXIAL AND SWIRL VELOCITIES USING EQ. (8.2)

R/D	x/D					
	0.0	0.5	1.0	1.5	2.0	2.5
0.495	0.000	0.825	0.596	0.457	0.397	0.375
0.447	0.000	0.732	0.572	0.463	0.412	0.382
0.406	0.000	0.544	0.460	0.411	0.376	0.346
0.365	0.000	0.299	0.325	0.330	0.316	0.291
0.327	0.000	0.084	0.197	0.238	0.241	0.228
0.275	0.000	-0.139	0.013	0.088	0.116	0.125
0.243	2.963	-0.252	-0.100	-0.010	0.034	0.059
0.175	0.403	-0.429	-0.311	-0.203	-0.131	-0.073
0.085	0.375	-0.558	-0.496	-0.383	-0.288	-0.199
0.012	-0.074	-0.591	-0.551	-0.437	-0.336	-0.238
			u/u ₀			

R/D	x/D					
	0.0	0.5	1.0	1.5	2.0	2.5
0.495	0.000	0.801	0.791	0.841	0.931	1.001
0.447	0.000	0.862	0.919	0.973	1.034	1.076
0.406	0.000	0.896	0.989	1.026	1.050	1.054
0.365	0.000	0.993	1.064	1.066	1.047	1.012
0.327	0.000	1.105	1.107	1.075	1.023	0.959
0.275	0.000	1.152	1.090	1.028	0.948	0.859
0.243	3.011	1.101	1.031	0.964	0.878	0.782
0.175	0.850	0.861	0.816	0.759	0.683	0.595
0.085	0.408	0.432	0.420	0.392	0.351	0.301
0.012	0.186	0.064	0.063	0.059	0.053	0.045
			w/u ₀			

(a) $\phi = 45$ deg.

TABLE XX (Continued)

R/D	x/D				
	0.0	0.5	1.0	1.5	2.0
0.495	0.000	0.592	0.441	0.377	0.345
0.447	0.000	0.610	0.477	0.404	0.364
0.406	0.000	0.553	0.440	0.382	0.349
0.365	0.000	0.412	0.359	0.336	0.316
0.327	0.000	0.203	0.264	0.276	0.271
0.275	0.000	-0.058	0.124	0.171	0.189
0.243	0.000	-0.161	0.034	0.100	0.133
0.175	1.881	-0.272	-0.141	-0.046	0.017
0.085	0.924	-0.333	-0.295	-0.188	-0.100
0.012	0.135	-0.346	-0.339	-0.231	-0.136

 u/u_0

R/D	x/D				
	0.0	0.5	1.0	1.5	2.0
0.495	0.000	0.525	0.520	0.538	0.594
0.447	0.000	0.547	0.571	0.602	0.645
0.406	0.000	0.556	0.601	0.633	0.660
0.365	0.000	0.583	0.651	0.670	0.672
0.327	0.000	0.646	0.704	0.698	0.675
0.275	0.000	0.761	0.746	0.704	0.652
0.243	0.000	0.779	0.735	0.680	0.618
0.175	1.866	0.641	0.615	0.563	0.501
0.085	0.811	0.320	0.327	0.301	0.266
0.012	0.191	0.047	0.049	0.046	0.040

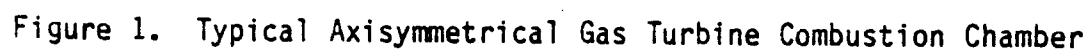
 w/u_0 (b) $\phi = 70$ deg.

TABLE XXI

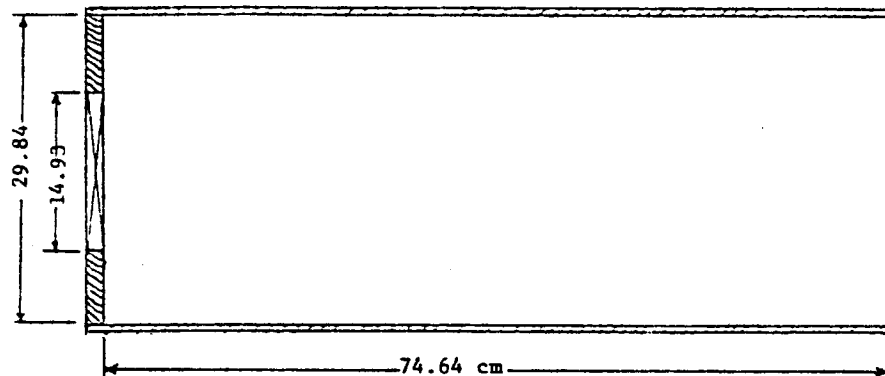
ϕ , S' AND G CORRESPONDENCE FOR PLUG FLOW
SOLID BODY ROTATION SWIRLERS WITH
 $d_n/d = 0.25$

ϕ	S'	G
0	0	0
38	0.547	1.094
45	0.700	1.400
60	1.212	2.425
70	1.923	3.846

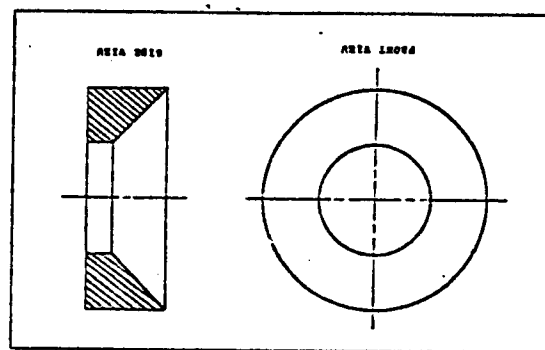
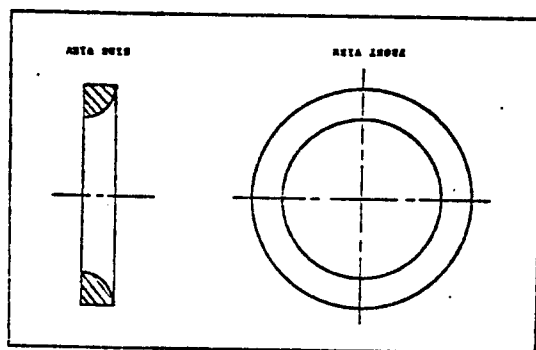
FIGURES



147

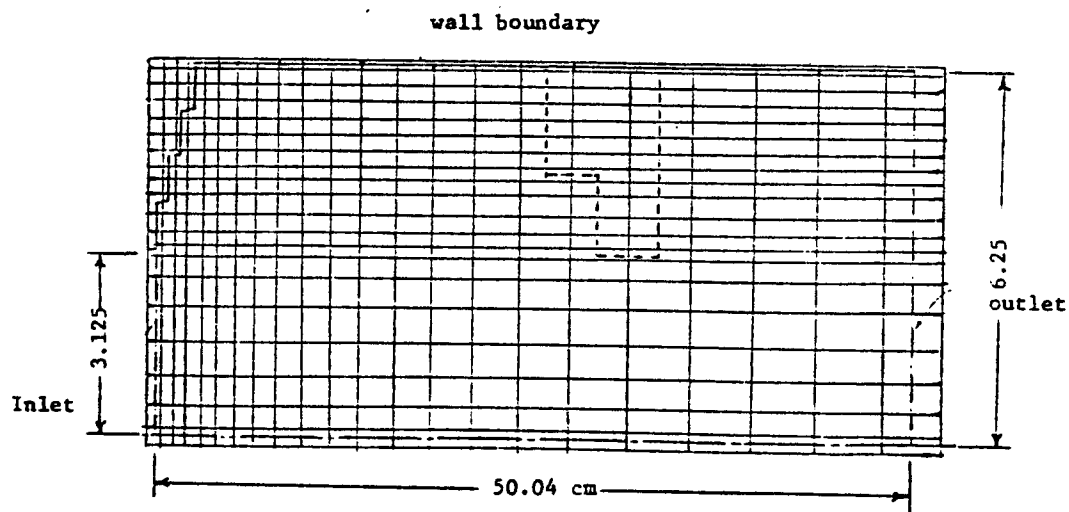


(a) Experimental Model



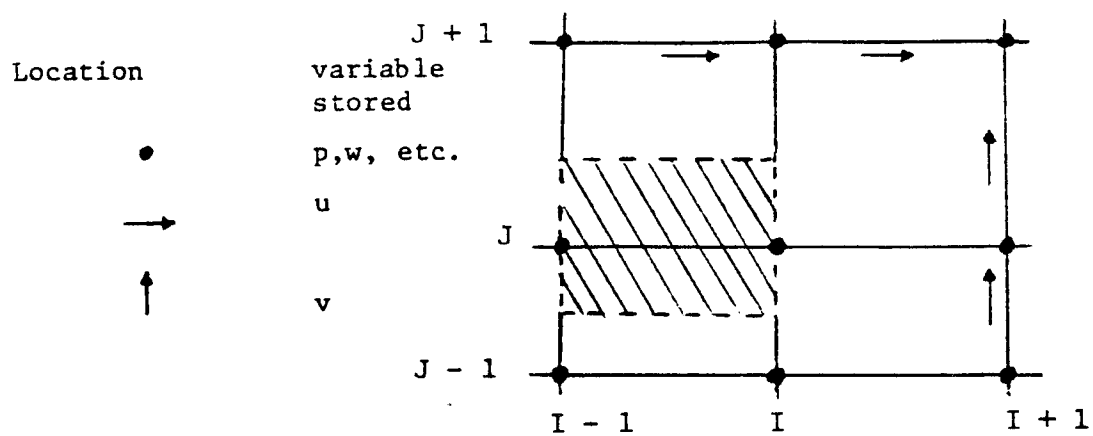
(b) The Weak Contraction Nozzle

(c) The Strong Contraction Nozzle

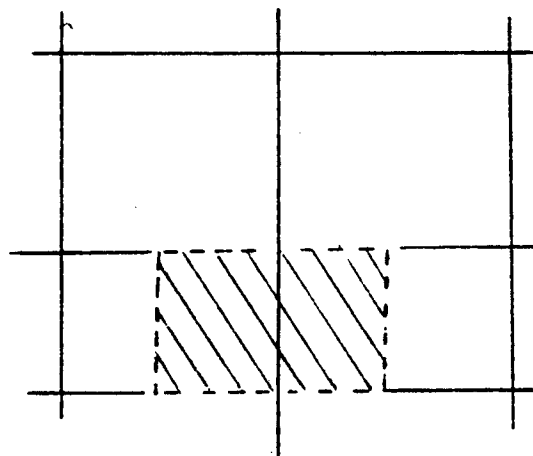


(d) Computer Model -- Possible Nozzle Boundary

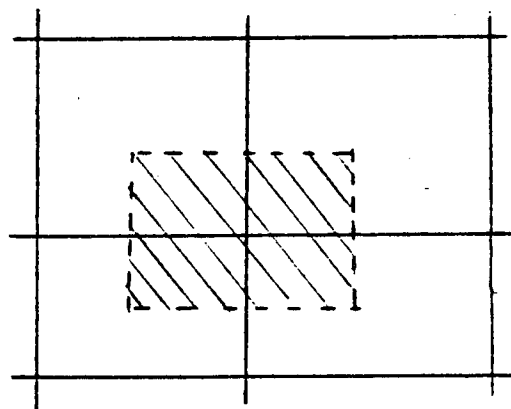
Figure 2. Combustion Chamber Flowfield Simulation



(a)



(b)



(c)

Figure 3. Typical Control Volumes of Staggered-grid System:
(a) u -cell; (b) v -cell; (c) $p, w, \text{ etc.}$ cell.

STARPIC

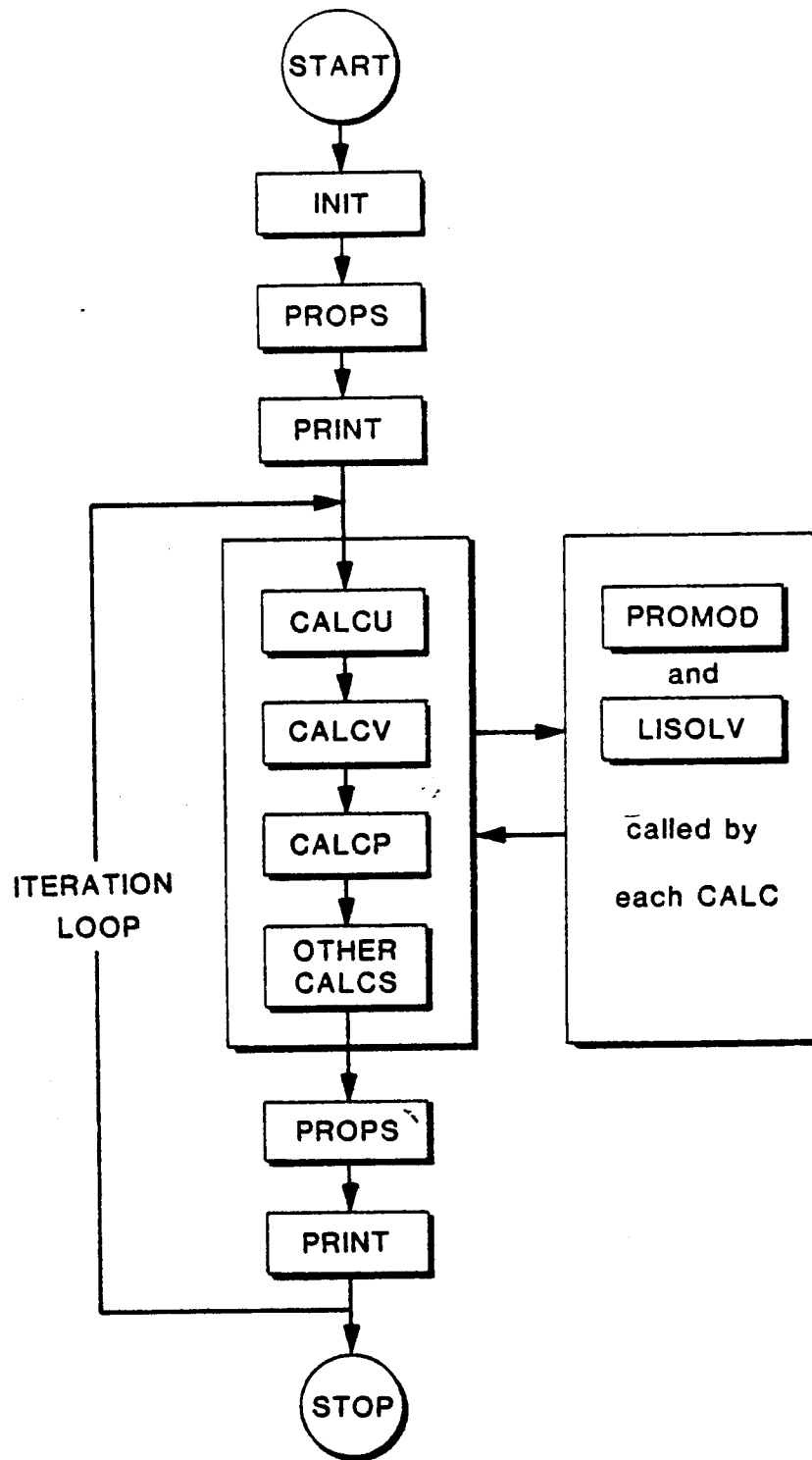


Figure 4. Flow Chart of the STARPIC Computer Code

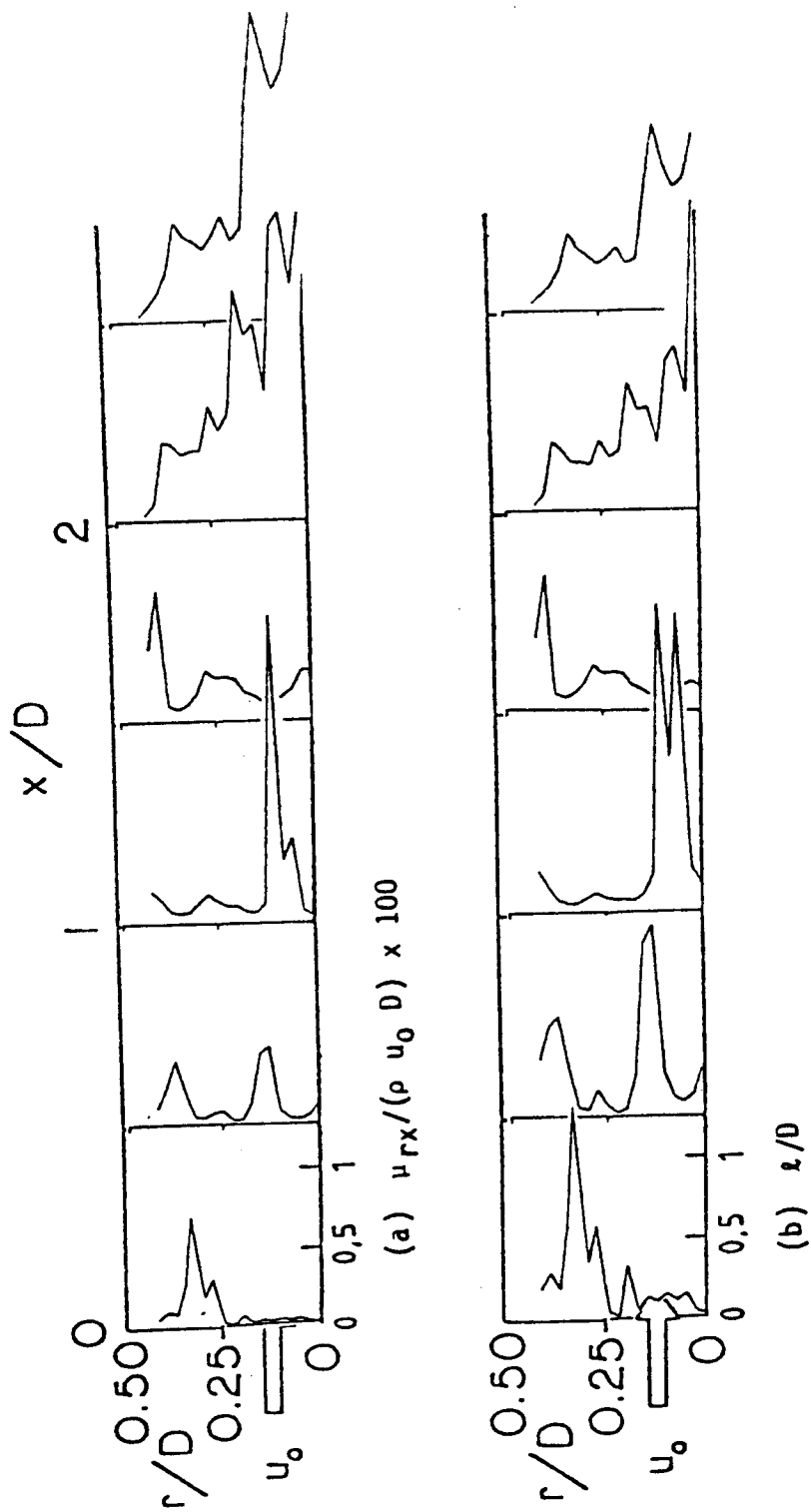


Figure 5. Normalized u_{rx} and u_z for Swirl Vane Angle $\phi = 0^\circ$.

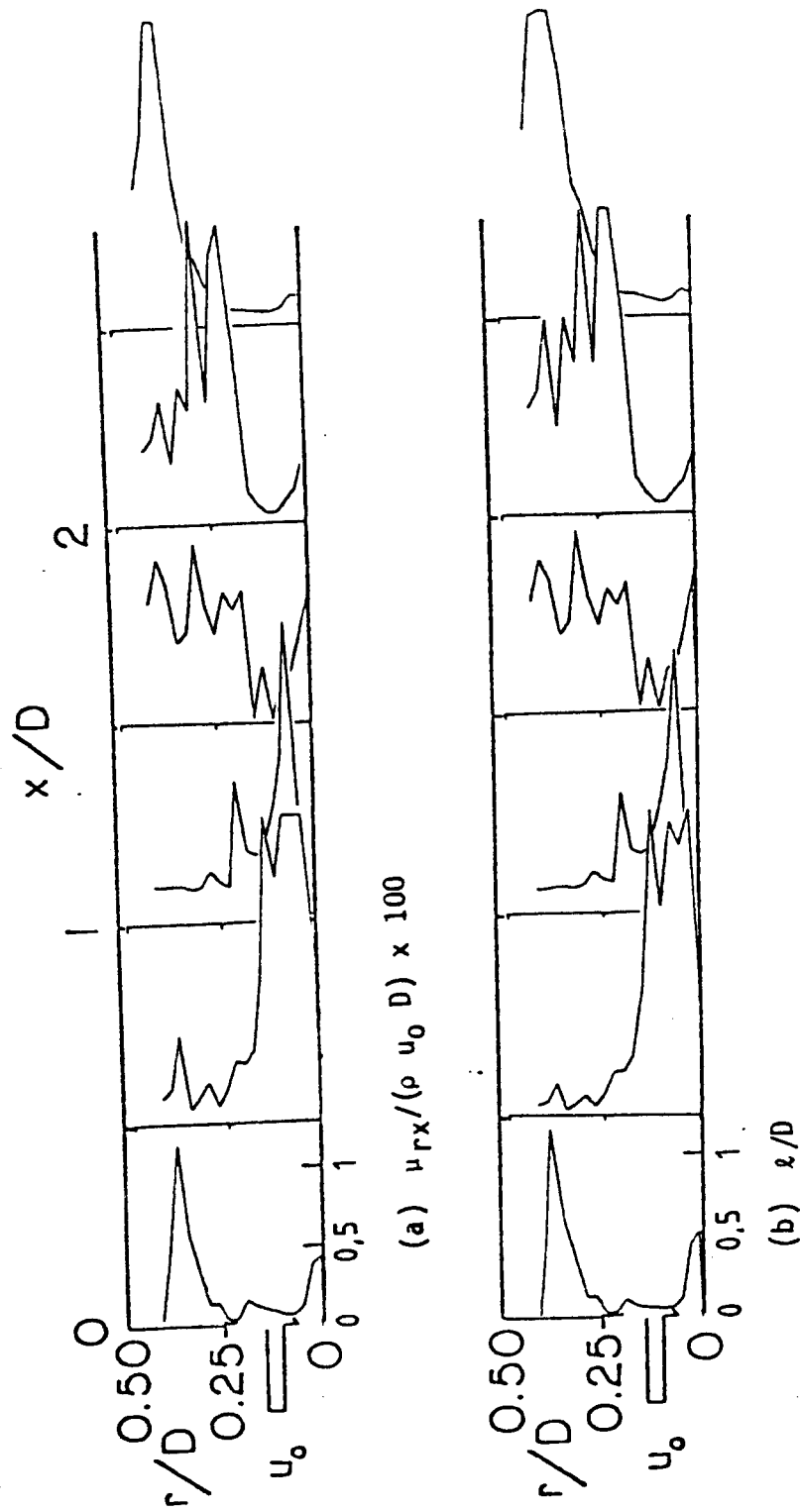


Figure 6. Normalized u_r and u_x for Swirl Vane Angle $\phi = 45^\circ$.

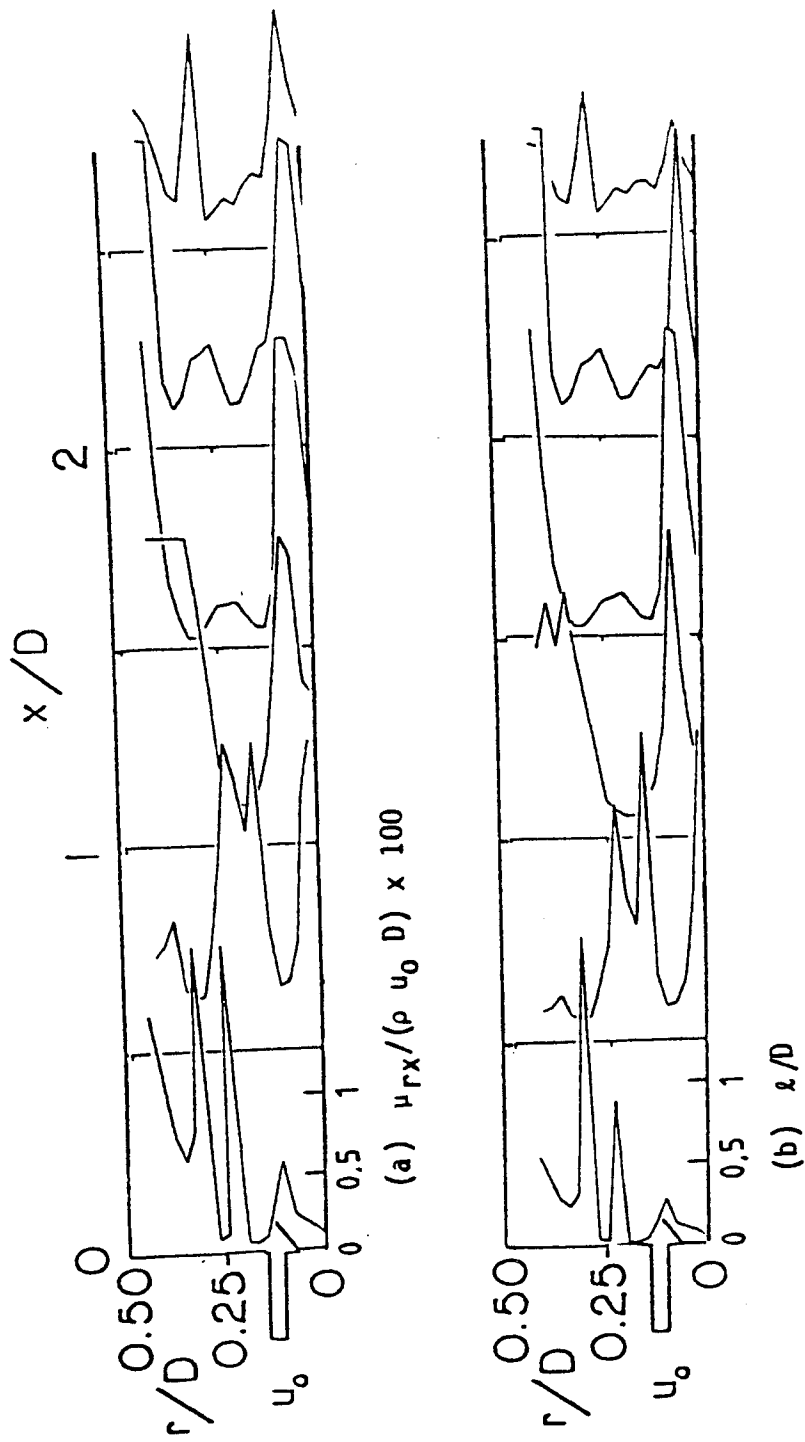


Figure 7. Normalized u_{rx} and λ for Swirl Vane Angle $\phi = 70$ deg.

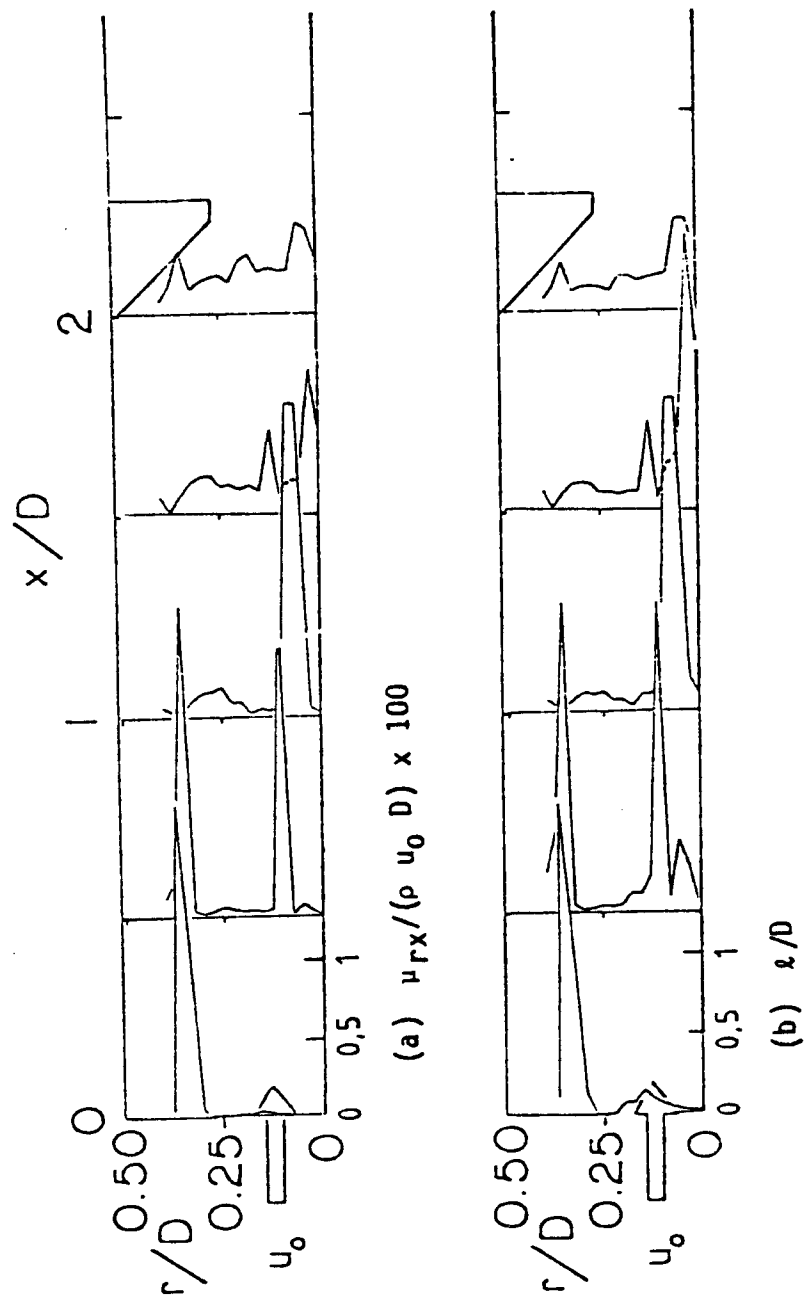


Figure 8. Normalized μ_{rx} and α for Swirl Vane Angle $\phi = 0$ deg.
with Strong Contraction Nozzle at $L/D = 2$

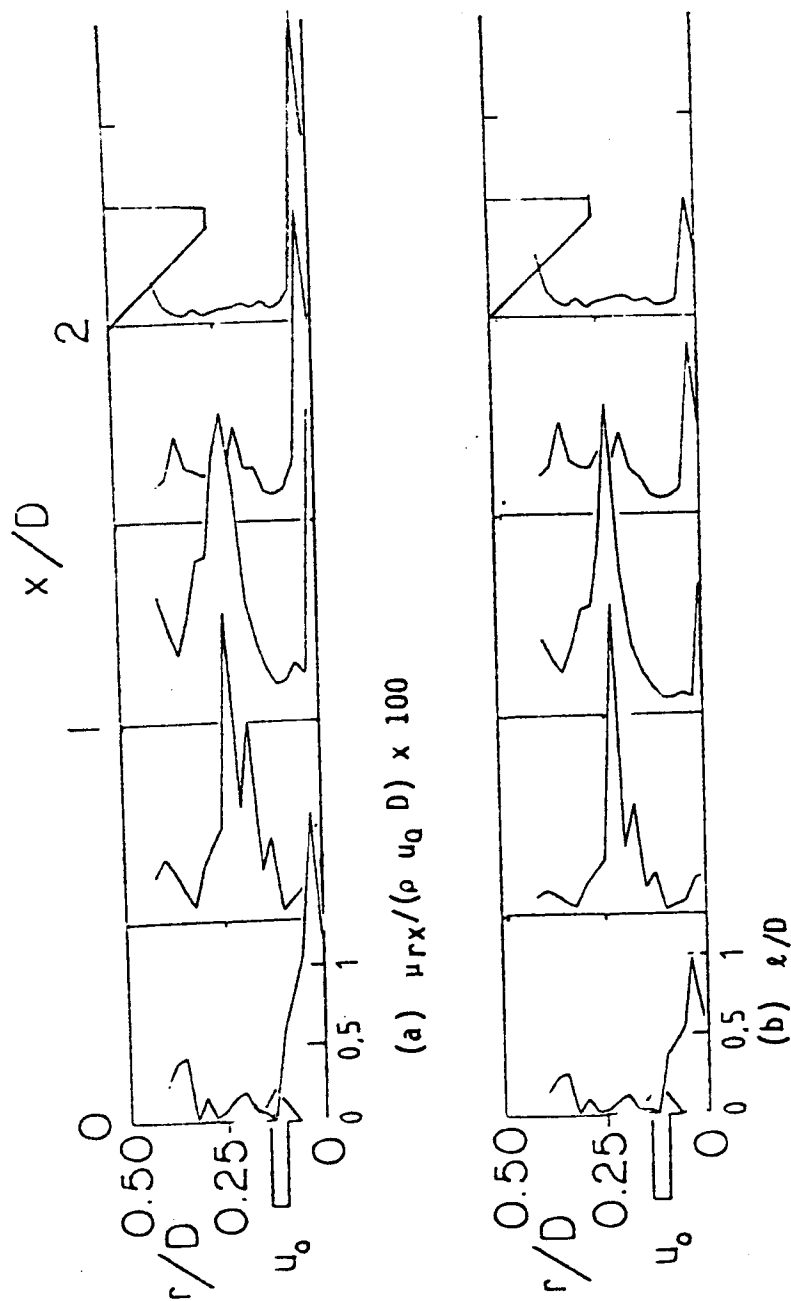


Figure 9. Normalized u_x and u_r for Swirl Vane Angle $\phi = 45^\circ$.
with Strong Contraction Nozzle at $L/D = 2$

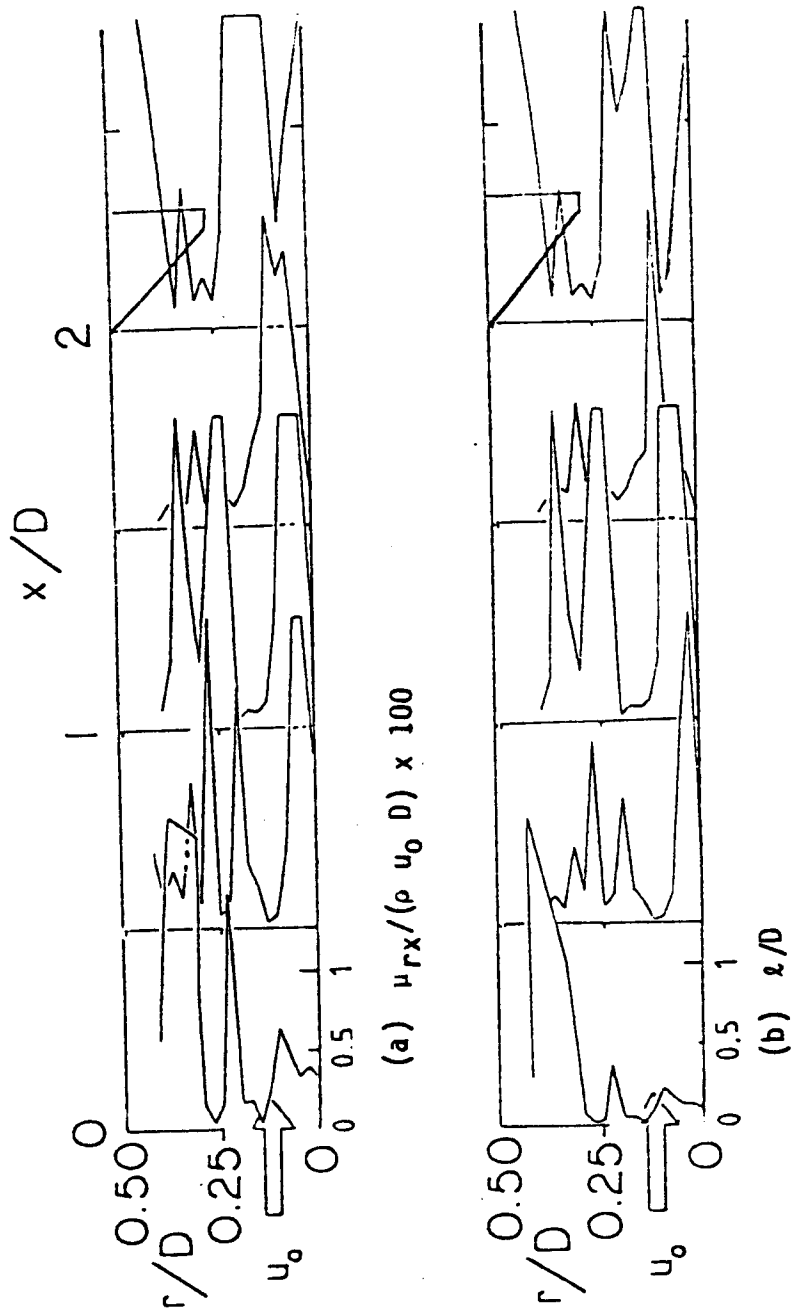


Figure 10. Normalized u_{rx} and u for Swirl Vane Angle $\phi = 70^\circ$ with Strong Contraction Nozzle at $L/D = 2$

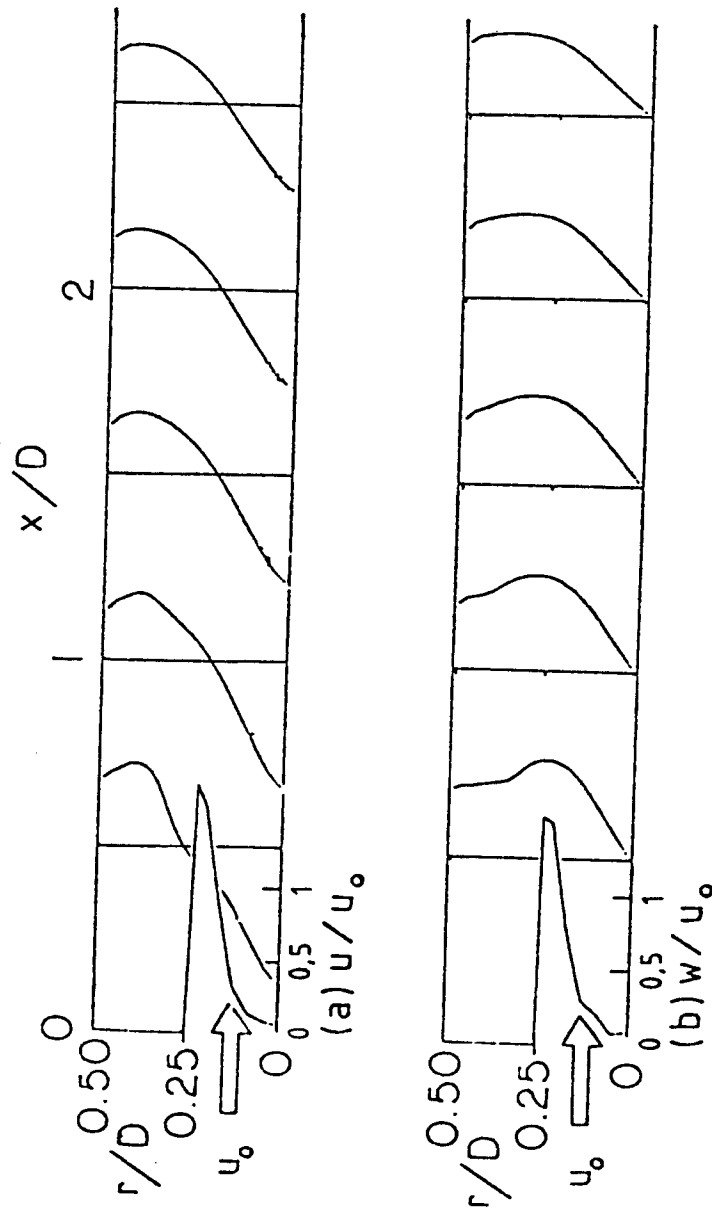


Figure 11. Predicted Velocity Profiles for Swirl Vane Angle $\phi = 45^\circ$.
Including Effect of Streamline Curvature

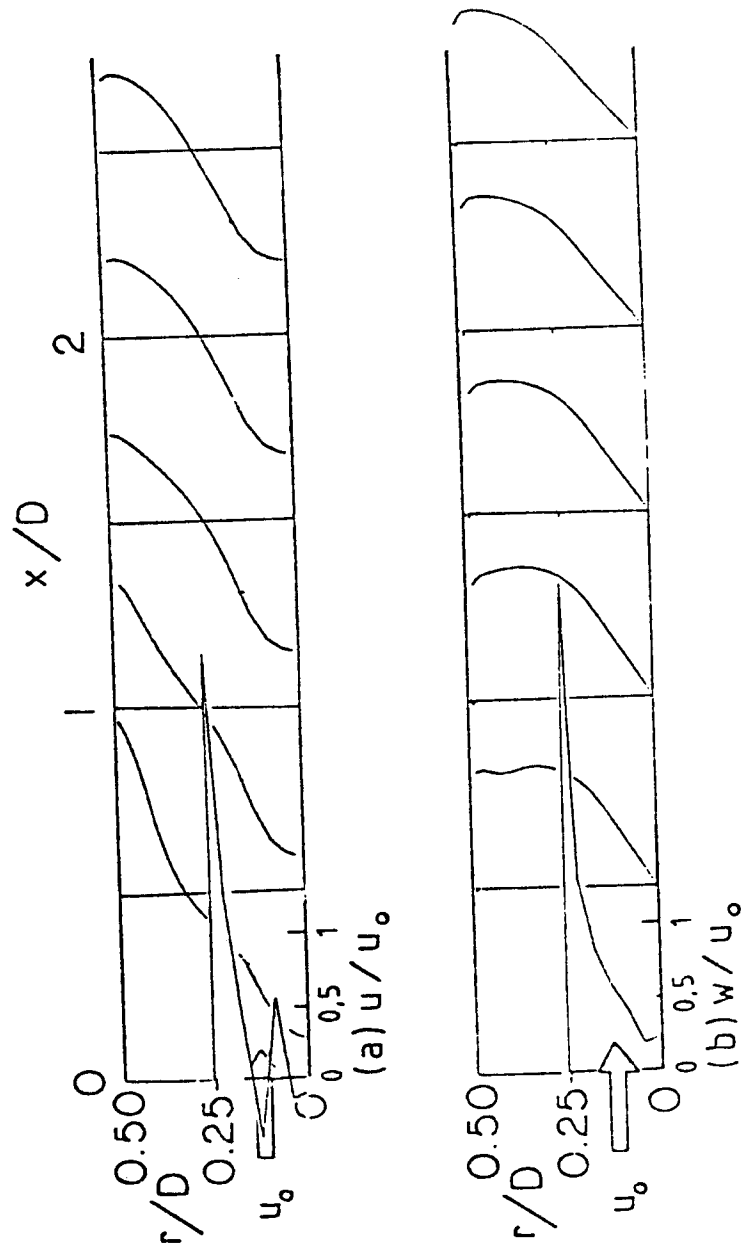


Figure 12. Predicted Velocity Profiles for Swirl Vane Angle $\phi = 70^\circ$. Including Effect of Streamline Curvature

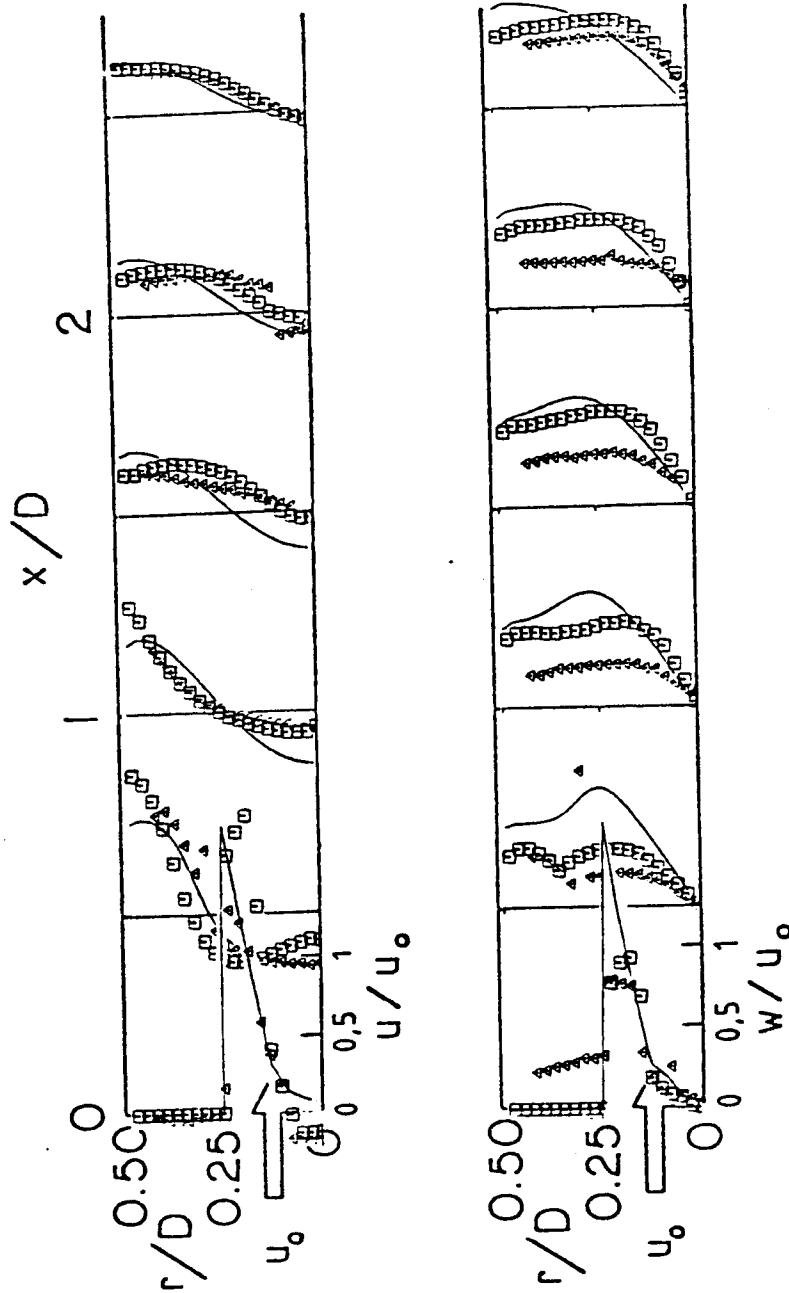


Figure 13. Predicted Velocity Profiles for Swirl Vane Angle $\phi = 45^\circ$.
Using Eq. (7.2) for C_μ Variation as Compared with
Experimental Data [\square --Ref. 9, \triangle --Ref. 10]

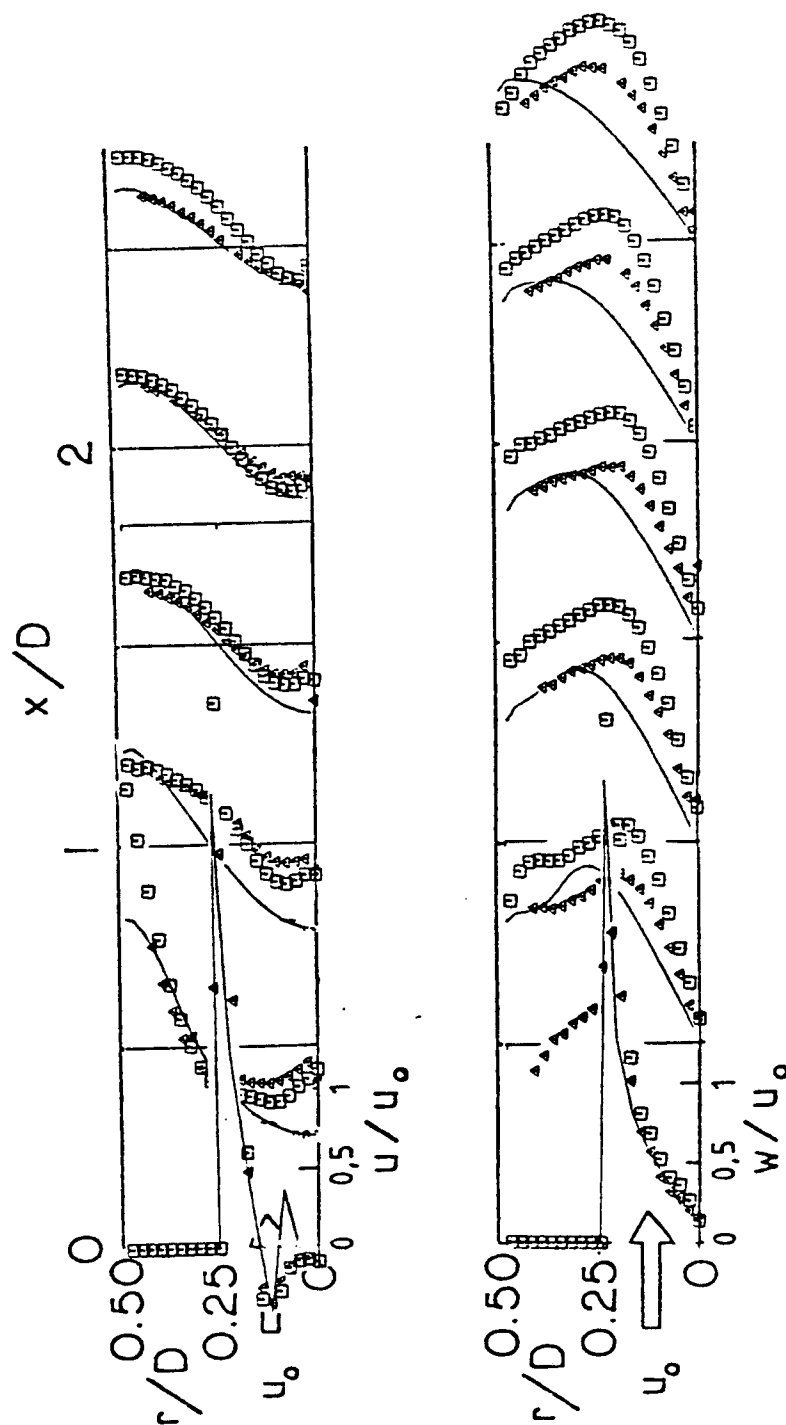


Figure 14. Predicted Velocity Profiles for Swirl Vane Angle $\phi = 70$ deg.
Using Eq. (7.2) for C_u Variation as Compared with
Experimental Data [□ --Ref. 9, Δ --Ref. 10]

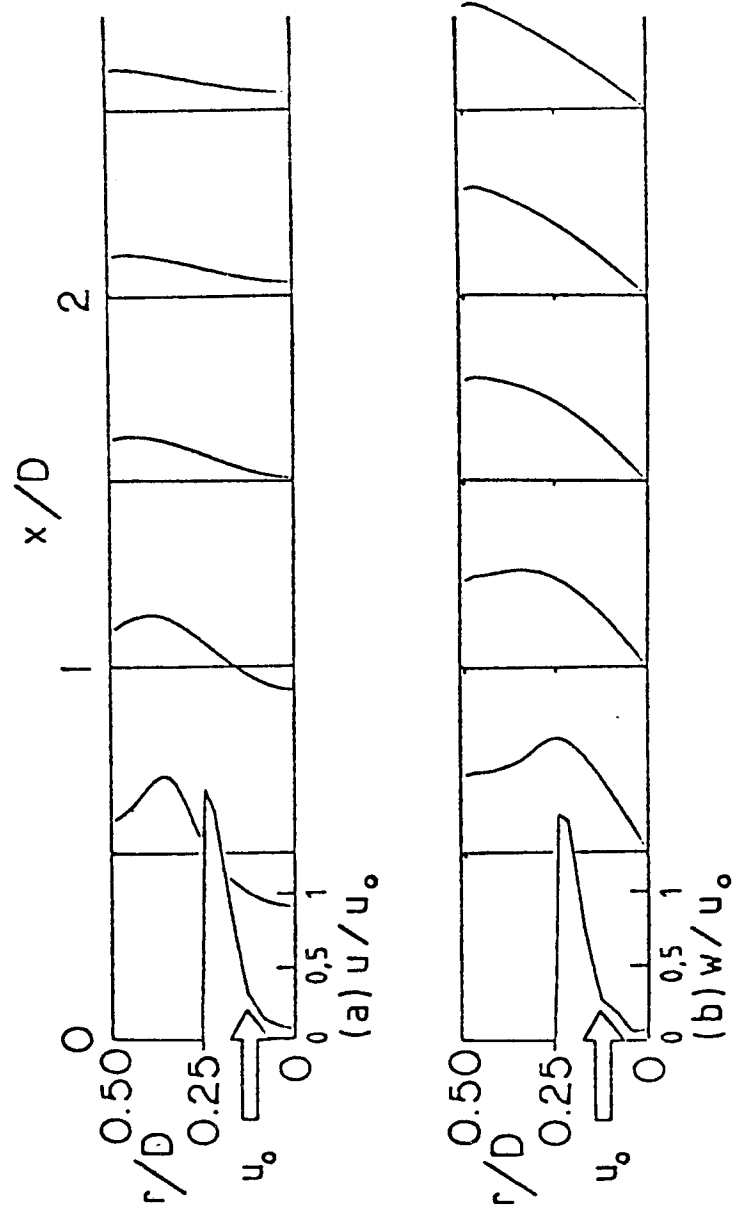


Figure 15. Predicted Velocity Profiles for Swirl Vane Angle $\phi = 45^\circ$.
Using Standard $k-\epsilon$ Model

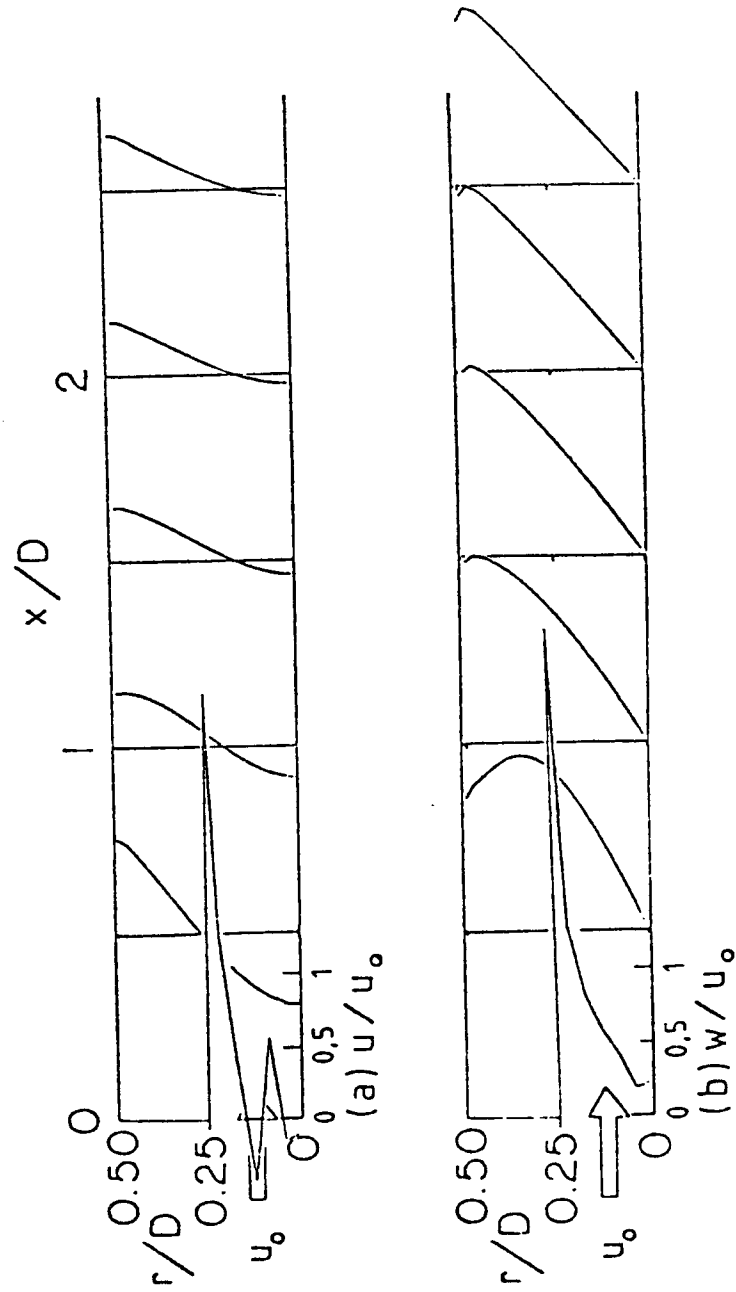


Figure 16. Predicted Velocity Profiles for Swirl Vane Angle $\phi = 70^\circ$.
Using Standard $k-\epsilon$ Model

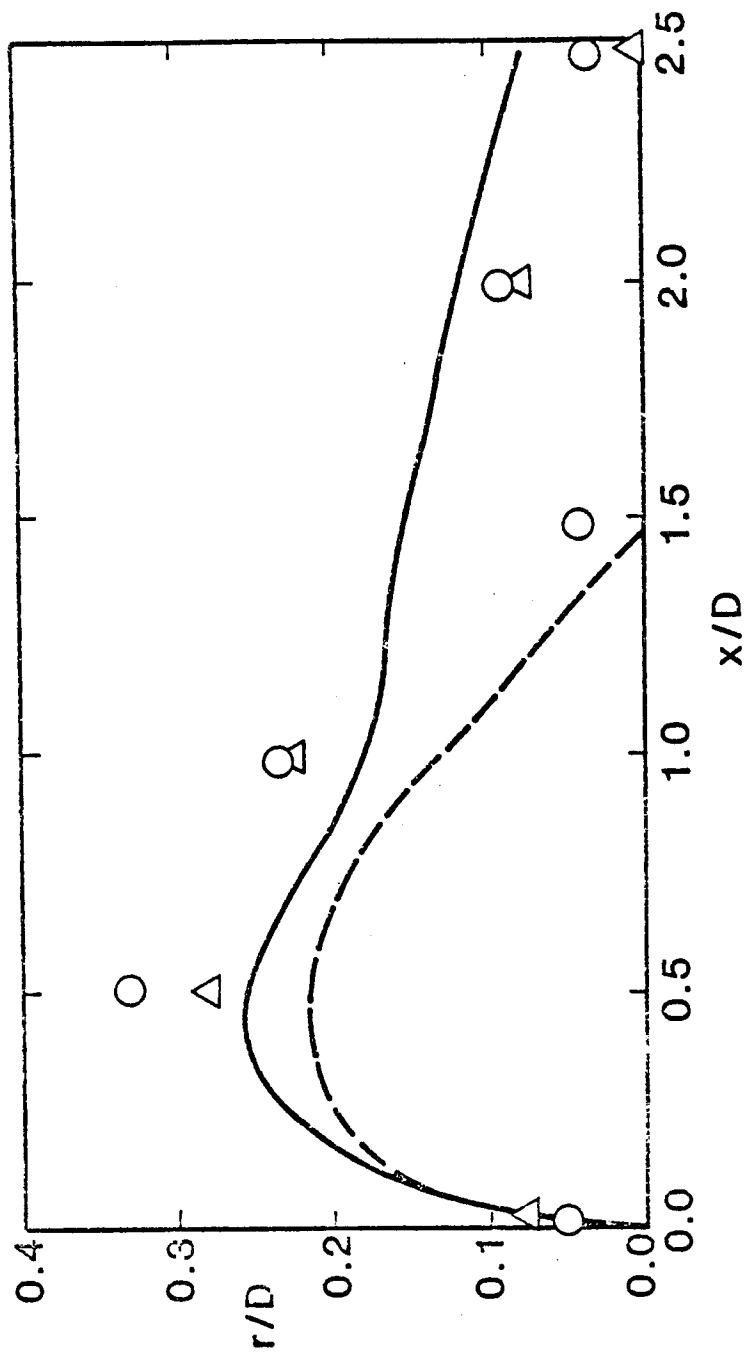


Figure 17. Predicted and Measured Central Recirculation Zone Envelope for Swirl Vane Angle $\phi = 45$ deg.
 [Predicted: --- Table IV; — Eq. (7.2); Measured: \circ --Ref. 9; \triangle --Ref. 10]

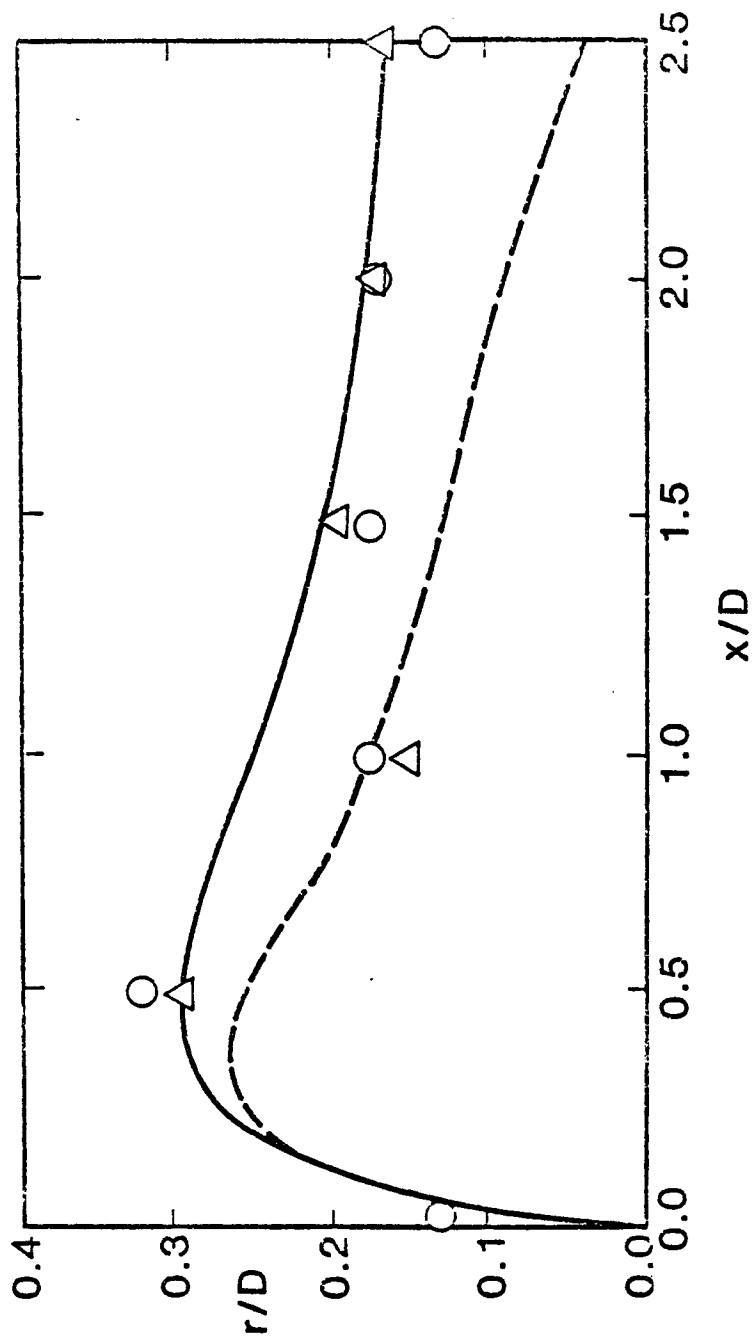


Figure 18. Predicted and Measured Central Recirculation Zone Envelope for Swirl Vane Angle $\phi = 70$ deg.
 [Predicted: --- Table IV; — Eq. (7.2); Measured:
 ○ --Ref. 9; △ --Ref. 10]

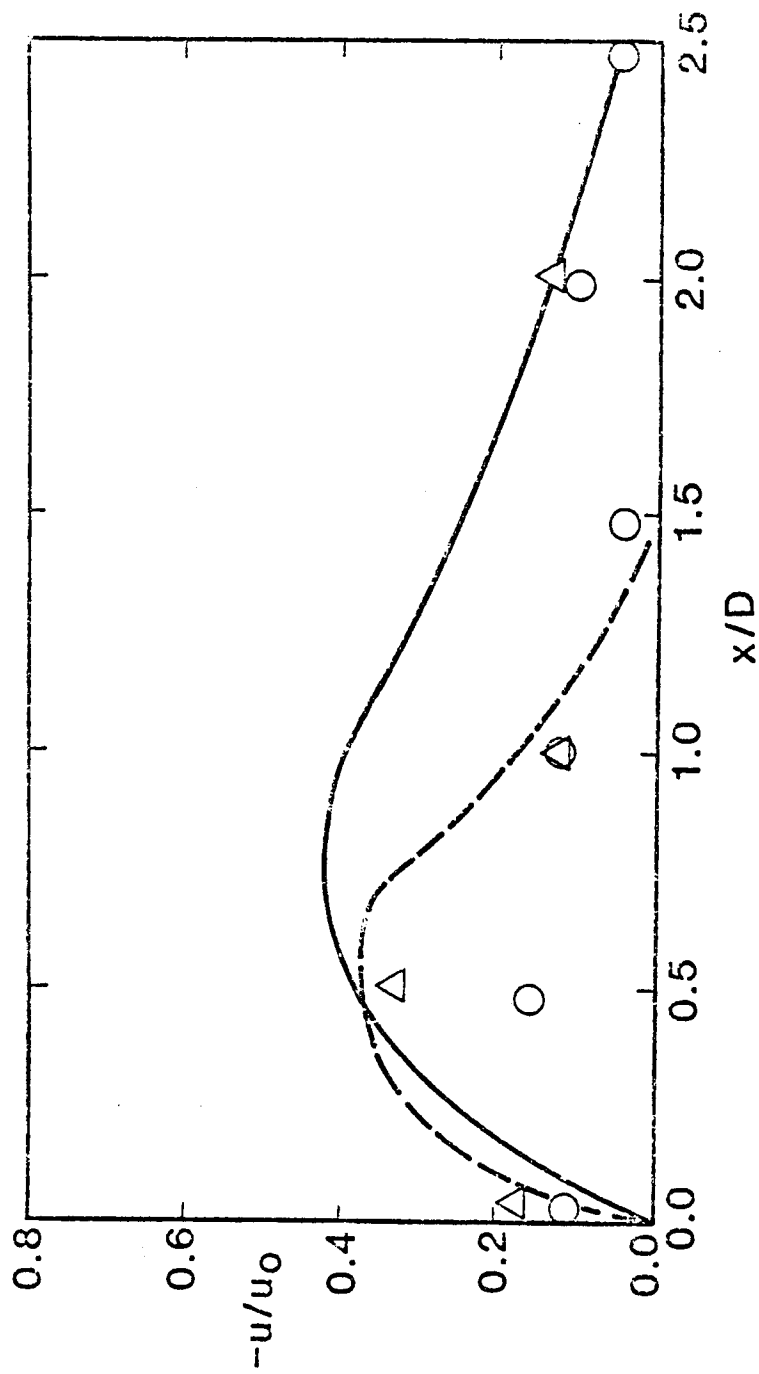


Figure 19. Predicted and Measured Centerline Velocity Longitudinal Variation for Swirl Vane Angle $\phi = 45$ deg.
 [Predicted: --- Table IV; — Eq. (7.2); Measured:
 O --Ref. 9; Δ --Ref. 10]

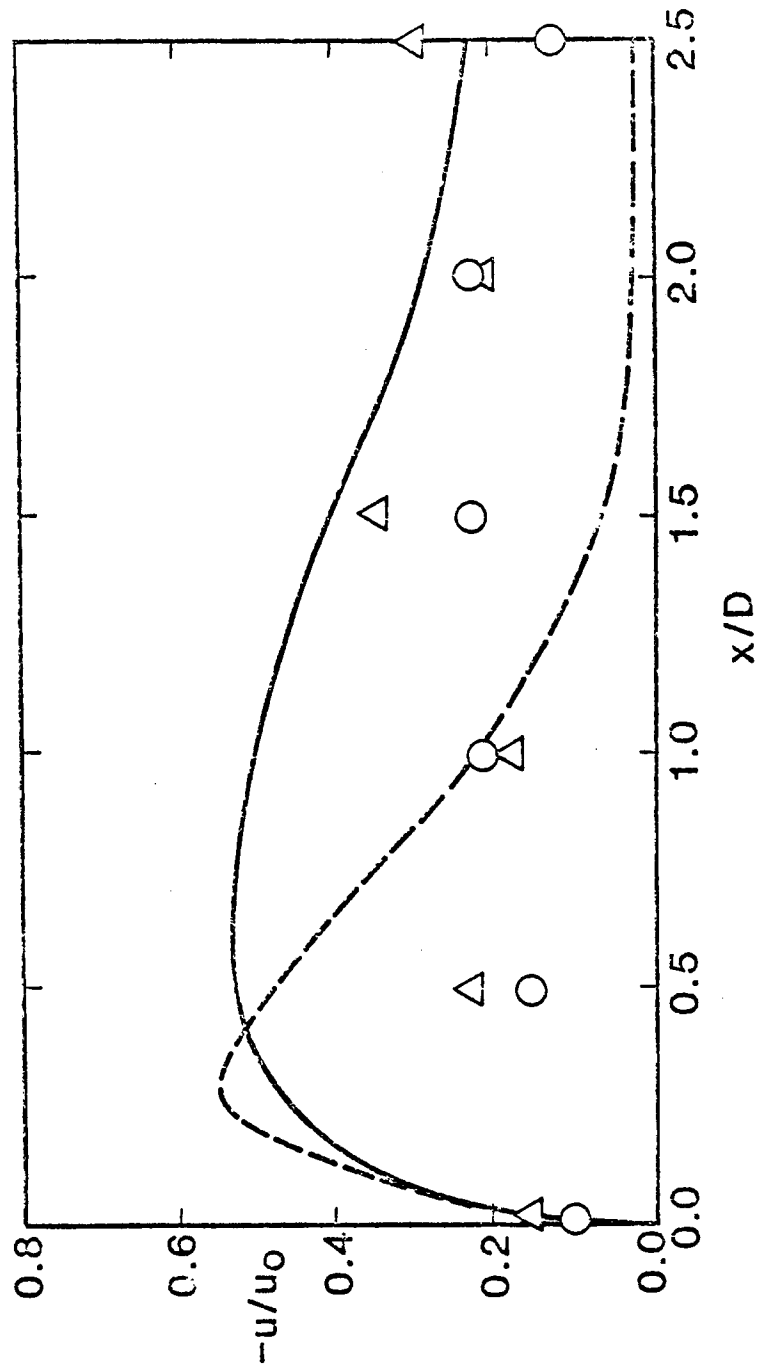


Figure 20. Predicted and Measured Centerline Velocity Longitudinal Variation for Swirl Vane Angle $\phi = 70$ deg.
 [Predicted: --- Table IV; — Eq. (7.2); Measured: O --Ref. 9; Δ --Ref. 10]

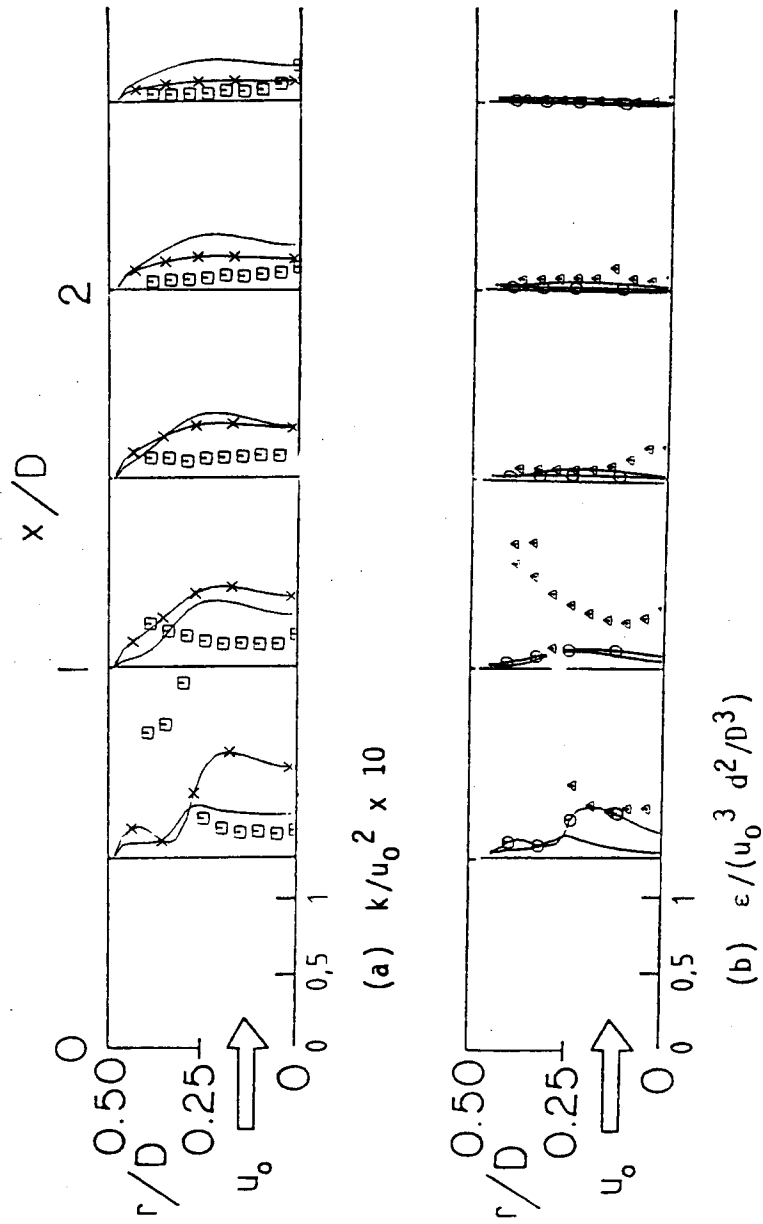


Figure 21. Predicted and Measured Turbulence Parameters for Swirl Vane Angle $\phi = 45$ deg.
 Δ , \times —Ref. 10, \circ Table IV, — Eq. (7.2)]

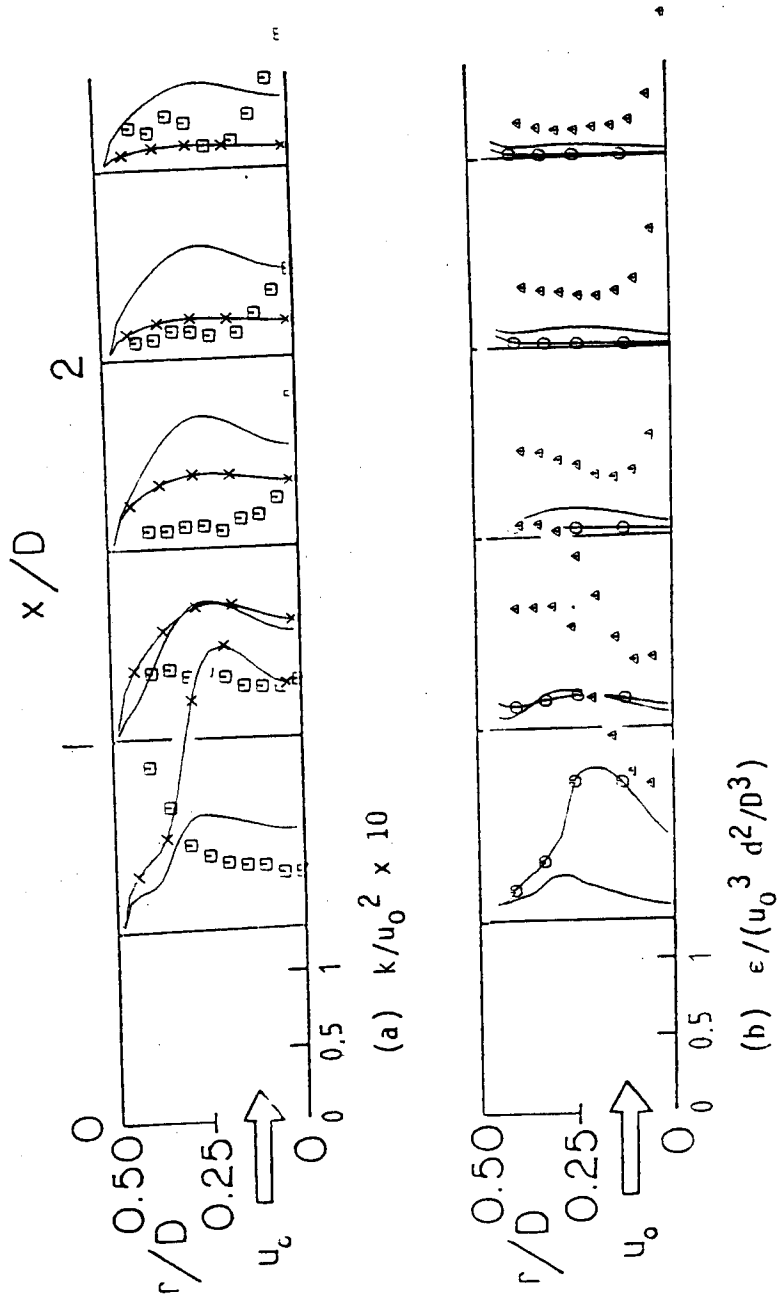


Figure 22. Predicted and Measured Turbulence Parameters for Swirl
 Vane Angle $\phi = 70$ deg.
 [Δ , \square --Ref. 10, \times , \circ Table IV, — Eq. (7.2)]

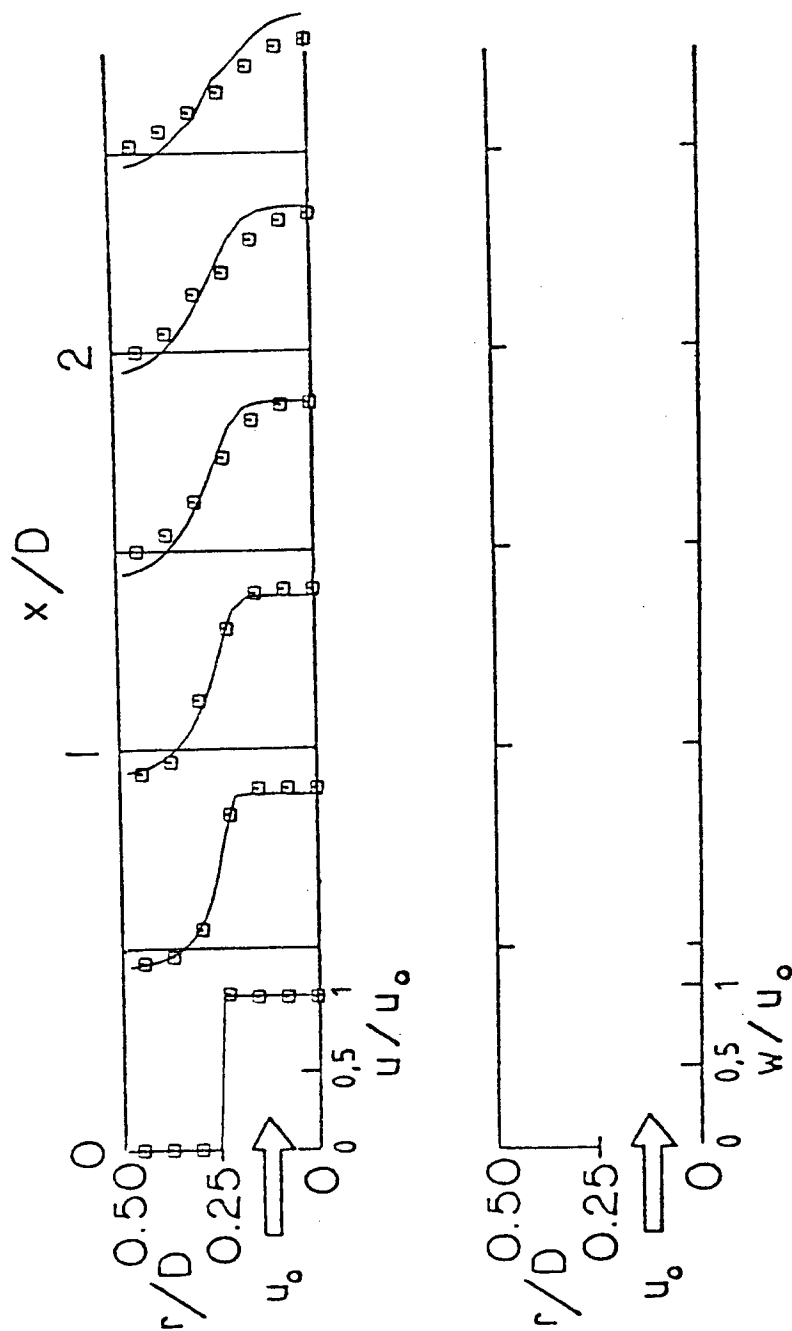


Figure 23. Predicted and Measured Velocity Profiles for Nonswirling Flow [17--Ref. 9]

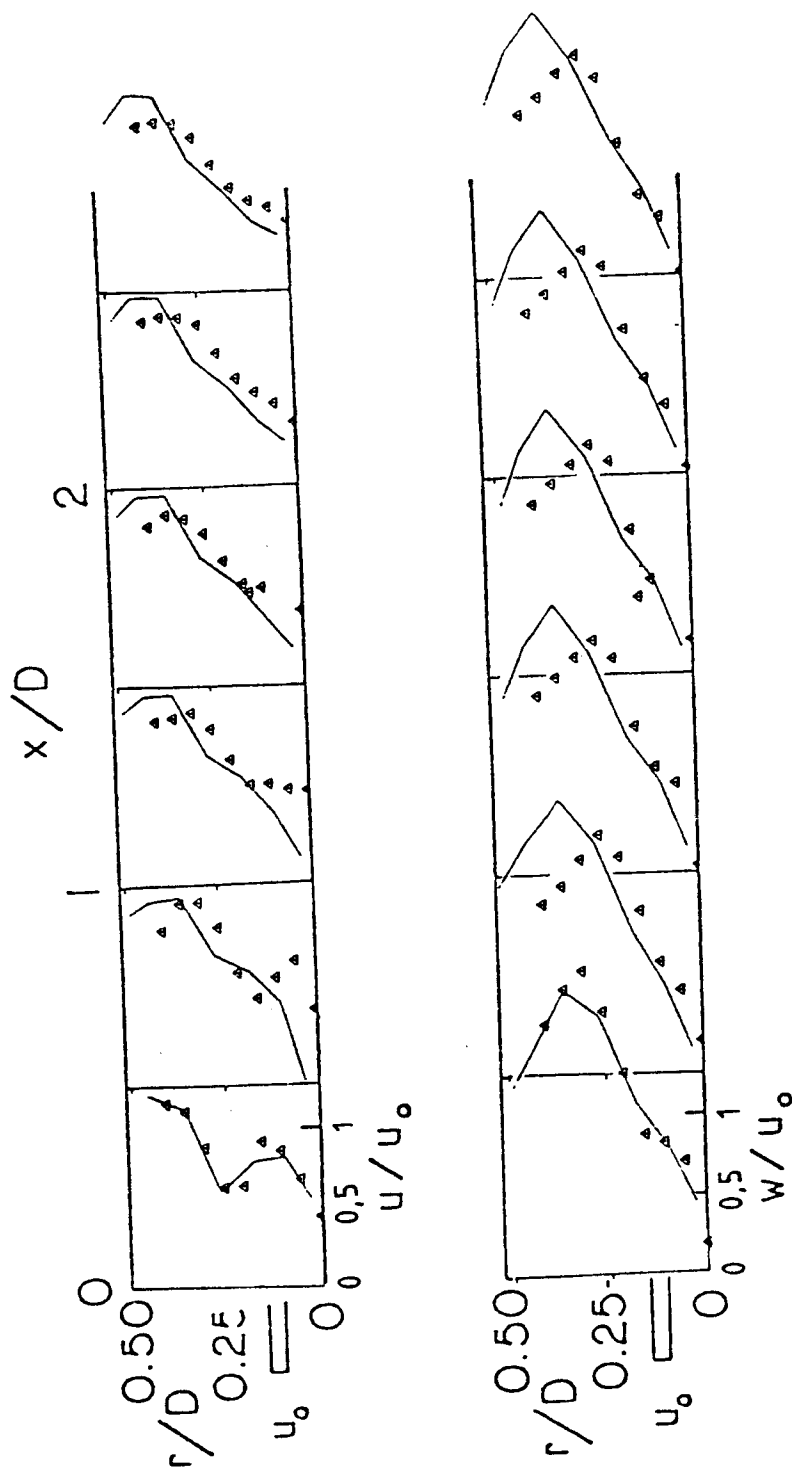


Figure 24. Predicted and Measured Velocity Profiles for Swirl Vane
Angle $\phi = 45^\circ$, $D/d = 1$ [Δ --Ref. 10]

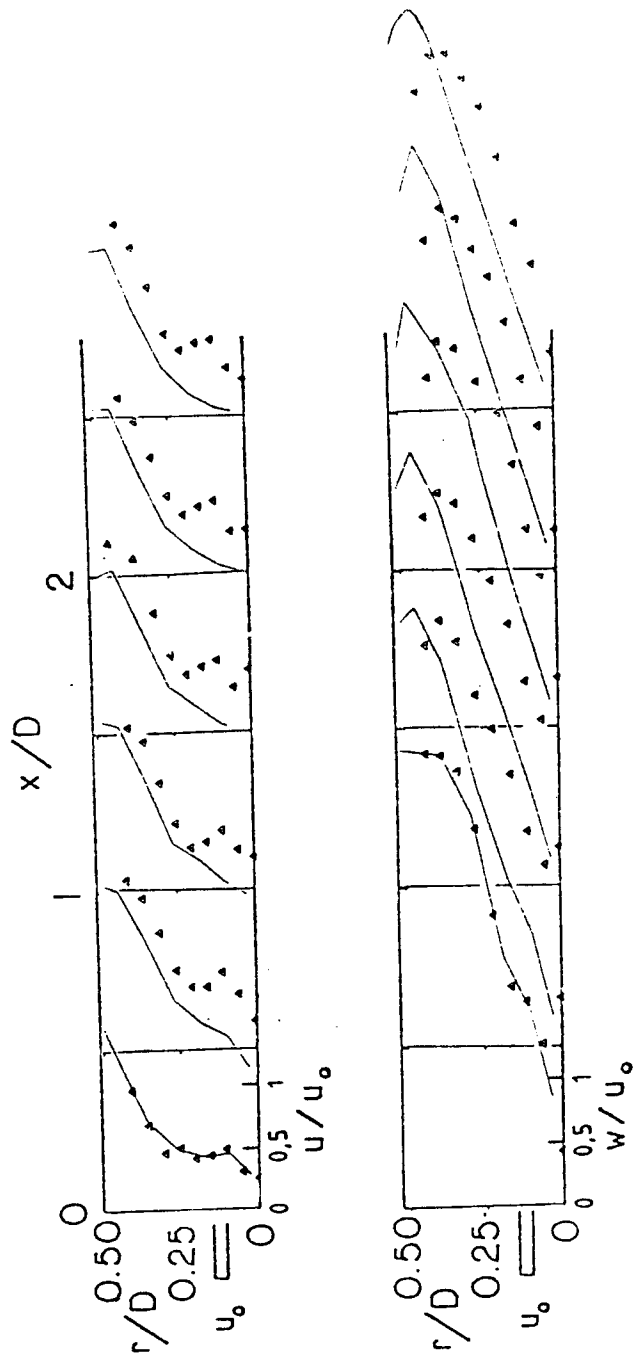


Figure 25. Predicted and Measured Velocity Profiles for Swirl Vane
Angle $\phi = 70$ deg., $D/d = 1$ [Δ --Ref. 10]

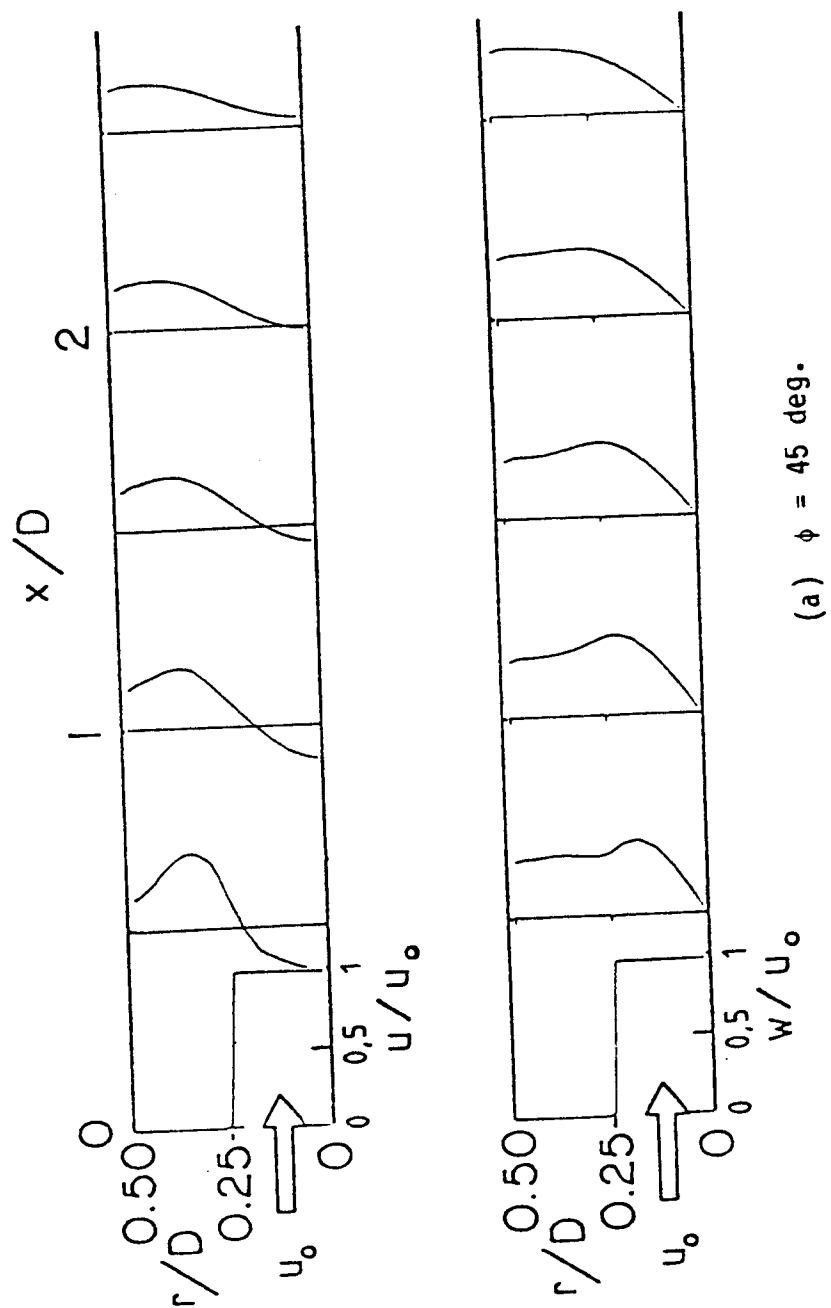
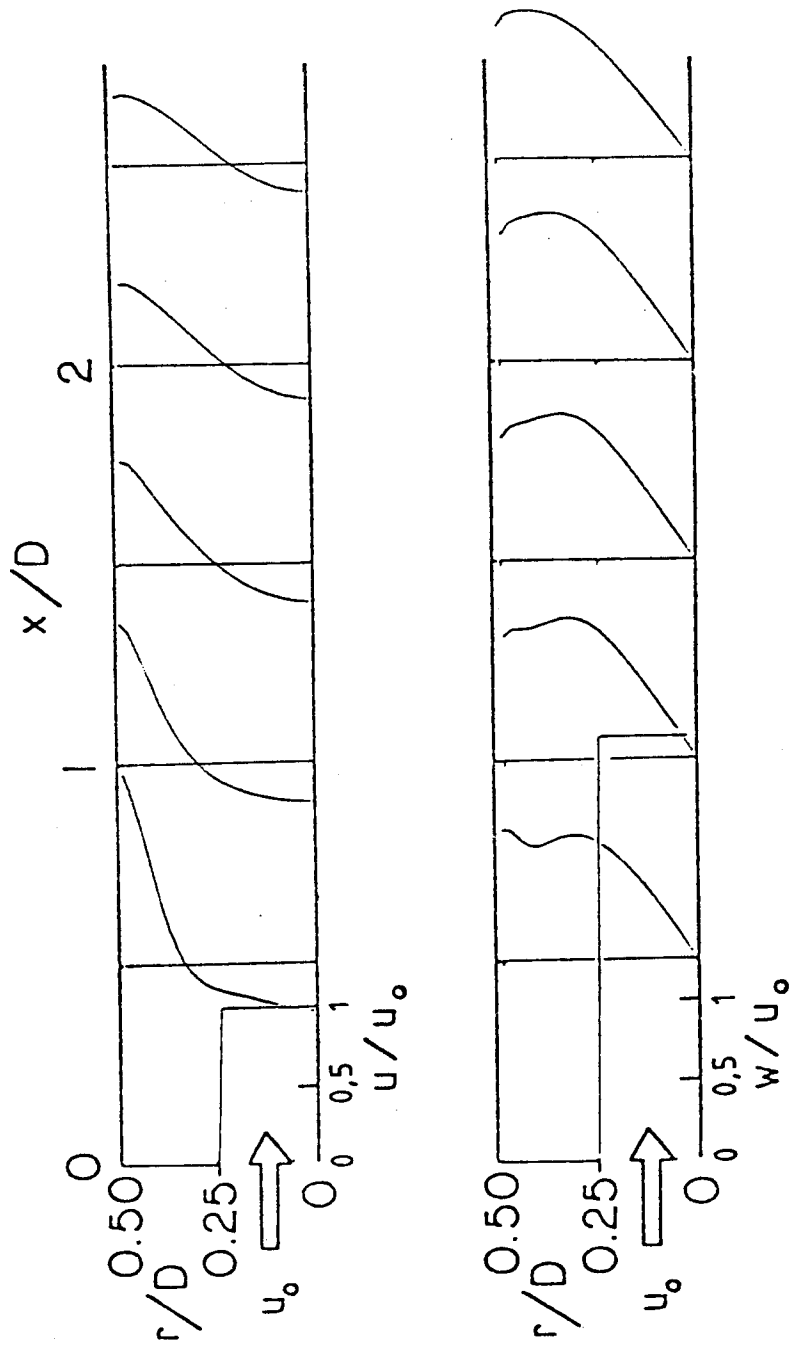


Figure 26. Predicted Velocity Profiles Using Flat Inlet Swirl and Axial Velocity Profiles



(b) $\phi = 70$ deg.

Figure 26 (Continued)

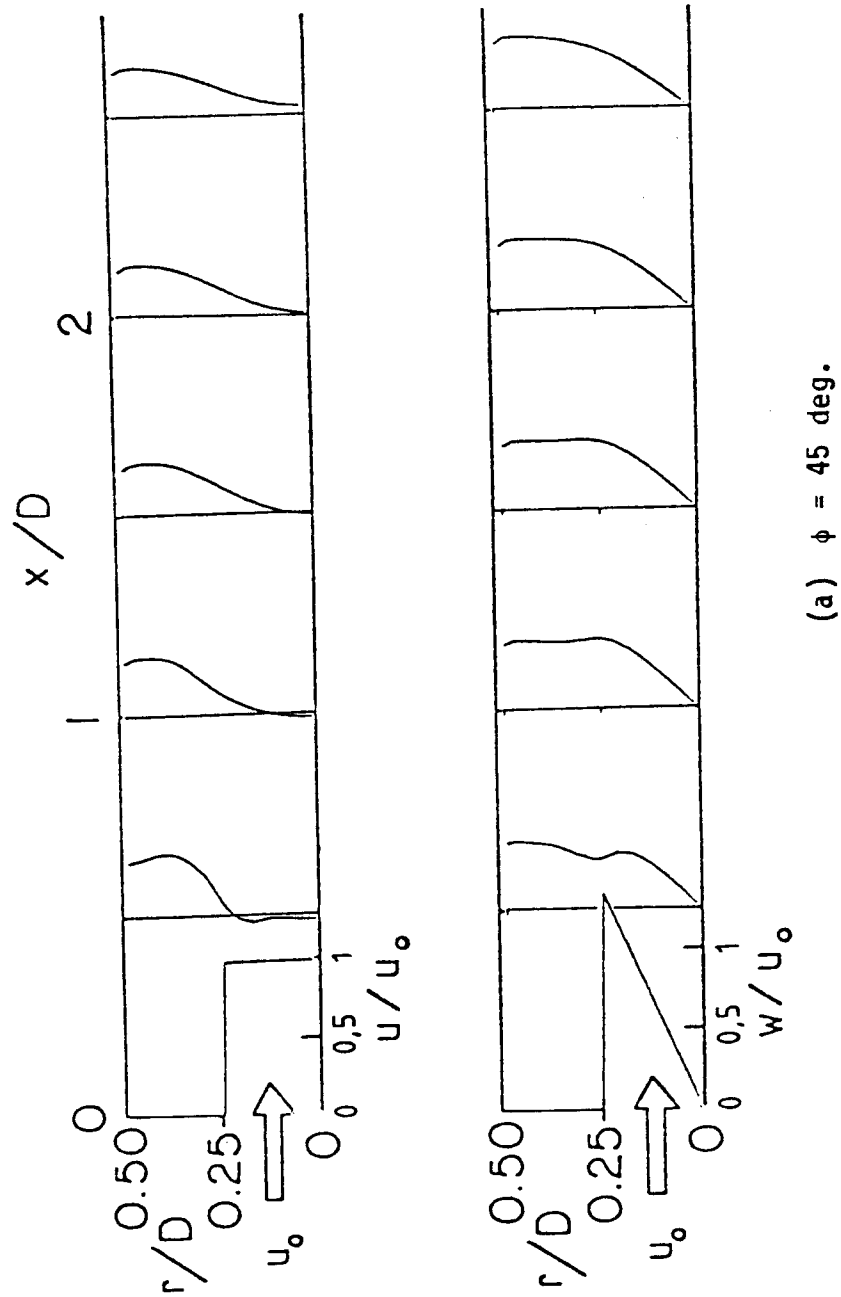
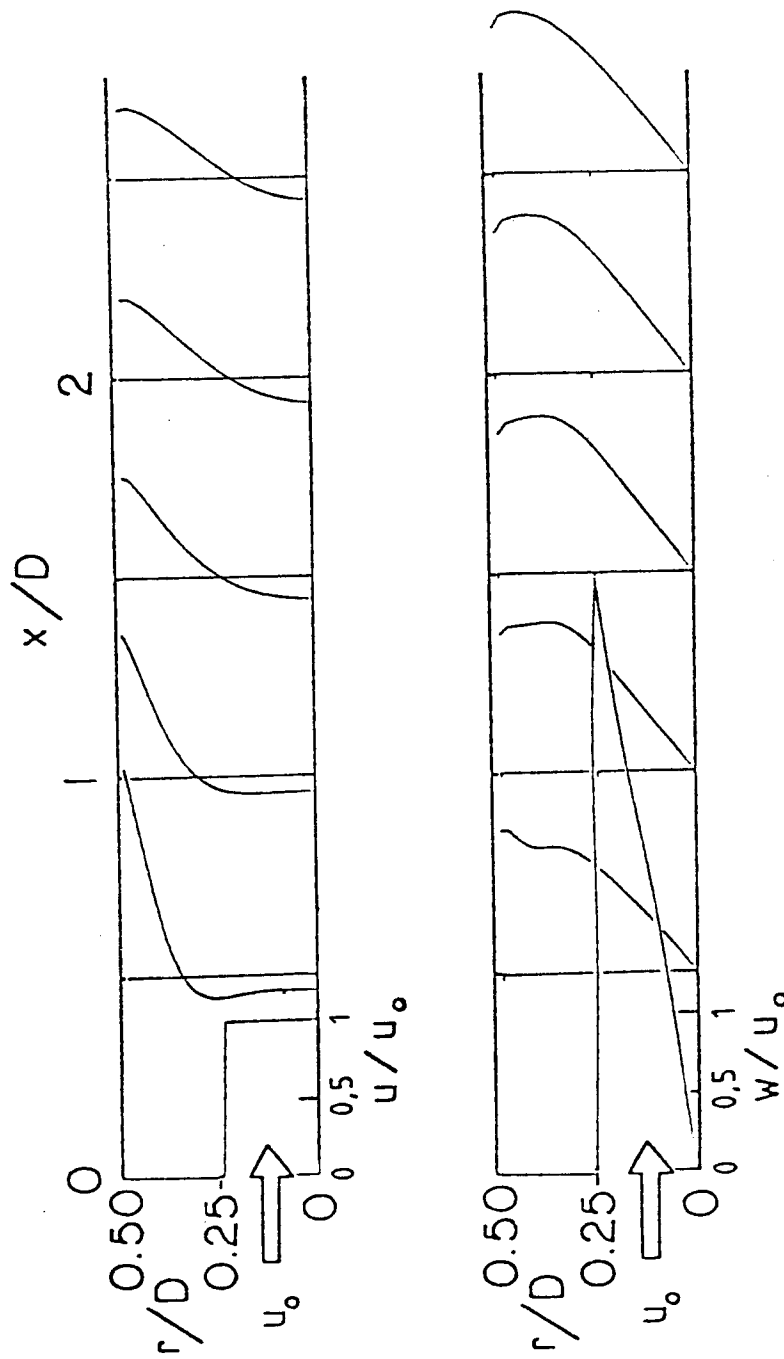


Figure 27. Predicted Velocity Profiles Using Flat Inlet Axial and Solid Body Rotation Swirl Velocity Profiles



(b) $\phi = 70$ deg.

Figure 27 (Continued)

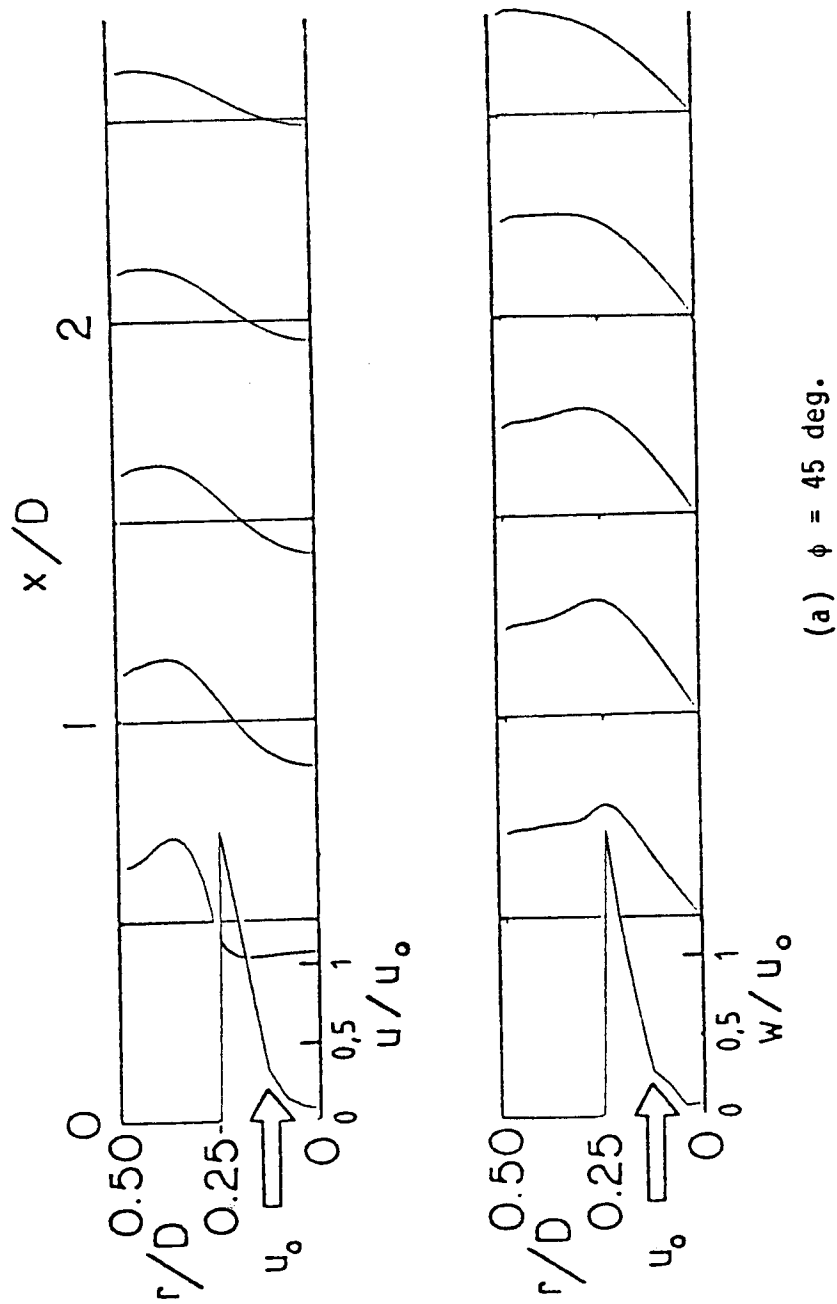
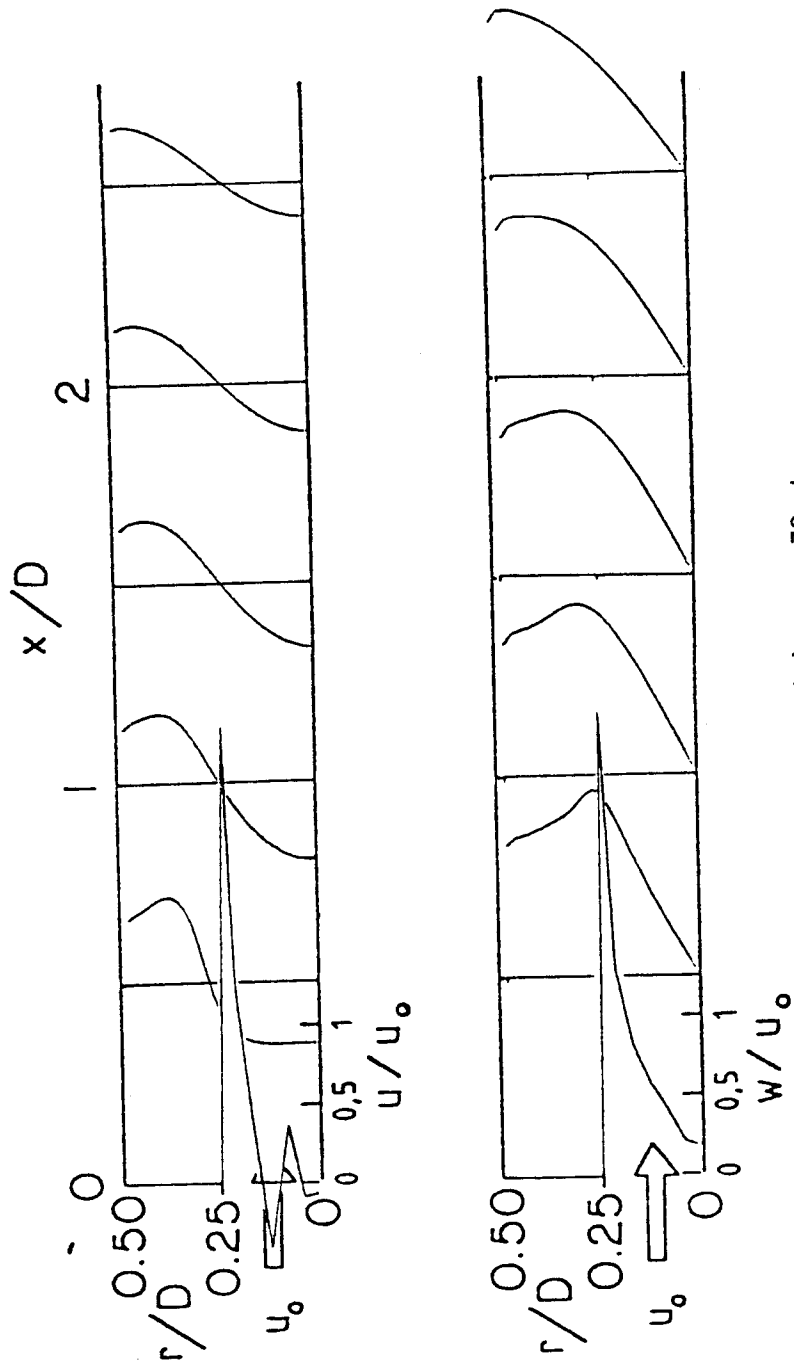


Figure 28. Predicted Velocity Profiles Using Measured Inlet Axial and Swirl Velocity Profiles



(b) $\phi = 70$ deg.

Figure 28 (Continued)

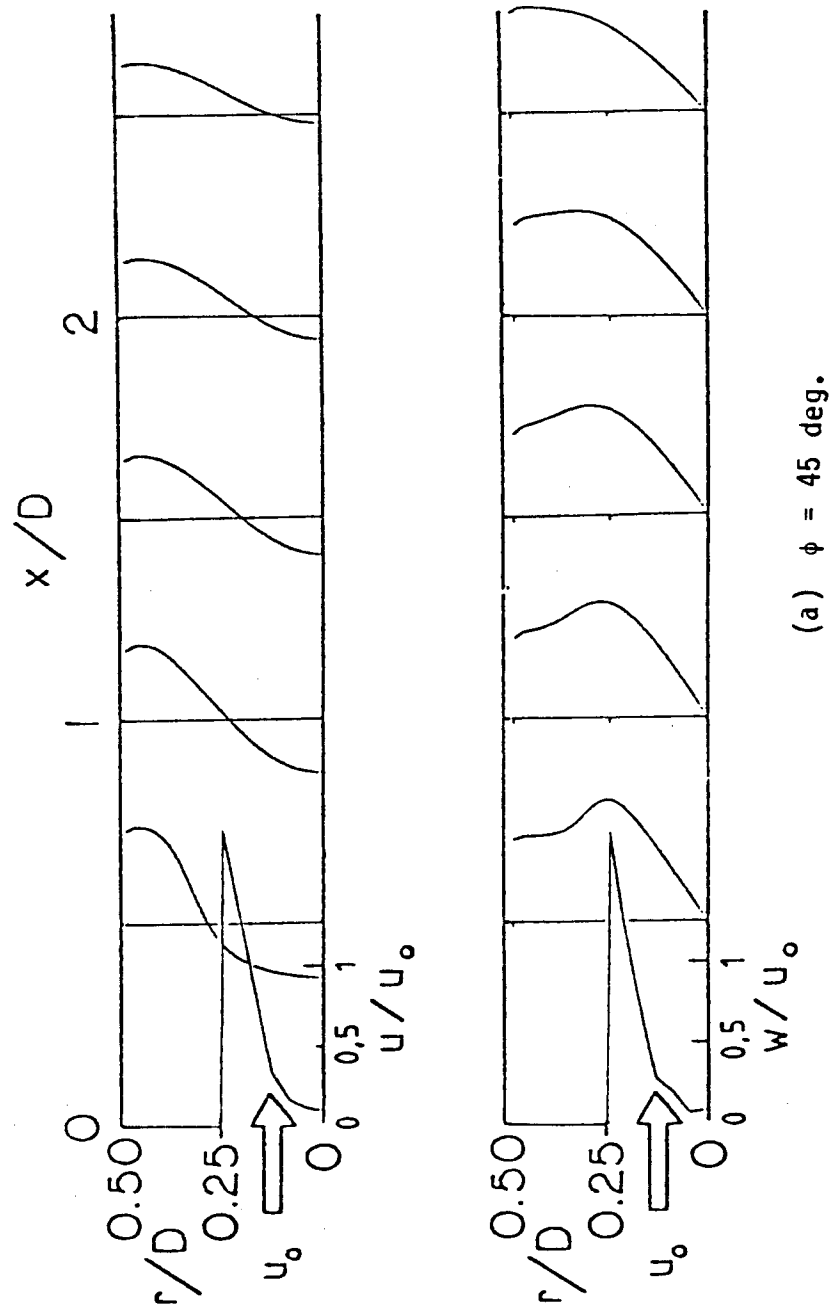
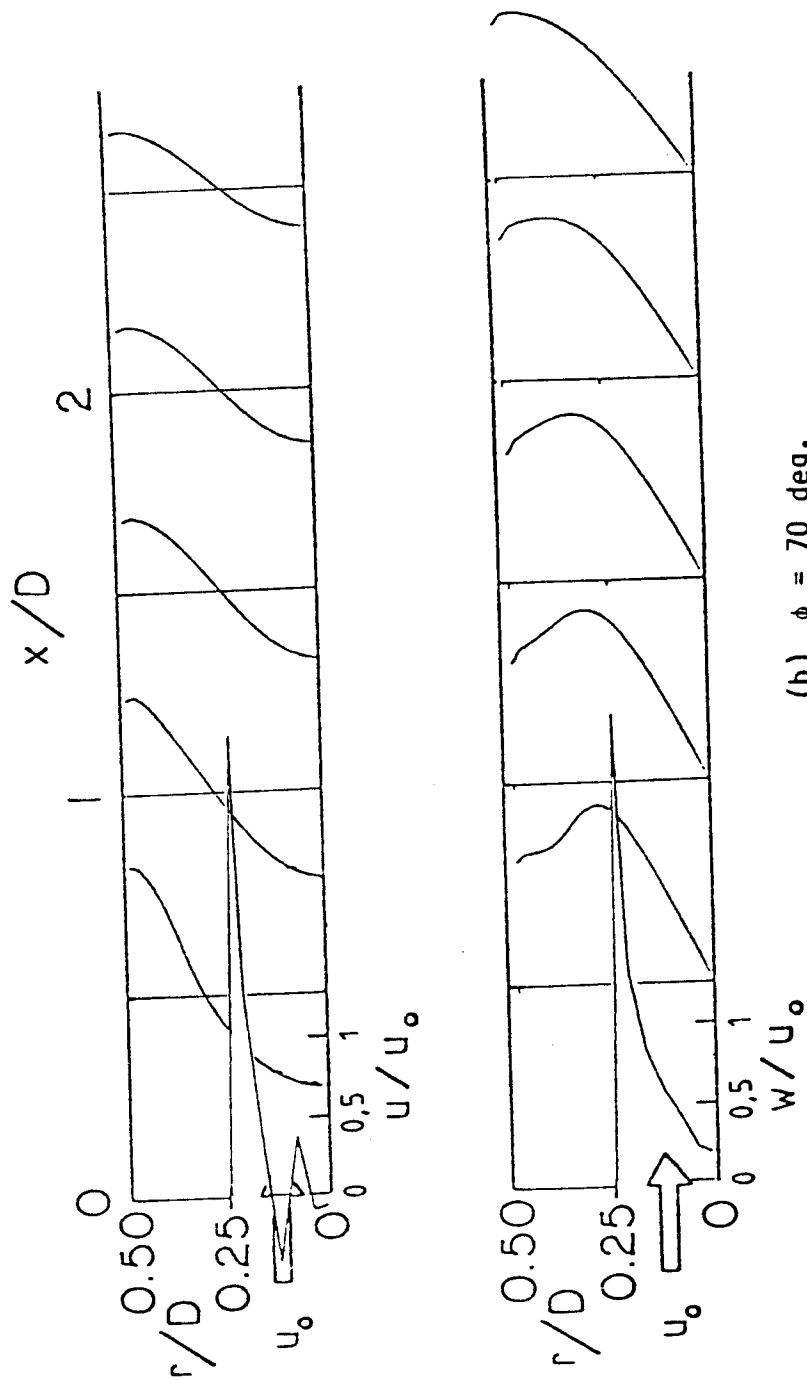
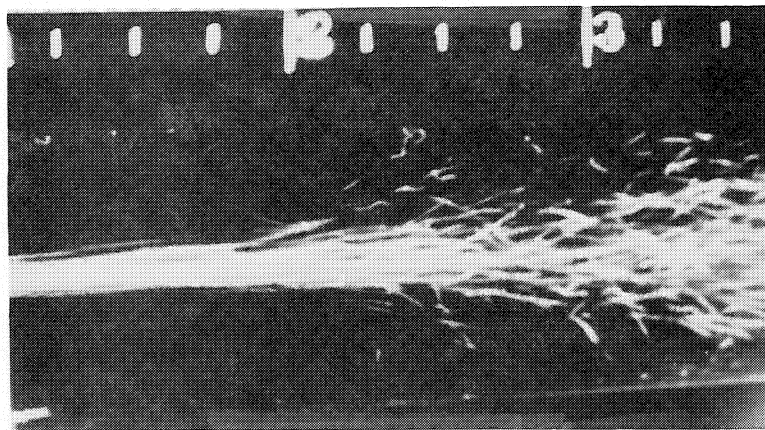


Figure 29. Predicted Velocity Profiles Using Measured Inlet Axial, Radial and Swirl Velocity Profiles

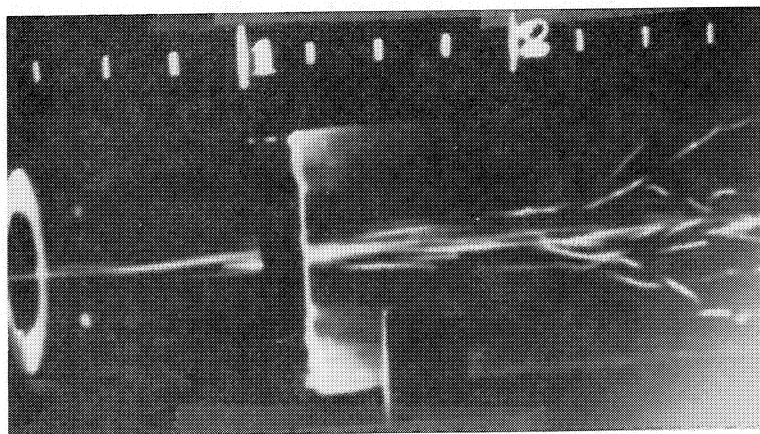


(b) $\phi = 70$ deg.

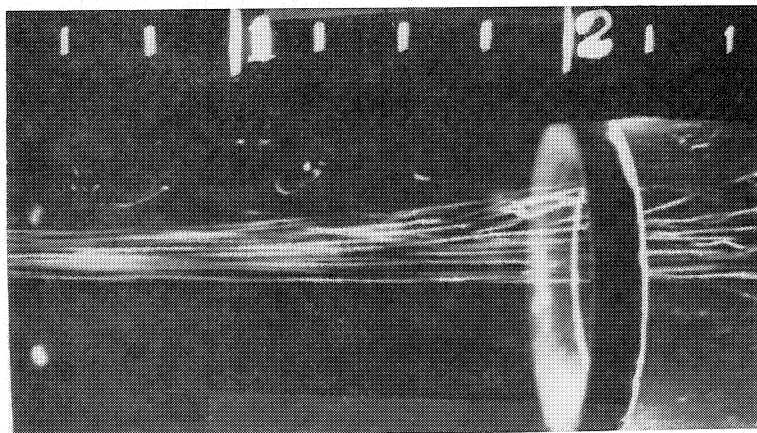
Figure 29 (Continued)



without nozzle



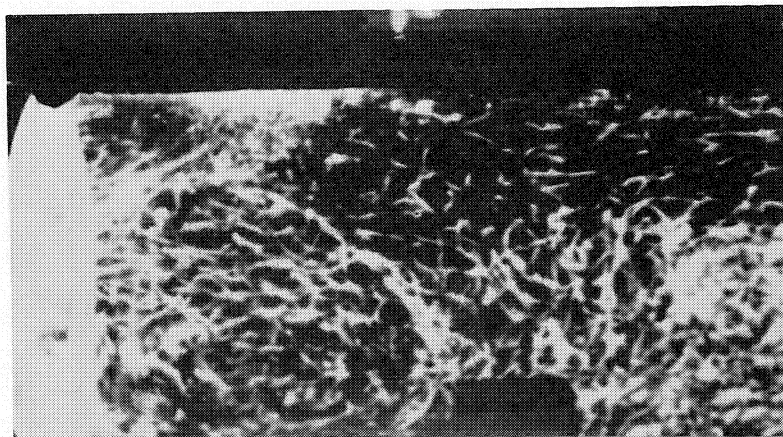
$L/D = 1$



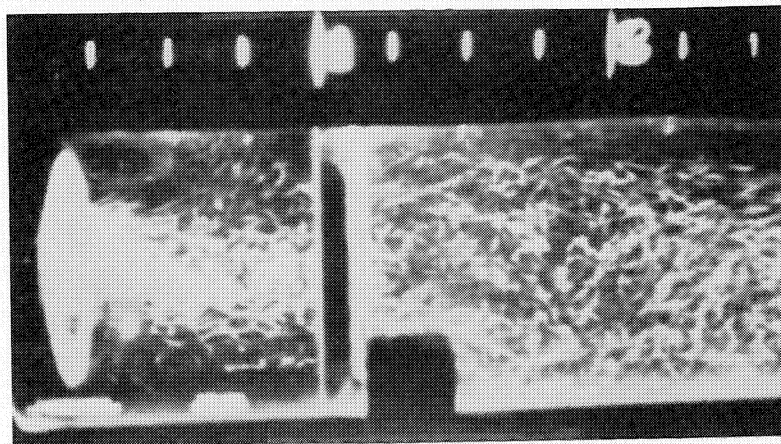
$L/D = 2$

(a) $\phi = 0$ deg.

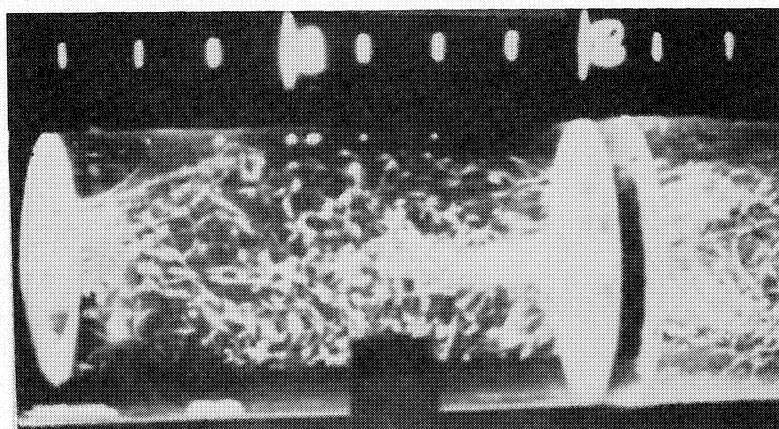
Figure 30. Flow Visualization of Flowfield with $D/d = 2$, With and Without Weak Nozzle



without nozzle



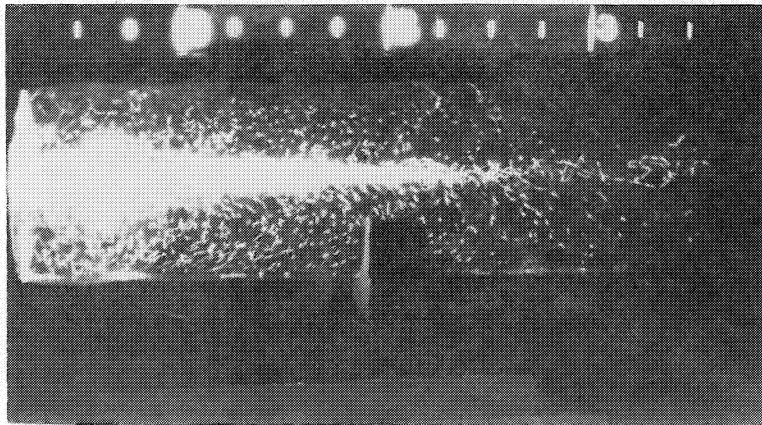
$L/D = 1$



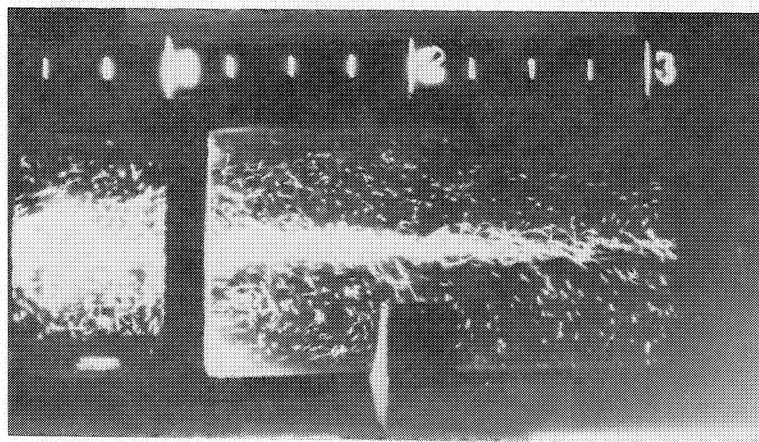
$L/D = 2$

(b) $\phi = 45$ deg.

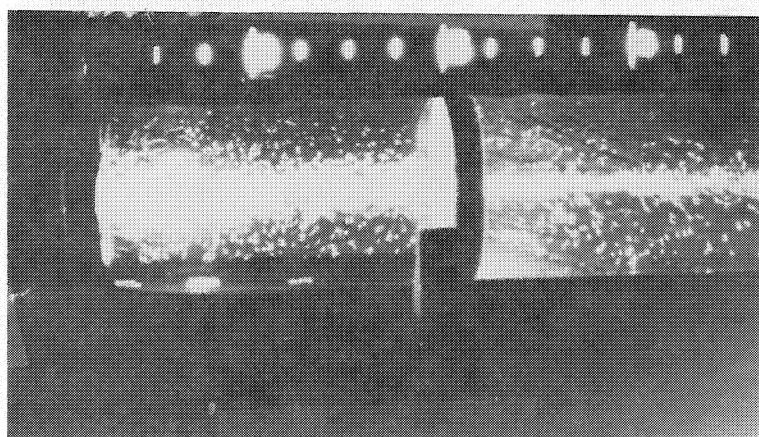
Figure 30 (Continued)



without nozzle



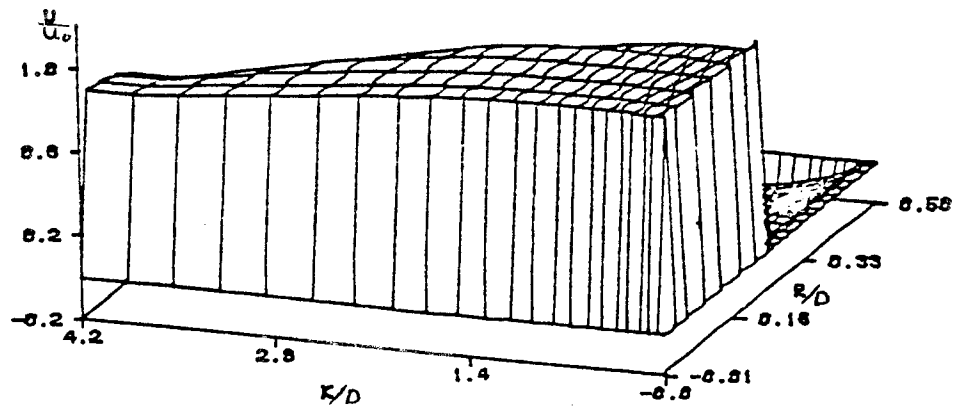
$L/D = 1$



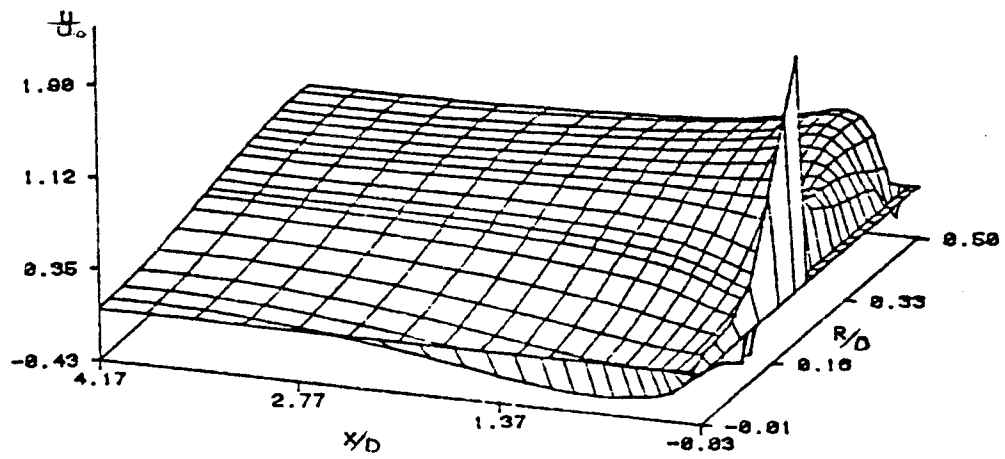
$L/D = 2$

(c) $\phi = 70$ deg.

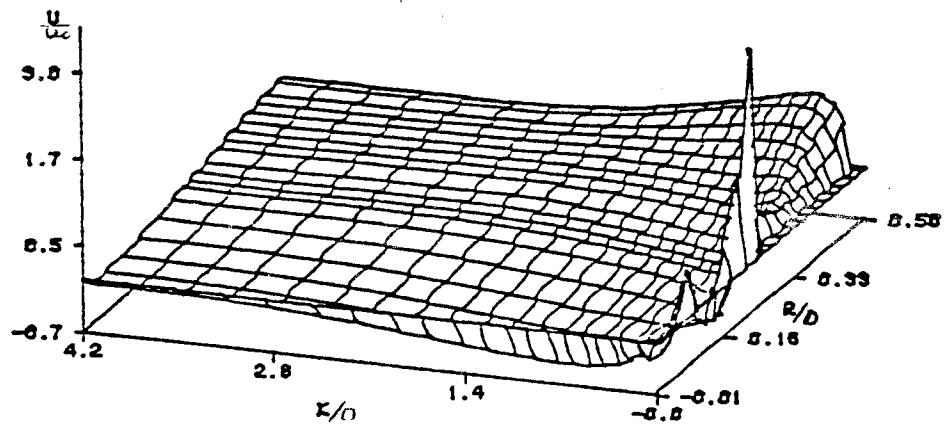
Figure 30 (Continued)



(a) $\phi = 0^\circ$.



(b) $\phi = 45^\circ$.



(c) $\phi = 70^\circ$.

Figure 31. Three-Dimensional Representation of Axial Velocity

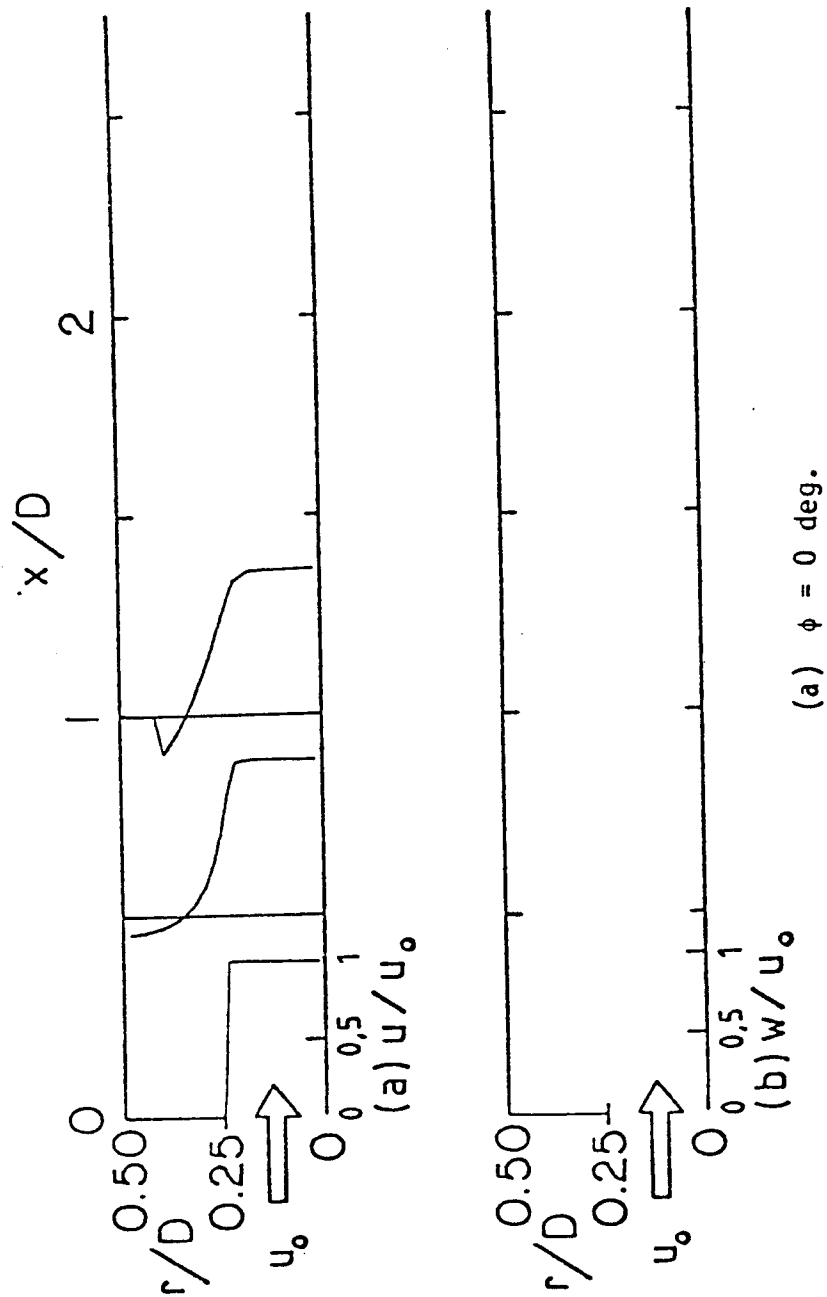
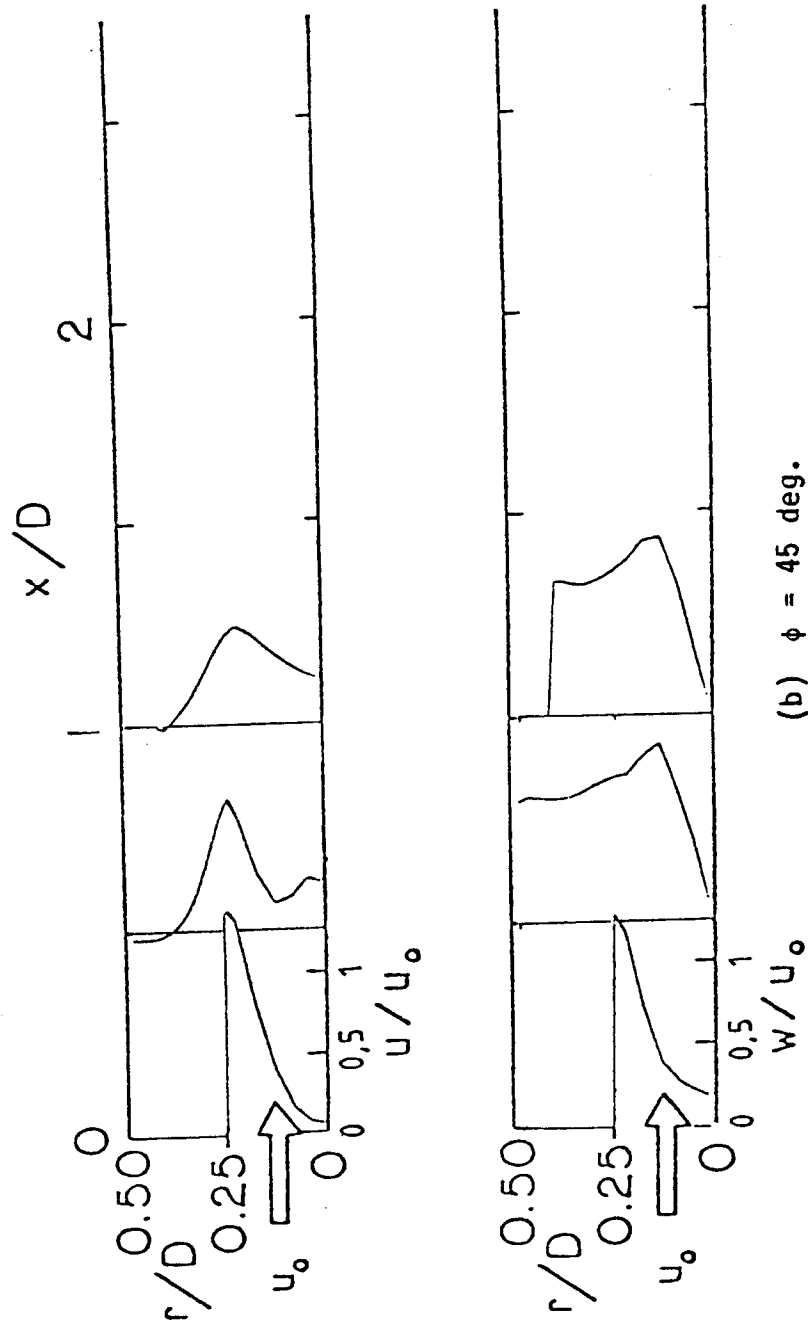
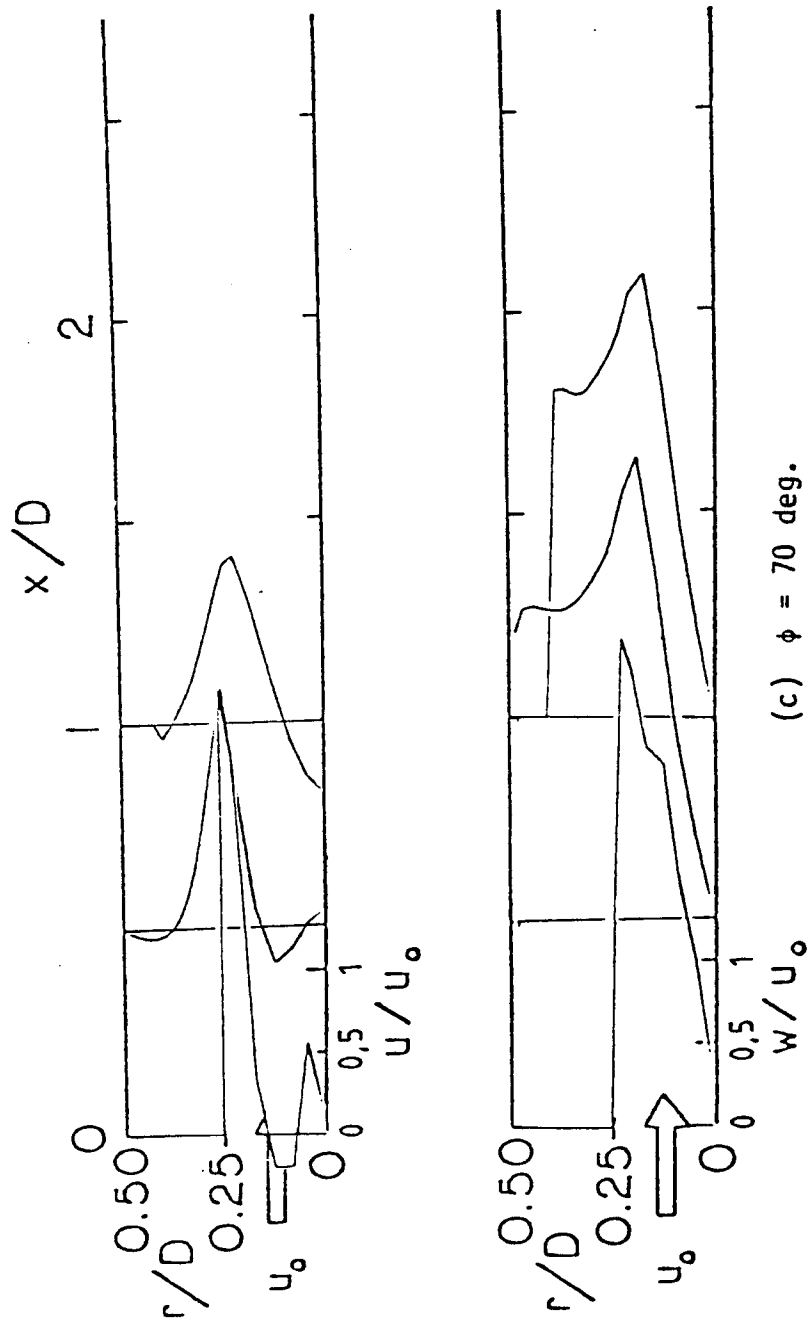


Figure 32. Predicted Velocity Profiles for Flowfield with $D/d = 2$ and Strong Nozzle at $L/D = 1$



(b) $\phi = 45$ deg.

Figure 32 (Continued)



(c) $\phi = 70$ deg.

Figure 32 (Continued)

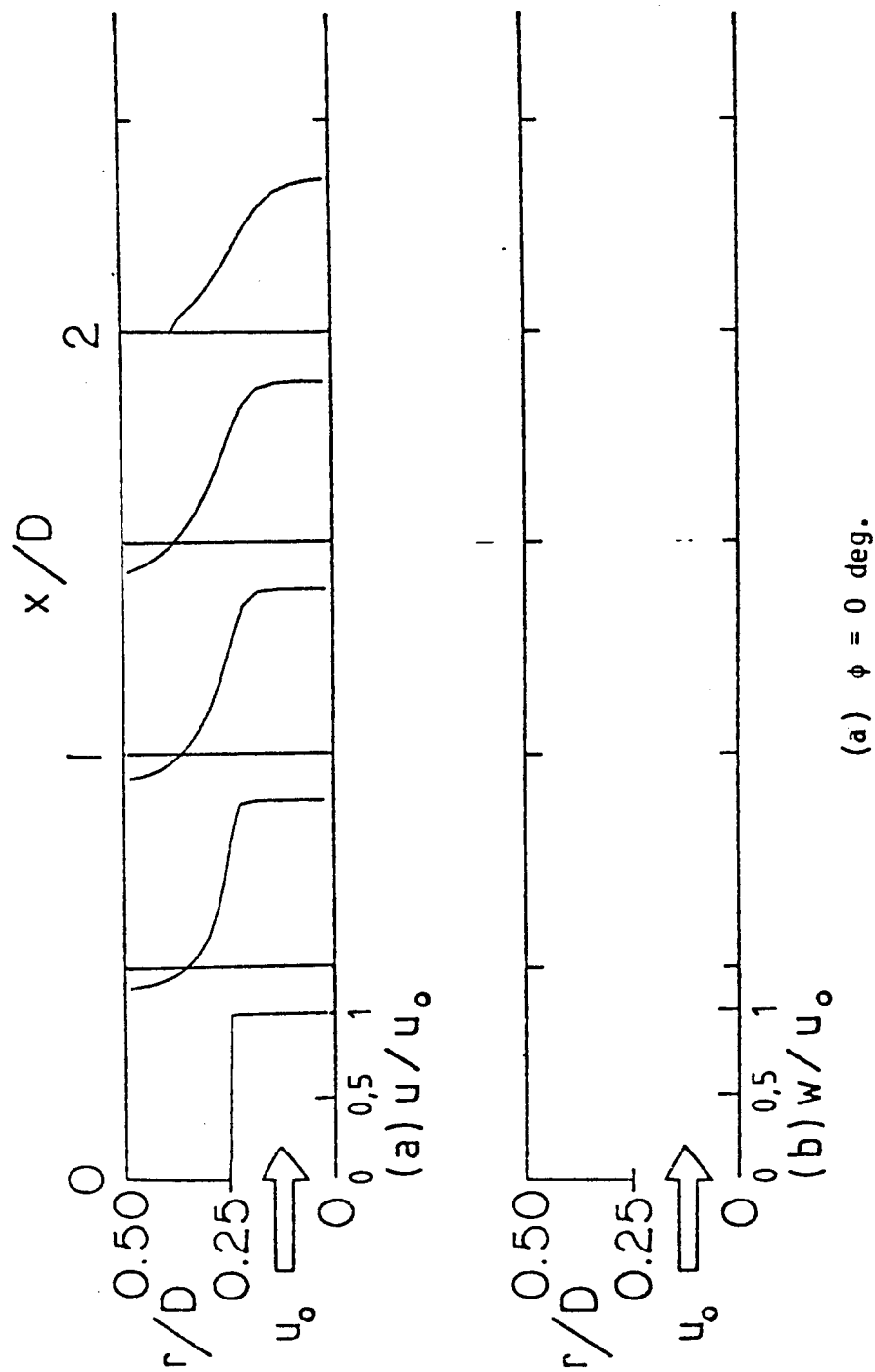
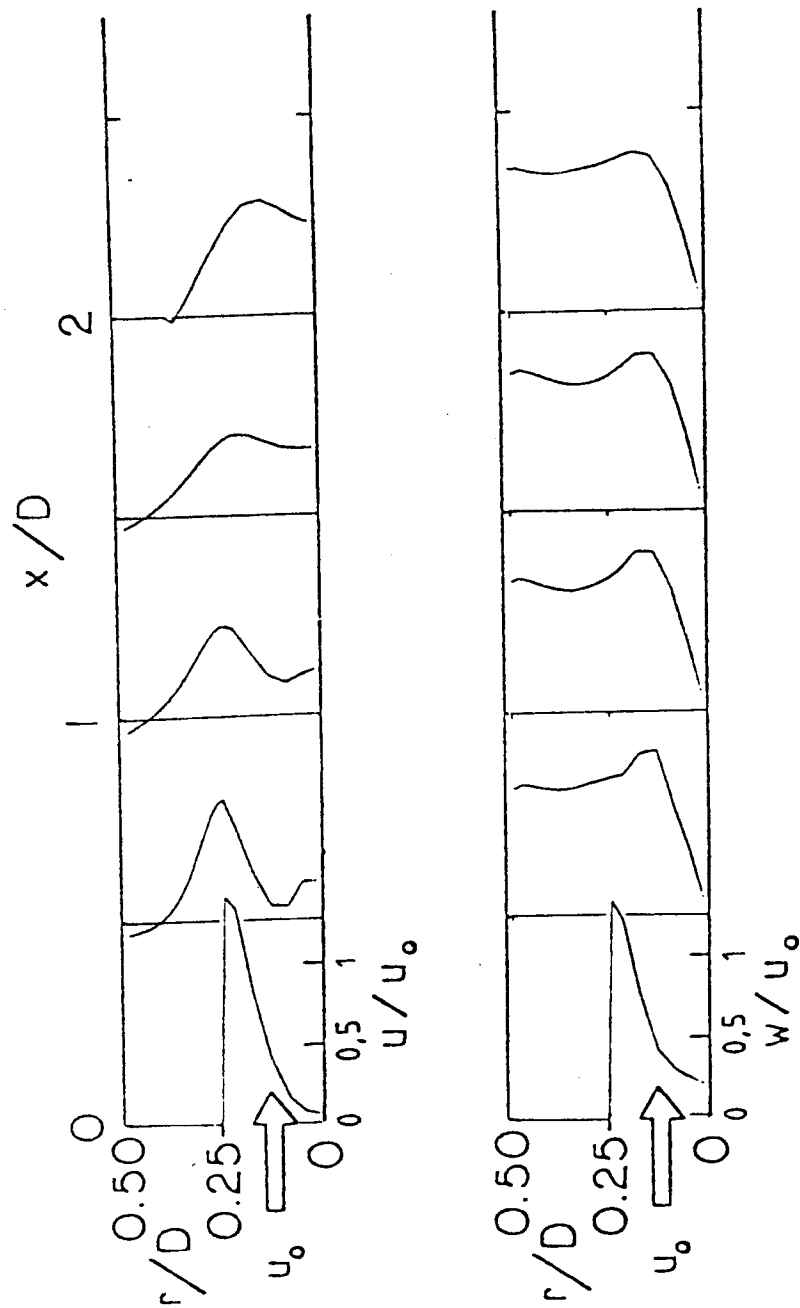
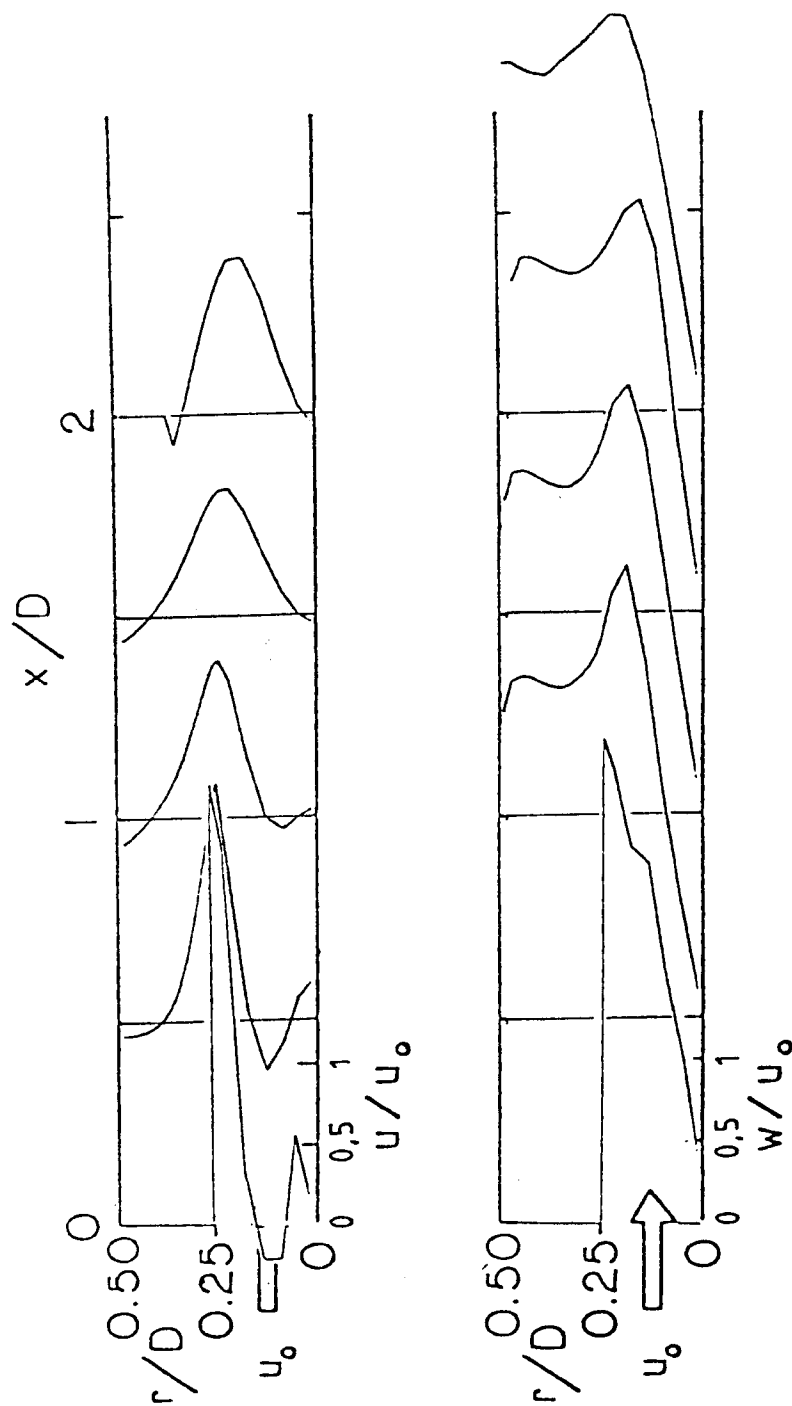


Figure 33. Predicted Velocity Profiles for Flowfield with $D/d = 2$ and Strong Nozzle at $L/D = 2$



(b) $\phi = 45^\circ$.

Figure 33 (Continued)



(c) $\phi = 70$ deg.

Figure 33 (Continued)

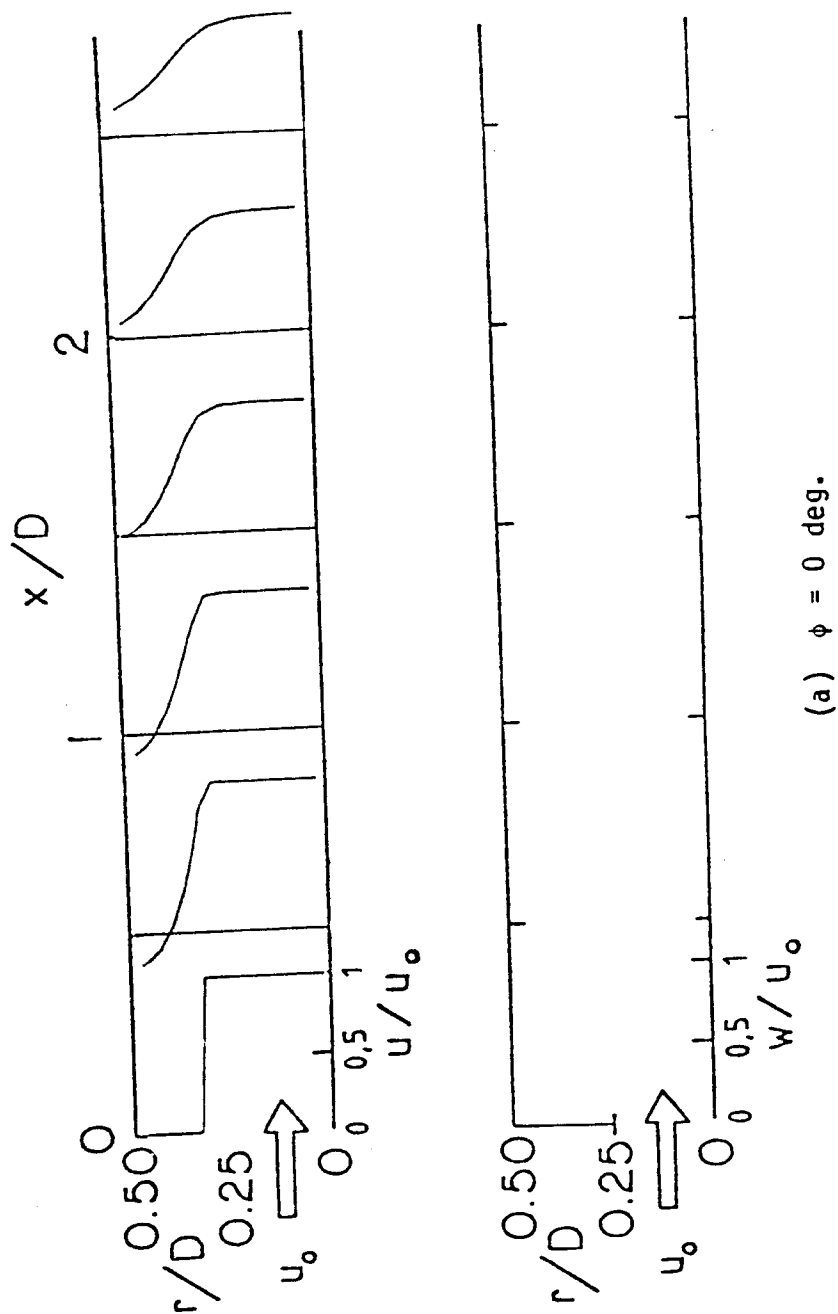
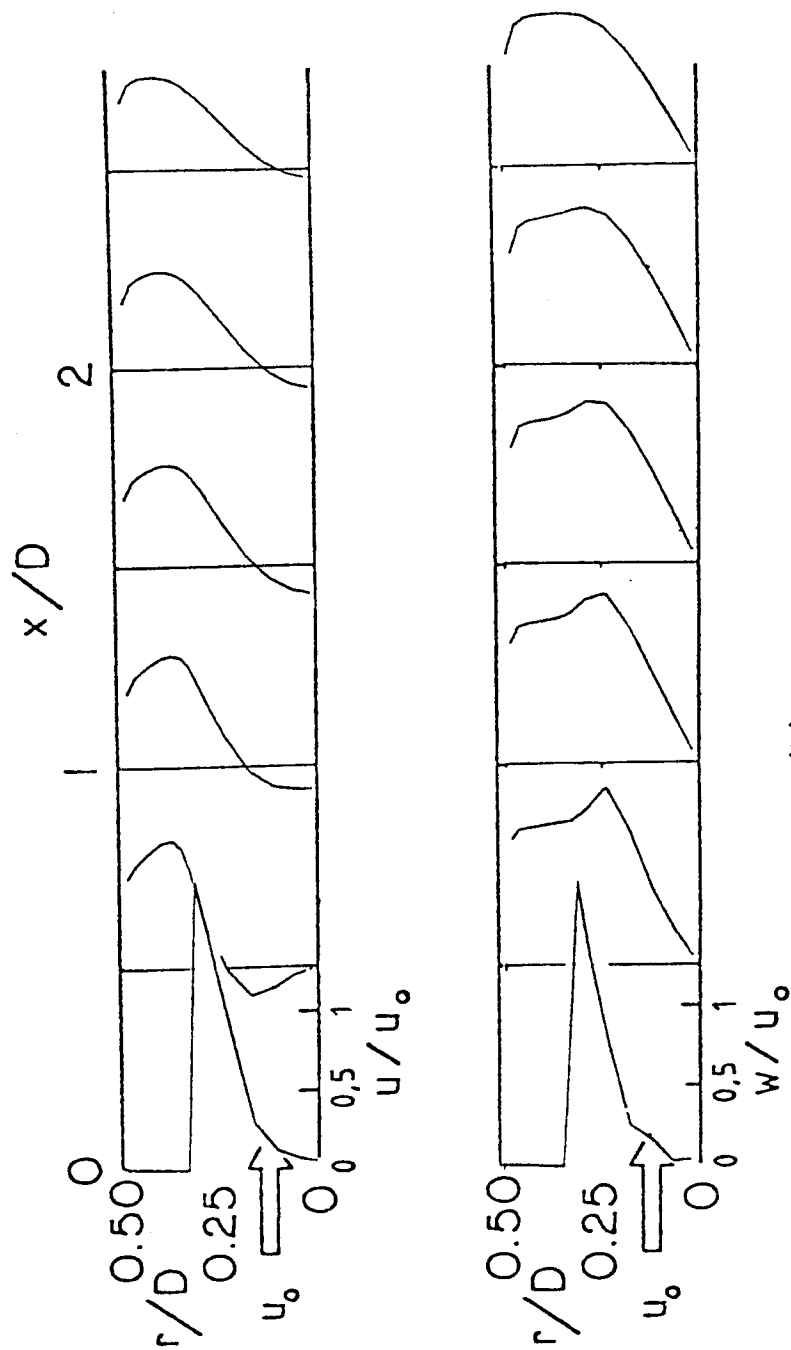
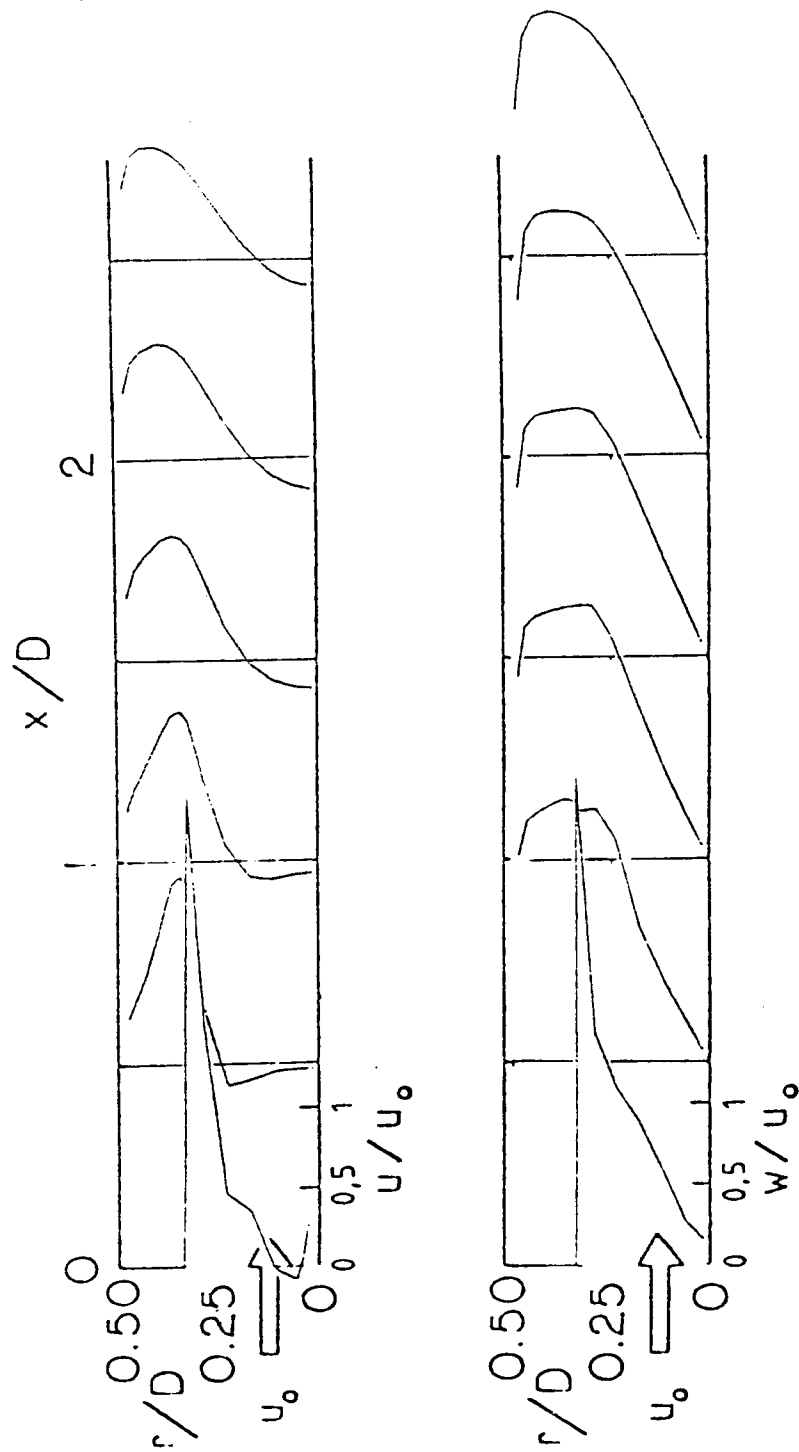


Figure 34. Predicted Velocity Profiles for Flowfield with $D/d = 1.5$



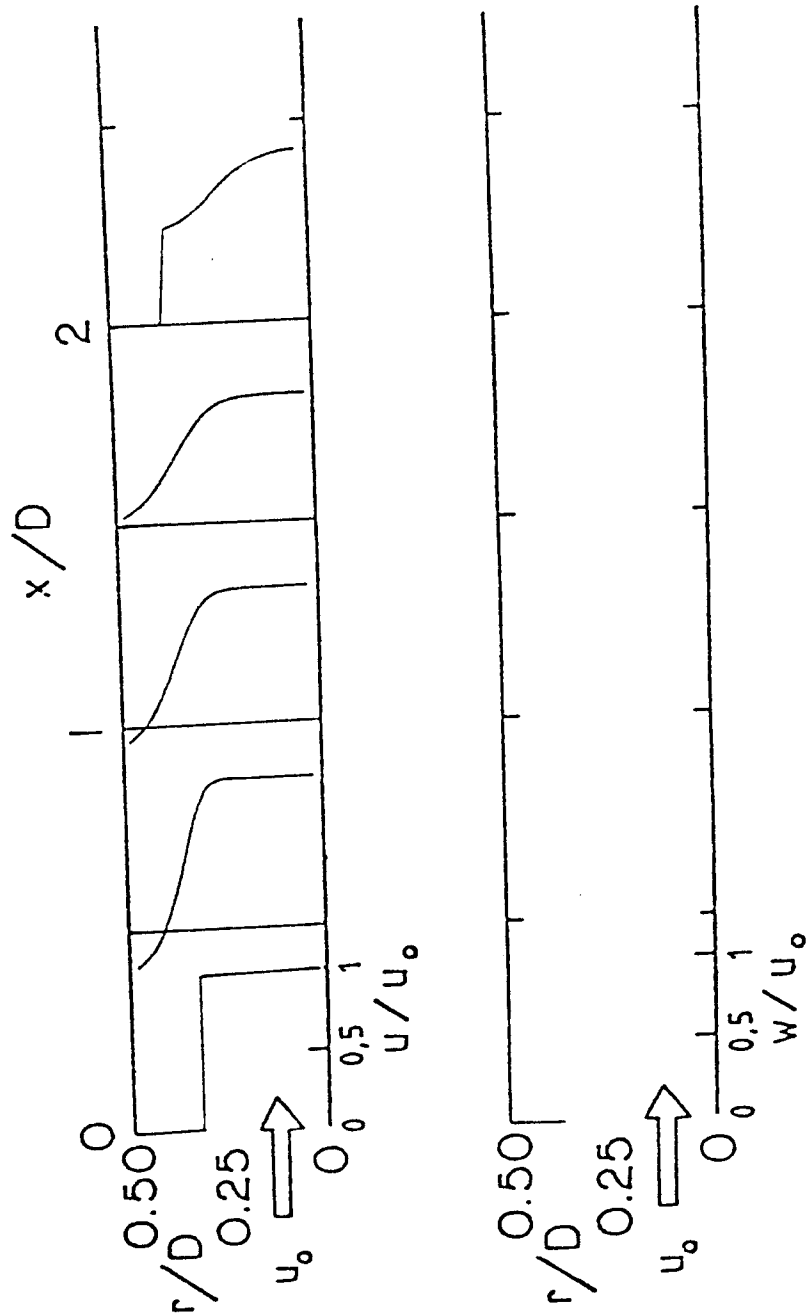
(b) $\phi = 45^\circ$.

Figure 34 (Continued)



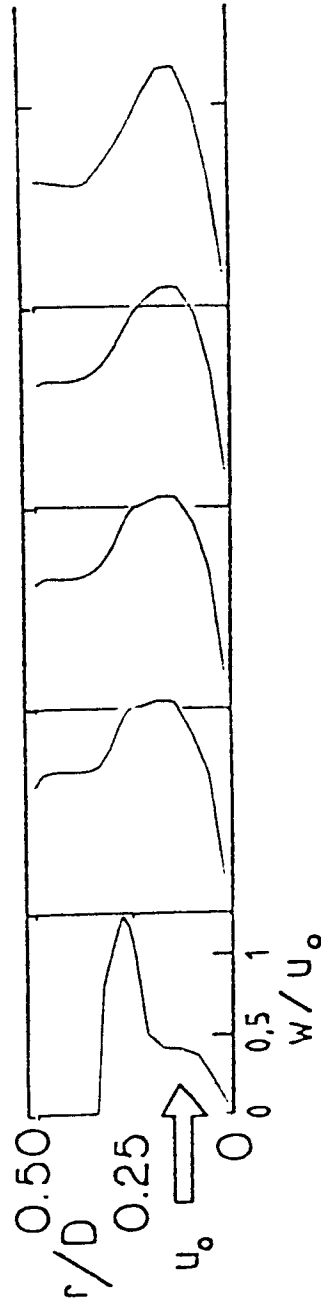
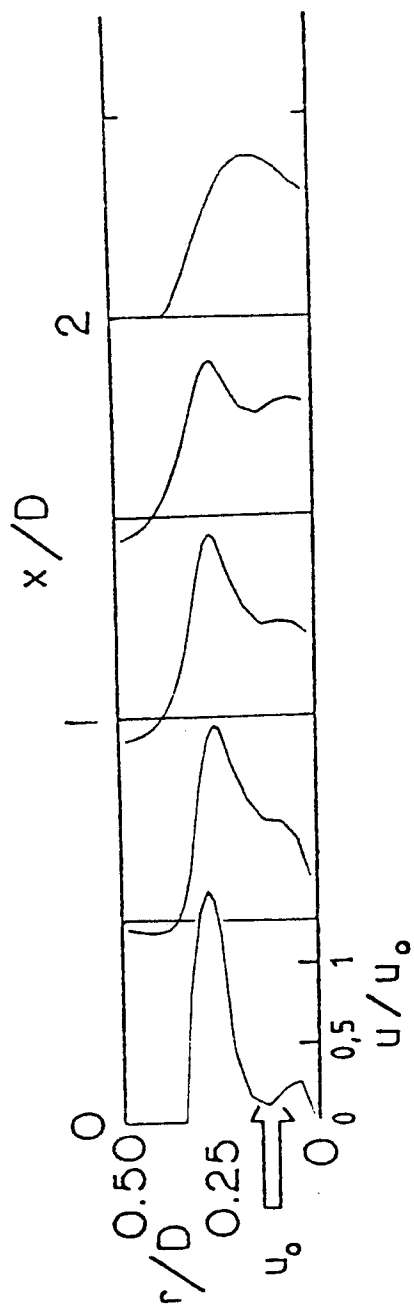
(c) $\phi = 70$ deg.

Figure 34 (Continued)



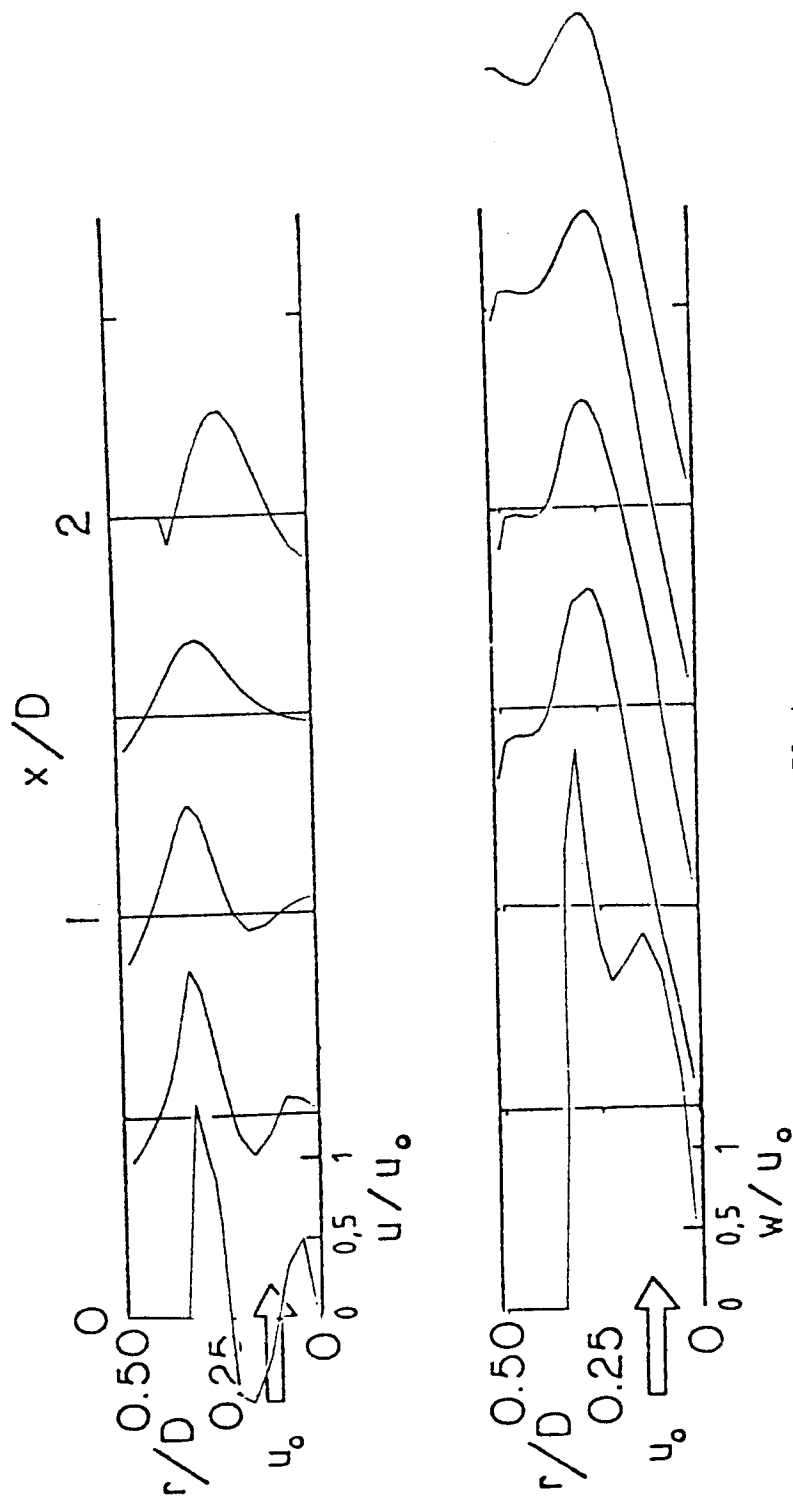
(a) $\phi = 0$ deg.

Figure 35. Predicted Velocity Profiles for Flowfield with $D/d = 1.5$ and Strong Nozzle at $L/D = 2$



(b) $\phi = 45 \text{ deg.}$

Figure 35 (Continued)



(c) $\phi = 70$ deg.

Figure 35 (Continued)

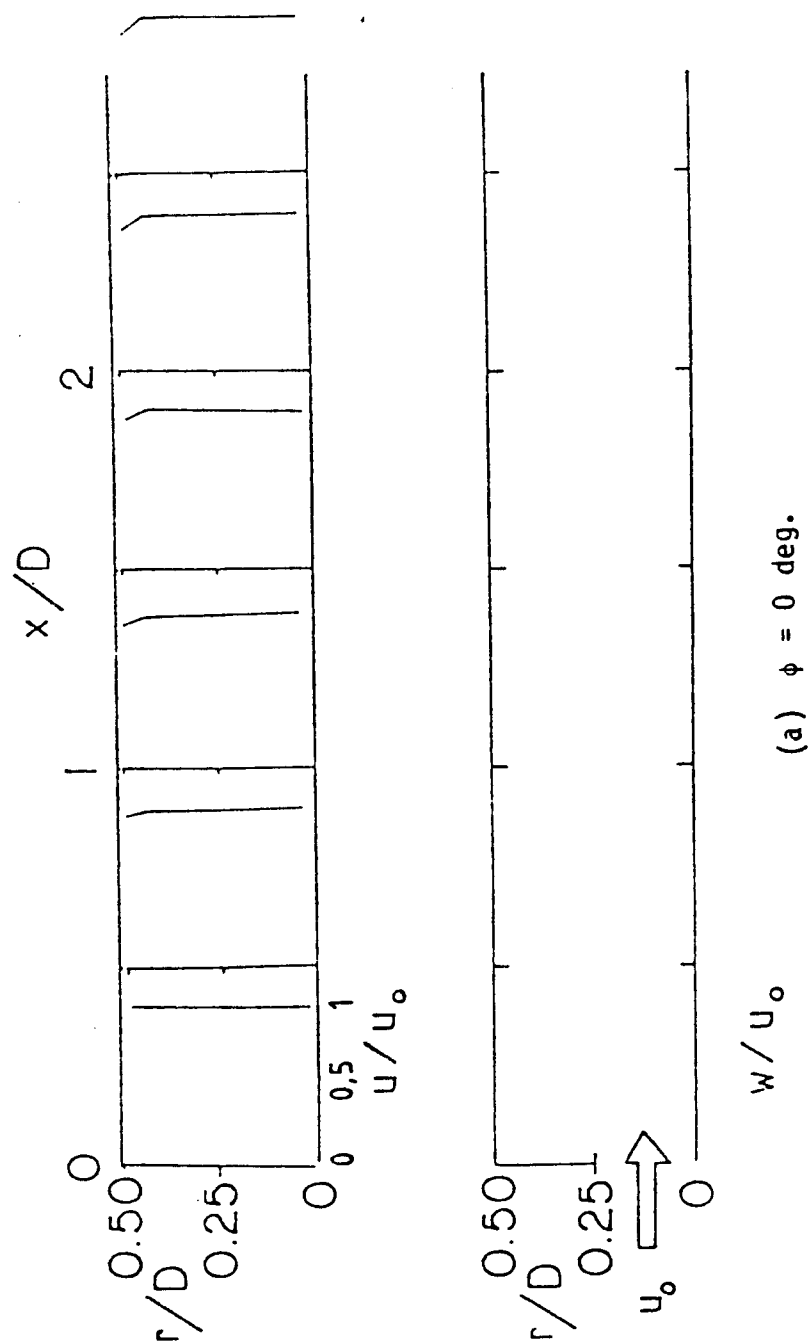
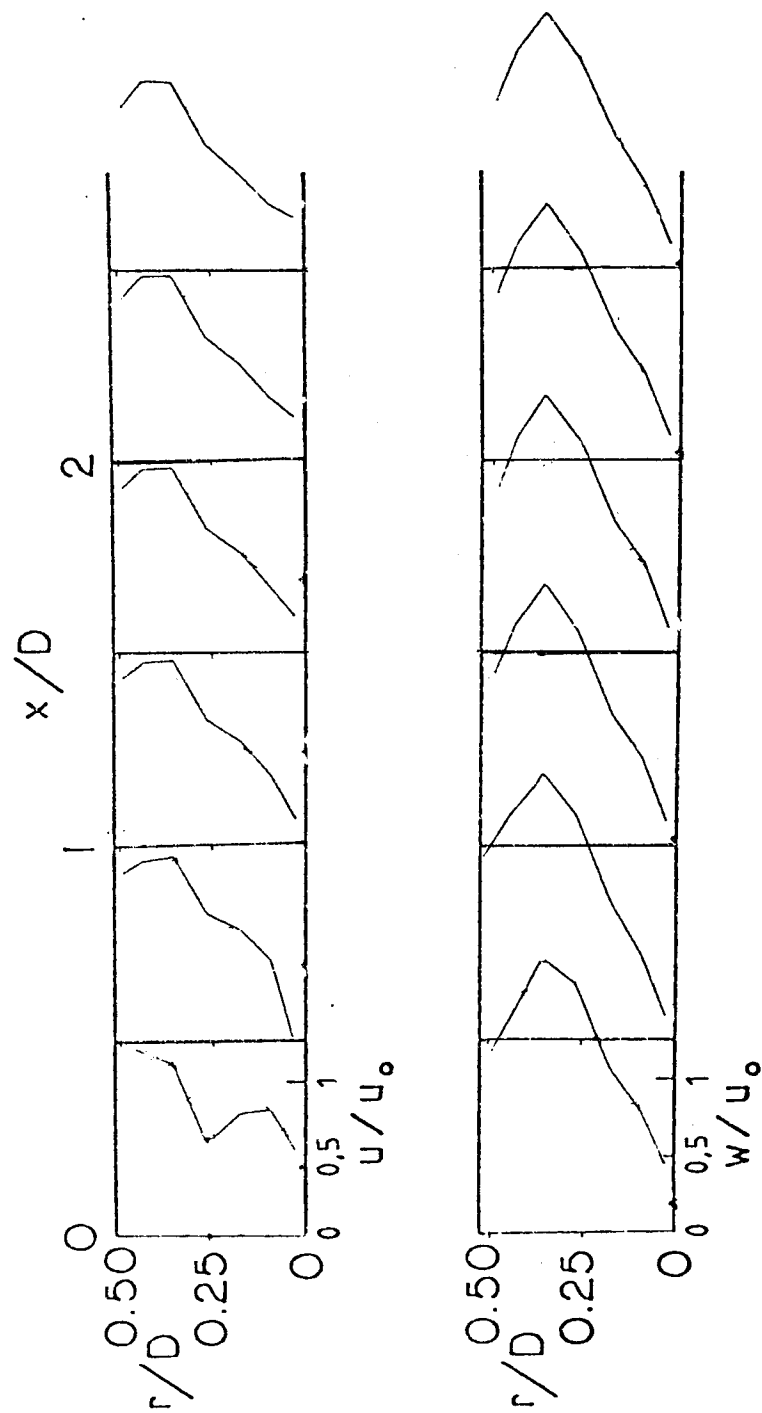
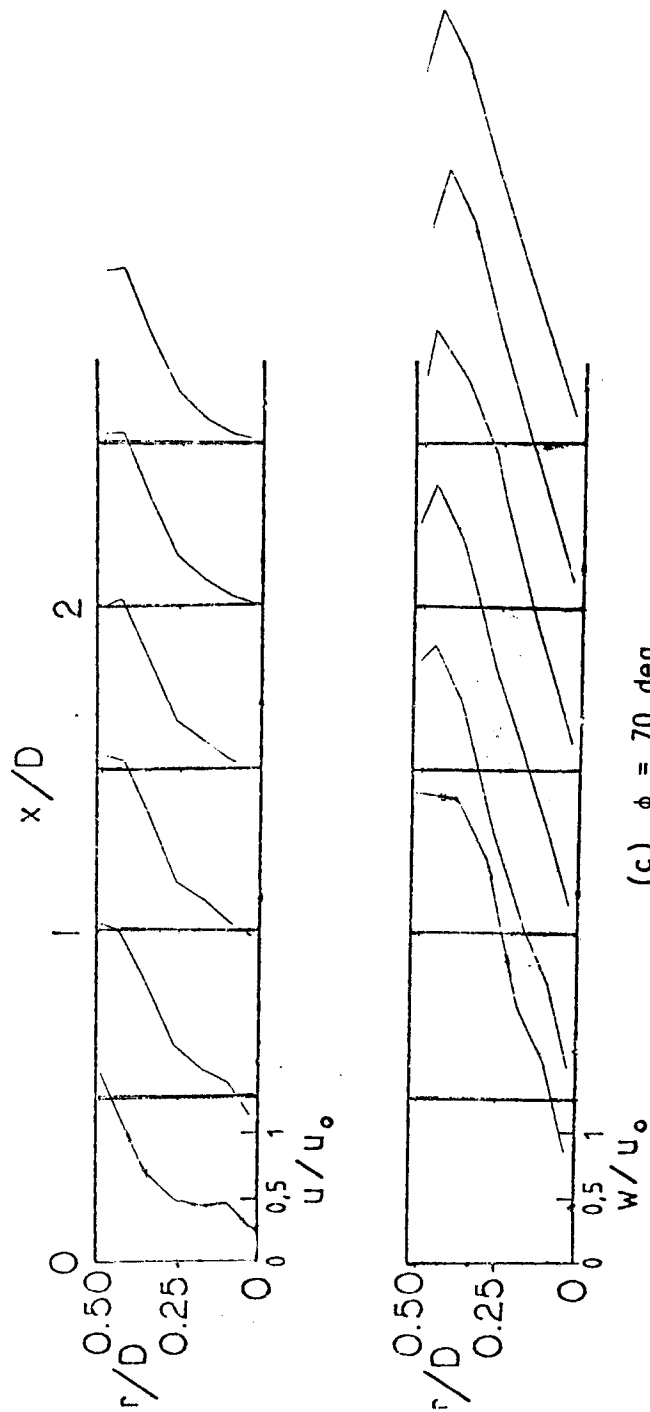


Figure 36. Predicted Velocity Profiles for Flowfield with $D/d = 1$



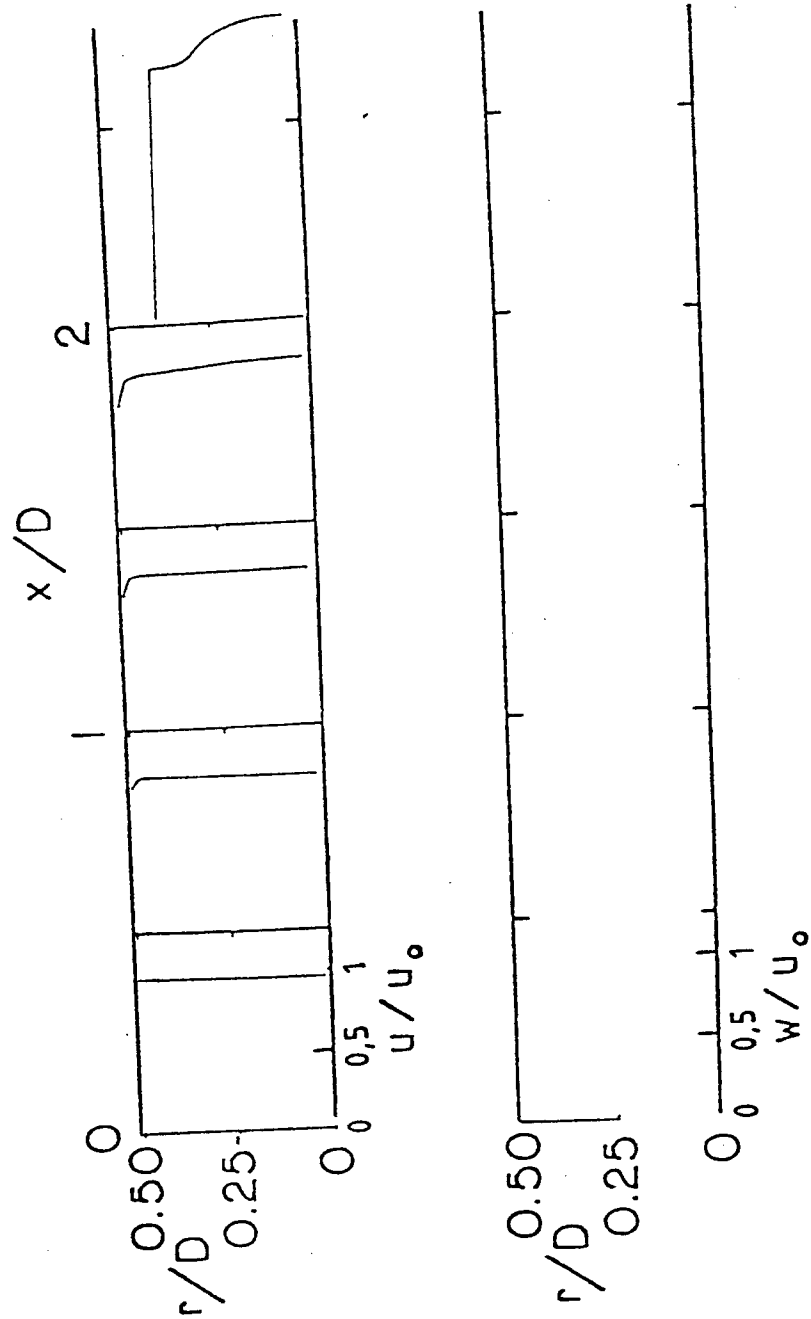
(b) $\phi = 45$ deg.

Figure 36 (Continued)



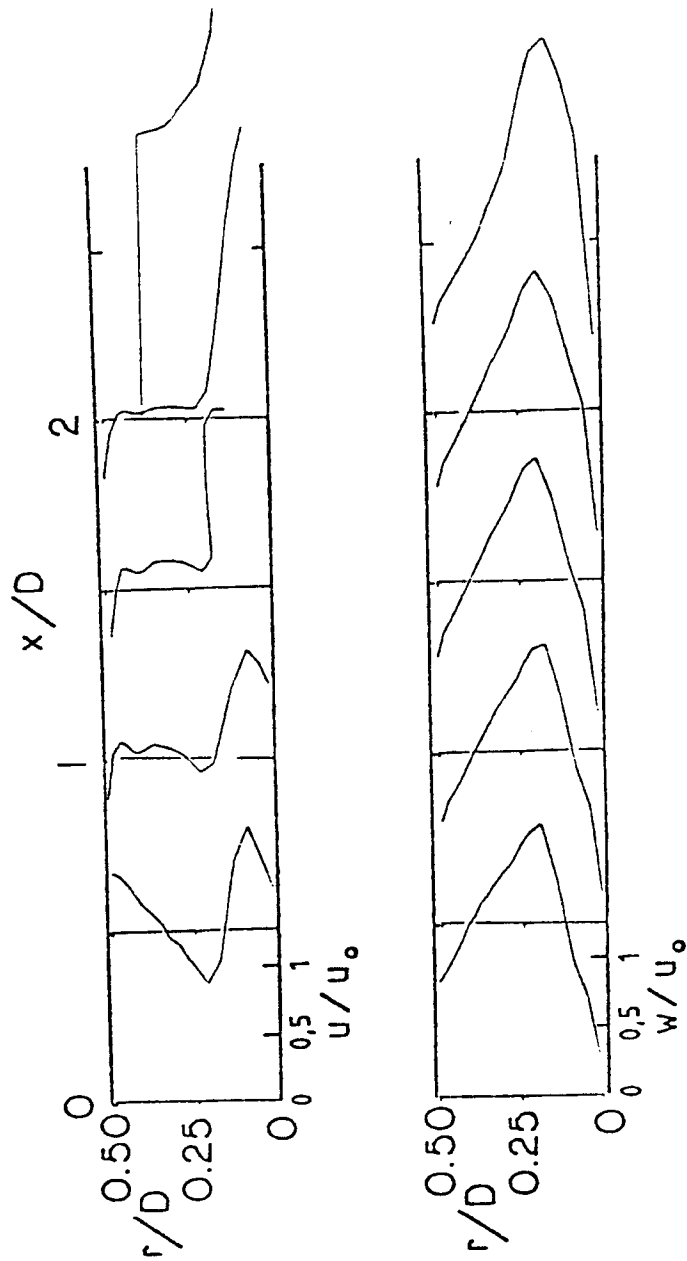
(c) $\phi = 70$ deg.

Figure 36 (Continued)



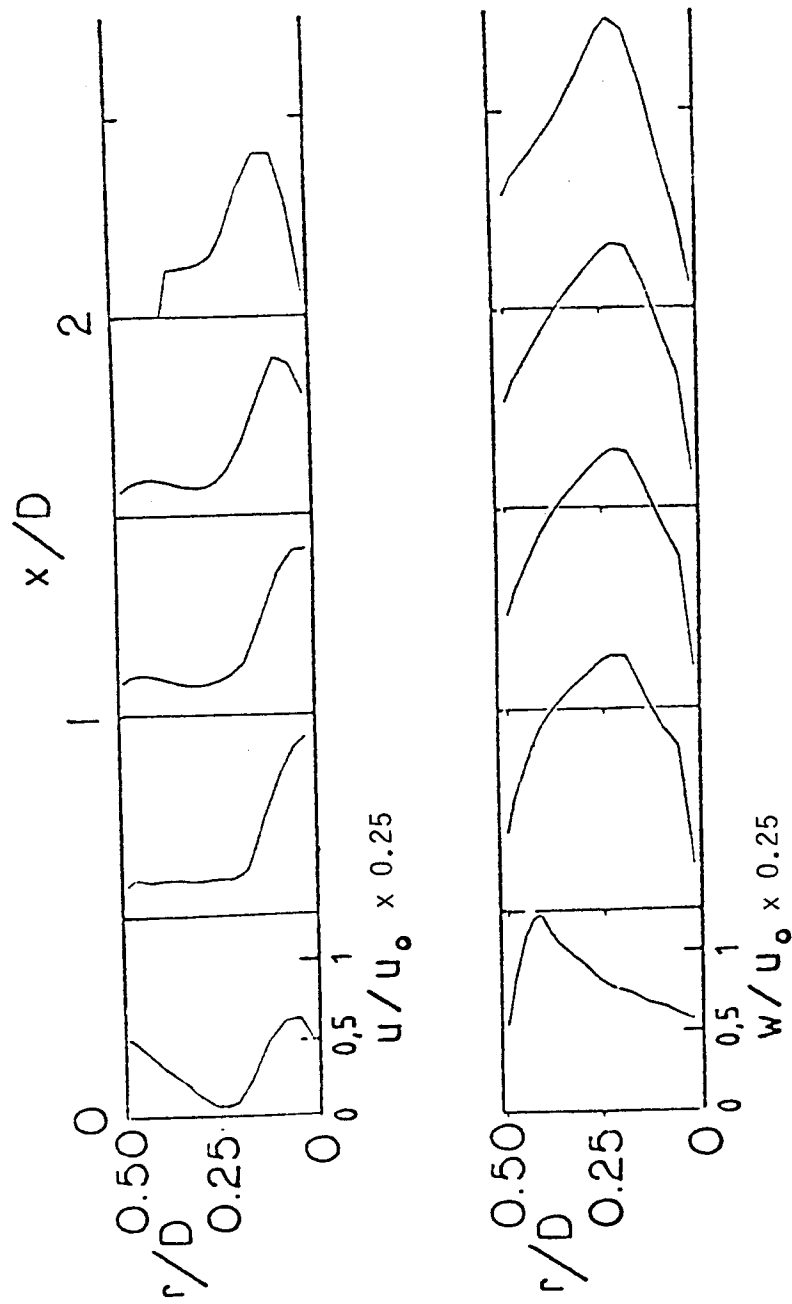
(a) $\phi = 0$ deg.

Figure 37. Predicted Velocity Profiles for Flowfield with $D/d = 1$ and Strong Nozzle at $L/D = 2$



(b) $\phi = 45$ deg.

Figure 37 (Continued)



(c) $\phi = 70$ deg.

Figure 37 (Continued)

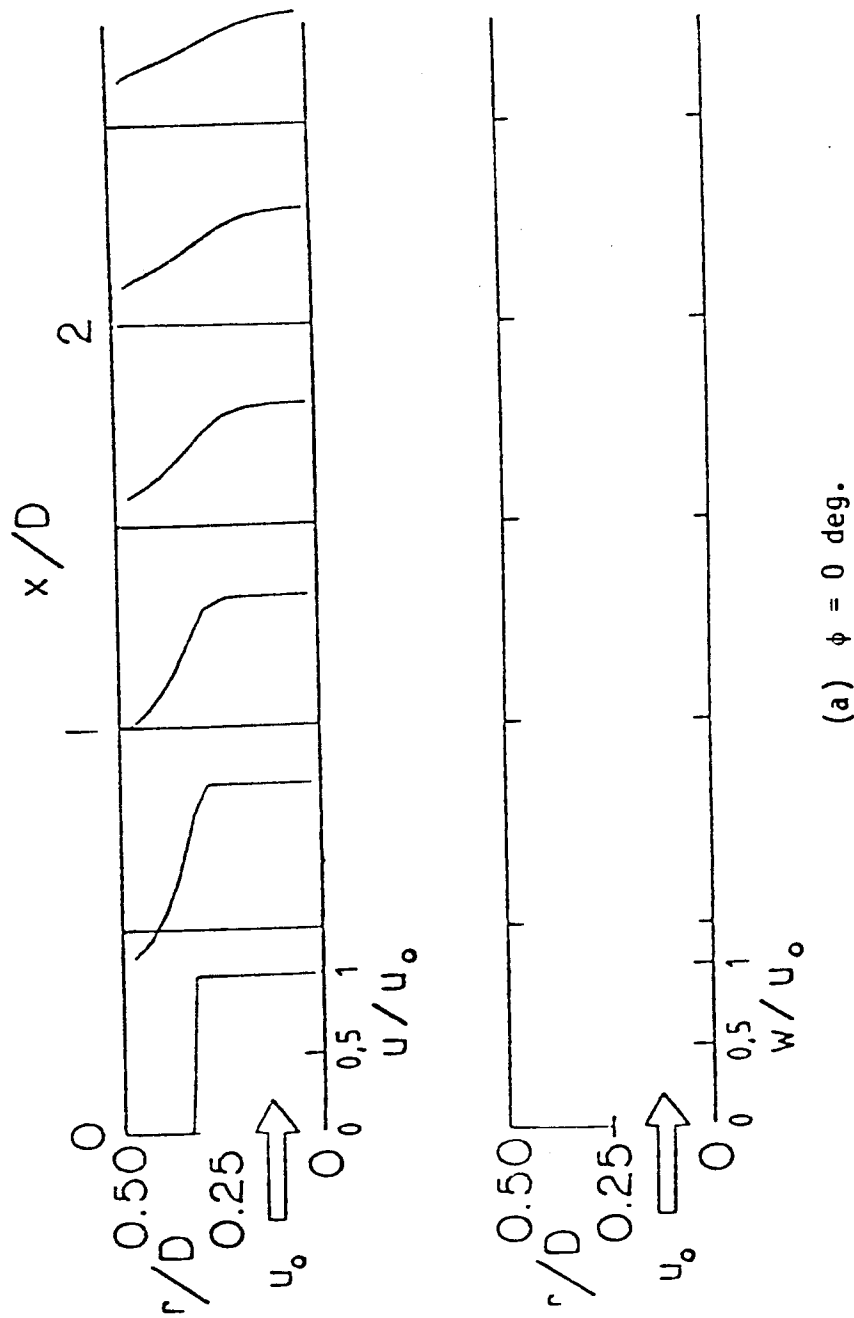
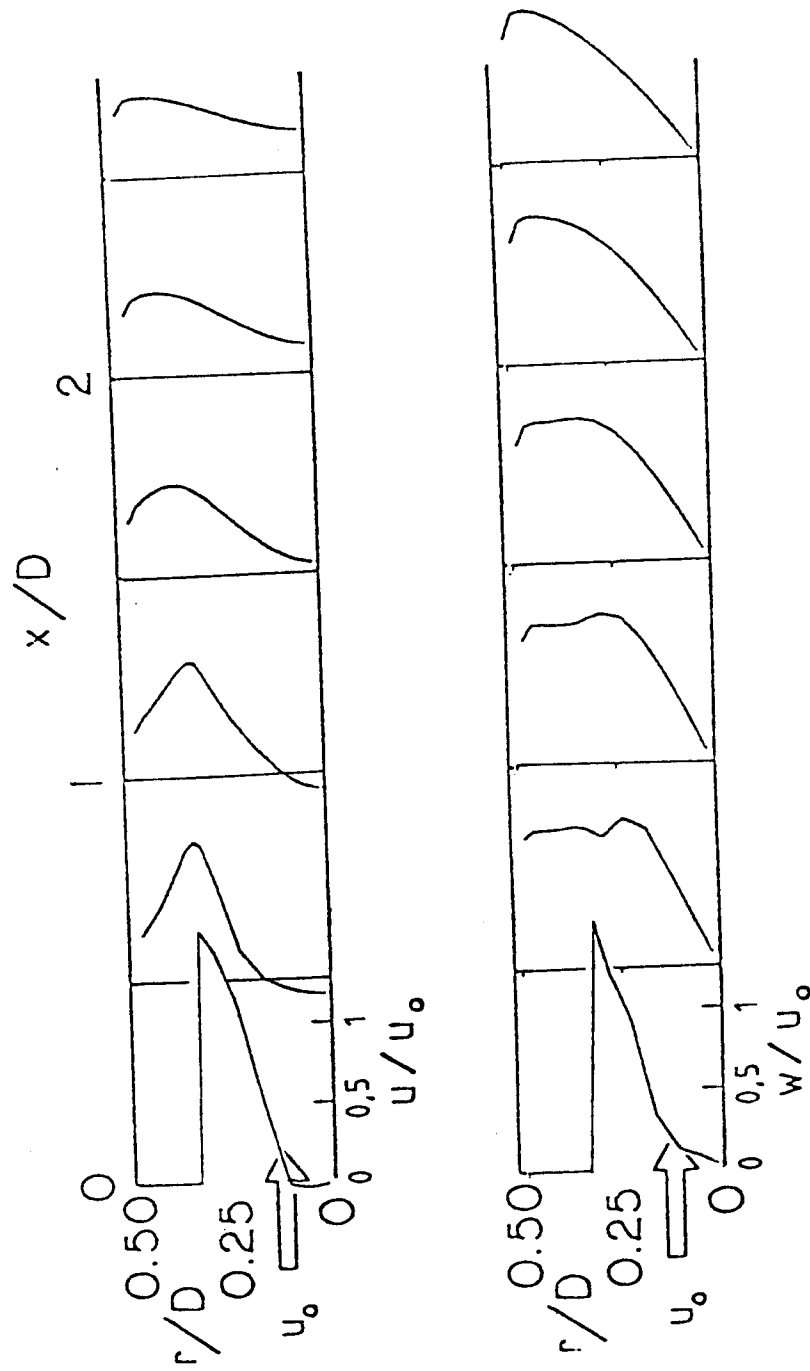
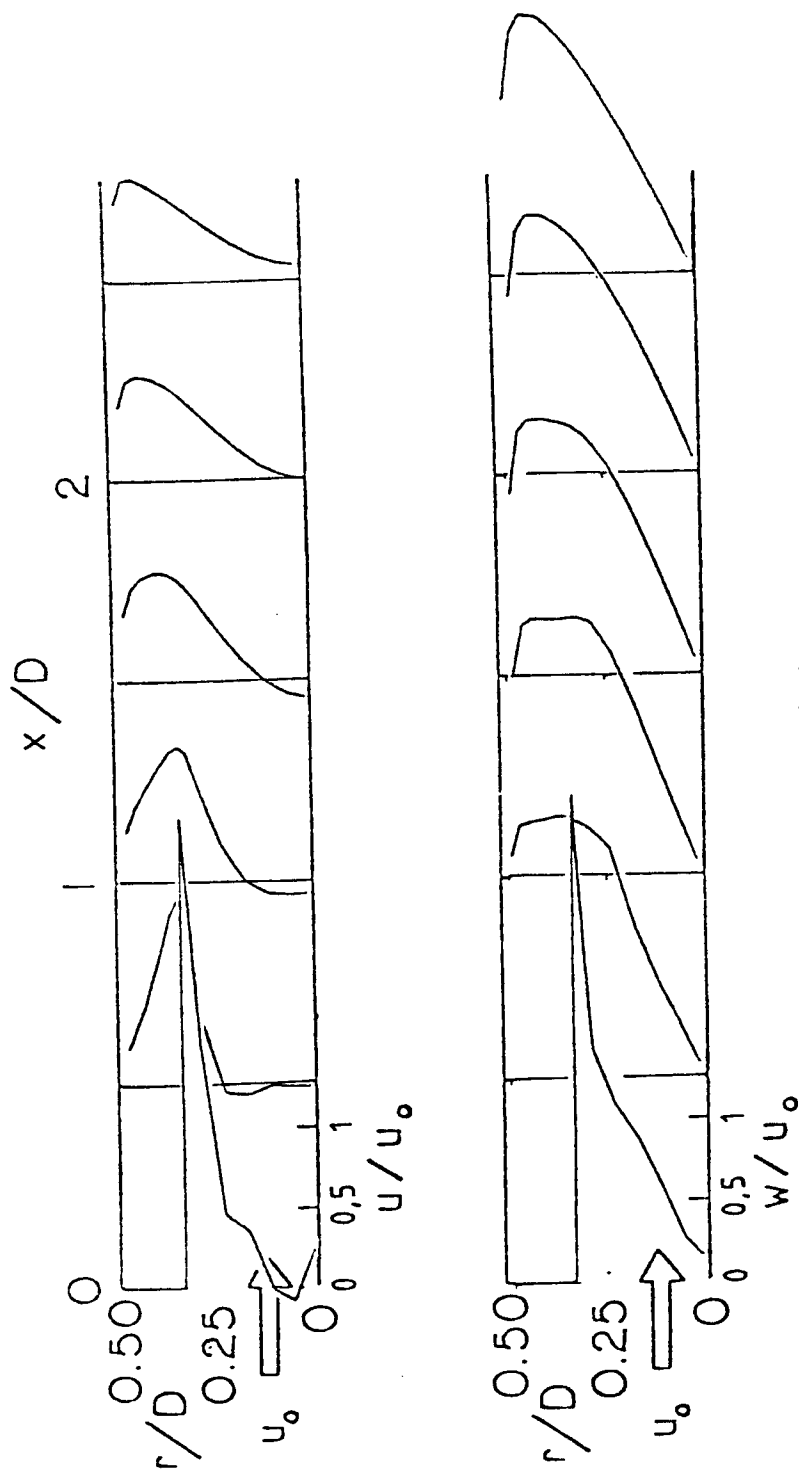


Figure 38. Predicted Velocity Profiles for Flowfield with $D/d = 1.5$
Using Standard $k-\epsilon$ Model



(b) $\phi = 45$ deg.

Figure 38 (Continued)



(c) $\phi = 70^\circ$.

Figure 38 (Continued)

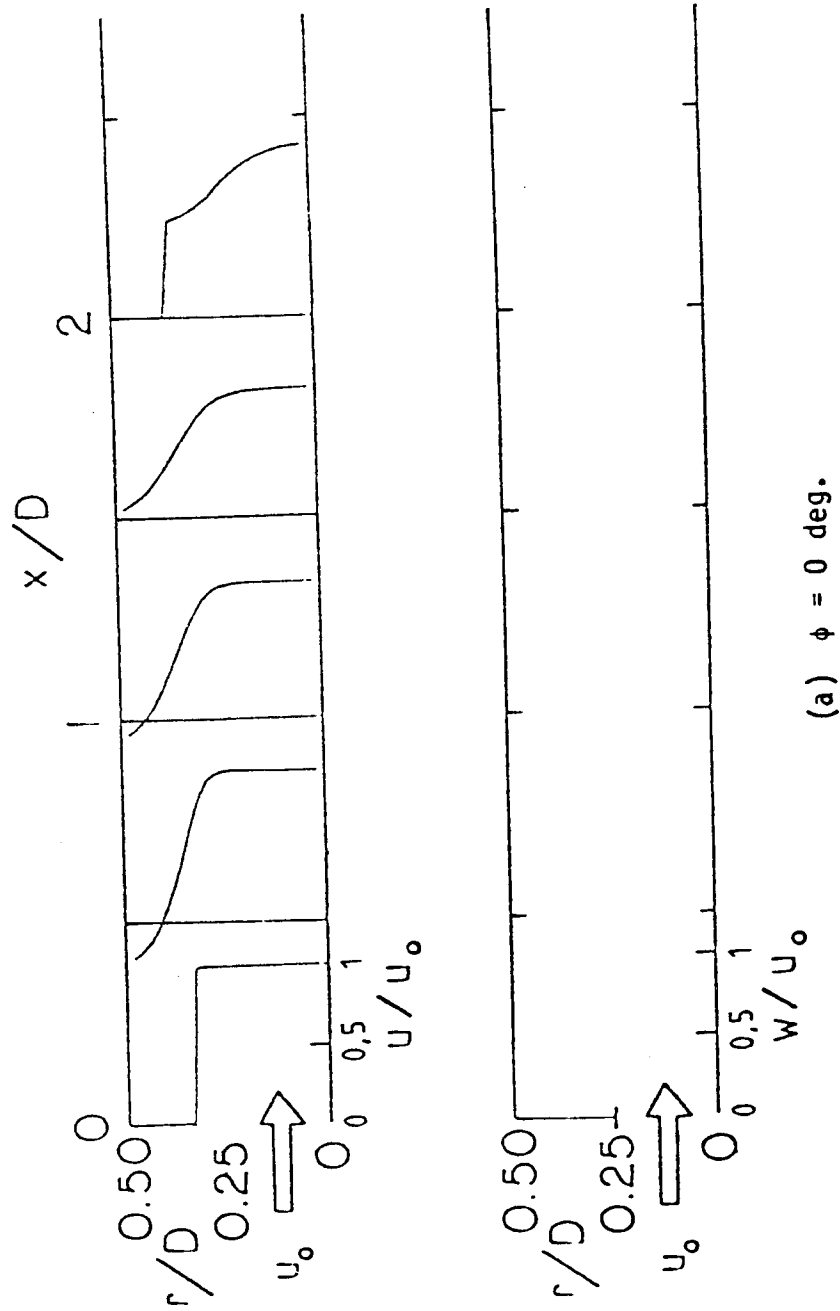
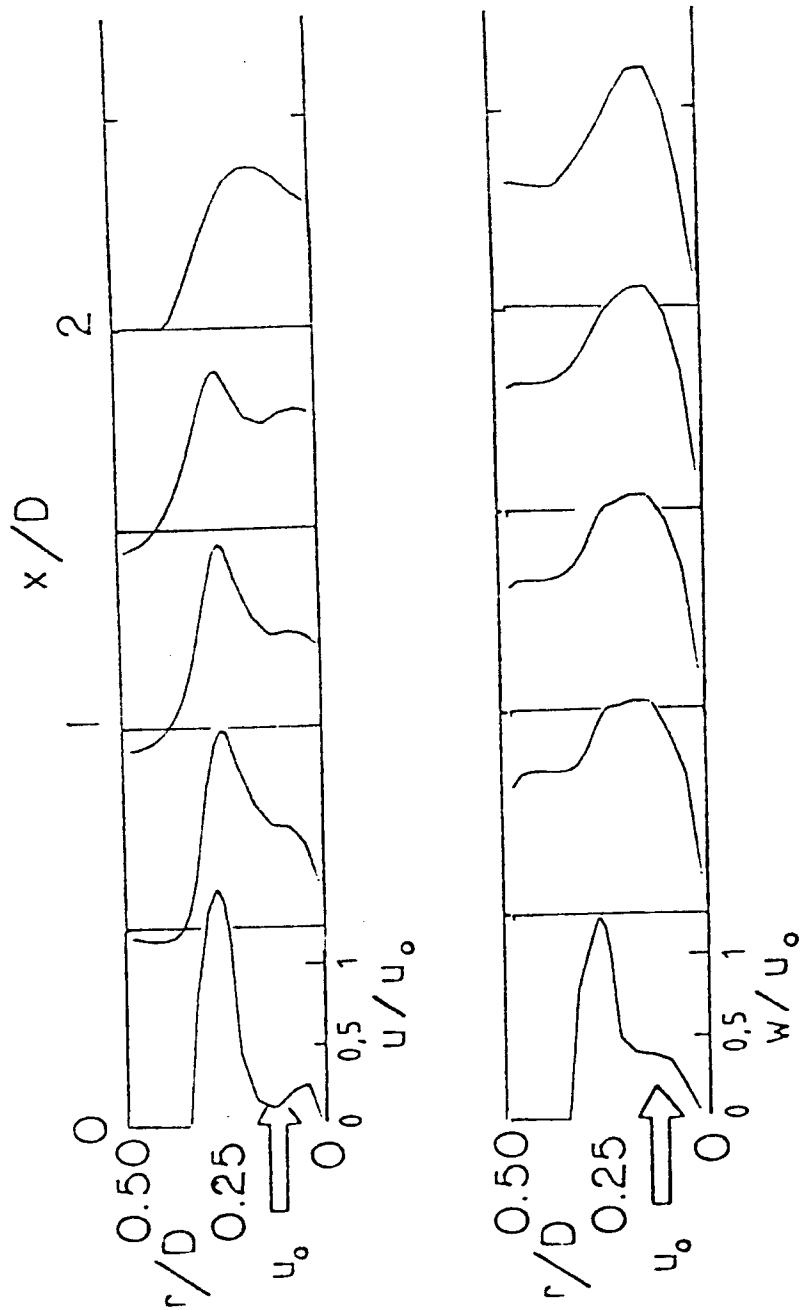
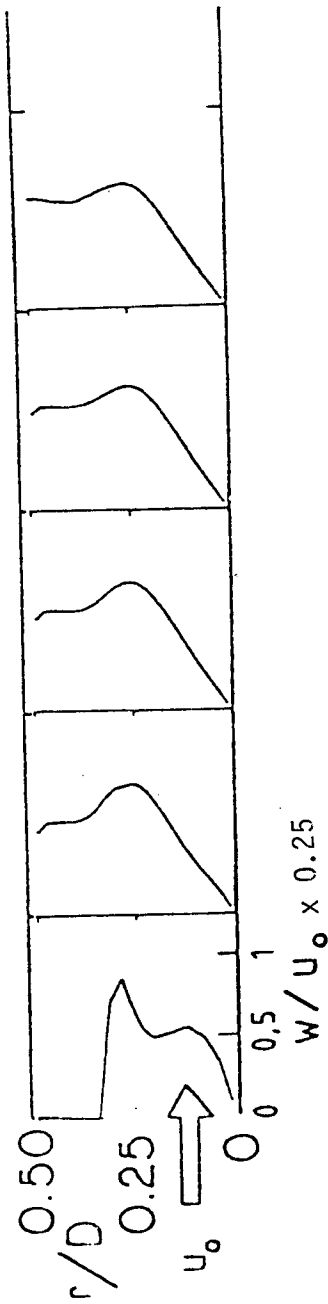
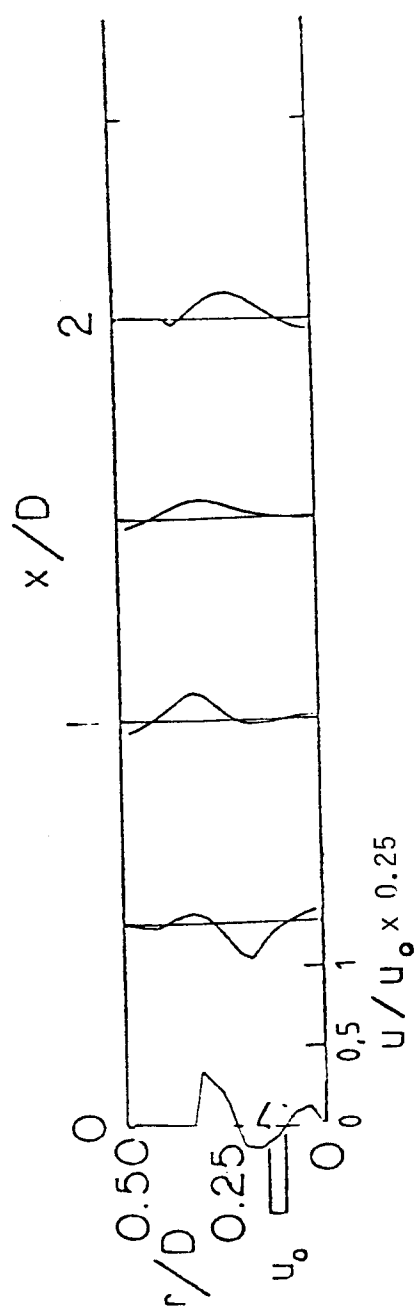


Figure 39. Predicted Velocity Profiles for Flowfield with $D/d = 1.5$ and Strong Nozzle at $L/D = 2$ Using Standard $k-\epsilon$ Model



(b) $\phi = 45$ deg.

Figure 39 (Continued)



(c) $\phi = 70$ deg.

Figure 39 (Continued)

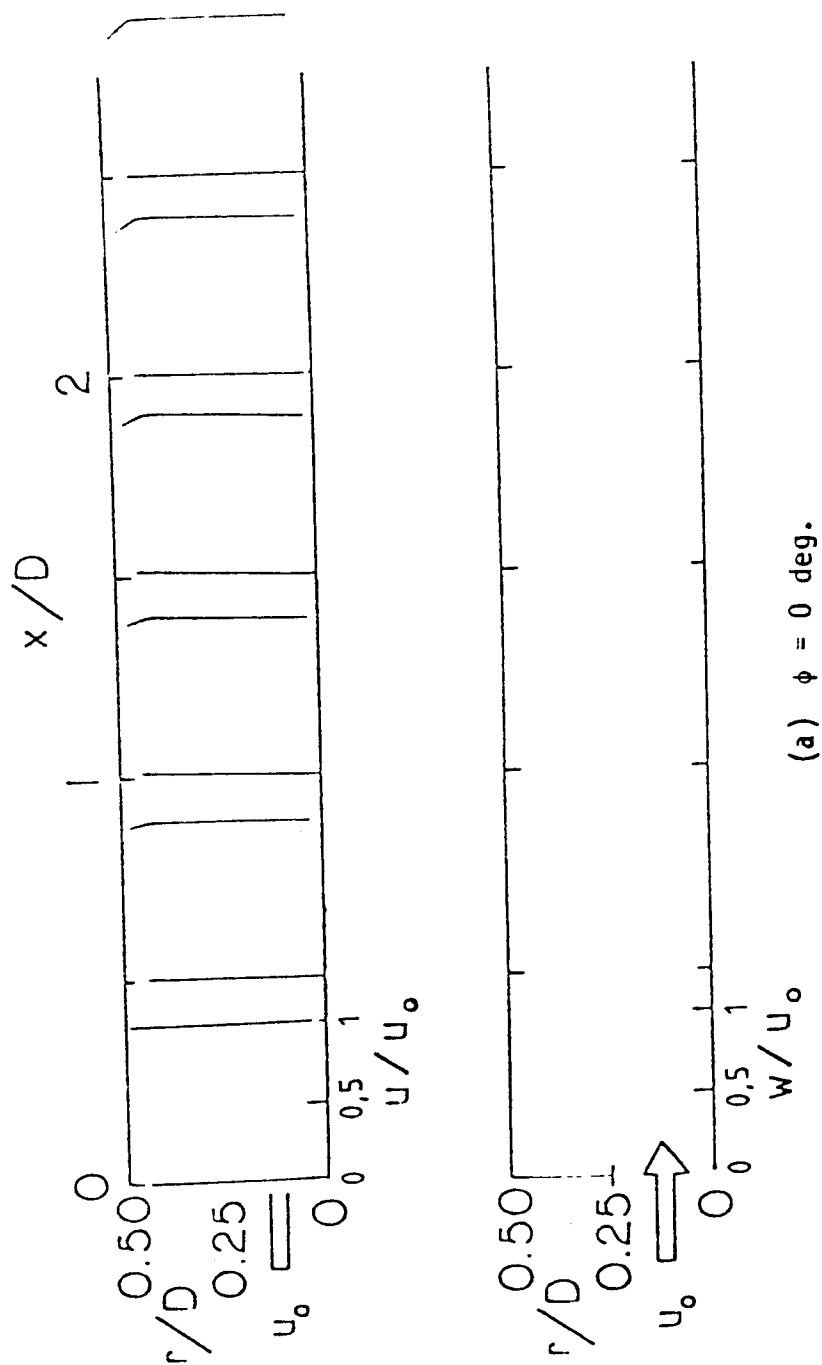
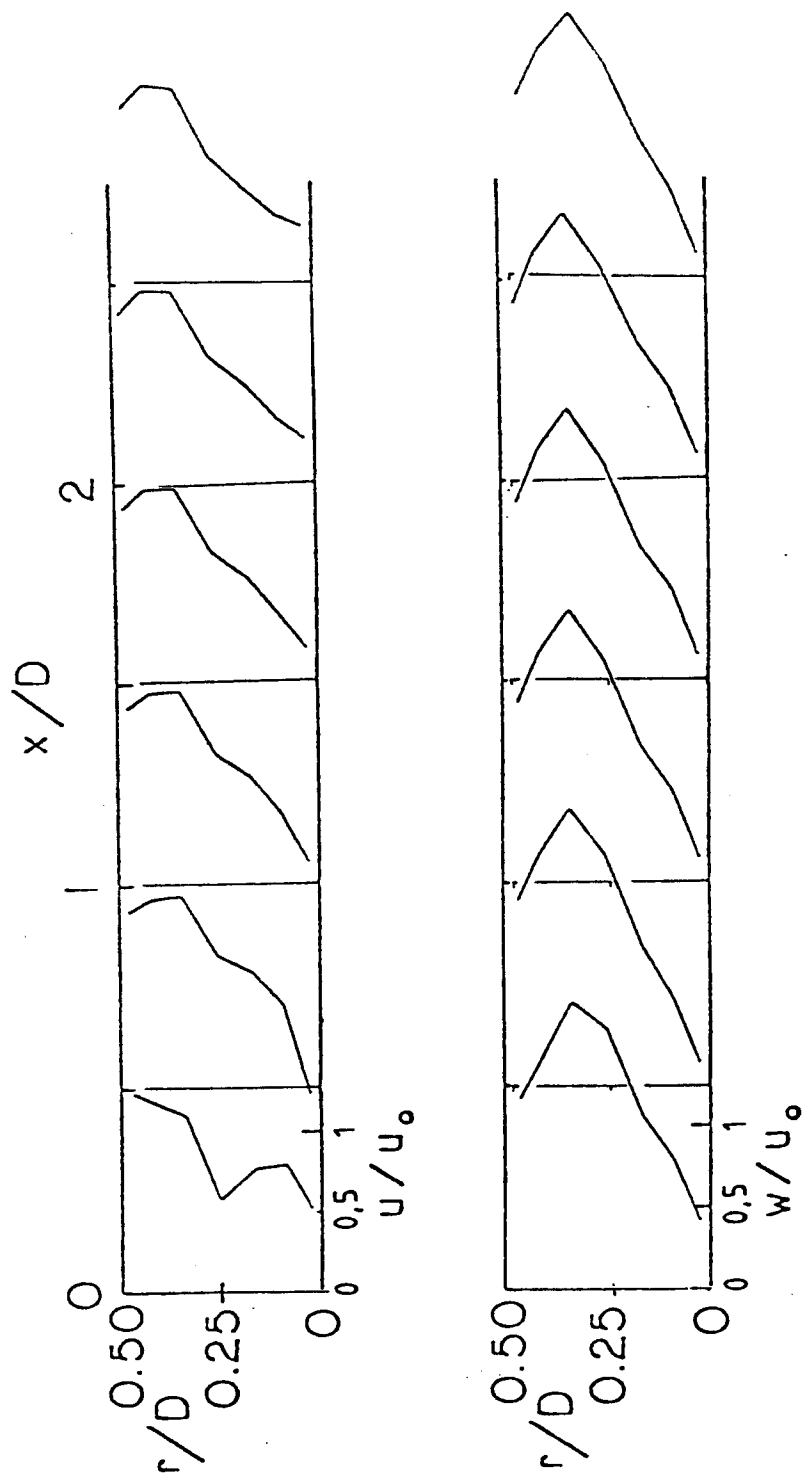
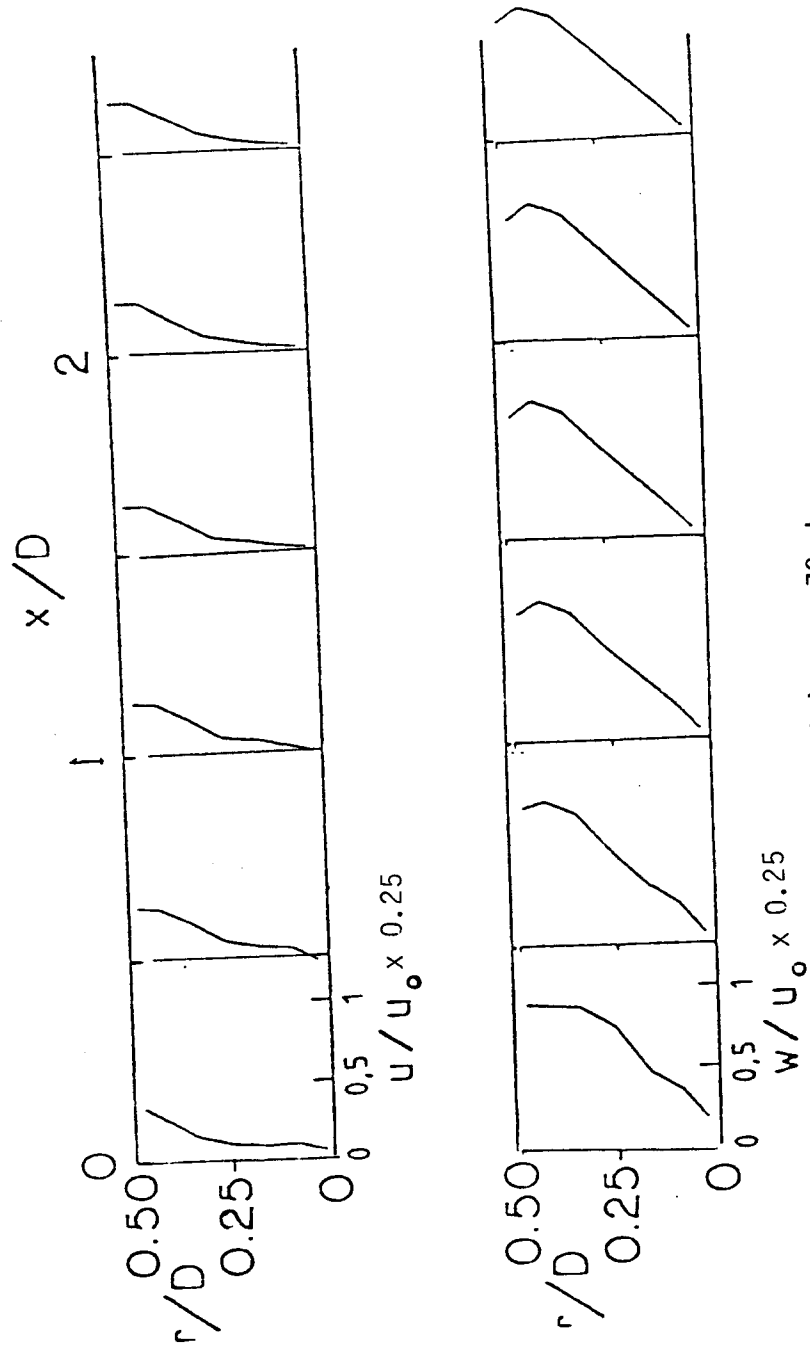


Figure 40. Predicted Velocity Profiles for Flowfield with $D/d = 1$
Using Standard $k-\epsilon$ Model



(b) $\phi = 45$ deg.

Figure 40 (Continued)



(c) $\phi = 70$ deg.

Figure 40 (Continued)

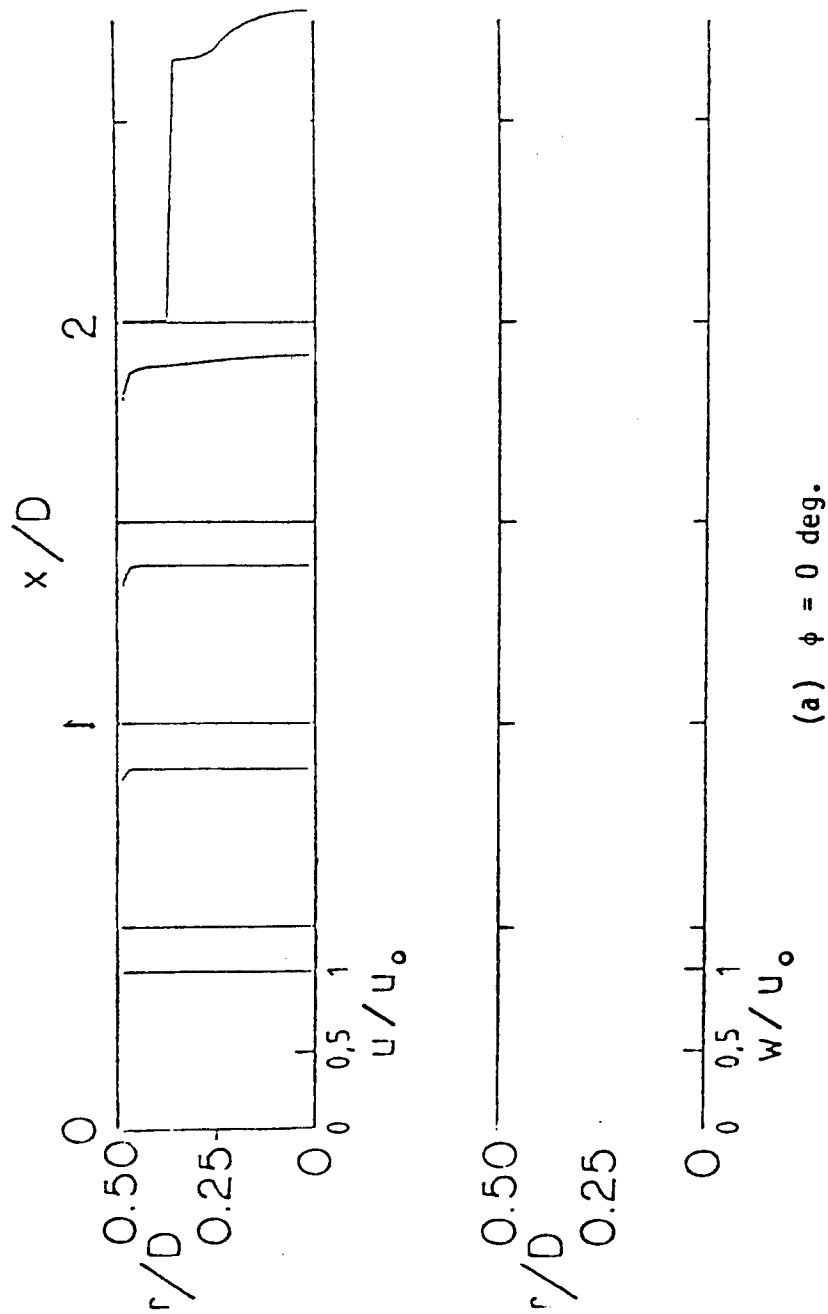
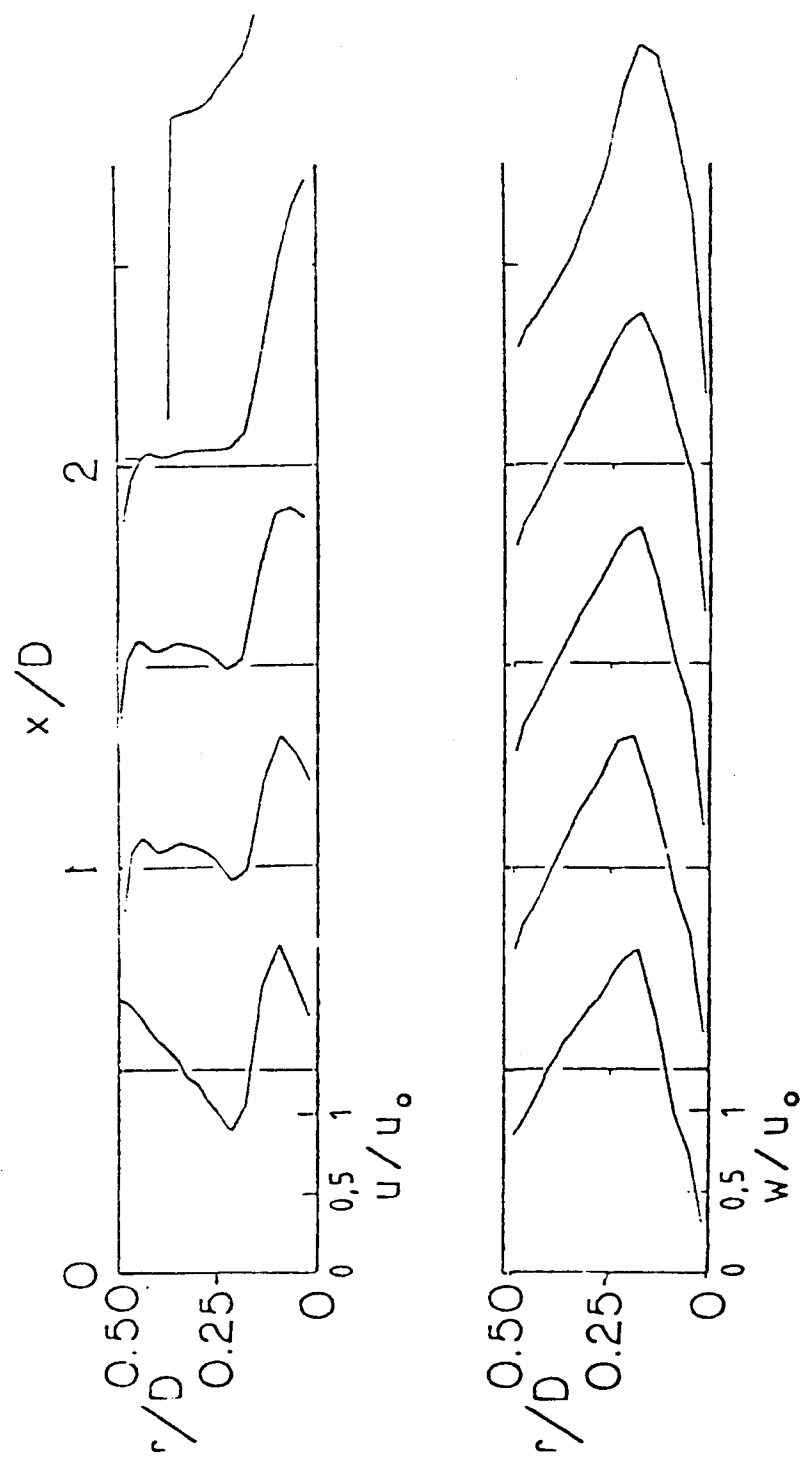
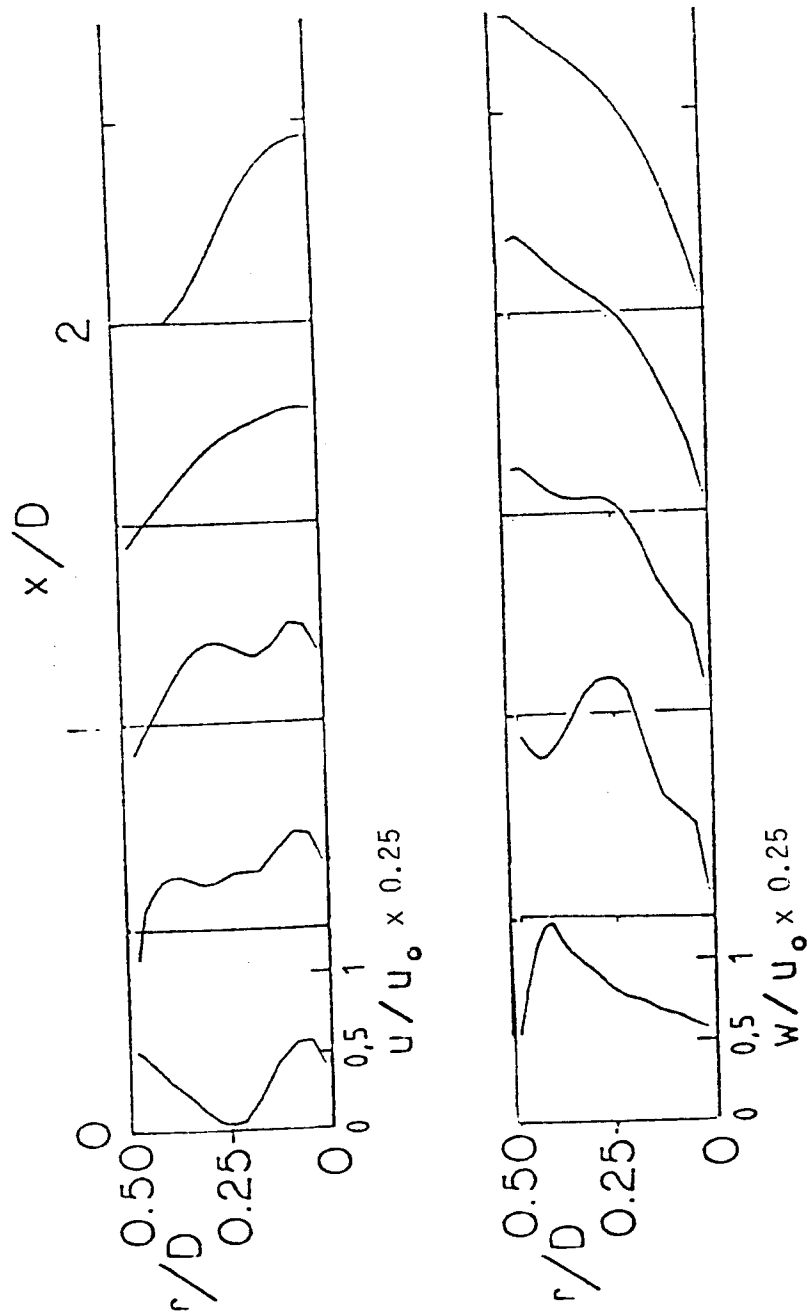


Figure 41. Predicted Velocity Profiles for Flowfield with $D/d = 1$ and Strong Nozzle at $L/D = 2$ Using Standard $k-\epsilon$ Model



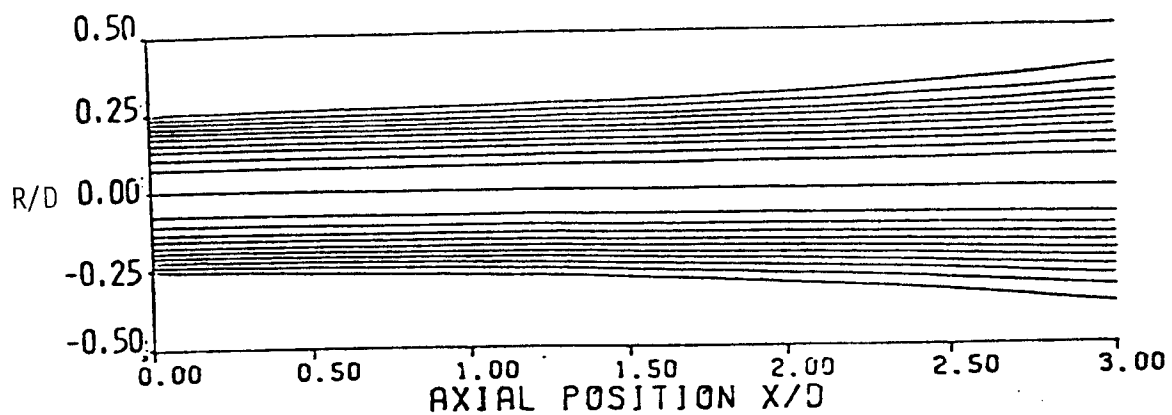
(b) $\phi = 45 \text{ deg.}$

Figure 41 (Continued)

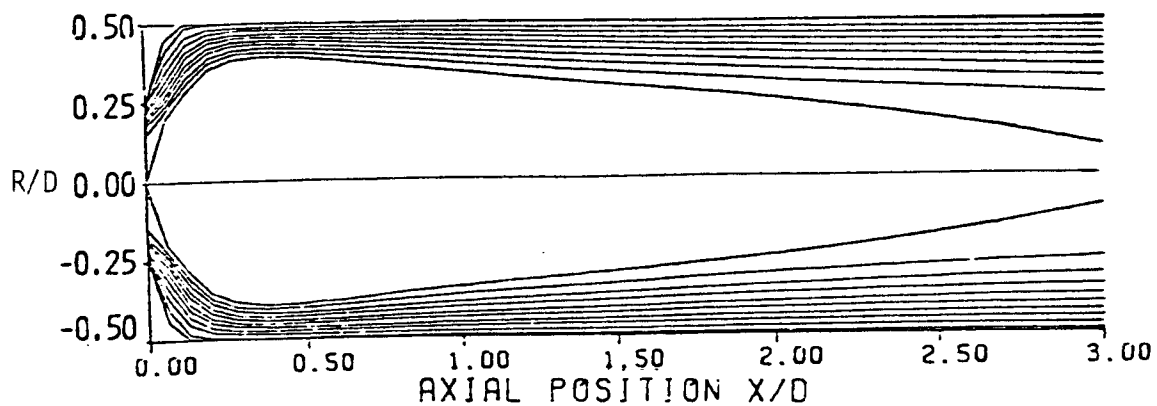


(c) $\phi = 70$ deg.

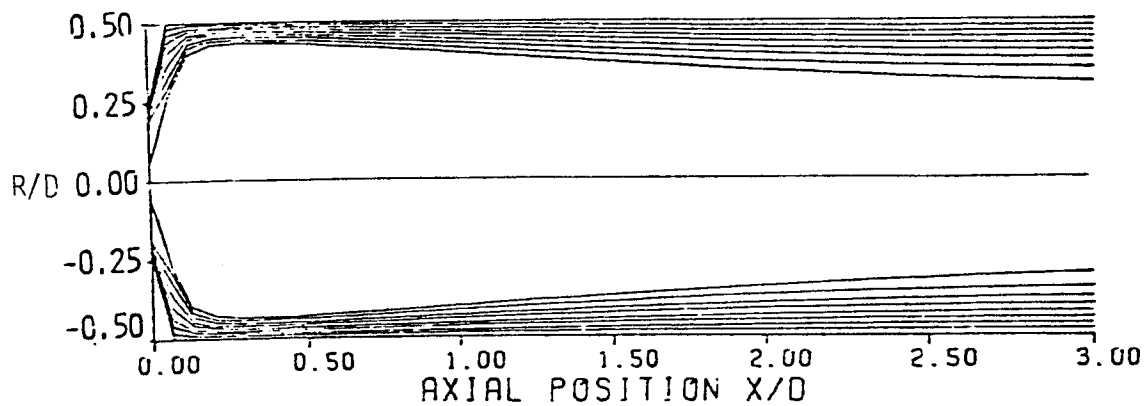
Figure 41 (Continued)



(a) $\phi = 0^\circ$.

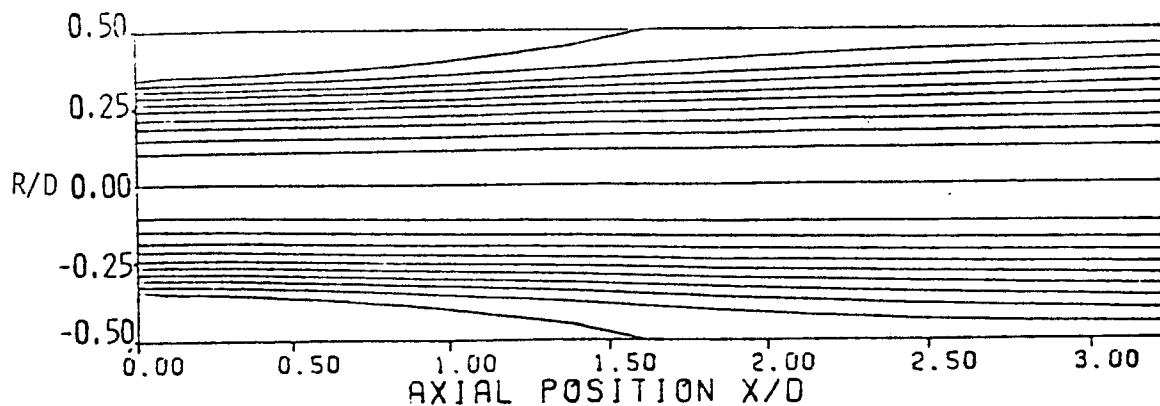


(b) $\phi = 45^\circ$.

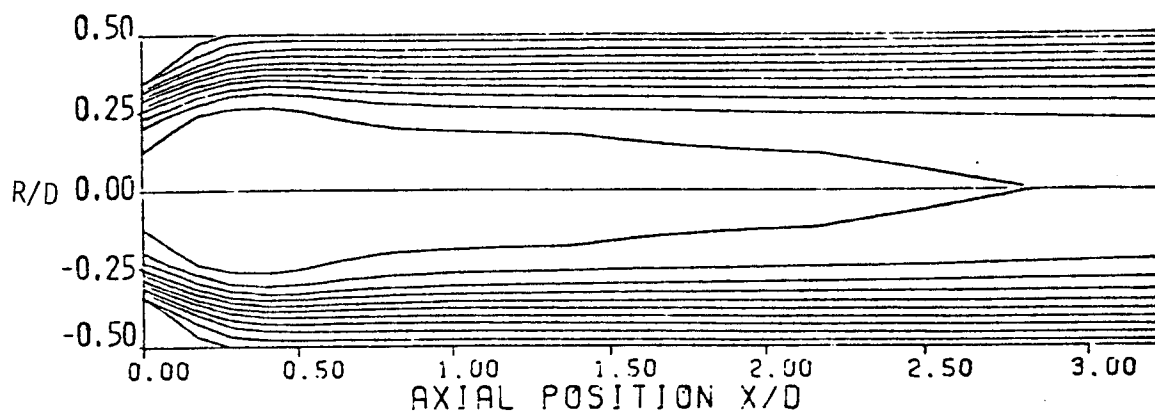


(c) $\phi = 70^\circ$.

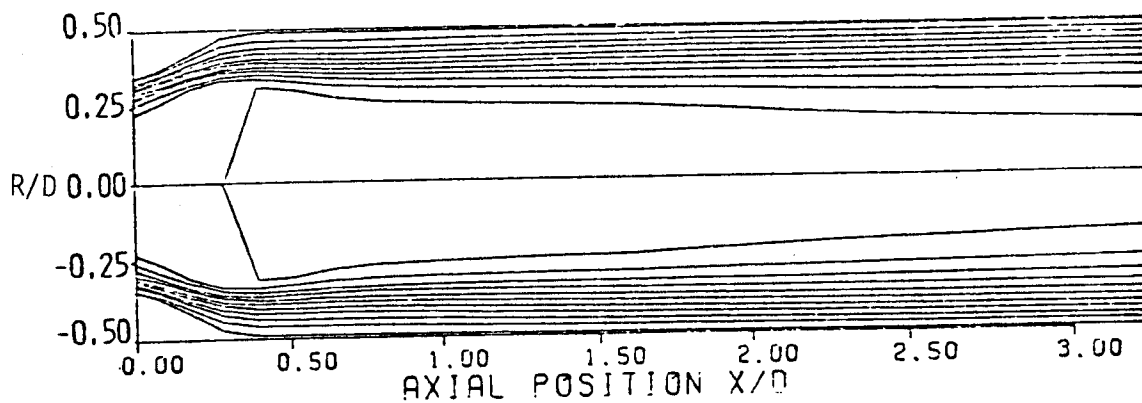
Figure 42. Predicted Streamline Pattern for
Flowfield with $D/d = 2$



(a) $\phi = 0$ deg.



(b) $\phi = 45$ deg.



(c) $\phi = 70$ deg.

Figure 43. Predicted Streamline Pattern for Flowfield with $D/d = 1.5$

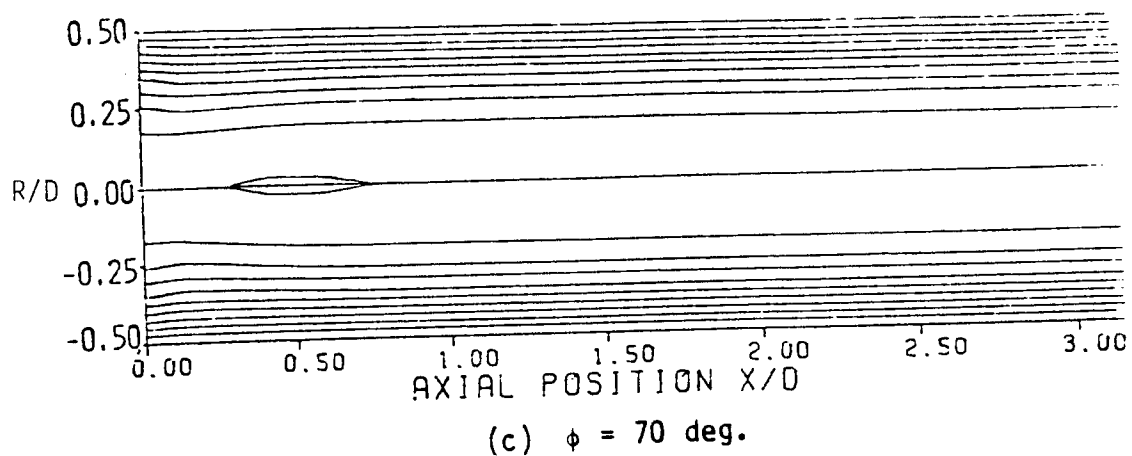
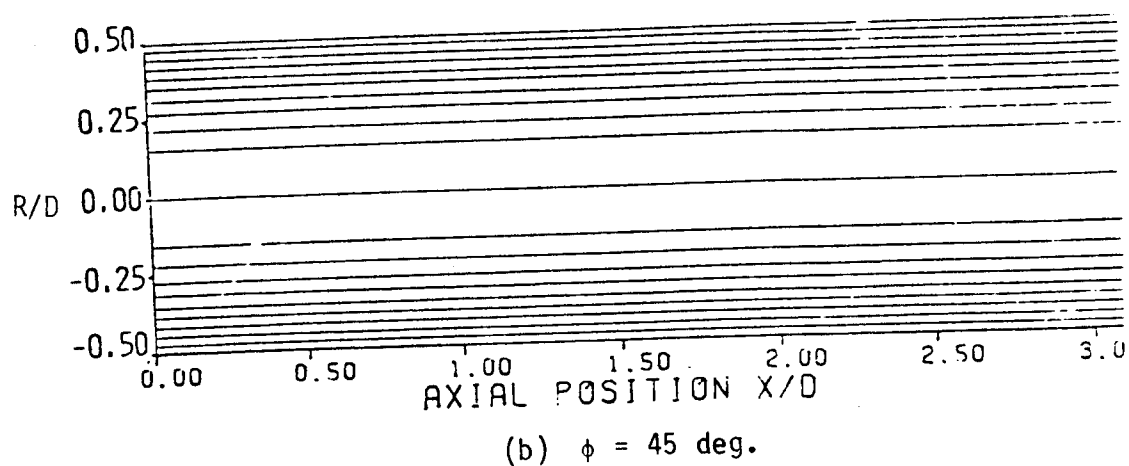
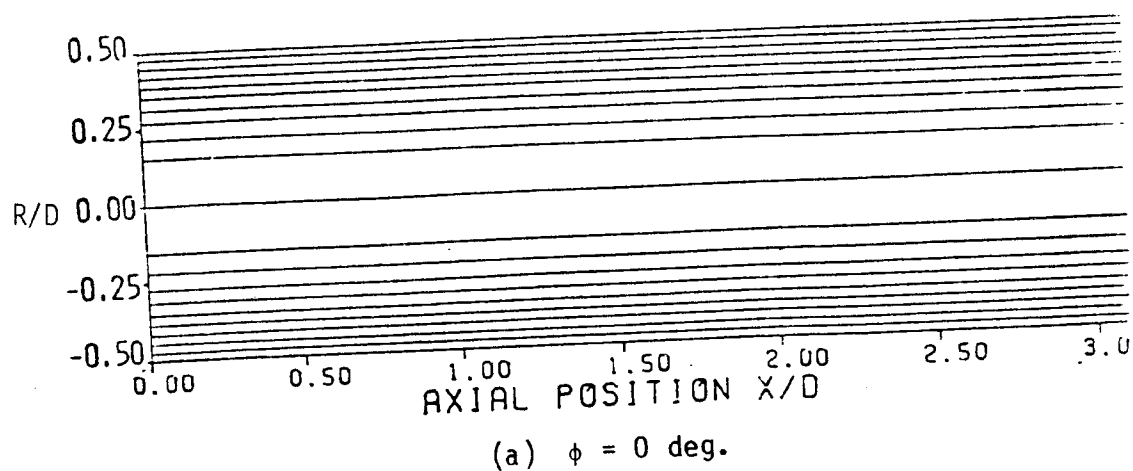


Figure 44. Predicted Streamline Pattern for Flowfield with $D/d = 1$

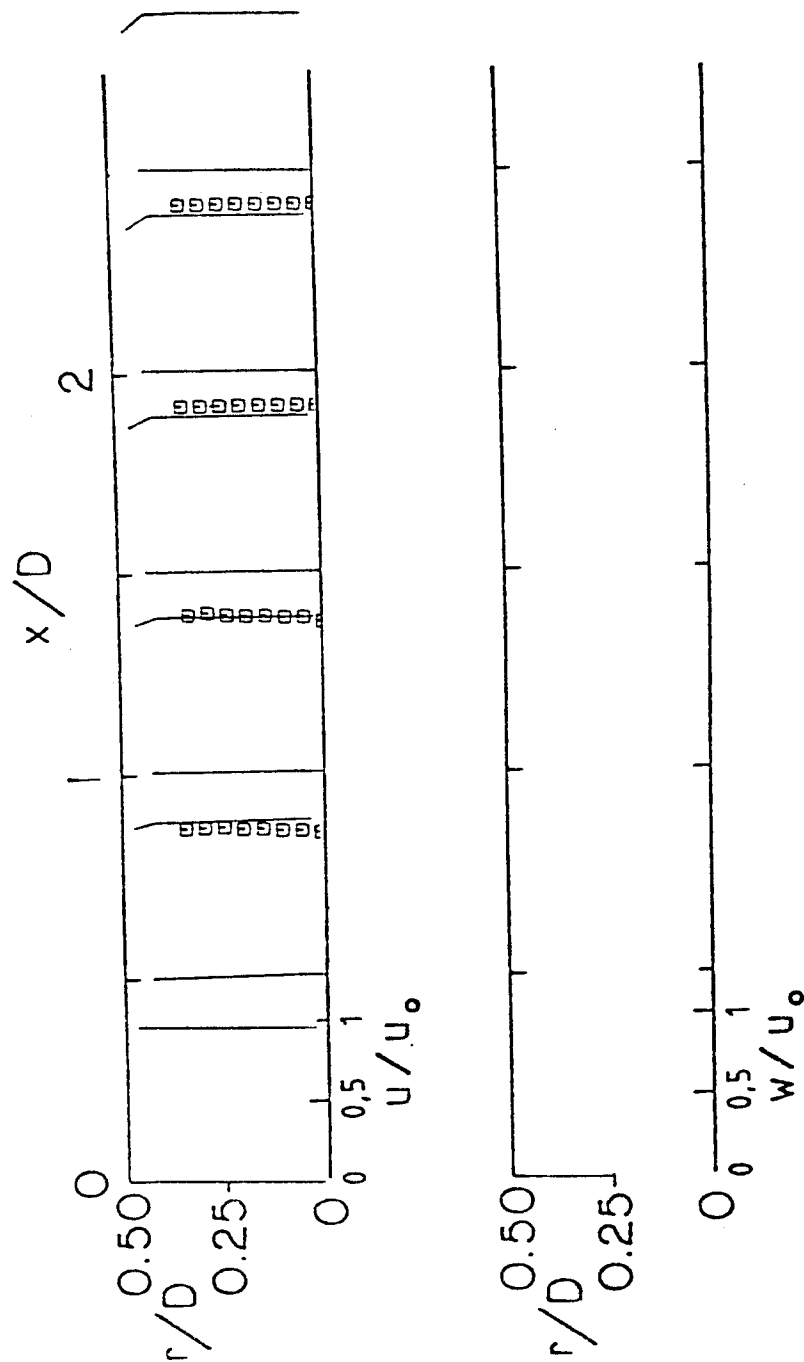
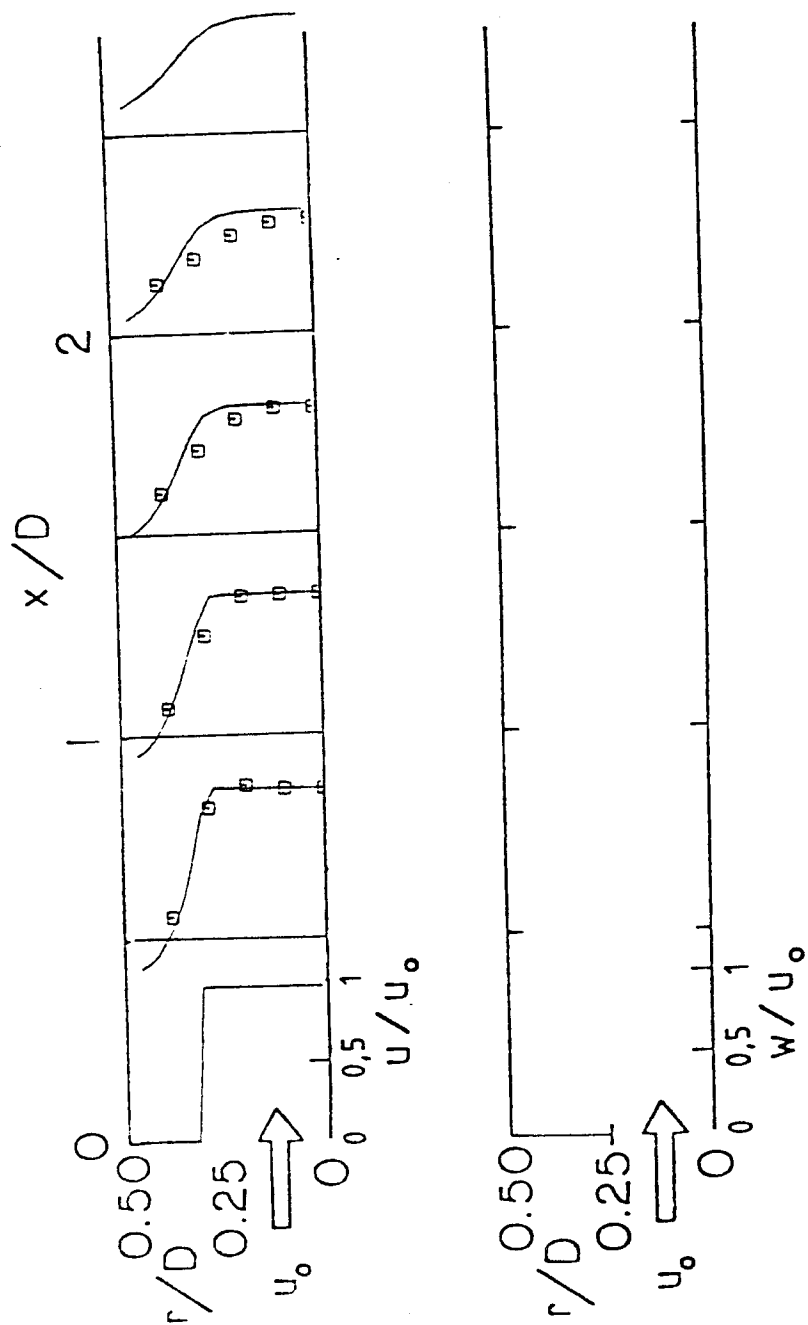
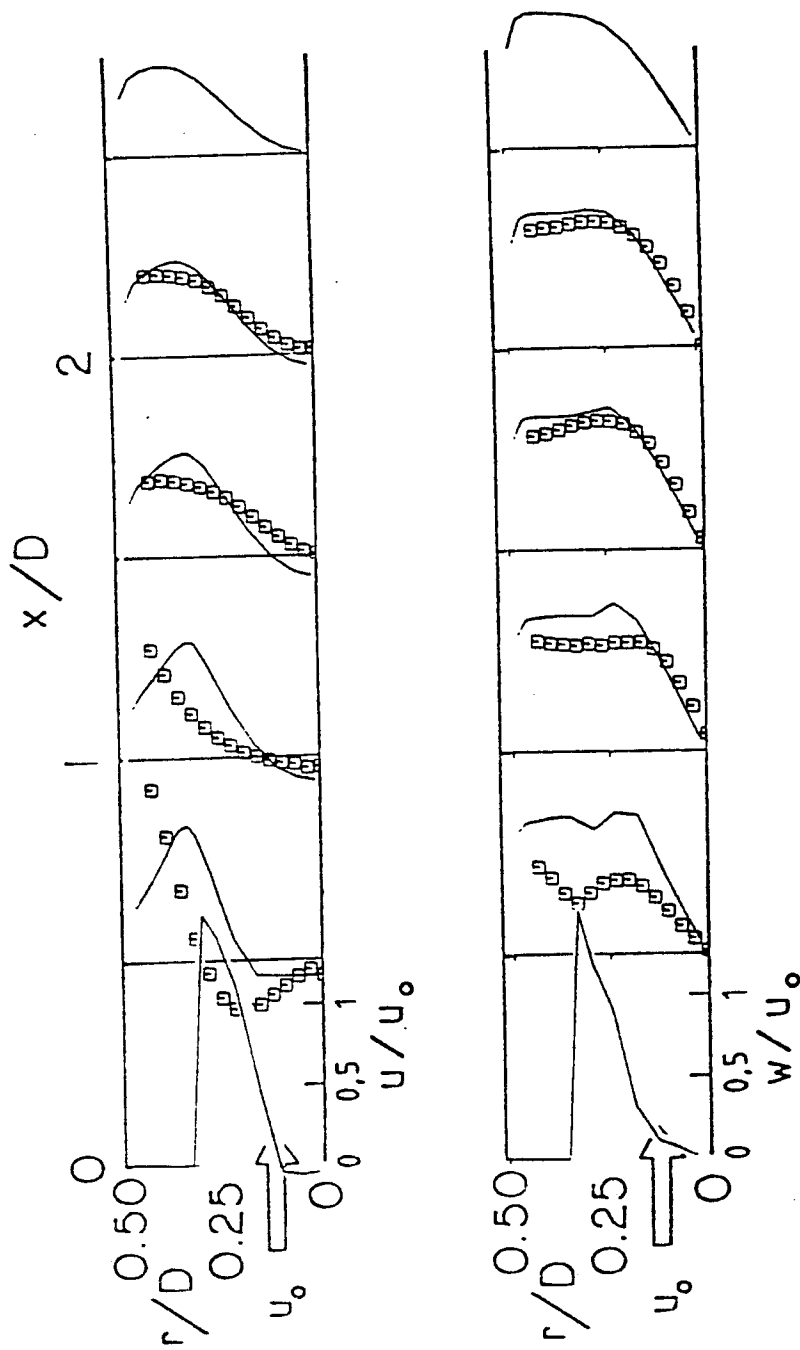


Figure 45. Predicted and Measured Velocity Profiles for Flowfield
with $D/d = 1$, $\phi = 0$ deg. (No Swirler) [□ --Ref. 122]



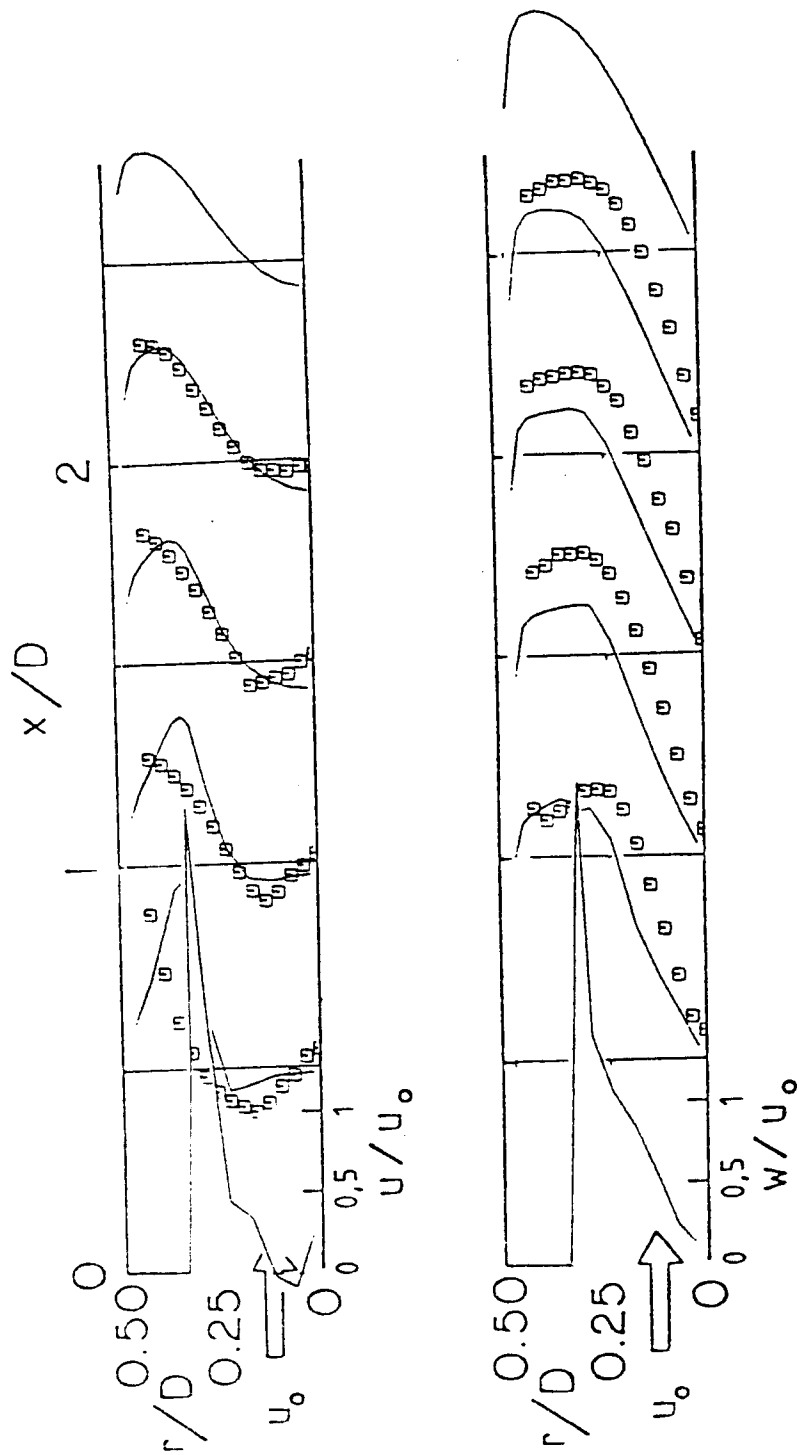
(a) $\phi = 0$ deg.

Figure 46. Predicted and Measured Velocity Profiles for Flowfield with $D/d = 1.5$ [□ --Ref. 122]



(b) $\phi = 45$ deg.

Figure 46 (Continued)



(c) $\phi = 70$ deg.

Figure 46 (Continued)

1. Report No. NASA CR-174917		2. Government Accession No.		3. Recipient's Catalog No.	
4. Title and Subtitle Confined Turbulent Swirling Recirculating Flow Predictions				5. Report Date May 1985	
				6. Performing Organization Code	
7. Author(s) M.T. Abujelala and D.G. Lilley				8. Performing Organization Report No. None	
				10. Work Unit No.	
9. Performing Organization Name and Address Oklahoma State University School of Mechanical and Aerospace Engineering Stillwater, Oklahoma 74074				11. Contract or Grant No. NAG 3-74	
				13. Type of Report and Period Covered Contractor Report	
12. Sponsoring Agency Name and Address National Aeronautics and Space Administration Washington, D.C. 20546				14. Sponsoring Agency Code 533-04-1A	
15. Supplementary Notes Final report. Project Manager, James D. Holdeman, Internal Fluid Mechanics Division, NASA Lewis Research Center, Cleveland, Ohio 44135. This report was a dissertation submitted by M.T. Abujelala to the Faculty of the Graduate School of Oklahoma State University in partial fulfillment of the requirements for the degree Doctor of Philosophy in May 1984.					
16. Abstract The main goal is to increase the capability and the accuracy of the STARPIC computer code in predicting confined turbulent swirling recirculating flows. Inlet flow boundary conditions have been demonstrated to be extremely important in simulating a flowfield via numerical calculations. Predictions with either flat inlet profiles, solid body rotation or zero radial velocity are inappropriate. The degree of swirl strength and expansion ratio have strong effects on the characteristics of swirling flow. In a nonswirling flow, a large corner recirculation zone exists in the flowfield with an expansion ratio greater than one. However, as the degree of inlet swirl increases, the size of this zone decreases and a central recirculation zone appears near the inlet. Generally, the size of the central zone increased with swirl strength and expansion ratio. Neither the standard $k-\epsilon$ turbulence mode nor its previous extensions show effective capability for predicting confined turbulent swirling recirculating flows. However, either reduced optimum values of three parameters in the mode or the empirical C_μ formulation obtained via careful analysis of available turbulence measurements, can provide more acceptable accuracy in the prediction of these swirling flows.					
17. Key Words (Suggested by Author(s)) Combustor; Swirl; Turbulent flow; Prediction; Turbulence models; STARPIC				18. Distribution Statement Unclassified - unlimited STAR Category 07	
19. Security Classif. (of this report) Unclassified		20. Security Classif. (of this page) Unclassified		21. No. of pages 224	
				22. Price* A10	